Imperial College London

The development of optical projection tomography instrumentation and its application to in vivo three dimensional imaging of zebrafish

Samuel Pascal Xia Davis

Photonics Group
Department of Physics
Imperial College London
Supervised by Prof. Paul M. W. French & Dr James McGinty

2019

Thesis submitted in partial fulfilment of the requirements for the degree of
Doctor of Philosophy (PhD)

Abstract

OPT is a three dimensional (3D) imaging technique that can produce 3D reconstructions of transparent samples, requiring only a widefield imaging system and sample rotation. OPT can be readily applied to chemically cleared samples, or to live transparent organisms such as nematodes or zebrafish. For preclinical imaging, there is a trade-off between optical accessibility and biological relevance to humans. Adult Danio rerio (zebrafish) represent a promising compromise, with greater homology to humans than smaller animals, and superior optical accessibility than mice. However, their size and physiology present a number of imaging challenges including non-negligible absorption and optical scattering, and limited time for image data acquisition if the fish are to be recovered for longitudinal studies. A key goal of this PhD thesis research was to develop OPT to address these challenges and improve *in vivo* imaging capabilities for this model organism.

This thesis builds on previous work at Imperial where angularly multiplexed OPT using compressed sensing was developed and applied to *in vivo* imaging of a cancer-burdened adult zebrafish, with a sufficiently short OPT data acquisition time to allow recovery of the fish after anaesthesia. The previous cross-sectional study of this work was extended to a longitudinal study of cancer progression that I undertook. The volume and quality of data acquired in the longitudinal study presented a number of data processing challenges, which I addressed with improved automation of the data processing pipeline and with the demonstration that convolutional neural networks (CNN) could replace the iterative compressed sensing algorithm previously used to suppress artifacts when reconstructing undersampled OPT data sets.

To address the issue of high attenuation through the centre of an adult zebrafish, I developed conformal-high-dynamic-range (C-HDR) OPT and demonstrated that it could provide sufficient dynamic range for brightfield imaging of such optically thick samples, noting that transmitted light images can provide anatomical context for fluorescence image data.

To reduce the impact of optical scattering in OPT, I developed a parallelised quasi-confocal version of OPT called slice-illuminated OPT (slice-OPT) to reject scattered photons and demonstrated this with live zebrafish. To enable 3D imaging with short wave infrared (SWIR) light, without the requirement of an expensive Ge or InGaAs camera, I implemented a single pixel camera and demonstrated single-pixel OPT (SP-OPT) for the first time.

Declaration

I declare that the work submitted in this thesis is original except where specifically referenced, and the following exceptions. The angularly multiplexed OPT system and acquisition software, and the laser diode based OPT system and acquisition software was developed by and with, respectively, Dr. Sunil Kumar, from the Photonics group, Imperial College London.

The longitudinal study presented in chapter 4 was performed with Laura Wisniewski, from Dr. Paul Frankel's laboratory in the Institute of Cardiovascular Science, University College London.

The zebrafish for biological imaging were provided for chapters 4 and 7 by Laura Wisniewski, from Dr. Paul Frankel's laboratory in the Institute of Cardiovascular Science, University College London, and in chapter 6 by Ralf Wenz, from Prof. Maggie Dallman's laboratory in the Department of Life Sciences, Imperial College London. The mouse pancreas samples were provided by Gabriela da Silva Xavier, from Prof. Guy Rutter's laboratory in the Faculty of Medicine, Imperial College London. The ovarian cancer biopsies were provided by Dr. Paula Cunnea and Prof. Christina Fotopoulou in the Faculty of Medicine, Imperial College London, and Moath Alamer, from Prof. Xiao Yun Xu's laboratory in the Department of Chemical Engineering, Imperial College London. The mouse lung samples were provided by Ajay Bhargava, from Prof. Erik Sahai's group at the Francis Crick Institute.

The zebrafish embryo data set presented in chapter 5 was acquired by Dr. Teresa Correia, Department of Computer Science, University College London, Dr. Sunil Kumar, from the Photonics group, Imperial College London, and Dr. Nicola Lockwood, from Dr. Paul Frankel's laboratory in the Institute of Cardiovascular Science, University College London. The pancreas data sets were acquired by Gabriela da Silva Xavier, from Prof. Guy Rutter's laboratory in the Faculty of Medicine, Imperial College London. The lung data sets were acquired by Dr. Sunil Kumar, from the Photonics group, Imperial College London, and Ajay Bhargava, from Prof. Erik Sahai's group at the Francis Crick Institute.

Samuel P X Davis
2019

Publications and Presentations

Publications

- **Davis SPX**, Kumar S, Alexandrov Y, Bhargava A, da Silva Xavier G, Rutter GA, Frankel P, Sahai E, Flaxman S, French PMW, McGinty J. Convolutional neural networks for reconstruction of undersampled optical projection tomography data applied to in vivo imaging of zebrafish. *Journal of Biophotonics.* 2019 Aug:e201900128.
- **Davis SPX**, Wisniewski L, Kumar S, Correia T, Arridge SR, Frankel P, McGinty J, French PMW. Slice-illuminated optical projection tomography. *Optics letters.* 2018 Nov 15;43(22):5555-8.
- Watson T, Andrews N, **Davis SPX**, Bugeon L, Dallman MD, McGinty J. OPTiM: Optical projection tomography integrated microscope using open-source hardware and software. *PloS one.* 2017 Jul 11;12(7):e0180309.

Presentations

- **Davis SPX**, Kumar S, Wisniewski L, Ramel MC, Bugeon L, Correia T, Dallman M, Arridge S, Frankel P, McGinty J, French PMW. Exploiting patterned illumination and detection in optical projection tomography. *SPIE BiOS Photonics West.* 2019 Mar 4 (Vol. 10883, p. 108830M).
- **Davis SPX**, Kumar S, Steele E, Wisniewski L, Ramel MC, Bugeon L, Correria T, Parrado T, Graham J, Dallman M, Arridge S, Frankel P, Mcginty J, French PMW. Lower cost, open source OPT and enhanced performance using structured illumination. *Frontiers in Bioimaging.* 2018 Jun 28.

To Mum and Dad

Acknowledgements

Firstly, I would like to thank my supervisors Paul French and James McGinty for the opportunity to work on this PhD project and for all the help, guidance, moral support and material support over the years. Thank you also to Sunil Kumar for his aid and wisdom in the lab, and Seth Flaxman for his advice on neural networks. I would like to thank Martin, Simon, and John in the Optics workshop, without whose expertise the systems described in this thesis would not exist. A special thanks to Laura Wisniewski and Paul Frankel, for their hard work on our longitudinal study collaboration, and other collaborators Ralf Wenz, Margaret Dallman, Guy Rutter, and Moath Alamer, who provided other zebrafish and tissue samples used in experiments.

Thank you to all my colleagues at Imperial: Tom, Vincent, Elizabeth, Natalie, Wenjun, Hugh, Nathan, Fred, Giulia, Terry, Jonny, Connor, Ricardo, Jack, Anita, Andrew, Joel, Yuchen, Cheryl, Daniel, Liuba, and many others. Thank you for lunches, pub trips, coffee, badminton, ping pong, and chess.

Thank you to my loved ones for being there, and helping me get this far. Thank you to Mum and Dad, for feeding and clothing me, and letting me crash at their place when needs be. Thank you to Alec and Abi, Tali and Jack, Phoebe, Caspar, and Leo for being my loving family. Thank you to Zu for going off to California, and giving all the inspiration I needed to get this written on time.

Finally, thank you to The Engineering & Physical Sciences Research Council for funding my PhD.

"There's always a bigger fish"
Qui-Gon Jinn

Contents

1 Thesis overview **21**

2 Introduction to whole organism optical imaging **24**

2.1 Interaction of light and tissue 24

2.1.1 Absorption and fluorescence 24

2.1.2 Scattering 26

2.1.2.1 Clearing 28

2.2 Fluorescence Microscopy 30

2.2.1 Laser scanning microscopy 32

2.2.2 Selective plane illumination microscopy 33

2.2.3 Optical projection tomography 33

2.3 Whole organism imaging 33

3 Optical projection tomography **36**

3.1 Developments and applications of optical projection tomography 36

3.2 Parallel projection and tomographic reconstruction 38

3.3 Optical projection tomography 41

3.4 Example optical projection tomography systems 42

3.4.1 Light emitting diode based optical projection tomography system 42

3.4.2 Laser diode optical projection tomography system 42

3.4.3 Acquisition and reconstruction 42

3.5 Compressive sensing 46

4 Optimisation of angularly multiplexed optical projection tomography **51**

4.1 Introduction 51

4.2 Methods 52

4.2.1 Experimental set up and acquisition 52

4.2.2 Longitunial study of tumour development 53

4.2.3 Processing 54

4.2.3.1 Registration 54

4.2.3.2 Alignment with rotation axis 55

4.2.3.3 Compressed sensing reconstruction 57

4.2.3.4 Segmentation 61

4.3 Results . . . 62
4.4 Conclusion . . . 64

5 Convolutional neural networks for reconstruction of undersampled optical projection tomography data 69
5.1 Methods . . . 70
5.1.1 Convolutional neural networks . . . 70
5.1.1.1 Network . . . 70
5.1.1.2 Stochastic gradient descent and backpropagation . . . 72
5.1.1.3 Batch normalisation . . . 75
5.1.2 Network architecture . . . 75
5.1.3 Data and training . . . 76
5.1.4 Samples and optical projection tomography data acquisition . . . 79
5.2 Results . . . 80
5.2.1 Application to *ex vivo* data from test data set . . . 80
5.2.2 Application to *in vivo* data from zebrafish embryo data set . . . 81
5.2.2.1 Sensitivity of iterative CS and CNN methods . . . 85
5.3 Conclusion . . . 85

6 Conformal high dynamic range optical projection tomography 88
6.1 Hardware and operation . . . 89
6.1.1 Hardware . . . 89
6.1.2 Data acquisition . . . 90
6.1.3 Projection fusion . . . 91
6.2 Characterisation on bead phantom . . . 96
6.3 Application to *in vivo* imaging . . . 97
6.4 Conclusion . . . 97

7 Slice illuminated optical projection tomography 102
7.1 Theory . . . 104
7.1.1 Optical projection tomography transfer function . . . 104
7.1.2 Slice-illuminated optical projection tomography transfer function . . . 106
7.1.2.1 Slice Illumination . . . 106
7.1.3 Structured illumination and confocal line detection . . . 107
7.2 Hardware and operation . . . 107
7.2.1 Hardware . . . 107
7.2.2 Alignment and calibration . . . 108
7.2.3 Acquisition and reconstruction software . . . 109
7.3 Characterisation on fluorescent beads in a scattering agarose phantom . . . 111
7.4 Application to *in vivo* imaging . . . 114
7.5 Conclusion . . . 115

8 Single pixel optical projection tomography 120
8.1 Single Pixel Camera . . . 121
8.2 Mathematical representation of single pixel optical projection tomography . . . 123
8.2.1 Undersampling in the 2D case . . . 126
8.3 Hardware and operation . . . 126
8.3.1 Single-pixel optical projection tomography experimental set up . . . 126
8.3.2 Single-pixel optical projection tomography data acquisition . . . 127
8.3.2.1 Test function videos . . . 127
8.3.2.2 Diagonal mounting . . . 128
8.3.2.3 Frame synchronisation . . . 128
8.3.2.4 Acquisition Software . . . 130
8.3.3 Reconstruction software . . . 130
8.4 System application to a bead phantom . . . 132
8.5 Future work: Region of interest and high dynamic range single pixel imaging . . . 138
8.5.1 Region of interest single pixel camera . . . 139
8.5.2 High dynamic range single-pixel camera . . . 139
8.5.2.1 Effects of saturation of single pixel detector . . . 141
8.5.2.2 Region-of-interest high-dynamic-range single pixel camera . . . 142
8.6 Conclusion . . . 144

9 Conclusions and outlook 146

A Convolutional neural networks for undersampled optical projection tomography: source code 165
A.1 Neural network architecture . . . 165
A.2 Optical projection tomography data set . . . 167
A.3 Optical projection tomography data set without labels . . . 170
A.4 Training . . . 172
A.5 Testing . . . 175
A.6 Speed test . . . 176

List of Figures

2.1 Absorption spectra for melanin [1], fat [2], water [3], and hemoglobin [4]. The variation in proportion of these chromophores in a tissue sample gives rise to absorption contrast in brightfield microscopy. 25

2.2 Jablonski diagram of the transitions between the electronic states of a model molecule – where S_0 is the ground state, S_1 and S_2 are the first and second excited singlet states, and T_1 is the first triplet excited state. Some of the vibrational energy levels associated with the electronic energy levels are also shown. 26

2.3 Reduced scattering coefficient for a number of tissue types in human, modelled with Mie scattering approximation, using the values presented in table 2.1 for other soft tissues, other fibrous tissues, and fatty tissue. 28

2.4 Transport mean free path for a number of tissue types in human, modelled using Mie scattering approximation, using the values presented in table 2.1 for other soft tissues, other fibrous tissues, and fatty tissue. 30

2.5 (**a**) Epifluorescence widefield microscope with the depth of field (DOF) set to cover the sample. Fluorescence is emitted by the whole sample. Each camera pixel measures fluorescence from a column of the sample, causing all depth information is lost. (**b**) Confocal microscope. Fluorescence is restricted in the sample by pinhole illumination. Only ballistic photons from the focal plane are efficiently admitted to the photomultiplier tube (PMT) by the pinhole. (**c**) Multiphoton laser scanning microscope. Fluorescence is restricted to the focal volume, removing the need for a pinhole. (**d**) Selective plane illumination microscope (SPIM). The sample is optically sectioned by illuminating the focal plane with a light sheet. (**d**) OPT. A widefield microscope can be adapted for 3D imaging by mounting the sample on a rotation stage. 31

3.1 Model OPT system. The sample can be illuminated in transmission for absorption measurements, or with excitation light for fluorescence imaging. Illumination from source S is focused onto diffuser D by lens L_1, and collimated by condenser L_2. The transmitted light or emitted fluorescence is imaged onto a camera by lenses L_3 and L_4, via emission filter F. An adjustable aperture stop, AP, is placed in the back Fourier plane of L_3 to give telecentric imaging. The size of AP is set such that the DOF covers half the depth of the sample. The sample is mounted on a rotation stage, so that 2D projection images can be acquired at a number of angular positions. 37
3.2 The central slice theorem. (**a**) A 2D object $f(y, z)$. (**b**) A projection of $f(y, z)$ along direction s onto an axis t at an angle θ to y, $p(t, \theta)$. (**c**) The Fourier transform, $\mathcal{P}(k_t, \theta)$, of $p(t, \theta)$ is equivalent to the central slice of (**d**), the object's 2D Fourier transform, $\mathcal{F}(k_y, k_z)$, at an angle θ to k_y. 39
3.3 To adequately sample the object, the angular separation between projections must be small enough that the slices through Fourier space cover all points. . . . 40
3.4 Images produced by alignment script for different alignment states. The rotation axis is horizontal. The image of the object rotated to 0° and the vertically flipped image of the object rotated to 180° are shown in red and green, respectively. The colour variations of the background are due to uneven illumination, which is not important for alignment of the rotation axis. (**a**) System aligned. (**b**) Rotation axis shifted in the image plane, creating red and green borders. (**c**) Tilt of the rotation axis in the image plane, causing a rotation between the two channels. (**d**) Tilt of the rotation axis out of the image plane, visible as a translation in the y axis for parts of the object away from the rotation axis (x, y) plane. 43
3.5 Demonstration of reconstruction of a slice from a typical OPT data set – the mouse pancreas, showing beta-cells labelled with guinea pig anti-swine insulin antibody and Alexa 594 goat anti-guinea pig antibody. (**a**) An (x, t) projection from an OPT data set. (**b**) The (t, θ) sinogram from the column of pixels indicated in (**a**). (**c**) FBP reconstruction of that slice of the sample. Scale bar 1 mm 44
3.6 3D reconstructions of cm sized samples acquired on different OPT systems. (**a**) Mouse pancreas, showing beta-cells labelled with guinea pig anti-swine insulin antibody and Alexa 594 goat anti-guinea pig antibody in red and autofluorescence in green. (**b**) Ovary biopsy, showing vasculature labelled with anti-CD34 rabbit monoclonal antibody and Alexa 488 anti-rabbit antibody in green. Scale bar not shown because these visualisations are renders incorporating perspective. 45

3.7 Demonstration of streak artifacts on slices reconstructed from too few angular projections. (**a**) Slice reconstructed from 400 projections. (**b**) An approximation to the Fourier sampling pattern for 400 projections. (**c**) Slice reconstructed from 80 projections. (**d**) An approximation to the Radon Fourier sampling pattern for 80 projections. (**e**) Slice reconstructed from 40 projections. (**f**) An approximation to the Radon Fourier sampling pattern for 40 projections. Scale bar 1 mm 47
3.8 Aliasing artifacts produced by different Fourier space sampling strategies. (**a**) Equispaced sampling mask, magnified to reduce display artifacts. (**b**) Reconstructed image from equispaced undersampling strategy, which produces ambigious coherent aliasing artifacts. (**c**) Random sampling mask. (**d**) Reconstructed image from random undersampling. The aliasing artifacts are incoherent – giving the appearance of random noise. Due to the object's gradient sparsity, the strongest gradients are visible above the noise floor, which will form the starting point for denoising based recovery. (**e**) An approximation to a 92 projection Radon sampling mask. (**f**) Reconstructed image from Radon sampling strategy. Although the noise does not have a random appearance, the aliasing artifacts are not coherent and not ambigious. Scale bar 1 mm 48
3.9 Demonstration of compressive sensing reconstruction. (**a**) Slice reconstructed from 80 angular projections using FBP. (**b**) Slice reconstructed from 80 projections using IST. 50

4.1 Schematic of angularly multiplexed OPT system. The two imaging arms each image a different quarter of the depth of the sample. The axis of rotation is indicated by a cross 53
4.2 Automatic registration of angularly multiplexed OPT data. (**a**),(**b**) Camera 1 and Camera 2 projections acquired with shifted focal planes and different illumination conditions. The images were bandpass Gaussian filtered and the rigid transformation estimated. The registered camera 1 and camera 2 images are shown in green and purple respectively after applying Gaussian bandpass filters (**c**) $10 < l < 25$ pixels, (**d**) $20 < l < 50$ pixels, (**e**) $30 < l < 75$ pixels. (**f**) Manually registered projections. (**g**) Automatically registered projection. The automatic result which had the greatest variance, in features smaller than 10 pixels, was selected. 56
4.3 Variation of contrast, measured using variance as a sharpness metric, across a registered angularly multiplexed OPT data set filtered to show alignment at different length scales, (**a**) unfiltered, (**b**) 100 pixel Gaussian high pass filtered, (**c**) 10 pixel Gaussian high pass filtered. 57

4.4 Alignment of the rotation axis. *Ex vivo* pancreas slice reconstructed from a sinogram translated (**a**) -16, (**b**) -8, (**c**) 0, (**d**) 8, and (**e**) 16 pixels in the y axis. (**f**) Variation of reconstructed slice variance with rotation axis shift. (**g**) 2D histogram of the y axis shift that produces the highest variance reconstruction, with position of slice along the x axis. Scale bar 1 mm 58
4.5 2D histogram of the y axis shift that produces the highest variance reconstruction, with position of slice along the x axis for an undersampled adult zebrafish data set. 59
4.6 Demonstration of the effect of the regularisation parameter on TwIST reconstruction quality. (**a**) Convergence of MSE between TwIST estimate of slice reconstructed from 80 projections and ground truth slice reconstructed from 400 projections. Final TwIST reconstructions (**b**) - (**d**) and their Fourier transforms (**e**) - (**g**) reconstructed with τ of (**b**),(**e**) 0.0004, (**c**),(**f**) 0.004 (**d**),(**g**) 0.04. Scalebar 1 mm. 60
4.7 The value for τ that produces reconstructions that are most similar to fully sampled reconstructions depends on a number of factors. Variation of MSE with τ for (**a**) different numbers of projections, and (**b**) 80 projection data sets with different spatial frequency content (labelling described in section 3.4.3) 61
4.8 Creation of mask for determining successful reconstruction metric. (**a**) Transfer function of $R^T R$. (**b**) Mask of spectrum that is not well sampled. (**c**) Low pass filter applied to reduce the influence of noise. 62
4.9 (**a**) Variation of ρ and MSE with τ for slices reconstructed with TwIST from 80 projection data sets. (**b**) Labelled pancreas slice reconstruction with lowest MSE. (**c**) Labelled pancreas slice reconstruction with lowest ρ. (**d**) Autofluorescence pancreas slice reconstruction with lowest MSE. (**e**) Autofluorescence pancreas slice reconstruction with lowest ρ. Scalebar 1 mm 63
4.10 MIPs of an adult zebrafish imaged with two channel angularly multiplexed OPT for 5 weeks after tumour liver induction showing eGFP (green) and vesselness of mCherryFP (red). Different gamma corrections and normalisations are used for each image to maximise contrast. Scalebar 1 mm. 65
4.11 (**a**) x-y and (**b**) y-z slices through an adult zebrafish, 4 weeks post tumour induction, imaged with two channel angularly multiplexed OPT showing eGFP (green), mCherryFP (red), and mCherryFP vesselness (blue). Different gamma corrections and normalisations are used for each image to maximise contrast. Scalebar 1 mm. 66
4.12 (**a**) Variation of tumour volumes over 5 weeks post induction. The black dashed line shows average volumes, and the coloured dash-dot lines show individual tumours. (**b**) Significance of tumour volume changes from week to week using an unpaired and paired test. The significance axis has been limited to 0.1 to make the first three results clearer. 67

4.13 Amplification of noise by the vesselness operator. (**a**) Slice and (**b**) MIP of a spherical shell with Gaussian noise. (**c**) Slice and (**d**) MIP of the shell after application of the vesselness operator. Despite having no vessel like structure, the vesselness operator produced a result that looks like a tortuous vessel network. 68

5.1 (**a**) A neural network node. The output of a node is a non-linear function applied to the weighted sum of its inputs. (**b**) A simple fully connected neural network. The value of each node is determined by its inputs, weighted by the trained strengths of the synapses that connect them – which then feed into the values of nodes in deeper layers. 71

5.2 (**a**) An example of a 3x3 convolutional layer, which has a stride of one and zero padding. Instead of training synapses for the 256 node to node connections, a common set of 9 synapses is trained and applied as a convolution. (**b**) The small filter size means that nodes are only affected by those nodes in the local vicinity on the previous layer. However, longer range patterns will affect deeper layers after more convolutions. 72

5.3 Other layer types used in convolutional neural networks. (**a**) A 2x2 max pool layer with a stride of two. (**b**) A 2x2 transpose convolutional layer with a stride of 2. 73

5.4 Convolutional neural networks for reconstructing undersampled OPT data sets: (**a**) represents an OPT data set of a 4 days post fertilization zebrafish larva, consisting of a series of 2D (x-t) projections acquired as the sample is rotated to a series of angles θ; Each (t-θ) cross section through the data set forms a sinogram, (**b**),(**d**), which can be processed with FBP to give a (y-z) reconstructed slice, (**c**),(**e**), of the sample volume. (**b**),(**c**) show the reconstruction of a highly sampled, 800 projection sinogram and (**d**),(**e**) show the result of reconstructing from an undersampled, 40 projection sinogram – resulting in a streak-corrupted slice. (**f**) shows the reconstruction obtained using a U-net deep learning architecture – consisting of convolutional layers, max-pooling, bilinear interpolation upscaling, and concatenated skip paths – to estimate the well-sampled reconstruction from the undersampled FBP reconstruction (**e**). (**g**) The 2D reconstructed slices are stacked together to give the 3D fluorescence distribution of the sample. Adapted from [5]. 77

5.5 U-net architecture CNN which takes streak corrupted slices reconstructed from angularly undersampled OPT data sets as inputs, and outputs estimates of streak-free slices reconstructed from well sampled data sets. Adapted from [5]. . 78

5.6 Comparison of a representative pancreas slice reconstructed using FBP, CS, and CNN, with decreasing numbers of projections, shown on a false colour intensity scale. Compared to FBP, the CS and CNN methods are both able to provide significantly improved reconstructions with fewer projections. For 40 and 32 projections, the CNN reconstructions have better rejection of background streaks compared to those produced with CS. Scalebar 2 mm. Adapted from [5]. 81
5.7 Variation of PSNR between reconstructions of well-sampled *ex vivo* data, and those produced using FBP, CS, and CNN methods from different numbers of projections. The graph plots mean and standard error of measurements across the test data set of 3,342 slices. Adapted from [5]. 82
5.8 Comparison of a representative zebrafish slice reconstructed using FBP, CS, and CNN, with decreasing numbers of projections, shown on a false colour intensity scale. Compared to FBP, the CS and CNN methods are both able to provide significantly improved reconstructions with fewer projections. The slice produced by CNN from 40 projections is of acceptable quality. Scalebar 200 μm. Adapted from [5]. 83
5.9 (**a**) Variation of PSNR between reconstructions of well-sampled *in vivo* data, and those produced using FBP, CS, and CNN methods from different numbers of projections. (**b**) Variation of slice recontruction time, using FBP, CS, and CNN. Both plots show mean and standard error of measurements across the zebrafish embryo data set of 2,218 slices. Adapted from [5]. 84
5.10 Sensitivity of iterative CS and CNN methods to dim features. (**a**) Slice of zebrafish embryo reconstructed with FBP from a well-sampled data set. Three regions of interest are highlighted. Scalebar 250 μm. (**b**) (**c**) (**e**) The indicated regions of interest (i, ii, iii) respectively, from the FBP, CS and CNN reconstructions for different numbers of angular projections. The feature in (i) is resolved in all cases shown. The feature in (ii) is resolved down to 48 and 40 projections for CS and CNN reconstructions respectively. (**d**) Line profiles through (ii) as indicated in (**c**). The feature (iii) is not resolved in the CS reconstructions but can be seen in the 80 projection CNN reconstruction. (**f**) Line profiles through feature (iii) as indicated in (**e**). Adapted from [5]. 86

6.1 C-HDR-OPT setup. The addition of a DMD in the illumination path enables control over which parts of the FOV are illuminated. 90

6.2 C-HDR-OPT mask calculation. (**a**) A 1 ms exposure image of a fish in transmission. The illumination has been masked so that only the sample body and fins, and the tubing are illuminated. (**b**) Based on the image in (**a**) a mask is made of all pixels that are not expected to be saturated at the next exposure. (**c**) This mask is multiplied by the previous mask, so that previously masked regions do not turn back on and over-saturate the detector. (**d**) The mask is cleaned with morphological processes. (**e**) A 10 ms image acquired with the mask in (**d**). (**a**) and (**e**) Displayed with logarithmic scale. 91
6.3 Removal of striping artifact. (**a**) Striping artifact caused from DMD pixel resetting and rolling camera shutter. (**a**) 100 μs exposure image of DMD with all pixels "on", at maximum pixel value in video mode. (**b**) Pixelwise maximum of 5 100 μs exposure images. 92
6.4 (**a**) Fusion of conformal HDR projection data using equation 6.4. (**b**) Fusion of conformal HDR projection data using equation 6.7. Scalebar 1 mm. 94
6.5 Adult zebrafish illuminated in transmission by the mask indicated in red. Background light can be seen across the FOV, and the illumination has been scattered beyond its boundaries. 94
6.6 Calculation of correction gain map. (**a**) Ratio of intensity between I_3 and I_4 over M_4. The ratio is highest at the edges and quickly falls off. (**b**) The same ratio over the mask created with a 6-pixel erosion. The ratio is much more slowly varying over this mask. (**c**) Gain map calculated using equation 6.6. 95
6.7 Transmission projections of a scattering bead phantom. (**a**) Conventional image. The phantom appears as a noisy silhouette (**b**) HDR image. The phantom appears as a silhouette without internal structure. (**c**) C-HDR image. Beads and surface features are visible. The blue box shows the 100 pixels over which the noise was measured. (**d**) Line profiles as indicated by red dashed line on (**a**)-(**c**). Scalebar 1 mm 98
6.8 Slice from reconstruction of scattering agarose phantom. (**a**) Reconstruction produced with HDR-OPT data. (**b**) Reconstruction produced with C-HDR-OPT. (**d**) Line profiles as indicated in (**a**) and (**b**) Scalebar 1 mm 99
6.9 Transmission projections of an adult zebrafish. (**a**) Conventional image. (**b**) HDR image. (**c**) C-HDR image. (**d**) Line profiles as indicated on (**a**)-(**c**). Scalebar 1 mm100
6.10 Orthogonal slices through *in vivo* adult zebrafish volumes reconstructed from (**a**), (**c**), (**e**) HDR and (**b**), (**d**), (**f**) C-HDR projections. (**a**), (**b**) xy plane, (**c**), (**d**) xz plane, and (**e**), (**f**) yz plane. The arrows indicate the swim bladder, which is visible in the C-HDR-OPT reconstruction. (**g**) Line profiles as indicated in (**a**), (**b**). Scalebar 1 mm 101

7.1 Diagram showing principle of Slice-OPT, the imaging and illumination systems are coaligned with the z axis (figure 7.3): (**a**) Separated slices of the sample are individually illuminated. (**b**) Fluorescence is detected from the illuminated slices, but also from neighbouring ones. (**c**) The spurious signal can be removed using a digital mask. A complete projection is built up by scanning the illumination and digital mask and repeating the process. 103
7.2 The transformation between object space (x, y, z) and camera space (x, t, s) is a rotation θ around the x axis, which goes into the page. A point object is placed at $(0, y_0, z_0)$ in object space. 104
7.3 Slice-OPT set-up. Gratings were displayed on the DMD, which is imaged onto the sample to illuminate multiple individual slices. 108
7.4 Calibration of mapping between DMD and CCD pixel positions using a test object calibration data set. (**a**) Raw camera image of fluorescent target illuminated with a two pixel wide slice. The fluorescence from the slice was imaged onto approximately the 1170th pixel column of the camera, the bright feature further along x_{CCD} was caused by reflection off the housing of the DMD. (**b**) The raw images for each slice position are averaged along y_{CCD}. (**c**) The median of the intensity map in the x_{DMD} direction was subtracted from each column to remove constant background features. (**d**) The location of the maximum of each column was used to fit the mapping between DMD and CCD pixel positions. 110
7.5 Self calibration of mapping between DMD and CCD pixel positions. (**a**) MIP of images of a zebrafish OPT taken with a particular illumination pattern. (**b**) The MIP is averaged along y_{CCD}, the fundamental of the grating is subsequently identified using the Fourier transform, and used to create the transmission mask. To avoid stripe artifacts, some lines of the mask are two pixels wide 111
7.6 40 μm thick zy slice of scattering bead phantom reconstructed from (**a**) widefield OPT and (**b**) 150 μm slice-separation slice-OPT projections. A logarithmic intensity scale has been used to highlight background features. Scalebar 1 mm . 112
7.7 Line profile through the MIP of a single bead within the volume of a scattering bead phanton, along the x axis, reconstructed with widefield OPT and slice-OPT with different slice separations. The confocal line illumination and detection reduces the degradation to the PSF caused by optical scattering. Adapted from [6].113
7.8 Radial spatial frequency power spectrum of scattering bead phantom volumes reconstructed with widefield OPT and slice-OPT with different slice separations. As the slice separation is increased spurious low spatial frequency information, caused by inter-pixel cross-talk, will be rejected – increasing the proportion of high spatial frequency information in the reconstruction. Adapted from [6]. . . . 114

7.9 Enhancement of high spatial frequencies (equation 7.17) with increasing slice separation and acquisition time for slice-illuminated OPT applied to a scattering phantom. The rejection of spurious low spatial frequency signal increases with slice separation at the cost of imaging speed. Above ten times slower there is no additional benefit. Adapted from [6]. 115
7.10 Projections used for OPT reconstructions: (**a**) pseudo-widefield projection (**b**) slice-illuminated projection. Scalebar 1 mm 116
7.11 MIPs of *in vivo* juvenile zebrafish volumes reconstructed from (**a**), (**c**), (**e**) pseudo-widefield and (**b**), (**d**), (**f**) slice-illuminated projections, along the (**a**), (**b**) z axis, (**c**), (**d**) y axis, and (**e**), (**f**) x axis. Inset on (**c**) and (**d**) shows a region of interest around the brain. A logarithmic intensity scale is used. Scalebar 1 mm 117
7.12 Orthogonal slices through *in vivo* juvenile zebrafish volumes reconstructed from (**a**), (**c**), (**e**) pseudo-widefield and (**b**), (**d**), (**f**) slice-illuminated projections. (**a**), (**b**) xy plane, (**c**), (**d**) xz plane, and (**e**), (**f**) yz plane. A logarithmic intensity scale is used. Scalebar 1 mm 118
7.13 (**a**) Radial spatial frequency power spectrum of juvenile zebrafish volumes reconstructed with widefield OPT and slice-OPT with different slice separations. (**b**) Enhancement of high spatial frequencies (equation 7.17) with increasing slice separation and acquisition time. The rejection of spurious low spatial frequency signal increases with slice separation at the cost of imaging speed. Above 8 times slower there is no additional benefit. Adapted from [6]. 119

8.1 Demonstration of compressed sensing single pixel reconstruction on a (**a**),(**b**) 4x undersampled and (**c**),(**d**) 16x undersampled simulated measurement of a test chart: (**a**),(**c**) Low resolution images of the object can be acquired analytically with a complete set of low resolution Hadamard test functions, (**b**),(**d**) or the object can be reconstructed using an incomplete set of higher resolution test functions. 122
8.2 Sampling considerations for single pixel reconstruction of a 4x undersampled acquisition: (**a**) If the positions of pixels are not randomly permuted before sampling with Hadamard test functions, the reconstruction is corrupted by artifacts. (**b**) Randomly permuting the positions of each pixel before Hadamard transforming, and re-ordering after inverse Hadamard transforming removes this artifact. . 124
8.3 Single Pixel regularisation: Reconstruction quality, calculated using the PSNR metric introduced in chapter 5, produced using TV and wavelet regularisation with varying degrees of compression, $(1 - M/N)$. 125
8.4 Variation of PSNR with degree of compression, $1 - M/N * N_\theta/\pi$, between a simulated phantom and the IST reconstruction (equation 8.8) produced from SP-OPT measurements. Each line is of constant N_θ and varying M. 126

8.5 SP-OPT system set-up. Instead of a camera, the sample is imaged onto a DMD, the reflections from which are collected by two bucket detectors. 127
8.6 Frame encoding: Binary test functions are sent to the DMD, packaged in 24 bit color images. (**a**) The intensity of each set of eight test functions is set to occupy a bit plane of an 8 bit monochromatic image. (**b**) Three of these monochromatic images form the red, green, and blue channels of a (**c**) 24 bit RGB frame 128
8.7 A 4x4 pixel arrangement, defined on an 8x8 mirror array, aligned at 45°, where colours indicate different pixels. 129
8.8 Frame desynchronisation: After displaying the first two frames correctly, the third is not sent in time and the second continues to display instead. After recovering, the system may catch up, by skipping the third frame, or it will display the third frame and enter a new delayed timeline. This creates an ambiguity about which frame is currently being displayed after these events. 130
8.9 Extracting Y from raw data: (**a**) voltages recorded from the photodiode and DMD hardware transistor–transistor logic output triggers. The DMD bit change and frame change triggers are used to bin the data. (**b**) Data binned by frame and bit plane. The synchronisation bit can be seen as the brightest bin in each frame 131
8.10 (**a**) Analytic reconstruction of a fully sampled bead phantom projection. (**b**) Analytic reconstruction of a fully sampled laser speckle background projection. (**c**) The analytic reconstruction shown in (**a**), after flatfield correction. (**d**) Line profiles, as indicated in (**a**) and (**c**). Scalebar 1 mm. 133
8.11 IST reconstructions of a bead phantom projection, with (**a**) no undersampling, (**b**) 2x undersampling, (**c**) 5x undersampling, and (**d**) 10x undersampling. 134
8.12 MIPs of bead phantom volumes reconstructed using TwIST from projections reconstructed using IST from single pixel data, with (**a**) no test function undersampling, (**b**) 2x test function undersampling, (**c**) 5x test function undersampling, and (**d**) 10x test function undersampling. 135
8.13 Slices of bead phantom volumes reconstructed using TwIST from projections reconstructed using IST from single pixel data, with (**a**) no test function undersampling, (**b**) 2x test function undersampling, (**c**) 5x test function undersampling, and (**d**) 10x test function undersampling. 136
8.14 (**a**) Simulated sinogram of a point object with fixed pattern noise. (**b**) Reconstructed slice produced from (**a**). (**c**) Variation of ring artifact peak intensity with radius of a single point of fixed pattern noise. Fixed pattern noise near the rotation axis causes brighter artifacts. (**d**) Projection of slice shown in (**c**). The fixed pattern noise does not produce a self consistent result when back projected and projected. (**e**) Variation of $\frac{1}{2}\left\|Y - RR^TY\right\|_2^2$ with ring artifact radius. Fixed pattern noise near the axis of rotation is the most self consistent, so will produce stronger artifacts when iteratively reconstructed. 137

8.15 Simulated 4096 pixel maps **a,c,e** (different colours correspond to different super-pixels) and least squares reconstructions **b,d,f** of a 16384 pixel image: **a,b** Using 4096 test functions, a half resolution image can be acquired. **c,d** By using variable super-pixel sizes, 4096 test functions give full resolution in the fovea and worse resolution in the peripheries. **e,f** By using low resolution $(32 * 32)$ test functions to identify gross morphology, the brightest $4096 - 32 * 32 = 3072$ pixels can be segmented and high resolution acquired only over that region. 140
8.16 Simulated least squares reconstructions using 5428 test functions. (**a**) ROI single pixel detection: the number of pixels included in the ROI can be adapted to suit the object. (**b**) Foveated single pixel detection: the size of the fovea can also be increased, but it is naturally circularly symmetric and includes pixels in the peripheries. 141
8.17 Simulated transmission projection of a 3D phantom. Intensity is displayed on a logarithmic scale. (**a**) Ground truth: the signal through the centre is on average 5000 times less intense than outside the sample. (**b**) Reconstructed from single pixel measurement: the desired absorption structure has fallen beneath the noise floor. 142
8.18 Simulated saturated single pixel signals **a,c,e** and reconstructions **b,d,f**: **a,b** With a degree of saturation of 200%, the image looks the same as in figure 8.17b. As the degree of saturation is increased, dim features do not become visible. In fact, even small further increases of saturation to 200.8% **c,d** and 208% **e,f** cause the image to be completely lost. 143
8.19 Simulation of an HDR single pixel acquisition. First a low resolution image was taken (**a**) (shown with linear intensity scale), which was used to mask out regions of different intensities (**b**), shown here with different colours. ROI single pixel acquisitions were performed over all or some of the masks to produce a HDR composite (**c**), here shown with a logarithmic intensity scale. 144

Chapter 1

Thesis overview

This thesis reports the development of optical projection tomography (OPT) instrumentation and its application to in vivo three-dimensional imaging of zebrafish. OPT is a 3D imaging technique that can produce 3D reconstructions of transparent samples, requiring only a widefield imaging system and sample rotation. It is therefore comparatively low-cost, straightforward to implement, and readily scalable to image samples from sub-mm to cm scale. OPT can be readily applied to chemically cleared samples, e.g. of cleared mouse brain or pancreatic tissue, or to live transparent organisms such as nematodes or zebrafish. It can provide absorption or fluorescence contrast to address the increasing interest in translating cell-based-assays from two-dimensional (2D) cell monocultures to more complex disease models for basic research and for drug discovery, and enables whole organism imaging for developmental biology and preclinical studies of cancer, diabetes and other diseases. The capability for in vivo imaging enables whole organism studies of disease progression and response to interventions to be undertaken as longitudinal studies, thereby increasing the value of the data and reducing the numbers of animals required for medical research.

For preclinical imaging, there is a trade-off between optical accessibility and biological relevance to humans. Smaller animals, such as *Caenorhabditis elegans* (*C. elegans*) can be imaged at high resolution with diffraction limited imaging but may miss key elements of physiology. Mice are more homologous to humans, but *in vivo* fluorescence imaging is limited to low-resolution diffuse optical tomography, or highly localised intravital microscopy. As vertebrates, *Danio rerio* (zebrafish) represent a promising compromise, with higher physiological relevance than *Drosophila melanogaster* or *C. elegans*. Zebrafish larvae are widely studied using standard microscope techniques, but they lack an adaptive immune system and full organ development. Adult zebrafish address these concerns while still providing much greater optical accessibility than mice. However, their size and physiology present a number of imaging challenges including non-negligible absorption and optical scattering, and limited time for image data acquisition if the fish are to be recovered for longitudinal studies. A key goal of this PhD thesis research was to develop OPT to address these challenges and improve *in vivo* imaging capabilities for this model organism.

This thesis builds on previous work at Imperial where angularly multiplexed OPT using compressed sensing was developed and applied to *in vivo* imaging of a cancer-burdened adult

zebrafish, with a sufficiently short OPT data acquisition time to allow recovery of the fish after anaesthesia. The previous cross-sectional study of this work was extended to a longitudinal study of cancer progression that I undertook at the start of this PhD thesis research alongside the development of low-cost OPT instrumentation for partner laboratories. The volume and quality of data acquired in the longitudinal study presented a number of data processing challenges, which I addressed with improved automation of the data processing pipeline and with the demonstration that convolutional neural networks (CNN) could replace the iterative compressed sensing algorithm previously used to suppress artifacts when reconstructing undersampled OPT data sets. To address the issue of high attenuation through the centre of an adult zebrafish and the challenge of capturing both transmitted light and light from around the edges of the fish, I developed conformal-high-dynamic-range (C-HDR) OPT and demonstrated that it could provide sufficient dynamic range for brightfield imaging of such optically thick samples, noting that transmitted light images can provide anatomical context for fluorescence image data. To reduce the impact of optical scattering in OPT, I developed a parallelised quasi-confocal version of OPT called slice-illuminated OPT (slice-OPT) to reject scattered photons and demonstrated this with live zebrafish. Slice-OPT used a digital micromirror device (DMD) to provide the required slice illumination. I also applied the DMD to implement a single pixel camera and demonstrated single-pixel OPT (SP-OPT) for the first time. This system can image in the short-wave infrared (SWIR) window, where the impact of scattering is reduced compared to the visible-near infrared coverage of silicon detectors, without the need for costly Ge or InGaAs cameras.

Following this introduction, chapter 2 briefly reviews fluorescence imaging instrumentation, starting with a description of light-matter interactions in tissue: absorption and subsequent fluorescence, and optical scattering and its reduction with optical clearing. An overview of 3D microscopy techniques is then presented followed by an overview of model organisms and a review of the 3D imaging techniques that have been used to study them.

Chapter 3 describes OPT in greater detail, outlining its experimental implementation, historical development and the theoretical basis of image reconstruction using the Radon transform. Two specific OPT implementations are then described, which I helped develop: a low-cost instrument using LED excitation and a more sophisticated OPT instrument using a newly available cost-effective multimode diode laser source. This chapter also introduces compressive sensing and outlines how it can be applied to accelerate OPT data acquisitions by providing reasonable 3D image reconstructions from undersampled OPT data sets.

Chapter 4 describes the refinement of the angularly multiplexed OPT previously developed in the Photonics Group at Imperial and its application to longitudinal study of cancer progression in adult zebrafish. The experimental system and the data handling challenges of image registration, alignment, and regularisation parameter selection are described, along with the work I undertook to address these challenges. The data from the longitudinal study is then presented, highlighting the benefits of using longitudinal data.

Chapter 5 addresses the long data processing times required when reconstructing undersampled OPT data sets using an iterative algorithm. I discuss how neural networks can be used

to reduce this reconstruction time and introduce the convolutional neural network architecture, function, and training. I then describe my implementation of CNN-OPT and show how its speed and reconstructed image quality surpasses that obtained with iterative reconstruction. I also show how training data acquired of fixed and cleared mouse tissue can be used for CNN-OPT of (live) zebrafish OPT data, which means that live fish do not have to be sacrificed to train the CNN.

Chapter 6 describes my development and application of conformal high dynamic range OPT (C-HDR-OPT) to enable brightfield OPT of adult zebrafish. I outline the motivation for absorption imaging, and how implementing this with larger (more attenuating) samples is confounded by the limited dynamic range of the detector. A previously reported high dynamic range (HDR) approach and its limitations are described and the principle of C-HDR is introduced, for which I discuss a method of image fusion. The application of the C-HDR-OPT system to an adult zebrafish is demonstrated.

Chapter 7 describes a new approach to reduce the impact of optical scattering on OPT experiments that uses a DMD to illuminate the sample with "slices" of light for each projection image and detect the resulting fluorescence with a co-aligned mask of virtual slits on the camera. The mechanism of action of slice-OPT is derived for a simple imaging model and the system design and data acquisition process is described. I then discuss its application to a juvenile zebrafish.

Chapter 8 discusses ongoing and unfinished work to reduce the impact of optical scattering by enabling the use of SWIR radiation. Since SWIR cameras are only recently available and are very costly, I decided to use the DMD to implement a single pixel camera with a low-cost Ge photodetector and demonstrated single pixel OPT (SP-OPT) for the first time, imaging a bead phantom. I also discuss a potential extension of the HDR approach to single pixel imaging to address a major limitation of this approach.

Chapter 9 concludes this thesis with a summary of progress and a discussion of the opportunities for future work to extend that reported here.

Chapter 2

Introduction to whole organism optical imaging

2.1 Interaction of light and tissue

Biological tissues are optically inhomogenous materials that interact strongly with ultraviolet to near infrared (NIR) wavelength photons through absorption and scattering. Unscattered light propagating through tissue is exponentially attenuated as described by the Beer-Lambert law [7]:

$$I(x) = I_0 \exp(-\mu_t x);\ \mu_t = \mu_a + \mu_s \tag{2.1}$$

where $I(x)$ is the intensity of unscattered light a distance x along its direction of propagation, I_0 is the intensity at $x = 0$, μ_t is the extinction coefficient, μ_a is the absorption coefficient, and μ_s is the scattering coefficient.

2.1.1 Absorption and fluorescence

Absorption of visible and near infrared light is caused by photons exciting electronic and vibrational molecular states respectively. The absorption spectrum in tissue therefore depends on its molecular composition and density; in soft tissue the spectrum is dominated by the absorption spectra of water, hemoglobin, fat, and melanin in skin [8] (figure 2.1). The amount of each of these components in a given tissue sets how deep light propagates into the sample, and the variation in proportion of these chromophores in a tissue sample gives rise to absorption contrast in brightfield microscopy. The effective absorption coefficient for a heterogenous material is given by the Beer-Lambert law with:

$$\mu_a = \sum a_i \mu_a^i, \tag{2.2}$$

where μ_a^i is the absorption coefficient of chromophore i with a volume fraction of the tissue, a_i. For typical lean tissue composition the absorption spectrum is dominated by blood at shorter wavelengths, with $\mu_a \sim 1\ cm^{-1}$ for blue and green light, which drops to $\mu_a \sim\ 10^{-3}\ cm^{-1}$

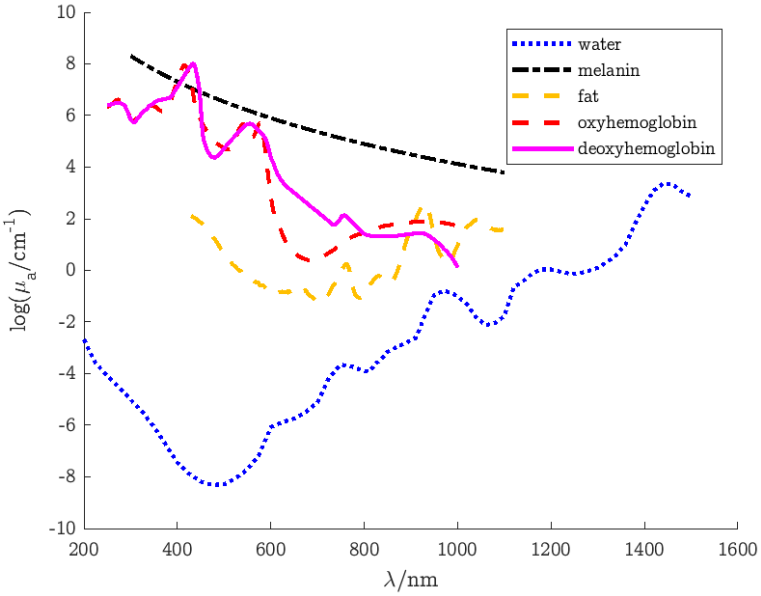

Figure 2.1: Absorption spectra for melanin [1], fat [2], water [3], and hemoglobin [4]. The variation in proportion of these chromophores in a tissue sample gives rise to absorption contrast in brightfield microscopy.

for red and near infrared light, and returns to $\mu_a \sim 1\ cm^{-1}$ for short wave infrared light due to increased water absorption. The region of low absorption between 650 nm and 1350 nm is known as the near-infrared optical window.

Most absorbed energy is dissipated as heat. However, some chromophores emit a new photon during relaxation from the excited state. This phenomenon is either fluorescence, if allowed by selection rules, or phosphorescence, if forbidden [9]. It can be represented using a Jablonski diagram, shown in figure 2.2 for a model chromophore with a ground state, S_0, and three excited states – two singlet, S_1 and S_2, and one triplet T_1. Additionally each electronic energy level is associated with a manifold of vibrational and rotational (not shown) energy levels.

Under standard biological conditions, all molecules will be in a vibrational level, close to the ground vibrational level, of S_0. A molecule can absorb a photon of appropriate energy to transition to an excited state. Once excited, the molecule will rapidly relax to the lowest energy vibrational state of S_1 through vibrational relaxation, and internal conversion. Subsequently, the molecule can fluoresce, decay non-radiatively, or phosphoresce via intersystem crossing. Phosphorescence is a forbidden transition, and is most common in larger atoms/molecules with larger atoms where the assumptions underlying the selection rules are not valid [9]. Internal conversion and vibrational relaxation cause the emission transition to be of lower energy than the excitation transition. This is known as the Stokes shift, linearly excited fluorphores emit photons of longer wavelength than that of the excitation light. With the use of spectral filters, the fluorescence can be separated from the excitation light and imaged – providing rich spectroscopic contrast, with no background from the much stronger excitation light.

The wavelength of fluorescence depends on the energy level structure of the emitting molecule.

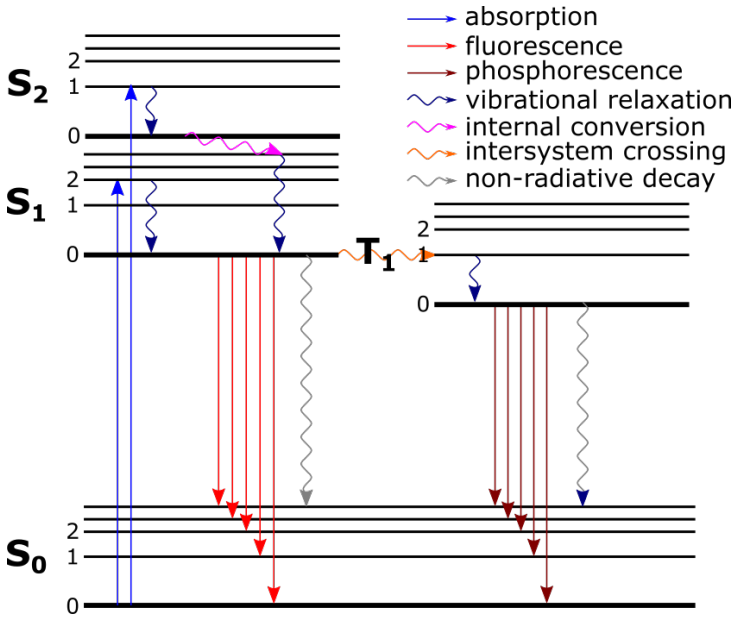

Figure 2.2: Jablonski diagram of the transitions between the electronic states of a model molecule – where S_0 is the ground state, S_1 and S_2 are the first and second excited singlet states, and T_1 is the first triplet excited state. Some of the vibrational energy levels associated with the electronic energy levels are also shown.

Spectrally resolved imaging can therefore be used to identify the locations and densities of different molecular species. Many endogenous chromophores fluoresce, such as nicotinamide adenine dinucleotide phosphate, collagen, and flavins [10]. However, a key advantage of fluorescence imaging is the ability to use exogenous dyes, and genetically encoded fluorescent proteins. Chemical labels can be added to samples to bind to specific targets [11]. However, due to toxicity, these are generally only appropriate for fixed tissues. Alternatively, fluorescent proteins can be genetically encoded into the organism, to be expressed alongside the target protein of the study [12]. Fluorescent proteins can also be used to create biosensers. If two different fluorescent proteins are in close proximity ($< \sim 10\ nm$), an excited "donor" fluorophore emitting at a shorter wavelength can non-radiatively couple to an "acceptor" fluorophore that emits at a longer wavelength, transferring the excitation and causing emission at the longer wavelength. This is Forster resonance energy transfer (FRET) [13], and how efficiently this occurs depends on the proximity and relative alignment of the fluorescence dipoles. If a biochemical sensor that changes its conformation upon binding its analyte is placed between the two fluorescent proteins then the amount of FRET can be used to quantify that process.

2.1.2 Scattering

At optical wavelengths, absorption is a comparatively weak effect; in tissue, the dominant light-matter interaction is elastic scattering. Optical scattering is caused by refractive index heterogeneities, which modify propagating wavefronts and reduce imaging quality. The scattering coefficient, μ_s, describes the inverse of the scattering mean free path. However, unlike in

the case of absorption the scattered wave is not removed from the system, and the result of the interaction – not just its rate – must be considered.

The strength of scattering into a particular direction is described by the phase function, $p(\phi, \phi')$; the probability density function for scattering into direction ϕ' from direction ϕ. For multiple scattering events in materials with randomly oriented scattering structures, this can be reduced to the scattering anisotropy parameter, the mean scattering cosine:

$$g = \int_0^{\pi} p(\theta)\cos\theta 2\pi\sin\theta \mathrm{d}\theta, \tag{2.3}$$

where $\theta = \phi' - \phi$ is the deflection angle. The value of g indicates how significantly the scattering affects the propagating wave:

$$g \begin{cases} < 0, & \text{backwards scattering,} \\ = 0, & \text{isotropic scattering,} \\ > 0, & \text{forwards scattering.} \end{cases} \tag{2.4}$$

If there is predominantly forward scattering, with small angles of deflection, photons will be able to travel significantly further before having their directions randomised and spatial information lost. This can be represented by modifying μ_s to give the reduced scattering coefficient, which measures the inverse of the transport mean free path, L, defined as:

$$\mu_s' = (1 - g)\mu_s. \tag{2.5}$$

Since many cells and microorganisms are approximately spherical, scattering can be modelled by treating tissue as a homogenous ensemble of spherical particles. This physical system is described by Mie scattering, which is the solution to Maxwell's equations of a plane wave incident on a sphere of different refractive index to its medium. This corresponds to Rayleigh scattering for particles, size r, with a small diffraction parameter; $x = 2\pi r/\lambda \ll 1$. Mie scattering results in a reduced scattering coefficient that can be approximated as [14]:

$$\mu_s'(\lambda) \approx a\left(\frac{\lambda}{500nm}\right)^{-b} \approx a'\left(f_{Ray}\left(\frac{\lambda}{500nm}\right)^{-4} + (1 - f_{Ray})\left(\frac{\lambda}{500nm}\right)^{-b_{Mie}}\right), \tag{2.6}$$

where in the first expression, b is the scattering power, which characterises the scattering wavelength dependence, and a is a normalisation constant. The second expression describes the scattering as a mixture of Rayleigh-like and non-Rayleigh-like scattering; f_{Ray} indicates the fraction of Rayleigh scattering, and b_{Mie} is the non-Rayleigh scattering power. The two representations are approximately equivalent for 400–1300 nm.

Table 2.1 shows a compilation of parameters for equation 2.6 from the literature for various human tissues. Figure 2.3 shows average scattering spectra for soft tissues, such as muscle or liver; fatty tissues; and fibrous tissues, such as tumour. Each tissue type shows the same trend; the reduced scattering coefficient monotonically decreases as wavelength increases. At shorter wavelengths, where the diffraction parameter is smaller, the Rayleigh scattering approximation

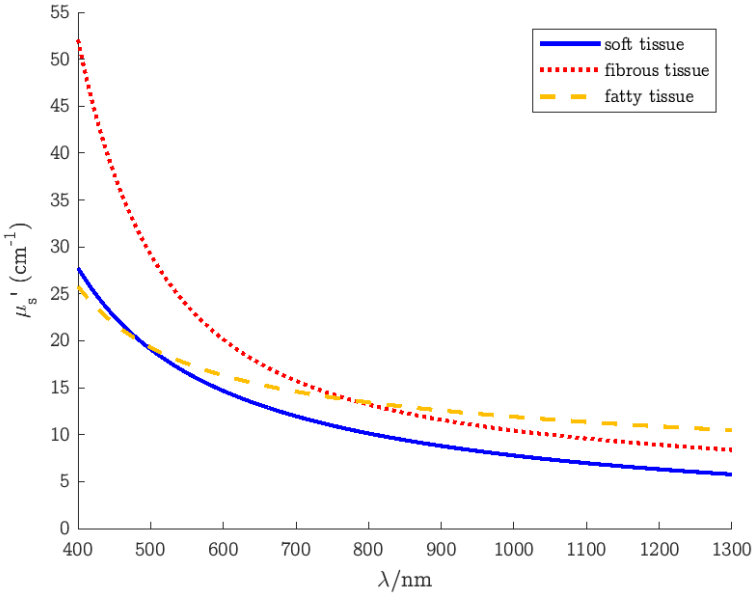

Figure 2.3: Reduced scattering coefficient for a number of tissue types in human, modelled with Mie scattering approximation, using the values presented in table 2.1 for other soft tissues, other fibrous tissues, and fatty tissue.

holds and μ_s' falls with the fourth power of λ. However, in the Mie scattering regime the improvements with wavelength are decreased.

The transport mean free path, the limit of ballistic imaging, is the inverse of the reduced scattering coefficient. Figure 2.4 shows how L varies with wavelength for the tissues modelled in figure 2.3. Due to the large reduced scattering coefficients, diffraction limited imaging is limited in tissue to $\sim 1\ mm$. Beyond this depth, imaging resolution is limited by scattering.

2.1.2.1 Clearing

Optical scattering can be reduced by chemical clearing techniques. This involves reducing refractive index inhomogeneities by replacing the water in a sample with interstitial fluid of a higher refractive index, or by changing the composition of tissue components to lower their refractive index [15]. Although localised clearing of skin can be performed with some agents without ill effect [16], both methods are incompatible with living cells and organisms, and therefore systematic clearing is only used for fixed *ex vivo* tissue.

An ideal clearing method would remove all optical scattering, preserve fluorescence and morphology, act quickly, have a low cost, and be safe to handle. In practice, any given method will only have some of these properties, and a compromise must be made for the requirements of any given study. For mesoscopic samples, the techniques can be broadly grouped as being based on hyperhydration, hydrogels, or organic solvents.

A mixture of the organic solvents benzyl alcohol and benzyl benzoate (BABB) can be applied in a two step approach [11]. First dehydration with lipid solvation and then clearing

	a	b	a'	f_{ray}	b_{mie}
Skin					
Mean:	50	1.4	50	0.4	0.7
SD:	10	0.5	10	0.2	0.4
Brain					
Mean:	20	2	30	0.3	1
SD:	10	1	10	0.4	1
Breast					
Mean:	17	1.1	19	0.3	0.7
SD:	8	0.8	7	0.3	1
Bone					
Mean:	23	0.7	15	0.02	0.3
SD:	15	0.7	8	0.03	0.3
Other soft tissues					
Mean:	20	1.3	20	0.2	1.1
SD:	10	0.5	10	0.2	0.5
Other fibrous tissues					
Mean:	27	1.6	29	0.5	0.6
SD:	5	0.1	5	0.3	0.6
Fatty tissue					
Mean:	18	0.7	19	0.2	0.4
SD:	9	0.2	9	0.1	0.3

Table 2.1: Compilation of scattering parameters for human tissue [14]

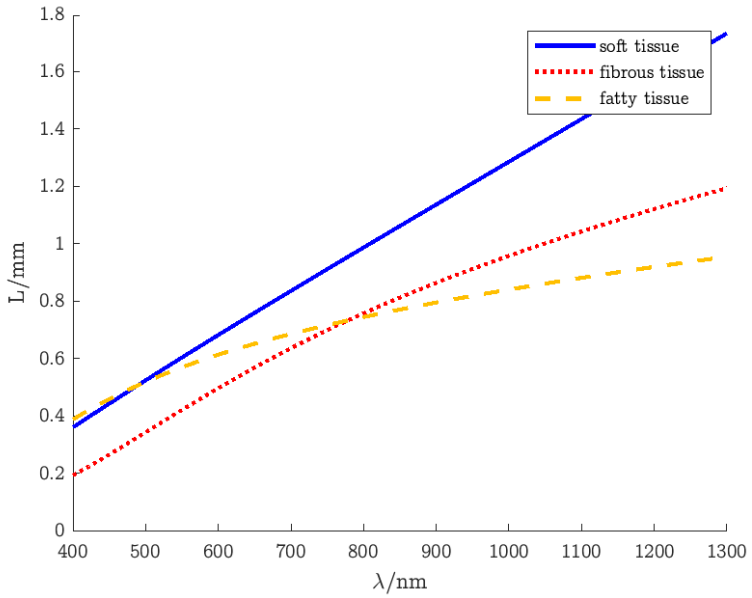

Figure 2.4: Transport mean free path for a number of tissue types in human, modelled using Mie scattering approximation, using the values presented in table 2.1 for other soft tissues, other fibrous tissues, and fatty tissue.

by refractive index matching. The necessary clearing protocol can be undertaken in a day, but it does not preserve fluorescent proteins. Better preservation of fluorescence can be achieved using BABB derivative methods using tetrahydrofurane [17], and by dehydrating with larger alcohols [18]. Better transparency can be achieved using dibenzyl ether instead of BABB, as used in the 3DISCO (three-dimensional imaging of solvent-cleared organs) family of methods [19–22], which variously preserve fluorescent proteins [19, 20, 22], sample morphology [21], and can clear whole rats [22].

A number of urea based acqueous reagents can clear samples over weeks and better preserve fluorescent signal. These include Scale [23], and its development CUBIC (clear unobstructed brain imaging cocktails and computational analysis) [24], which alleviates some of the swelling produced by Scale. The last family of techniques clear samples by replacing lipid bilayers with a hydrogel scaffold. CLARITY (clear lipid-exchanged acrylamide-hybridized rigid imaging/immunostaining/in situ hybridization-compatible tissue-hydrogel) renders the sample permeable to both photons and macromolecules [25] – enabling multiround phenotyping.

2.2 Fluorescence Microscopy

Optical microscopy has been limited, historically, to thin samples [26] – by both the inability to reject out-of-focus signal, and from the loss of spatial information due to optical scattering (figure 2.5a). Imaging of three dimensional samples has become possible due to developments in controlling illumination and rejecting both scattered and out-of-focus light. Confocal microscopy combines point illumination and detection to produce sectioned images of 3D samples [27] (figure

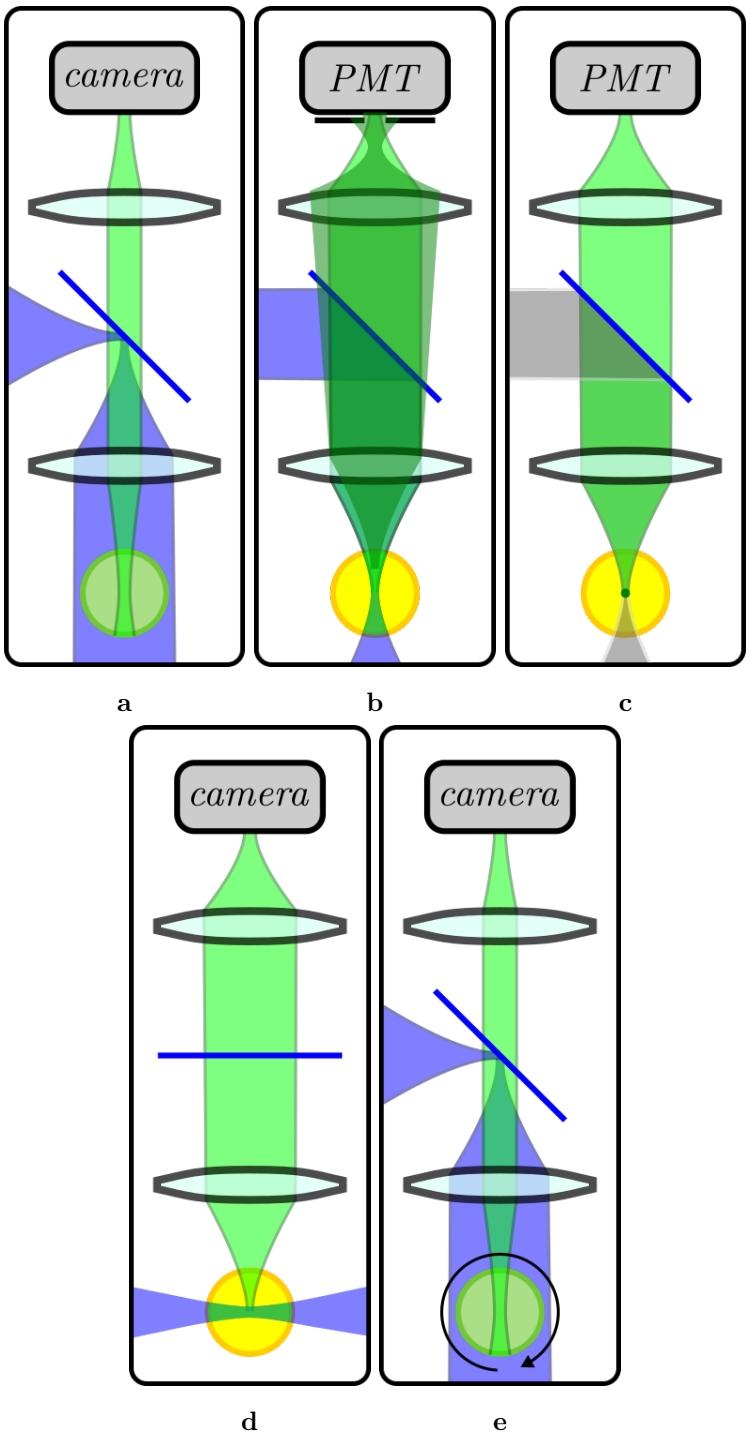

Figure 2.5: (**a**) Epifluorescence widefield microscope with the depth of field (DOF) set to cover the sample. Fluorescence is emitted by the whole sample. Each camera pixel measures fluorescence from a column of the sample, causing all depth information is lost. (**b**) Confocal microscope. Fluorescence is restricted in the sample by pinhole illumination. Only ballistic photons from the focal plane are efficiently admitted to the photomultiplier tube (PMT) by the pinhole. (**c**) Multiphoton laser scanning microscope. Fluorescence is restricted to the focal volume, removing the need for a pinhole. (**d**) Selective plane illumination microscope (SPIM). The sample is optically sectioned by illuminating the focal plane with a light sheet. (**d**) OPT. A widefield microscope can be adapted for 3D imaging by mounting the sample on a rotation stage.

2.5b). Only photons emitted from the focal point of the illumination and detection are efficiently admitted by a pinhole located in front of the detector, so scattered photons and those not from the focal volume are suppressed in the measured signal. Multiphoton laser scanning microscopy exploits the optical window in the near infrared to reach greater depths [28]. The illumination intensity is only high enough for multiphoton excitation at the focal spot of the illuminating laser – so no pinhole is required to section the emitted light, and emitted photons that are scattered can contribute to the signal (figure 2.5c).

Laser scanning techniques can use relatively high peak intensity during imaging, and confocal microscopy excites out-of-plane fluorophores whose fluorescence is subsequently rejected, which accelerates photobleaching. Furthermore, reactive chemical species created during excitation can damage live cells, a process called phototoxicity. Selective plane illumination microscopy (SPIM) illuminates the sample with a light sheet coincident with the focal plane — so that only areas being imaged are illuminated [29] (figure 2.5d). OPT uses low peak intensity widefield illumination and detection – separating depth information by acquiring projections at many angles [11] (figure 2.5e).

2.2.1 Laser scanning microscopy

The utility of standard widefield microscopy with three dimensional samples is limited by the background of out-of-focus light – restricting imaging to monolayer cell cultures and physically sectioned tissues. Confocal microscopes use pinhole detection and point illumination to reject photons that do not come from the focal volume. By rejecting out of focus signal, the confocal microscope is able to optically section the sample with a typical axial resolution of around 0.8 μm [27]. Images are acquired by raster scanning the laser across the sample, recording the intensity with a point detector. Three dimensional images are produced by repeating this process at different focal planes. Imaging depth is limited by optical scattering of the fluorescence on the way out of the sample, and also of the illumination on the way in. Confocal microscopy cannot normally image deeper than 50 μm into tissue [27].

Although capable of imaging three dimensional samples, confocal microscopy's imaging depth is limited by scattering and absorption, which degrade resolution and contrast [30]. This challenge can be addressed by multiphoton laser scanning microscopy, which exploits the observation that μ_a and μ_s are smaller in the NIR than for visible wavelengths. Short-pulse high-power NIR lasers can produce sufficient intensity for nonlinear excitation in the focal region, which can be used to excite visible fluorophores [28]. Significant excitation only occurs at the focal volume, so multiphoton-excited fluorescence images are directly sectioned. This removes the need for a pinhole, dramatically increasing efficiency. Since optical scattering only affects the precision of excitation, scattered emission photons can contribute to the signal, as their source is still known to be the focal point. Limiting excitation to the focal point also significantly reduces out-of-plane phototoxicity. However, the efficiency of multiphoton excitation is much lower than single photon excitation and so laser scanning multiphoton microscopy imaging is relatively slow.

Laser scanning techniques usually interrogate the sample one pixel at a time – limiting

imaging speed. Spinning disk confocal microscopy parallelises the process by using an array of pinholes, instead of one, imaged onto a pixelated detector [31]. The pinholes are spaced far enough apart that cross talk is minimised. The array of pinholes are on a rotating disk and placed so that every position in the field of view (FOV) is interrogated at some point in time. Multiphoton microscopy can also be implemented by scanning multiple excitation beams [32].

2.2.2 Selective plane illumination microscopy

Confocal and multiphoton microscopy can image three dimensional samples. However, both techniques illuminate parts of the sample that do not contribute to the image; the photon efficiency is low because of the collection pinhole and inefficient excitation, respectively. Also, in confocal microscopy phototoxicity is induced in regions not being imaged. Selective plane illumination microscopy (SPIM) produces 2D optical sections by selectively illuminating the sample, and imaging the resulting fluorescence onto a camera [29]. The sample is illuminated with a sheet of light, with the imaging optic axis normal to its plane. Excitation is restricted to the illuminated plane, creating an optically sectioned image. SPIM is significantly faster than laser scanning methods; in confocal microscopy each pixel has an integration time of one to ten μs, so a 1000 by 1000 pixel image will take one to ten seconds compared to a tenth of that for SPIM [33]. Illumination is spread across a sheet, which reduces the peak intensity, and therefore the phototoxicity. Furthermore, only parts of the volume that are currently being imaged are ever illuminated – minimising phototoxicity, and allowing for extended time series studies [34].

2.2.3 Optical projection tomography

SPIM illuminates efficiently by only exciting single planes. Tomographic methods use conventional widefield illumination, and gain efficiency from using all the signal integrated through the sample. OPT reconstructs a three dimensional sample from a series of two dimensional projections.

Unlike SPIM, OPT uses widefield illumination. Therefore, image quality is not limited by the ability to propagate the light sheet through the sample, which can be degraded by optical scattering and places constraints on system and sample geometry. This allows for the imaging of larger samples, such as adult zebrafish [35]. Widefield illumination also reduces the requirements on the excitation sources, and illumination optics. So three dimensional microscopy systems may be implemented at lower cost using OPT, compared to laser scanning microscopy or SPIM [36]. It is also possible to implement OPT on conventional microscope stages adapted for OPT [37]. Developments in OPT will be discussed further in chapter 3.1.

2.3 Whole organism imaging

A number of model organisms have emerged as popular subjects for biological studies, including imaging. Important qualities are optical accesibility, fecundity, development time, whether that development is internal or external, cost of maintenance, physiology, and homology for disease models. The general trend follows that the homology of a model to humans improves at the

detriment to other qualities. The development of 3D microscopy techniques has stimulated studies in (nearly) transparent organisms such as nematode worms and zebrafish, although preclinical imaging is still dominated by mouse models of disease.

The nematode worm *Caenorhabditis elegans* (*C. elegans*) is a multicellular eukaryote with a number of attractive features for optical imaging. They are microscopic, even into adulthood – on the order of a mm long and 50 μm across [38] – and are transparent. The species is eutilic; every wildtype *C. elegans* of the same sex has an identical cell lineage – the development of which has been mapped from zygote to a final adult count of 1031 cells for males, and 959 for hermaphrodites [39, 40]. The consistency of cell lineage makes *C. elegans* an attractive choice for developmental studies. During its early stages, embryogenesis can be adequately imaged by confocal microscopy [41, 42]. Light sheet microscopy has been applied to late stage embryo and larval development, for its impovements in imaging speed and reduced phototoxicity [43] and potential for isotropic resolution [44].

The similarity between members of the species provides excellent statistical robustness for high-throughput studies. Additionally, the rapid generation time of 3 days to adulthood allows for vast populations to be produced for imaging. For example, a system has been built from photograph scanners that is capable of monitoring 30000 organisms in 2D to track survival curves under different conditions [45].

Eutely of *C. elegans* extends to their nervous system, which totals 302 neurons for hermaphrodites [46] and 385 for males [47]. Their simple neural circuitry, and slow movement speed makes them an attractive model for imaging while freely behaving [48, 49]. In Nguyen *et al.* [48], the sample is tracked with low magnification imaging, which is used to adjust the stage position to keep the brain within the FOV of a spinning disk microscope. Alternatively, the sample can be manipulated into a desirable imaging position using microfluidic devices [50, 51].

C. elegans' transparency, small size, eutely, and rapid generation time make it an ideal candidate for certain studies. However, they lack a circulatory system, respiratory system, liver, pancreas, or blood, which precludes them from many others. An alternative vertebrate model organism is *Danio rerio* (zebrafish). Similarly to *C. elegans*, zebrafish develop externally and rapidly – reaching larval stage in 3 days, and breeding age in 90 – and are transparent for the first weeks of development [52]. They have the advantage of being vertebrates, with greater homology to humans; they also possess a liver, pancreas, and circulatory system.

The transparancy and external development of the zebrafish embryo makes it a useful model for vertebrate developmental biology. Embryogenesis has been imaged over the course of a day using the first digital light sheet microscopy [34], which benefited from low phototoxicity and high speed compared to confocal imaging. Light sheet microscopy has also been used to acquire time lapse 3D images of the development of vasculature in the larvae [53], and videos of the beating heart [54].

Slower processes, such as neural development, have been imaged using confocal microscopy [55]. Conversely, neural activity imaging in freely behaving larvae requires fast imaging with a mobile FOV to keep up with their 200 $mm\ s^{-1}$ movement. This has been studied in 3D using structured illumination [56].

OPT can be applied to single time point or low temporal resolution time series measurements to provide anatomical contrast from transmission images. For example, for imaging immune system response [37, 57, 58], and organogenesis of the brain taken at 10 minute intervals from 16 to 38 hours post fertilisation [59]. The rapid generation time of zebrafish has been leveraged by creating 3D imaging flow cytometry for high content screening, based on OPT [60] and SPIM [61].

For some disease types the lack of mature immune system and vasculature make zebrafish embryos a less suitable choice. For example, the immune system forms a critical component of the tumour microenvironment interaction. Without it, immunotherapies and anti-cancer drugs that act on the immune system cannot be studied. *Mus musculus* (mouse) models are a common choice for cancer studies [62]. However, their large size and opacity limits *in vivo* fluorescent imaging to localised intravital imaging [63, 64], or low resolution diffuse tomography [65]. Pre-clinical versions of clinical imaging modalities can be used for system wide 3D imaging, but cannot use genetically expressed labels [66]. Photoacoustic tomography can produce high resolution images deep in scattering tissue using fluorophores for contrast [67]. However, it does not have the same degree of specificity as fluorescence imaging; it collects signal from all absorption, the contrast of which is dominated by the chromophores discussed in section 2.1.1.

The difficulty of murine imaging has played a part in the development of zebrafish as a cancer disease model – the greater part being their high fecundity and their rapid, transparent and external development simplifying and accelerating compound screening [68]. Zebrafish are less homologous with humans than mice – sharing 70% and 83% of protein coding genes respectively – but still possess over 80% of disease related genes, indicating suitability for disease models including cancer [69].

Zebrafish lose their transparancy as they develop into adulthood. Their eponymous pigmentation pattern, composed of black melanophores, reflective iridophores, and yellow xanthophores, starts to develop two weeks after fertilisation [70]. Several mutants have been developed to remove these chromatophores and enable *in vivo* imaging into adulthood. *Casper* zebrafish, are double mutants that combine the *roy orbinson* mutation – which lacks iridophores – and the *nacre* mutation – which lacks melanophores [71]. The *TraNac* mutant similarly combines *roy orbison* with the *transparent* mutation, which leads to a lack of iridophores [72]. The *Casper* mutant has been further combined with albino mutants to stop melanin production in non-melanophore cells, such as the retinal pigment epithelium [73].

Imaging of non-pigmented adults has been mostly limited to 2D epifluorescence longitudinal imaging [74–77], or localised confocal or multiphoton imaging [76, 78, 79]. The work in this thesis focuses on the development of OPT for 3D imaging of these models *in vivo* and *in toto*.

Chapter 3

Optical projection tomography

OPT is the optical analogue of X-ray computed tomography [11]. 2D projections of a sample are acquired at a number of angular positions, which are then used to reconstruct its 3D structure.

With the addition of a rotation stage, a widefield microscope can perform tomography on transparent samples to measure 3D structure. A model system is shown in figure 3.1. The sample is mounted on a rotation stage and illuminated with widefield illumination in transmission or fluorescence geometry. The transmitted or emitted fluorescence photons are imaged onto a camera. These minimal requirements make OPT relatively low-cost, simple to implement, and readily scalable to a variety of sample sizes.

This chapter begins with a description of developments and applications of OPT in section 3.1. Next the theoretical basis of parallel computed tomography, and how it must be adapted when working with optical wavelengths is described in sections 3.2 and 3.3, respectively. Section 3.4 describes two OPT implementations. The end of the chapter, section 3.5, explains how compressive sensing can be used to accelerate OPT data acquisitions.

3.1 Developments and applications of optical projection tomography

OPT can be used to reconstruct the 3D distribution of a number of different contrast mechanisms in weakly scattering samples, from microscopic to over a cm in size. Optical wavelength computed tomography developed originally as optical-CT [80], a technique applied to verifying radiotherapy treatment plans in gel dosimetry phantoms. The original systems passed a focused laser through the sample and measured the attenuation of the beam with a photodetector [80, 81]. The sample was mechanically scanned to build up a full projection. Pixelated detectors were incorporated into these systems to remove the need for scanning and shorten acquisition times [82–84]. OPT developed from optical-CT with the application to cleared, fluorescent samples; the technique was first applied to image the 3D fluorescence and absorption distribution of a fixed and cleared mouse embryo [11]. It has since been applied to a wealth of other fixed and cleared tissues, and developed for *in vivo* applications.

For *ex vivo* applications, OPT offers an alternative method to serial sectioning for pheno-

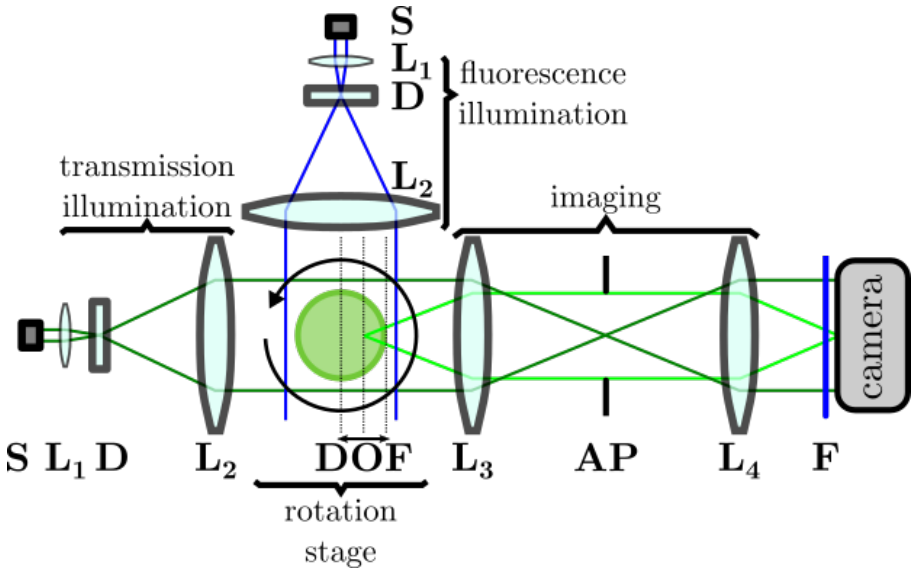

Figure 3.1: Model OPT system. The sample can be illuminated in transmission for absorption measurements, or with excitation light for fluorescence imaging. Illumination from source S is focused onto diffuser D by lens L_1, and collimated by condenser L_2. The transmitted light or emitted fluorescence is imaged onto a camera by lenses L_3 and L_4, via emission filter F. An adjustable aperture stop, AP, is placed in the back Fourier plane of L_3 to give telecentric imaging. The size of AP is set such that the DOF covers half the depth of the sample. The sample is mounted on a rotation stage, so that 2D projection images can be acquired at a number of angular positions.

typing and histology in 3D. The sample can be imaged while being kept intact, avoiding serial sectioning artifacts and sample destruction. OPT has been applied to imaging fixed and cleared samples of human embryos [85] and tumours [86, 87], *Drosophila* [88], chicken embryos [89], zebrafish embryos [90], mouse pancreas [91] and brain [92], various rat organs [93], and the reptilian heart [94].

The developments in OPT from the standard method can be broadly grouped into computational and optical innovations. These have the goals of removing reconstruction artifacts, producing improved contrast, overcoming the resolution compromise (section 3.3), and necessary improvements for *in vivo* applications. Common artifacts can be removed by accounting for variable illumination, hot pixels, refractive index mismatch and rotation axis misallignment [95–97]. Computational methods have also been developed to incoorporate the effects of diffraction and absorption into the reconstruction algorithm, either as a deconvolution filter to reduce blurring [98–100], to improve quantitativeness [101, 102], or to reject streak artifacts as unphysical – accelerating the acquisition [100].

Imaging speed is one of the important innovations needed for *in vivo* imaging, where anaesthetic tolerance, phototoxicity, and photobleaching are all important. Iterative compressed sensing [72] and ordered subsets expectation maximization reconstruction [103] algorithms have been applied to reconstruct OPT data taken with fewer angular projections than needed by

filtered back projection (FBP) (section 3.5).

Imaging speed and resolution have also been improved by increasing the light collection efficiency with higher NA OPT methods; a good approximation to parallel projection can be achieved with pseudo-projections produced by focal scanning [104–106] and angularly multiplexed imaging [107, 108]. Focal scanning OPT was originally applied to fixed cells [104], and large scan ranges were achieved on zebrafish embryos using remote refocusing [105]. The focally swept modulation transfer function is dominated by low spatial frequencies, which can be corrected for using a deconvolution filter [106]. Angular multiplexing [107] – creating pseudo-projections from simultaneously acquired shorter DOF projections focused on shifted focal planes – has been applied to even larger adult zebrafish. The technique also enables cell tracking [109]. Higher collection efficiencies have also been achieved by using laser scanning optical-CT with fluorescence imaging in scanning laser optical tomography (SLOT) [110].

Larger *in vivo* samples, such as adult zebrafish, also suffer from greater optical scattering [111]. This can be mitigated for transmission measurements by time-gating ballistic photons [112, 113], and in general using slice-illuminated OPT [6]. Applications of *in vivo* OPT include imaging of *Drosophila* [114, 115], the developing mouse embryo [116], zebrafish embryos [57, 117, 118] and adults [6, 103, 107, 108] and – by correcting for sample motion – *C. elegans* [119, 120].

OPT has been combined with FLIM [57, 100, 117] and speckle analysis [121] for greater functional contrast. Others have improved the dynamic range of OPT [122, 123]. Alternative OPT configurations have been developed for high throughput, based on flow cytometry, using phase [124] and transmission contrast [60]. A low-cost configuration has also been created as a microscope frame insert, reducing the marginal cost of 3D imaging for biology labs [118].

3.2 Parallel projection and tomographic reconstruction

In OPT a 3D object is reconstructed from a set of 2D projections acquired at different angles. This can be understood by examining the forward process of projection, and how that leads to a method of backprojection. Before introducing optical effects it is instructive to explore an idealised 2D system with perfect imaging [125]. Consider the parallel projection $p(t, \theta)$ of a 2D object $f(y, z)$ at an angle θ to the y axis, as shown in figure 3.2:

$$p(t,\theta) = \int_{-\infty}^{\infty} f\left(t\cos\left(\theta\right) - s\sin\left(\theta\right), t\sin\left(\theta\right) + s\cos\left(\theta\right)\right) \mathrm{d}s, \tag{3.1}$$

where (t, s) describe a coordinate system at an angle θ to (y, z):

$$\begin{bmatrix} t \\ s \end{bmatrix} = \begin{bmatrix} \cos\left(\theta\right) & \sin\left(\theta\right) \\ -\sin\left(\theta\right) & \cos\left(\theta\right) \end{bmatrix} \begin{bmatrix} y \\ z \end{bmatrix}.$$

The transformation of the object to a set of angular projections is called the Radon transform, and is inverted with a process called filtered back projection (FBP), or the inverse Radon transform.

To see how the object can be recovered, consider the 1D Fourier transform of a projection:

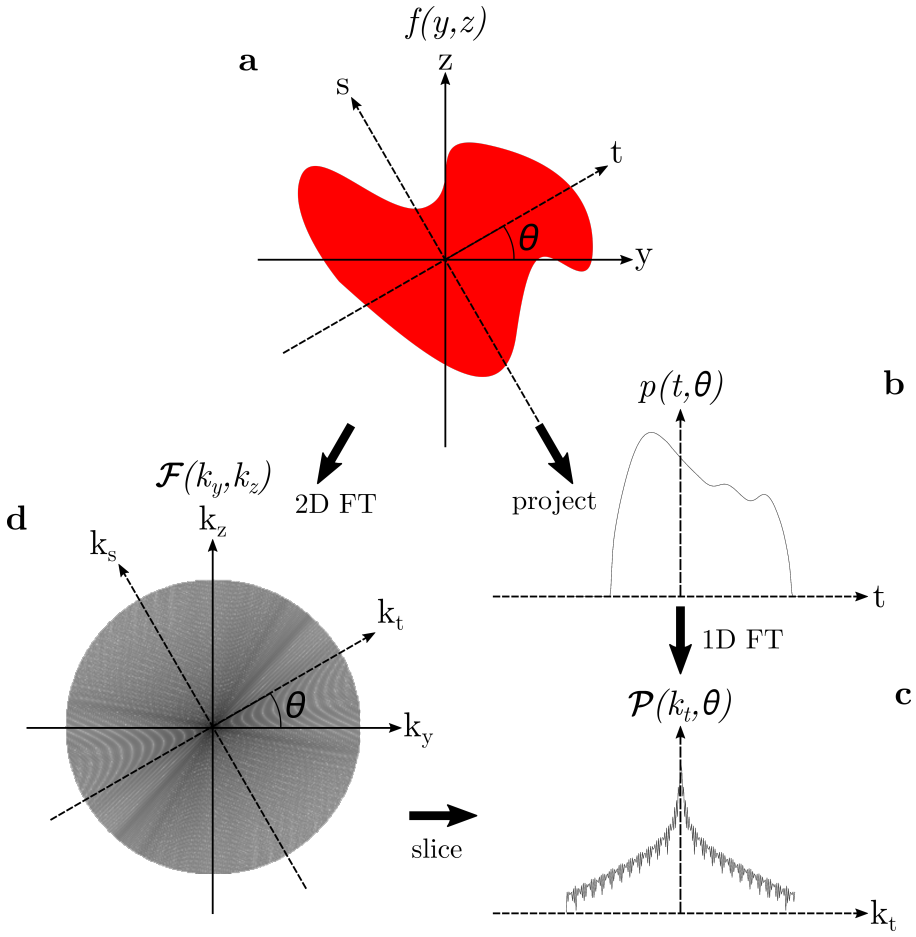

Figure 3.2: The central slice theorem. (**a**) A 2D object $f(y,z)$. (**b**) A projection of $f(y,z)$ along direction s onto an axis t at an angle θ to y, $p(t,\theta)$. (**c**) The Fourier transform, $\mathcal{P}(k_t,\theta)$, of $p(t,\theta)$ is equivalent to the central slice of (**d**), the object's 2D Fourier transform, $\mathcal{F}(k_y,k_z)$, at an angle θ to k_y.

$$\begin{aligned}\mathcal{P}(k_t,\theta) &= \int_{-\infty}^{\infty} p(t,\theta)\, e^{-2\pi i k_t t}\mathrm{d}t \\ &= \int_{-\infty}^{\infty}\int_{-\infty}^{\infty} f(t,s)\, e^{-2\pi i k_t t}\mathrm{d}s\mathrm{d}t. \end{aligned} \tag{3.2}$$

If we compare this to the 2D Fourier transform of the object,

$$\begin{aligned}\mathcal{F}(k_y,k_z) &= \int_{-\infty}^{\infty}\int_{-\infty}^{\infty} f(y,z)\, e^{-2\pi i k_y y} e^{-2\pi i k_z z}\mathrm{d}z\mathrm{d}y \\ &= \int_{-\infty}^{\infty}\int_{-\infty}^{\infty} f(t\cos(\theta) - s\sin(\theta), t\sin(\theta) + s\cos(\theta))\, e^{-2\pi i k_s s} e^{-2\pi i k_t t}\mathrm{d}s\mathrm{d}t, \end{aligned} \tag{3.3}$$

it can be seen that equation 3.2 is equivalent to the $k_s = 0$ slice through Fourier space:

$$\mathcal{F}(k_t\cos\theta, k_t\sin\theta) = \mathcal{P}(k_t,\theta). \tag{3.4}$$

Equation 3.4 is a statement of the central slice theorem [126]; each projection samples a rotated slice in the object's 2D Fourier space, as shown in figure 3.2. $\mathcal{F}(k_y, k_z)$ can be fully sampled by acquiring projections at sufficient slice angles. The object can then be reconstructed with an inverse Fourier transform:

$$f(y,z) = \frac{1}{2\pi}\int_{-\infty}^{\infty}\int_{-\infty}^{\infty}\mathcal{P}(k_t,\theta)\,e^{2\pi i k_y y}e^{2\pi i k_z z}\mathrm{d}y\mathrm{d}z \tag{3.5}$$

$$= \frac{1}{2\pi}\int_{0}^{\pi}\int_{-\infty}^{\infty}\mathcal{P}(k_t,\theta)\,e^{2\pi i k_t \cos\theta y}e^{2\pi i k_t \sin\theta z}\,|k_t|\,\mathrm{d}k_t\mathrm{d}\theta, \tag{3.6}$$

To reconstruct the object, its Fourier space must be fully sampled. This is achieved when the rotation between angular projections, θ_{min}, is small enough that $\mathcal{F}(k_{max}, k_{min})$ is covered as shown in figure 3.3, where $k_{max} = 1/(2r)$ – where r is the resolution of the system – and $k_{min} = 1/Nr$ – where N is the number of resolution elements across the FOV. This sets the minimum number of projections at

$$N_{\theta min} = \frac{2\pi}{\theta_{min}} = \frac{2\pi k_{max}}{k_{min}} = \pi N. \tag{3.7}$$

If the highest spatial frequencies are adequately sampled, all the lower spatial frequencies will be over sampled. To fix this over-sampling, a ramp filter, $w = |k_t|$, is applied to the projections before back projection – which can be seen appearing in equation 3.6 after the change in coordinates. However, this filter will also amplify high spatial frequency noise. Hann, Hamming, and other windows can be applied to this filter to reduce this effect [127].

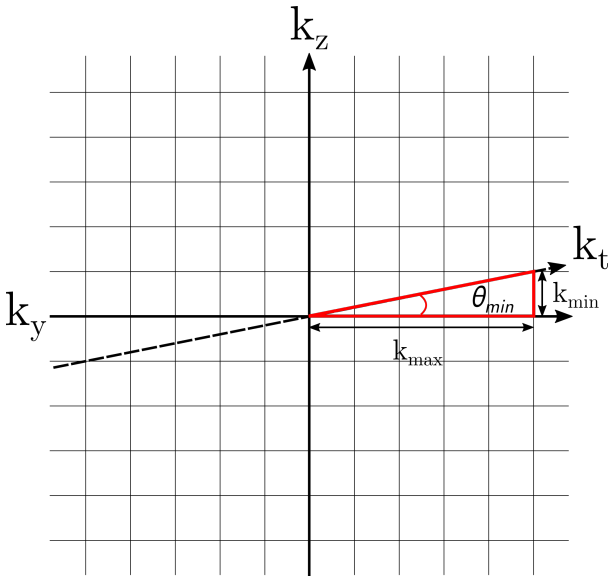

Figure 3.3: To adequately sample the object, the angular separation between projections must be small enough that the slices through Fourier space cover all points.

For parallel projections, equations 3.1-3.4 are trivially extended to 3D objects, $f(x,y,z)$, with x as the axis of rotation:

$$\begin{bmatrix} x \\ t \\ s \end{bmatrix} = \begin{bmatrix} 0 & 0 & 1 \\ \cos(\theta) & \sin(\theta) & 0 \\ -\sin(\theta) & \cos(\theta) & 0 \end{bmatrix} \begin{bmatrix} x \\ y \\ z \end{bmatrix}. \tag{3.8}$$

Each plane of constant x can be treated as a separate 2D reconstruction problem.

3.3 Optical projection tomography

OPT is the implementation of computed tomography with optical wavelengths [11]. Compared to X-ray computed tomography, OPT has the advantage of rich anatomic and functional spectroscopic contrast, both from absorption and fluorescence. OPT is also more readily applied to microscopic and mesoscopic samples, due to the ubiquity of appropriate pixelated detectors and focusing optics. However, radiation at optical wavelengths undergoes stronger diffraction and optical scattering, which must be considered if the assumption of parallel projection is to hold.

To approximate parallel projection, the DOF of the imaging system must extend through the whole sample. This creates a trade-off between sample size and spatial resolution. According to the Rayleigh criterion, two points can be resolved if the maximum of the point spread function of the first coincides with the first minimum of the second. For an Airy disk point spread function, at the focal plane this limiting distance is given by [128]:

$$r_{airy} = \frac{0.61\lambda}{NA}, \tag{3.9}$$

where λ is the wavelength of the imaged light, and NA is the numerical aperture of the imaging system. The DOF is given by [129]

$$DOF = n_{bath}\left(\frac{n\lambda}{\mathrm{NA}^2} + \frac{n}{M\mathrm{NA}}e\right), \tag{3.10}$$

where M is the lateral magnification of the imaging system, n_{bath} is the refractive index of the sample medium, and e is the pixel size of the CCD. These equations show the trade off between resolution and sample size in OPT; imaging a larger sample requires a larger DOF, which in turn requires a smaller NA, a result of which is reduced resolution. As a compromise, an NA is chosen that produces a DOF to cover only the front half of the sample. With this configuration a good approximation to parallel projection is achieved by combining projections acquired at 180° to one another, which are projections in the same direction but with DOFs covering different halves of the sample.

Achieving parallel projection puts further restraints on the optics and sample. Firstly, the imaging optics must be telecentric so that the magnification is constant across the DOF. This is achieved by placing the aperture in the back focal plane of the objective, which ensures that the chief rays of objects within the depth of focus are approximately parallel to the optic axis. Secondly, optical scattering should be negligible, so OPT is typically applied to samples that are optically cleared or inherently transparent.

3.4 Example optical projection tomography systems

Two fluorescence OPT systems were developed in the configuration shown in figure 3.1. One of these used light emitting diode (LED) illumination, the other used a bank of laser diodes coupled into a multimode fibre.

3.4.1 Light emitting diode based optical projection tomography system

An LED based OPT system was built to image three-dimensional samples in the mm to cm range. LED radiation at 470 nm, 660 nm, and 730 nm (Multiline, Cairn) was spectrally filtered (480/30x, 655/30m, and 720/60m, Chroma) and collimated with lenses L1 (G063208000, $f = 40\ mm$, Linos) and directed to illuminate the sample. The sample was suspended into an in-house built octagonal cuvette – with windows normal to the excitation and imaging axes – filled with deionised water, for water based samples, or benzyl alchohol benzyl benzoate (BABB), for cleared samples. The sample was attached to a stepper motor (NM08AS-T4, Zaber). The motor was mounted on a 6-axis gantry for alignment. Fluorescence, selected using emission filters (535/40m, 705/30m, and 810/90m, Chroma) placed in a sliding mount (CFS1ND/M, Thorlabs), was imaged with a commercial 0.5x magnification telecentric lens (TL) with an adjustable aperture (TECHSPEC SilverTL, Edmund Optics) onto a 1360x1024 6.45x6.45 μm pixel charge-coupled device (CCD) camera (R1, Q-imaging). For most aperture settings the system was pixel limited; the pixel size was too great to achieve Nyquist sampling of the image. This sets the resolution to two times the pixel size at the sample; 25.8 μm.

3.4.2 Laser diode optical projection tomography system

A laser diode based OPT system was built to image three-dimensional samples in the mm to cm range. Multimode fibre coupled laser radiation at 638 nm, 525 nm, 465 nm, and 555 nm (MultiLine LaserBank, Cairn) was spectrally filtered (432/36, 631/36, 554/23, 510/20, 445/45), focused onto a holographic diffuser (ED1-C50, Thorlabs), collimated by a fresnel lens (FRP251, Thorlabs), and directed to the sample to produce widefield illumination. Laser speckle was averaged out by vibrating the multimode fibre. The emitted fluorescence was spectrally filtered (474/27, 535-50, 708/75, 609/54, 540/15, 500/24) and imaged with a 1x telecentric lens (58-430; Edmund Optics) with a 5 mm DOF, onto a scientific complementary metal-oxide-semiconductor (sCMOS) camera (Zyla 5.5, Andor Instruments).

3.4.3 Acquisition and reconstruction

Control of an OPT system requires two components; a process for alignment, and a process for acquisition. From equation 3.8 the rotation axis is defined as parallel to the x axis, and runs through the centre of the FOV. If this is not the case, the results of FBP will be incorrect; if the error is small the reconstruction will be blurred, for larger shifts the reconstruction will be corrupted by ring artifacts. To ensure this condition is met, a high contrast test object (such as an Allen key or bent needle) is imaged, rotated 180°, and imaged again. If the effects of

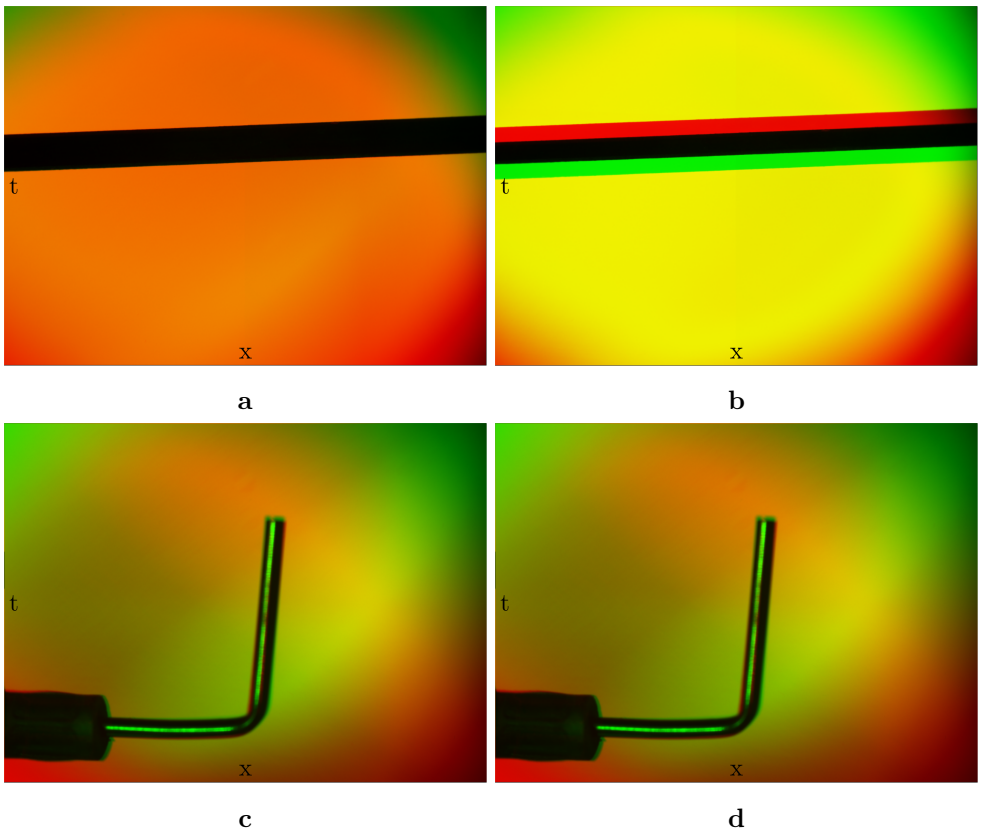

Figure 3.4: Images produced by alignment script for different alignment states. The rotation axis is horizontal. The image of the object rotated to 0° and the vertically flipped image of the object rotated to 180° are shown in red and green, respectively. The colour variations of the background are due to uneven illumination, which is not important for alignment of the rotation axis. (**a**) System aligned. (**b**) Rotation axis shifted in the image plane, creating red and green borders. (**c**) Tilt of the rotation axis in the image plane, causing a rotation between the two channels. (**d**) Tilt of the rotation axis out of the image plane, visible as a translation in the y axis for parts of the object away from the rotation axis (x, y) plane.

diffraction, noise, uneven illumination, object opacity are ignored, these two images should be identical – mirrored in the x axis. Any mismatch in position or orientation of these images shows that the axis of rotation and the pixelated detector are not aligned (figure 3.4).

For the OPT data acquisition, the sample is rotated to a set of angular positions and 2D projection images are captured at each. Figure 3.5a shows an (x, t) 2D projection from an (x, t, θ) *ex vivo* fluorescence OPT data set of a fixed and cleared mouse pancreas in which the beta cells are labelled with a fluorescent dye, acquired with the LED based OPT system. As described in section 3.2, each (t, θ) cross section or "sinogram" can be reconstructed separately. An example sinogram is shown in figure 3.5b – so called because each point in the object projects a sinusoidal trajectory when rotated. The sinogram is the Radon transform of the (y, z) slice of the sample volume, which can be reconstructed using FBP (figure 3.5c).

This process is repeated for each (t, θ) sinogram to reconstruct the entire volume of the sample. Figure 3.6a shows a 3D reconstruction of a cm sized mouse pancreas volume recon-

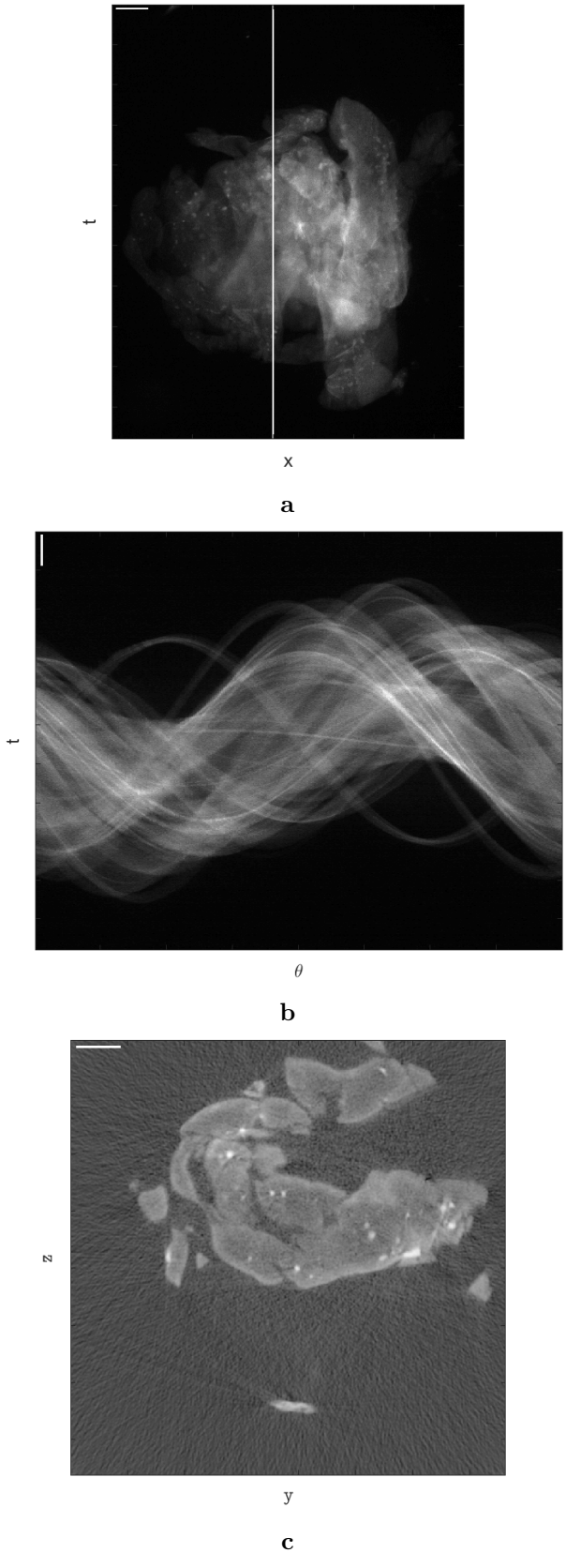

Figure 3.5: Demonstration of reconstruction of a slice from a typical OPT data set – the mouse pancreas, showing beta-cells labelled with guinea pig anti-swine insulin antibody and Alexa 594 goat anti-guinea pig antibody. (**a**) An (x, t) projection from an OPT data set. (**b**) The (t, θ) sinogram from the column of pixels indicated in (**a**). (**c**) FBP reconstruction of that slice of the sample. Scale bar 1 mm

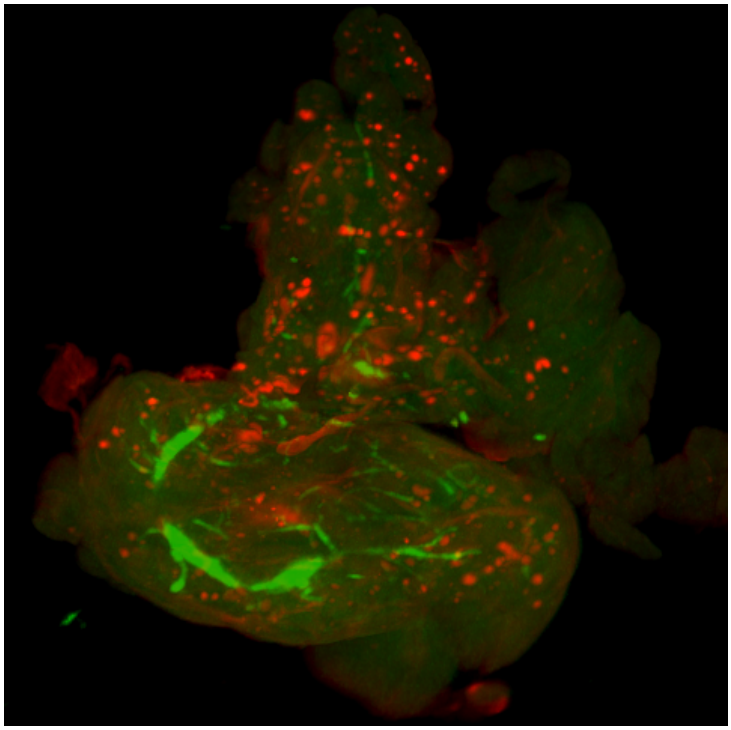

a

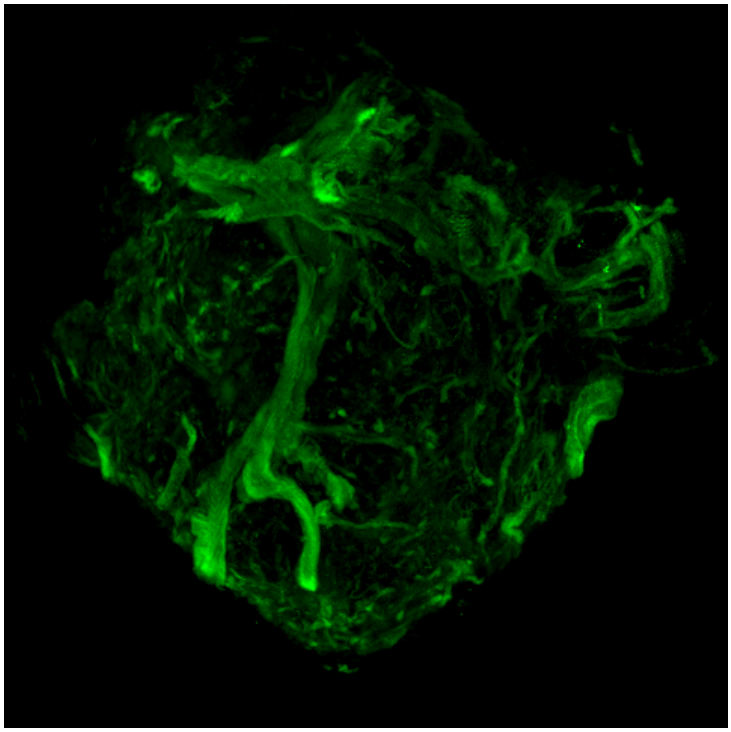

b

Figure 3.6: 3D reconstructions of cm sized samples acquired on different OPT systems. (**a**) Mouse pancreas, showing beta-cells labelled with guinea pig anti-swine insulin antibody and Alexa 594 goat anti-guinea pig antibody in red and autofluorescence in green. (**b**) Ovary biopsy, showing vasculature labelled with anti-CD34 rabbit monoclonal antibody and Alexa 488 anti-rabbit antibody in green. Scale bar not shown because these visualisations are renders incorporating perspective.

structed from OPT acquired on the LED based system. The pancreas was prepared following the protocol as described in [130]; the beta-cell mass of the whole fixed mouse pancreas was labelled with guinea pig anti-swine insulin antibody and Alexa 594 goat anti-guinea pig antibody. It was mounted in 2% agarose, dehydrated in increasing concentrations of methanol up to 100% and subsequently chemically cleared in a 1:2 mixture of benzyl alcohol: benzyl benzoate. Labelled fluorescence excitation was provided by the 660 nm LED, and the emitted fluorescence was spectrally selected with the 705 ± 15 nm emission filter. Autofluorescence excitation was provided by the 470 nm LED, and the emitted autofluorescence was spectrally selected with the 535 ± 25 nm emission filter. 400 equally spaced projections were acquired over a full rotation.

Figure 3.6b shows a 3D reconstruction of a cm sized ovary biopsy volume reconstructed from OPT acquired on the laser diode based system. The sample was prepared as follows: the vasculature of the fixed sample was labelled with anti-CD34 rabbit monoclonal antibody and Alexa 488 anti-rabbit antibody. It was mounted in 2% agarose, dehydrated in increasing concentrations of methanol up to 100% and subsequently chemically cleared in a 1:2 mixture of benzyl alcohol: benzyl benzoate. Labelled fluorescence excitation was provided by the 470 nm LED, and the emitted fluorescence was spectrally selected with the 535 ± 20 nm emission filter. 1280 equally spaced projections were acquired over a full rotation.

3.5 Compressive sensing

If fewer projections are acquired than required by equation 3.7, FBP of the undersampled projection data set will produce reconstructions corrupted by streak artifacts (figure 3.7c, and 3.7e). If the angular separation between projections is too large, their corresponding slices in Fourier space (figure 3.3) will have gaps between them, resulting in a star-like Radon sampling pattern (figure 3.7d, and 3.7f).

In most circumstances, undersampling artifacts produce ambiguities in measurement; for example undersampling in the spatial domain will cause high spatial frequency signals to be aliased into low spatial frequencies, and undersampling in Fourier space will cause identical copies of the true signal to be aliased to different locations. However, this is not what is seen when undersampling the Radon transform; although the streak artifacts significantly degrade image quality, they do not form ambiguous copies of the correct data.

The difference between archetypal aliasing and what is seen in the case of the Radon transform is caused by the coherence of the undersampling. Figure 3.8 shows a sample slice reconstructed from a quarter of its Fourier components, which are chosen using different sampling strategies: in the first the spatial frenquencies are sampled at equal intervals, in the second they are sampled randomly, and in the final example an approximation to the Radon star-shaped sampling pattern is used. The slice reconstructed from equispaced components is corrupted with archetypal coherent aliasing artifacts, whereas in the case of random sampling the aliasing artifacts are incoherent and have the appearence of random noise, rather than ambigious copies. This re-casts the ill-posed problem of guessing at missing information, to a de-noising problem. Although more structured than the random sampling case, the Radon sampling pattern also

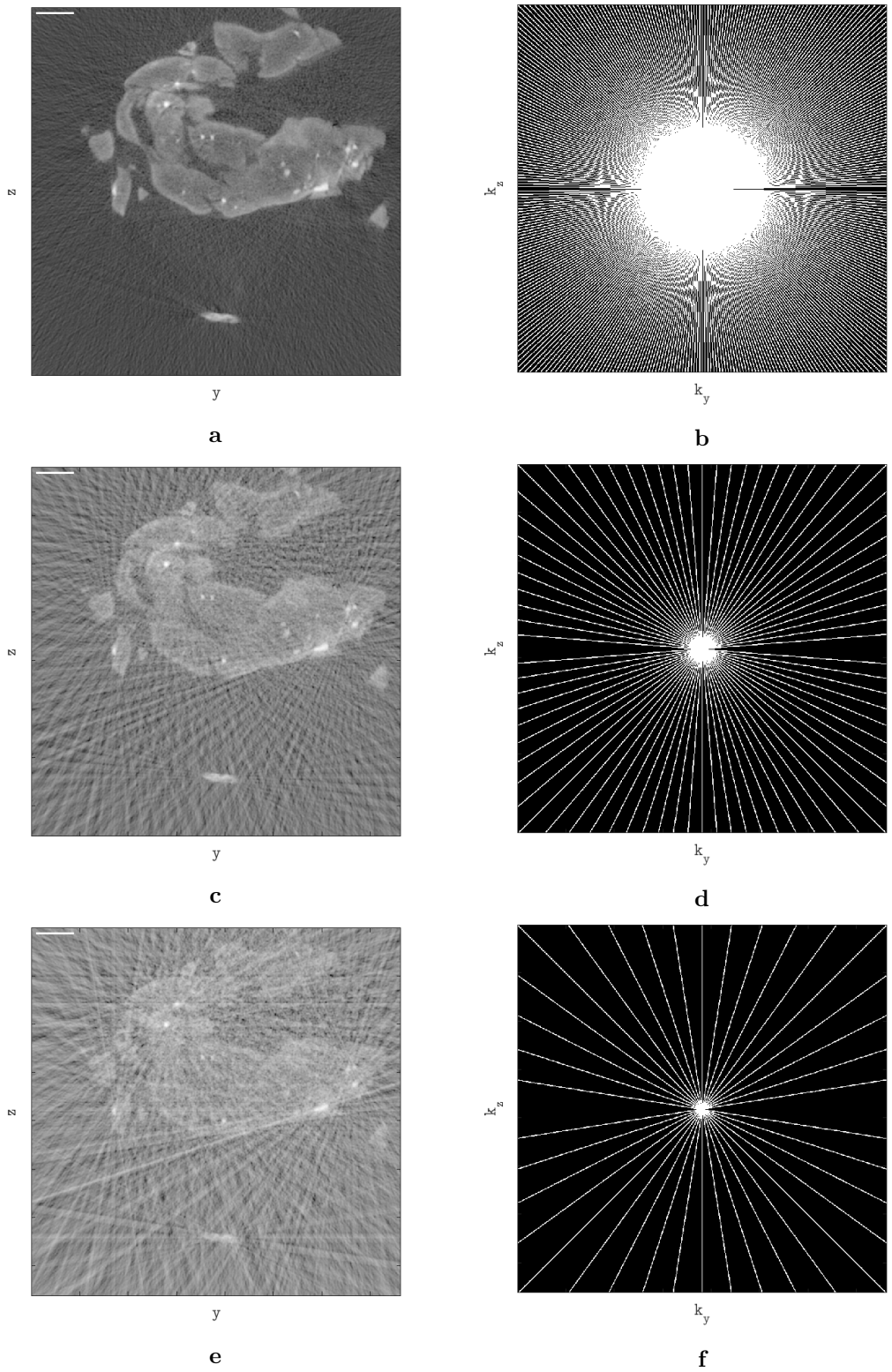

Figure 3.7: Demonstration of streak artifacts on slices reconstructed from too few angular projections. (**a**) Slice reconstructed from 400 projections. (**b**) An approximation to the Fourier sampling pattern for 400 projections. (**c**) Slice reconstructed from 80 projections. (**d**) An approximation to the Radon Fourier sampling pattern for 80 projections. (**e**) Slice reconstructed from 40 projections. (**f**) An approximation to the Radon Fourier sampling pattern for 40 projections. Scale bar 1 mm

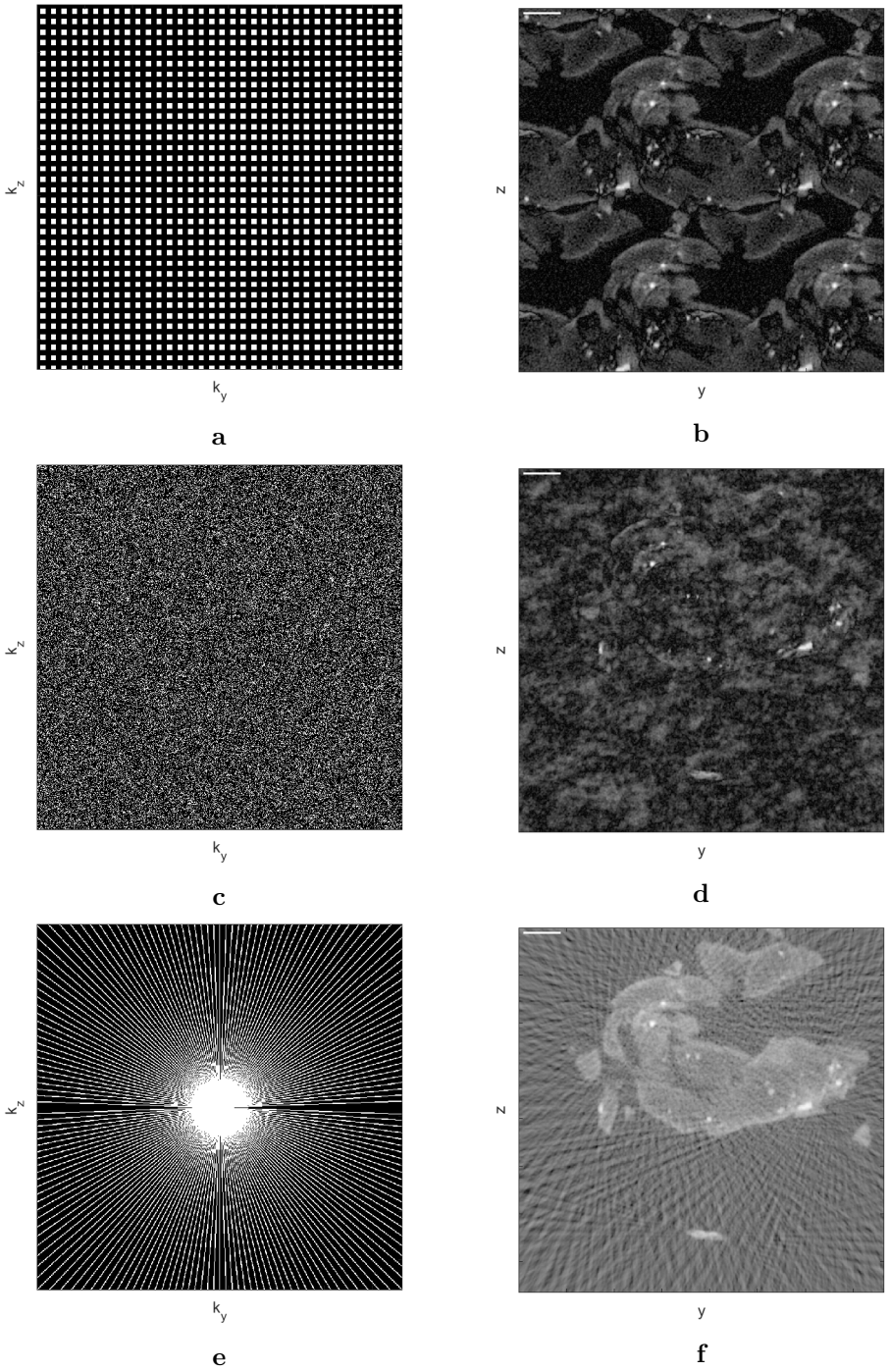

Figure 3.8: Aliasing artifacts produced by different Fourier space sampling strategies. (**a**) Equispaced sampling mask, magnified to reduce display artifacts. (**b**) Reconstructed image from equispaced undersampling strategy, which produces ambigious coherent aliasing artifacts. (**c**) Random sampling mask. (**d**) Reconstructed image from random undersampling. The aliasing artifacts are incoherent – giving the appearance of random noise. Due to the object's gradient sparsity, the strongest gradients are visible above the noise floor, which will form the starting point for denoising based recovery. (**e**) An approximation to a 92 projection Radon sampling mask. (**f**) Reconstructed image from Radon sampling strategy. Although the noise does not have a random appearance, the aliasing artifacts are not coherent and not ambigious. Scale bar 1 mm

does not produce coherent aliasing artifacts and can be treated in the same way.

Compressive sensing (CS) is a signal processing technique that exploits this effect to recover a sparse signal recorded with an undersampled measurement [131, 132]. As long as the original signal is sparse (compressible in some basis) the true signal can be distinguished from the incoherent aliasing artifacts, and recovered with an iterative denoising algorithm.

The undersampled forward moded can be described by:

$$Y = RX + \text{noise}, \tag{3.11}$$

where Y is the length M measurement corrupted by noise, R is the $M \times N$ forward operator – and X is the length N sparse signal to be estimated. For $M < N$ the system of linear equations is underdetermined, and there are infinite solutions. In CS a sparse solution is sought by solving the optimisation problem

$$minimise_X \frac{1}{2} \|Y - RX\|_2^2 + \tau\Phi(X), \tag{3.12}$$

where the first term is the l_2 norm of the residual, τ is the regularisation parameter and Φ is the regularisation functional, which measures the sparsity. If X itself is sparse, this will be the l_1 norm. For image recovery, gradient sparsity can be used [132]. In that case the total variation functional is

$$\Phi_{TV}(X) = \sum_i \sqrt{\left(D_i^H\right)^2 + \left(D_i^V\right)^2}, \tag{3.13}$$

where D_i^H and D_i^V are horizontal and vertical gradients of X at pixel index i.

Equation 3.12 can be solved using iterative shrinkage thresholding (IST) [133]:

$$X_{t+1} = \Psi_\tau(X_t + R^T(Y - RX_t)/w), \tag{3.14}$$

where R^T is the adjoint operator of R, and w is a relaxation parameter. R^TY is the noisy first estimate of X, from which the incoherent artifacts predicted for the current estimate are subtracted; R^TRX_t. This reveals smaller peaks – and their incoherent patterns – previously obscured by the artifacts of the larger peaks. These are then added to the current estimate, X_t, before thresholding is performed by the sparsifying operator, Ψ_τ.

The choice of sparsifying operator depends on the particular application. For l_1 regularisation problems Ψ_τ is the soft thresholding functional:

$$\Psi_\tau(x) = \begin{cases} 0, & \text{for } |x| \leq \tau \\ x - \tau, & \text{for } x > \tau \\ x + \tau, & \text{for } x < -\tau, \end{cases} \tag{3.15}$$

where x is an element of X. For image processing tasks using total variation regularised reconstruction, $\Psi_\tau(X)$ is a total variation denoising iterative algorithm, which solves [134]:

$$minimise_X \frac{1}{2} \|X - X_0\|_2^2 + \tau\Phi_{TV}(X), \tag{3.16}$$

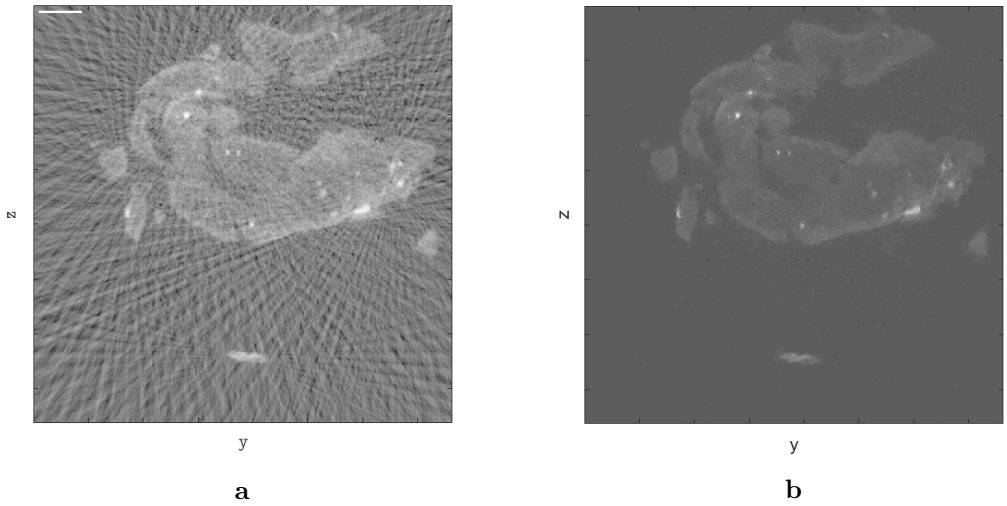

Figure 3.9: Demonstration of compressive sensing reconstruction. (**a**) Slice reconstructed from 80 angular projections using FBP. (**b**) Slice reconstructed from 80 projections using IST.

where X_0 is the noisy input data.

For the specific case of CT: Y is the measured sinogram, R and R^T are the Radon and inverse Radon transforms, and X is the slice. Due to interpolation between cartesian and polar coordinates, the Radon transform is non-unitary. As a result, w must be set to $O(10)$ to ensure convergence. Figure 3.9 shows an undersampled slice reconstructed with FBP and with 200 IST iterations, with $\tau = 0.001$. The iterative method is able to remove the streak artifacts and significantly improve the reconstruction quality. Compressed sensing has many other applications [135], and will be applied to reconstructing single-pixel camera data in chapter 8.

Chapter 4

Optimisation of angularly multiplexed optical projection tomography

4.1 Introduction

As discussed in chapter 2.3, adult zebrafish are a promising model for *in vivo* imaging cancer studies; zebrafish embryos lack a mature vasculature network and immune system, and fluorescent imaging of mice requires the sacrifice of the animal – precluding longitudinal studies – or is limited to localised intravital imaging [63,64], or low resolution diffuse tomography [65]. OPT is an attractive choice for *in vivo* imaging of these cm sized samples, due to the low phototoxicity associated with the widefield illumination, simplicity, relatively low cost of implementation and ease of scaling the imaging system to larger samples.

However, the acquisition lengths for the conventional approach to OPT are too long for survival of the anaesthetic procedure [136], due to the low NA required to approximate parallel projection and the large number of projection images required for artifact free reconstruction (see chapter 3). Angularly multiplexed compressed sensing OPT was developed to overcome this limitation [72,107,108]. This chapter describes developments to the multiplexed OPT data processing workflow, and the application of the system to a longitudinal study.

To achieve higher resolution and collection efficiency, angularly multiplexed OPT was developed [107, 108], in which a pseudo-projection is created by combining projections from two separate imaging arms, whose DOFs cover different quarters of the sample depth. This shorter DOF allows for a $\sim \sqrt{2}$ increase in NA, which improves the resolution by $\approx 20\%$ and the collection efficiency by a factor of two for the larger NA, and a further two by having two cameras.

In combination with compressed sensing reconstruction (chapter 3.5), this system has been demonstrated imaging tumour burdened adult zebrafish in two spectral channels within the time window of anaesthetic tolerance, between 10 and 20 minutes [108, 136]. Therefore, the zebrafish can be kept alive for repeated measurements of disease progression in a longitudinal

study.

Previously, the ability to handle longitudinal and high-throughput studies was practically limited by the requirements for manual selection of alignment and reconstruction parameters. Furthermore, this manual parameter search produced inconsistent and sub-optimal results. To address this, a number of processes have been automated, minimising human supervision and improving reconstruction quality.

With the optimisations to data processing, the system has been applied to a longitudinal study of liver tumour growth in adult zebrafish. Section 4.2 describes the optical set-up (section 4.2.1), longitudinal study design (section 4.2.2), and data processing (section 4.2.3). Section 4.3 shows the results of the longitudinal study. Section 4.4 concludes with a discussion of those results and further work.

4.2 Methods

4.2.1 Experimental set up and acquisition

A schematic of the angularly multiplexed OPT set up is shown in figure 4.1. Laser radiation (labelled as S in figure 4.1) at either 561 nm (Jive, Cobolt) or 488 nm (MLD, Cobolt) was directed to a rotating diffuser D (ED1-C50, Thorlabs), collimated using lens L_1 (FRP251, Thorlabs), and directed to illuminate the sample. The emitted fluorescence was imaged using two 0.49x telecentric imaging arms – comprising achromatic lenses, L_2, L_3 and L_4, (AC504-200-A, $f = 200$ mm, AC508-180-A, $f = 180$ mm, AC508-250-A, $f = 250$ mm) and meniscus lens, L_5 (LF1988-A, $f = -500$ mm, Thorlabs), with an adjustable aperture stop AP (SM2D25D, Thorlabs) in the Fourier plane of the first achromat – onto sCMOS cameras (Zyla 5.5 sCMOS, Andor Technology Ltd). The NA was set to 0.02, to give a DOF of 2.5 mm and a diffraction limited resolution of 14 and 16 μm for 488 nm and 561 nm, respectively – so that the system resolution was pixel limited to 26.3 μm. The two imaging arms were orientated 90° to one another, and have their focal planes placed 1.25 mm and 3.75 mm from the rotation axis.

Samples were placed in FEP tubing (EW-06406-12, Cole Parmer), filled with water, sealed, and suspended from a stepper motor (T-NM17A200, Zaber) attached to tip-tilt and translation stages. The tube was suspended into a water filled custom octagonal imaging chamber, with windows normal to the imaging and excitation paths.

The system was controlled with custom software written in LabVIEW (National Instruments). Both cameras were aligned such that the rotation axis was parallel to the x axis (coordinate system defined in chapter 3.2) and in the centre of their respective FOVs. This was achieved by acquiring projections separated by 180° of a high contrast object, such as an Allen key, and comparing the first projection to the second – mirrored in the x axis. The tip-tilt and translation stages were adjusted until the pairs of projections matched on both cameras; when this occured the rotation axis was aligned. OPT data sets were acquired simultaneously on the two cameras. The sample was rotated to 64 equally spaced positions around 360°, with a low angular acceleration of 1.6° s^{-2}, to minimise the sample slipping in the tube. Multi-spectral imaging was achieved by acquiring sequential data sets with either the 561 nm or 488 nm laser

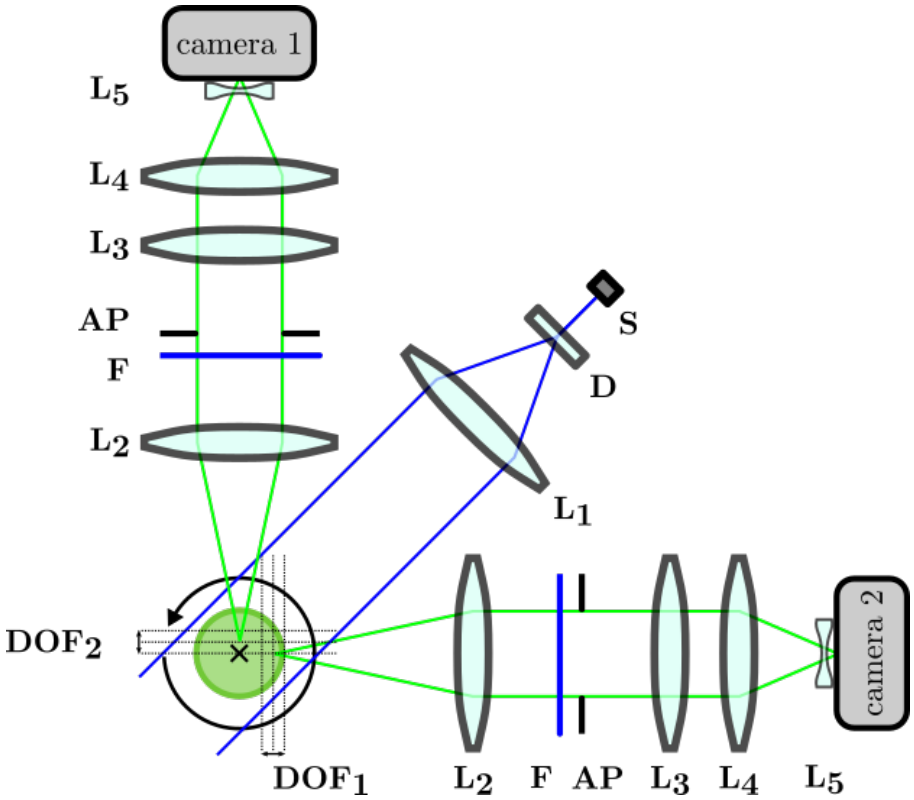

Figure 4.1: Schematic of angularly multiplexed OPT system. The two imaging arms each image a different quarter of the depth of the sample. The axis of rotation is indicated by a cross

unshuttered, for which 2 *s* and 1 *s* exposure times were respectively used. Fluorescence emission was selected using emission filters (FF02-472/30-32 and FF01-562/40-25, Semrock), placed in motorised filter wheels (FW102C, Thorlabs) close to the Fourier plane of the imaging optics.

4.2.2 Longitunial study of tumour development

The system was applied to longitudinal imaging of a zebrafish tumour model. The model used, TraNac Tg (KDR:mCherry:Fabp10-rtTA:TREeGFPKRAS^{V12}), inducibly expresses the eGFP-tagged oncogenic kras^{V12} transgene in hepatocytes when exposed to tetracycline, or a tetracycline derivative such as doxycycline. This controllable expression of kras^{V12} means that liver tumours can be induced with exposure to doxycycline, and reduced through withdrawal. To overcome the issues with pigmentation in the adult zebrafish, the tumour model was bred onto the background of the mutant TraNac line. This line is a double homozygous recessive mutant for two genes, nacre and transposase, which are required for pigmentation. Other non-pigmented lines include Caspar [71], and Crystal [73].

28 fish were treated with doxycycline and imaged with two channel angularly multiplexed OPT every week for five weeks of treatment. During the study, the concentration of doxycycline was adjusted as the protocol was optimised. Higher concentrations caused the water salinity and acidity to become unhealthy for the fish, but the concentration was also found to fall within the experimentally relevant time period of 24 hours. The water in which the fish were housed

was dosed with a doxycycline concentration of 7.5 mg/L for the first nine days, then 5 mg/L for five days, then 7.5 mg/L for the third week, and 10 mg/L for the remainder of the study.

For the first four weeks of imaging, the zebrafish were anaesthetised using water containing 175 ppm tricaine methanesulfonate, and 175 ppm isoflurane [136]. Once the zebrafish had entered deep anaesthesia – determined by a lack of response to any stimuli – samples were placed in FEP tubing and mounted in the system for imaging. A wedge of agarose was placed in the FEP tubing to firmly hold the zebrafish in place and reduce the risk of sample movement during the OPT acquisition. After imaging, the samples were recovered by returning them to water.

4.2.3 Processing

4.2.3.1 Registration

Angularly multiplexed OPT achieves superior resolution compared to conventional OPT for the same effective DOF by creating a pseudo-projection from two higher NA projections that image two different quarters of the sample. In principle, creating this pseudo-projection should be achievable by simply adding the corresponding projections together – as they have both been aligned to the rotation axis and should have the same FOV. However, placement and removal of samples in the system caused slight misalignments through the day. Therefore, each pair of data sets required individual co-registration.

Previously, each data set was manually co-registered in software written in LabVIEW by visual inspection; every corresponding pair of projections could be viewed, and the translation, angle, and magnification adjusted until both sets of projections appeared to be aligned. The transformation was then applied globally to every projection from camera 1 to camera 2. For longitudinal or high-throughput studies this requires significant user input and it is challenging to find a good solution in the large parameter space. Furthermore, using a single global transformation is not tolerant to the required transformation changing from projection to projection, which may occur due to small sample movements, or either data set being subtly misaligned with the rotation axis. It was therefore desirable to automate this process.

The autoregistration software was written in Matlab. Each pair of projections from camera 1 (4.2a) and camera 2 (4.2b) were individually registered. The projection from camera 2 was first demagnified by the known magnification between the two imaging systems, $M = 0.998$. Next, filtered images were created from the projection pairs with different spatial scales, l, by applying empirically chosen Gaussian bandpass filters of $10 < l < 25$ pixels (4.2c), $20 < l < 50$ pixels (4.2d), and $30 < l < 75$ pixels (4.2e), which removed both high spatial frequency noise, and low spatial frequency differences in illumination. Registration between each pair of filtered images was performed with the built in *imregtform* Matlab function – limited to rigid transformations and using the Mattes mutual information as its target metric [137], which is suitable for images acquired under different illumination conditions. The three estimated transformations were then applied to the original projection pair, passed through a 10 pixel wide Gaussian high pass filter, and the transformation that produced the final projection with the highest variance was

retained.

The relative performance of manual and automatic registration for a single projection image is shown in figure 4.2. The anatomy appears correctly aligned in the manual registration image. However, in comparison to the automatic registration, it appears blurred. This is further explored in figure 4.3, which quantifies alignment quality using variance as a sharpness metric; the variance has been plotted for the 64 projections of an angularly multiplexed OPT data set after registration using the manual and automatic method. In figure 4.3a the contrast appears very similar. In figures 4.3b and 4.3c the variance has been calculated on projections processed with Gaussian high pass filters of 100 and 10 pixel widths respectively. In these, the improvements to alignment of higher spatial frequency content in the automatically registered images are clear.

4.2.3.2 Alignment with rotation axis

During sample mounting and removal, the rotation axis is regularly misaligned from the centre of the FOV, which needs to be corrected during processing. This can be achieved manually using in-house software written in LabVIEW by visually inspecting opposite projections, which should be mirror images of one another, and applying a y axis shift and a rotation that aligns the projections. However, as with registration, this requires user intervention, and the exploration of a large parameter space. Therefore, this process has also been automated using the method described in [95], which seeks the y axis shift and the rotation that produces reconstructions with the greatest variance – which is assumed to correspond to the highest spatial resolution.

Figure 4.4 shows a slice of *ex vivo* cleared mouse pancreas that was reconstructed with different shifts applied to the x axis – producing varying degrees of rotation axis misalignment. The misalignment caused blurring and ring artifacts, which reduced the variance in the image. The sharpest reconstruction appears to be figure 4.4d, which had a rotation axis shift of 8 pixels – corresponding to the peak seen in figure 4.4f. This measurement was repeated at various points along the length of the sample, which is shown for the pancreas in figure 4.4g. If the rotation axis is tilted in the FOV, this can be seen by the rotation axis correction changing with x. To complete the correction, a linear fit was made between x position and rotation axis shift – and the measured rotation and shift was applied to the raw projections. The angle measured in this process is a shear correction, which only approximates the rotation correction, so the process was repeated until the corrected projections showed a rotation axis through the centre of the FOV.

In undersampled adult zebrafish data the peak is much less clear; the object has a greater contribution from low spatial frequencies, which disguise the effects of misalignment, and the undersampling introduces noise and streak artifacts. To mitigate the strong background from low spatial frequencies, the slices are passed through a 30-pixel wide high pass Gaussian filter. The equivalent of the histogram shown in figure 4.4g for a zebrafish data set is shown in figure 4.5. The result is significantly noisier than that measured for the *ex vivo* mouse pancreas, but an average measurement can be taken for the data set. The alignment measured for the mCherryFP channel was applied to the GFP channel, to enforce registration between the two

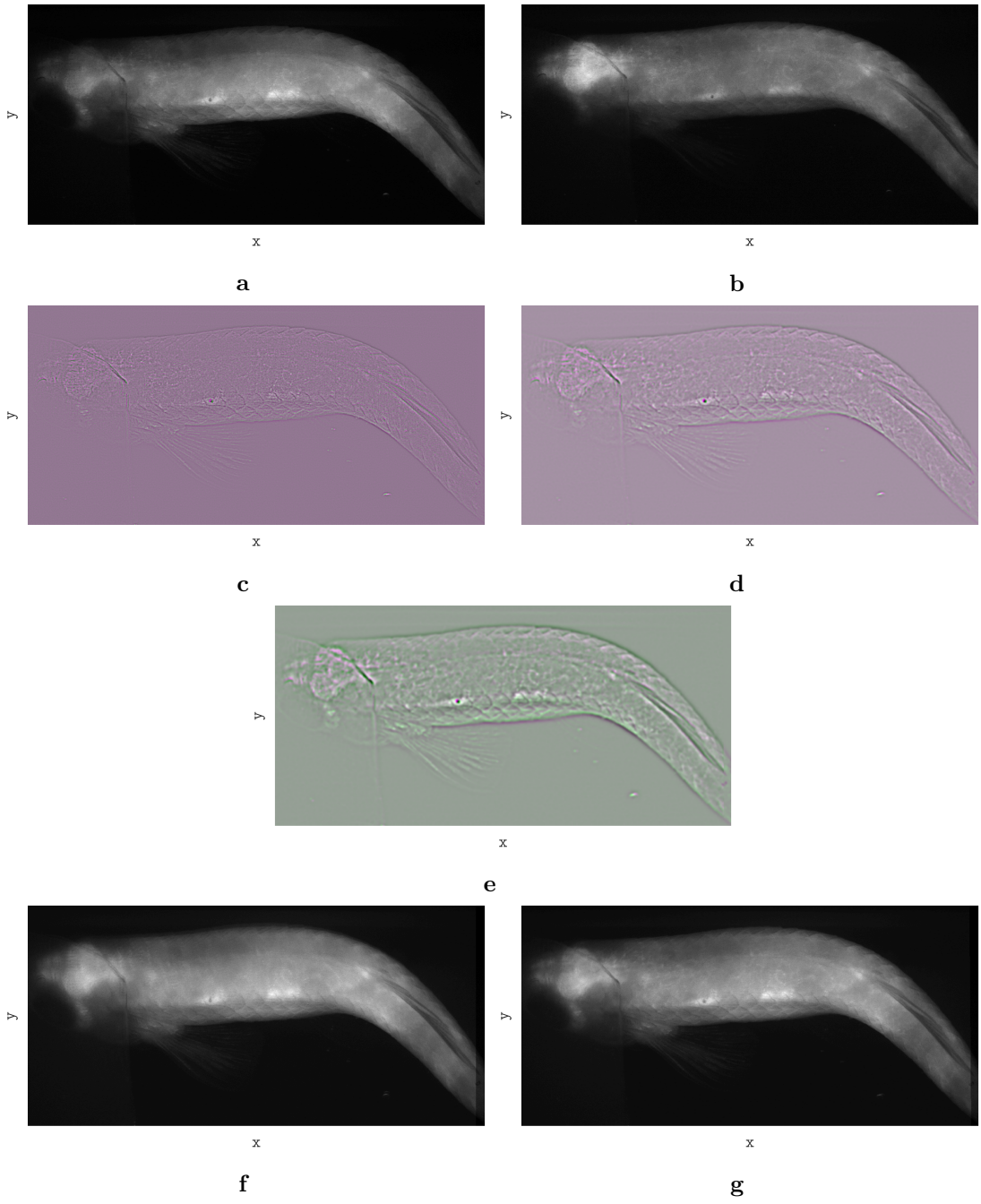

Figure 4.2: Automatic registration of angularly multiplexed OPT data. (**a**),(**b**) Camera 1 and Camera 2 projections acquired with shifted focal planes and different illumination conditions. The images were bandpass Gaussian filtered and the rigid transformation estimated. The registered camera 1 and camera 2 images are shown in green and purple respectively after applying Gaussian bandpass filters (**c**) $10 < l < 25$ pixels, (**d**) $20 < l < 50$ pixels, (**e**) $30 < l < 75$ pixels. (**f**) Manually registered projections. (**g**) Automatically registered projection. The automatic result which had the greatest variance, in features smaller than 10 pixels, was selected.

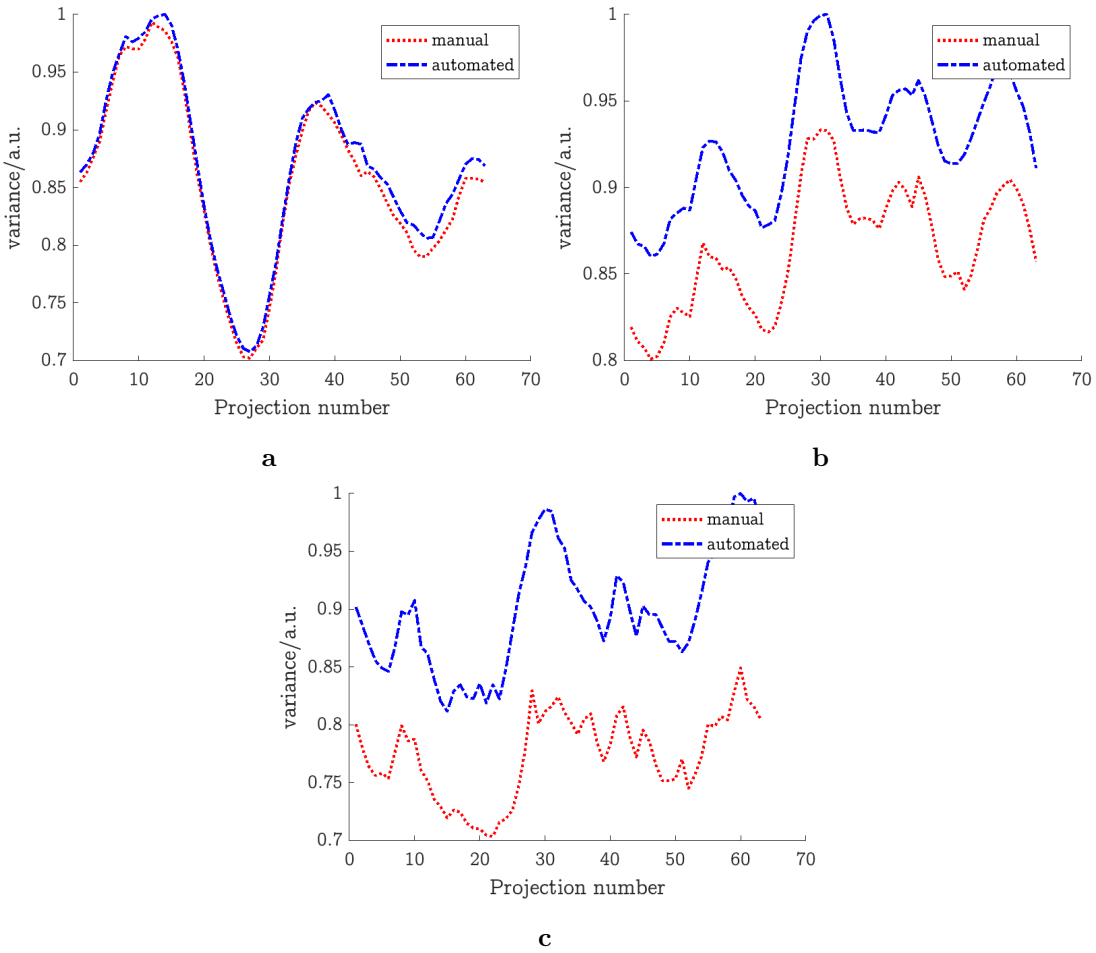

Figure 4.3: Variation of contrast, measured using variance as a sharpness metric, across a registered angularly multiplexed OPT data set filtered to show alignment at different length scales, (**a**) unfiltered, (**b**) 100 pixel Gaussian high pass filtered, (**c**) 10 pixel Gaussian high pass filtered.

channels.

4.2.3.3 Compressed sensing reconstruction

For the longitudinal study of vascular and tumour development in the TraNac-based cancer model discussed above, the vasculature and tumour volumes were reconstructed from the aligned projection image data sets using the two step weighted iterative shrinkage thresholding (TwIST) compressive sensing algorithm [72,138]. This is a development of IST, described in chapter 3.5, which converges faster by adding a contribution to the new estimate from both the current and previous estimate:

$$X_1 = \Psi_\tau(X_0 + R^T(Y - RX_0)/w), \tag{4.1}$$

$$X_{t+1} = (1-\alpha)\,X_{t-1} + (\alpha-\beta)\,X_t + \beta\Psi_\tau(X_t + R^T(Y - RX_t)/w), \text{ for } t > 1, \tag{4.2}$$

where α and β are constant parameters determined by the eigenvalues of $R^T R$. The regulari-

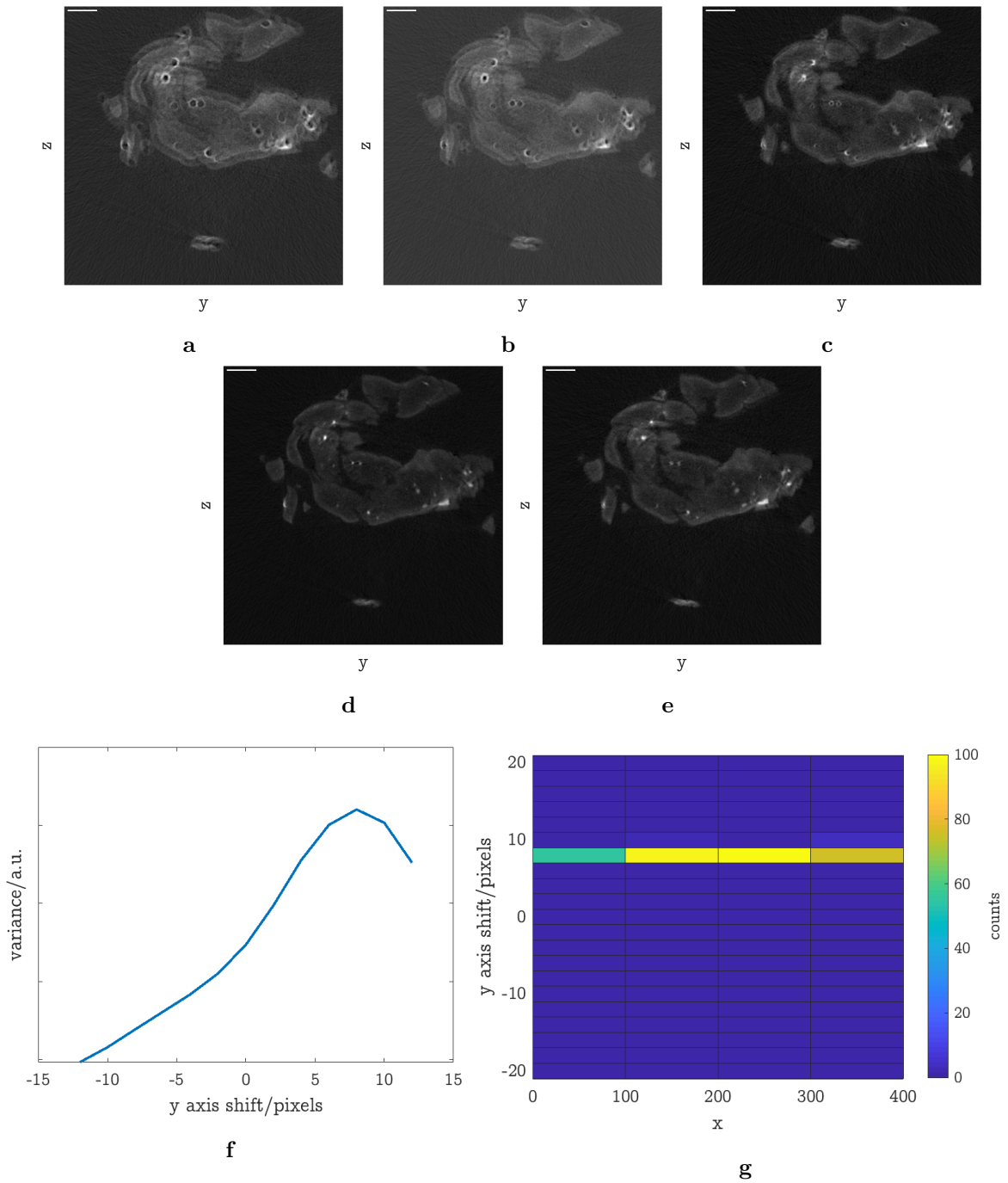

Figure 4.4: Alignment of the rotation axis. *Ex vivo* pancreas slice reconstructed from a sinogram translated (**a**) -16, (**b**) -8, (**c**) 0, (**d**) 8, and (**e**) 16 pixels in the y axis. (**f**) Variation of reconstructed slice variance with rotation axis shift. (**g**) 2D histogram of the y axis shift that produces the highest variance reconstruction, with position of slice along the x axis. Scale bar 1 mm

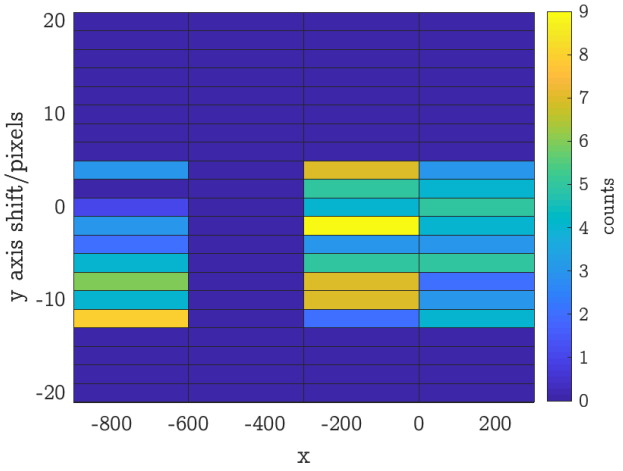

Figure 4.5: 2D histogram of the y axis shift that produces the highest variance reconstruction, with position of slice along the x axis for an undersampled adult zebrafish data set.

sation parameter, τ, sets the aggressiveness of the sparsifying operator. Figure 4.6 shows the mean squared error (MSE) between an *ex vivo* mouse pancreas slice reconstructed from 400 projections and CS reconstructions produced from 80 projections using TwIST with a number of different values of τ. If τ is too small, the algorithm is non-specific and does not fully reject the streaks. If it is too large, the streaks are removed, but so is significant detail from the reconstruction. Therefore, selection of an appropriate value for τ is necessary for successful reconstruction.

The value for τ that produces reconstructions with the lowest error depends on a number of factors, including degree of undersampling, and sparsity of the slice. Figure 4.7a shows the variation of the final MSE for the mouse pancreas slice with τ for different numbers of angular projections. As fewer projections are used in the reconstruction (i.e. the degree of undersampling increases), the optimum reguralisation parameter increases. Figure 4.7b shows the variation of final MSE for two mouse pancreas slices with τ, one of which is the signal from a fluorescent label, while the other is only autofluorescence signal – the best values for τ are separated by a factor of two. To address the challenge this presents, i.e. how to ensure each volume is reconstructed with the best parameters, a method of selecting the best regularisation parameter, in the absense of a ground truth, has been developed.

To select the best τ, it is necessary to find a metric which describes whether or not a CS reconstruction has been successful. Figures 4.6e–g show the Fourier transforms of the labelled pancreas slice reconstructed with different values of τ. In figure 4.6b, τ is too low; the regularisation has not been aggressive enough, and the under-sampled Radon Fourier sampling pattern (figure 3.7) can still be seen in figure 4.6e. As it is increased, more information is inferred, and the gaps are filled in. After a certain point however, higher spatial frequencies are suppressed, and the reconstruction quality is degraded (figure 4.6d). Therefore, a metric can be made by maximising the energy in spatial frequencies outside the sampled region.

Figure 4.8 shows a mask, $M(k_y, k_z)$ made from the transfer function of $R^T R$, $H(k_y, k_z) =$

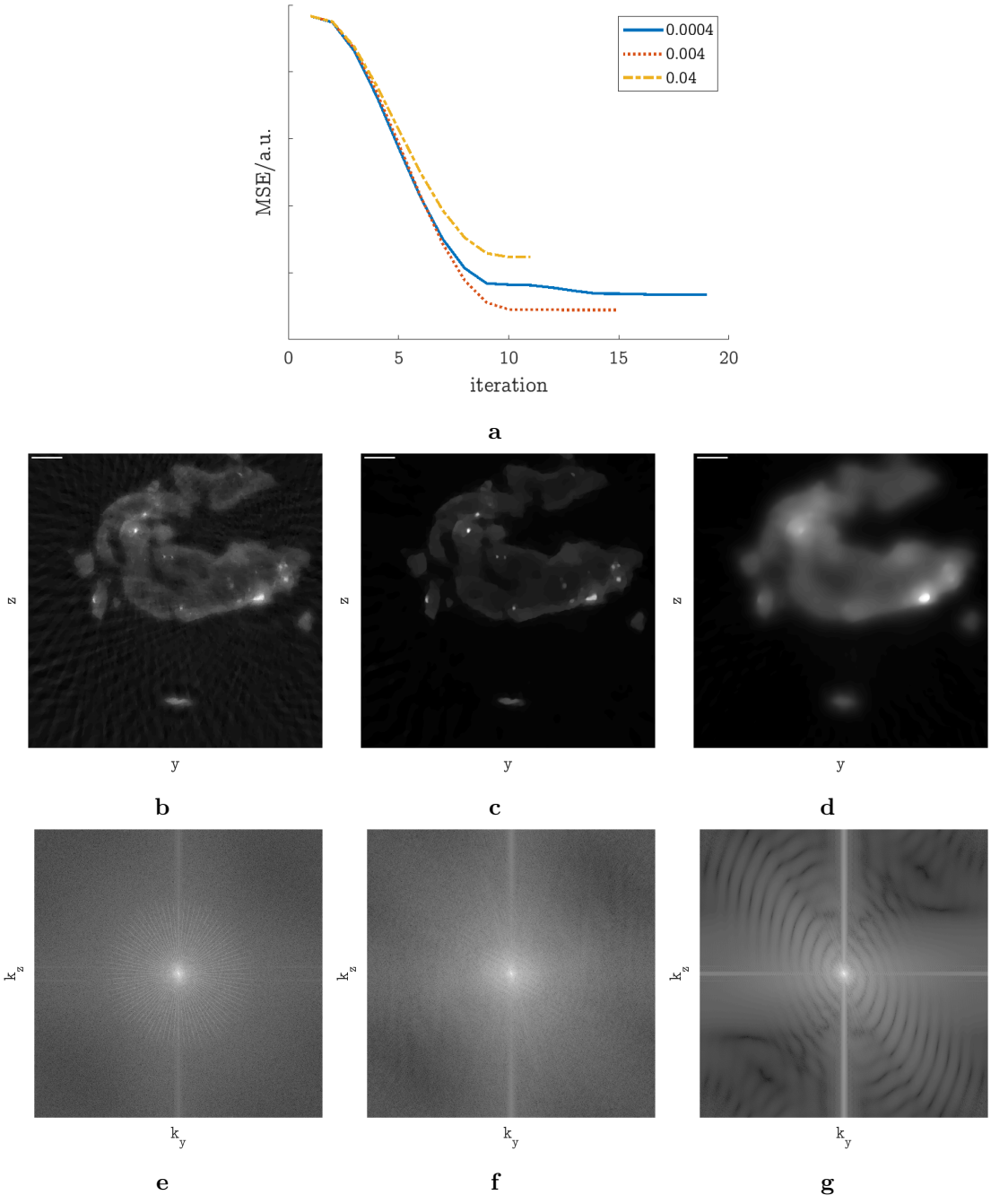

Figure 4.6: Demonstration of the effect of the regularisation parameter on TwIST reconstruction quality. (**a**) Convergence of MSE between TwIST estimate of slice reconstructed from 80 projections and ground truth slice reconstructed from 400 projections. Final TwIST reconstructions (**b**) - (**d**) and their Fourier transforms (**e**) - (**g**) reconstructed with τ of (**b**),(**e**) 0.0004, (**c**),(**f**) 0.004 (**d**),(**g**) 0.04. Scalebar 1 mm.

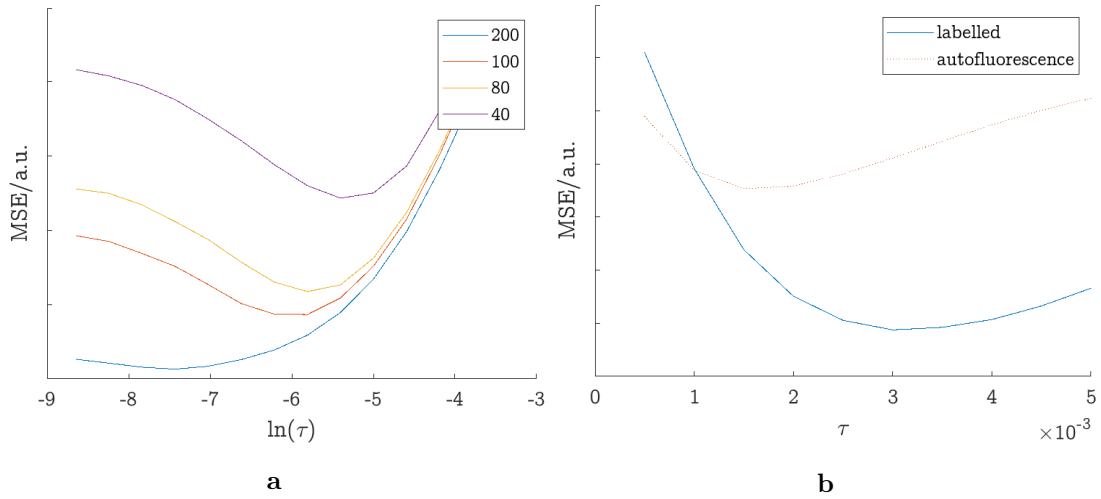

Figure 4.7: The value for τ that produces reconstructions that are most similar to fully sampled reconstructions depends on a number of factors. Variation of MSE with τ for (**a**) different numbers of projections, and (**b**) 80 projection data sets with different spatial frequency content (labelling described in section 3.4.3)

$\left|\mathcal{F}\left(R^T R\left(\delta\left(x,y\right)\right)\right)\right|$, where $\mathcal{F}$ denotes the Fourier transform. The threshold of the mask was chosen as the lowest value in the well sampled region, $k_{min} < 1/\Delta\theta$. This is combined with a low pass filter with cutoff $k_{max} = 1/2$, to suppress high spatial frequency noise. The metric, ρ, is defined as the negative of the proportion of intensity inside this mask:

$$M\left(k_y,k_z\right) = \left(H\left(k_y,k_z\right) < \min[\,H\left(|k| < k_{min}\right)\,]\right)\left(|k| < k_{max}\right) \tag{4.3}$$

$$\rho = -\frac{\sum M\left(k_y,k_z\right)\mathcal{F}\left(k_y,k_z\right)}{\sum \mathcal{F}\left(k_y,k_z\right)} \tag{4.4}$$

where $\mathcal{F}\left(k_y,k_z\right)$ is the Fourier transform of the reconstructed slice. Figure 4.9a shows the variation of ρ and the MSE for the fluorescently labelled and autofluorescence only pancreas slices. ρ is minimised for a larger value of τ than the MSE in both cases. However, the reconstructions with the lowest ρ, shown in figures 4.9d and 4.9e, appear to be successful. Compared to minimising MSE, minimising ρ selects a different compromise point between rejecting streaks and blurring the reconstruction.

A value for τ was chosen for each OPT data set by minimising ρ with respect to τ for a sample of 10 slices of the data set and then taking the median result.

4.2.3.4 Segmentation

To quantify the changes in vasculature and tumour, GFP and mCherryFP volumes were segmented with manually selected global thresholds. Tumour size was measured by counting the voxels within the segmented volume and multiplying by the voxel size. The vasculature was enhanced using a multiscale Hessian-based method [139]. The likelihood of a voxel being part of vessel – or its vesselness – was determined from local image structure by analysing the Hessian matrix, H, of the volume, I:

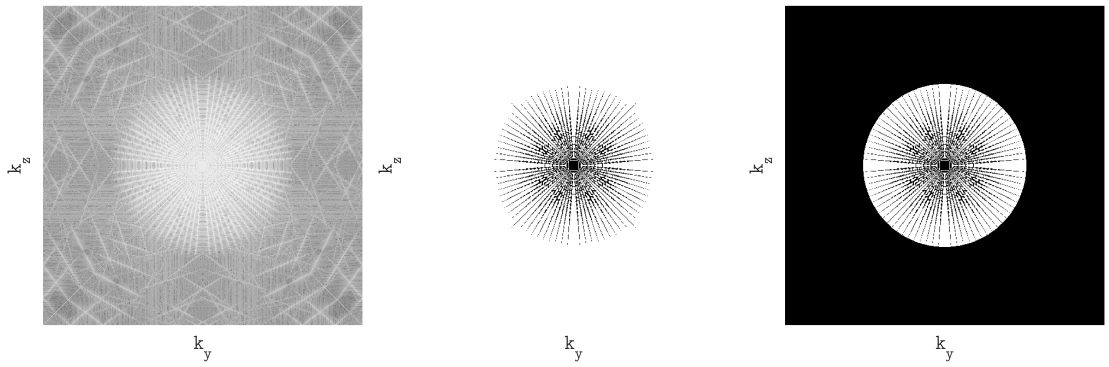

a **b** **c**

Figure 4.8: Creation of mask for determining successful reconstruction metric. (**a**) Transfer function of $R^T R$. (**b**) Mask of spectrum that is not well sampled. (**c**) Low pass filter applied to reduce the influence of noise.

$$H = \begin{bmatrix} I_{xx} & I_{xy} & I_{xz} \\ I_{yx} & I_{yy} & I_{yz} \\ I_{zx} & I_{zy} & I_{zz} \end{bmatrix}, \tag{4.5}$$

where I_{ij} is the partial second derivative of I with respect to directions i and j. The eigenvalues of H, $|\lambda_1| \leq |\lambda_2| \leq |\lambda_3|$, describe the local curvature at each voxel. For bright signal over a dark background, voxels with λ_1 approximately zero, and λ_2 and λ_3 large, negative, and similar in value will more likely be part of a vessel-like structure. In this case the curvature is strong in two directions, but there is little change in the third direction – the direction of the vessel [72].

The vesselness at each pixel is defined as:

$$V = \begin{cases} 0, & if\ \lambda_2 > 0 \text{ or } \lambda_3 > 0 \\ \left(1 - exp\left(-\frac{R_A^2}{2a^2}\right)\right) exp\left(-\frac{R_B^2}{2b^2}\right)\left(1 - exp\left(-\frac{S^2}{2c^2}\right)\right), & \text{otherwise,} \end{cases} \tag{4.6}$$

where $a = 0.5$, $b = 0.5$, and $c = 500$ are empirically selected sensitivity measures for each factor, and

$$R_A = \frac{|\lambda_2|}{|\lambda_3|},\ R_B = \frac{|\lambda_1|}{\sqrt{|\lambda_2 \lambda_3|}},\ S = \sqrt{\lambda_1^2 + \lambda_2^2 + \lambda_3^2}. \tag{4.7}$$

The three terms in equation 4.6 reflect that for voxels that form part of a vessel, R_A should be approximately 1, R_B should be small, and S should be large. These each indicate that the structure is not a plane, not a sphere, and has strong curvature respectively. V is calculated on Gaussian filtered volumes, with σ of one to five voxels. The final vesselness of each voxel is the maximum of V from these five calculations.

4.3 Results

Figure 4.10 shows maximum intensity projections (MIP) of reconstructed volumes of an adult Tg zebrafish imaged with two channel angularly multiplexed OPT at 1 to 5 weeks post induction.

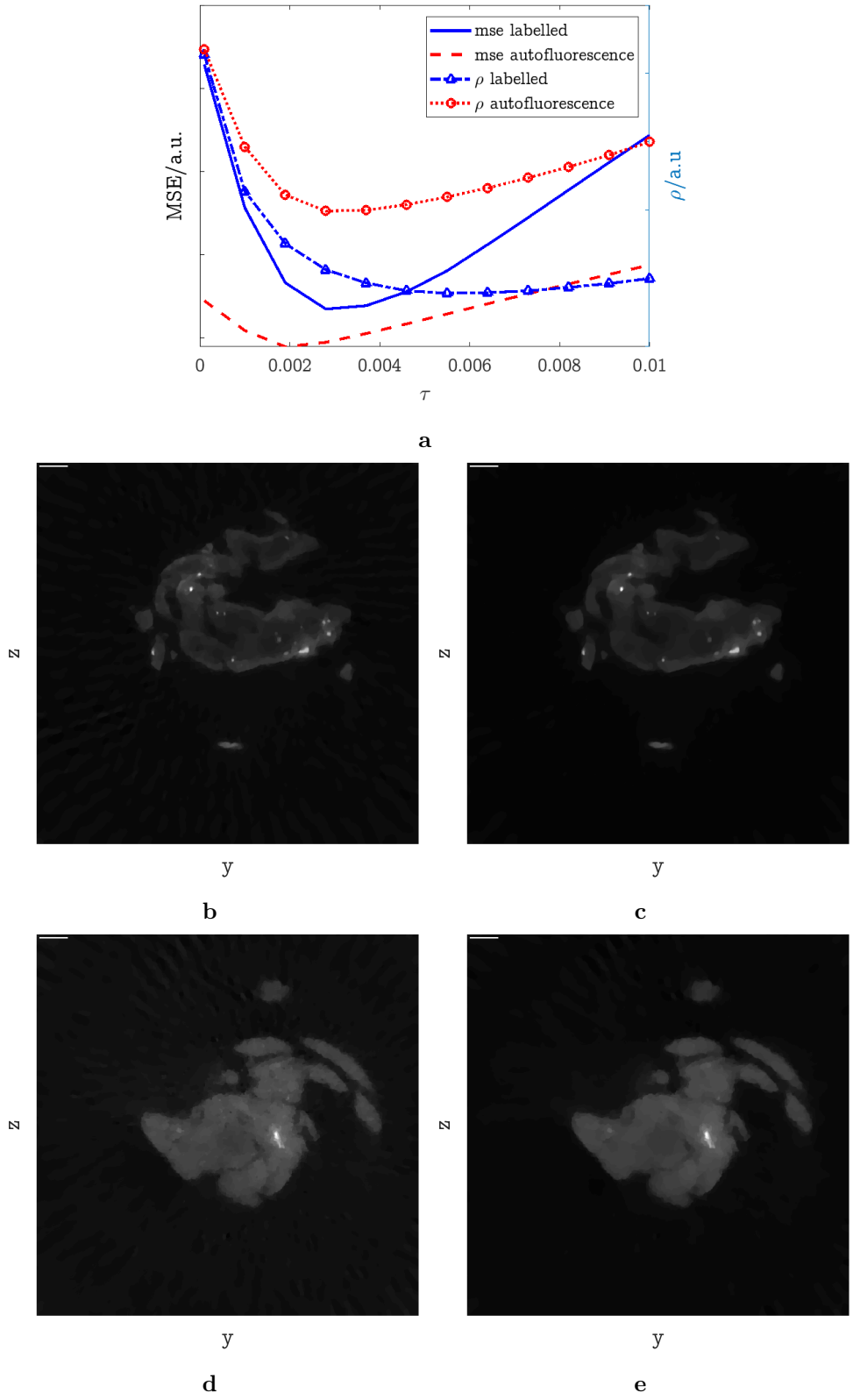

Figure 4.9: (**a**) Variation of ρ and MSE with τ for slices reconstructed with TwIST from 80 projection data sets. (**b**) Labelled pancreas slice reconstruction with lowest MSE. (**c**) Labelled pancreas slice reconstruction with lowest ρ. (**d**) Autofluorescence pancreas slice reconstruction with lowest MSE. (**e**) Autofluorescence pancreas slice reconstruction with lowest ρ. Scalebar 1 mm

The images show the tumour in green and vesselness in red. Orthogonal slices through the 4 week post induction volume are shown in figure 4.11, with GFP (tumour) in green, mCherryFP (vasculature) in red, and vesselness in blue.

The longituinal study tumour volumes are shown in figure 4.12a. The average tumour volumes and standard errors are shown for each week, and the volumes for the individual fish. 24 fish were successfully imaged after one week, 10 after two, 9 after three, 9 after four, and 7 after five. To show the statistical benefits of zebrafish survival the statistical significance of the weekly tumour volume variation was measured. In the first measurement the volumes were treated as independent measurements from a cross-sectional study, and in the second they were treated correctly as paired data. The independent test used was the Wilcoxon rank sum test, a non-parametric test of whether the volume sizes are sampled from distributions with the same median. The dependent test used was the Wilcoxon signed rank test, which tests whether the changes in volume size come from a distribution with a median of zero. The changes between the first four measurements were significant when treated dependently. However, if the same data were taken in a longitudinal study the significance of weeks 1 to 2 and weeks 2 to 3 would have been lost in the intersample variation.

4.4 Conclusion

Optically accessible transgenic adult zebrafish permit imaging of a disease state repeatedly over the course of several weeks by acquiring angularly undersampled OPT data within the anaesthetic recovery window and reconstructing with CS. A cohort of zebrafish had liver tumours induced, and OPT imaging enabled the measurement of the variation in tumour volume on an individual basis.

The variations do not in themselves answer any medical or biological question, due to the lack of control or condition group. But, the improvements to significance show the benefits of being able to perform measurements longitudinally; responses to treatment are less likely to be lost in the noise of intersample variability – which is visible in the wide variety of tumour sizes observed (figure 4.12a).

The vasculature measurements should be treated with greater scepticism. In the MIPs shown in figure 4.10 the vesselness appears to have been reconstructed successfully. However, in figure 4.11 the vessels only appear in a thin shell 500 μm into the sample. Thus it must be concluded that despite being non-pigmented, the optical scattering within the sample is too great to reconstruct high spatial frequency features.

Futhermore, the results of the vesselness operator must be treated with caution. In Correia *et al.* [72], the vesselness operator was applied to zebrafish embryos. In the raw embryo reconstructions, the vasculature is qualititatively discernible. The vesselness operator is not being used to find the vasculature – it is being used to isolate what is visible, for segmentation and further quantification. However, no clear vasculature network is apparent in the raw adult zebrafish reconstructions, so any network "discovered" by the vesselness operator should be treated with caution. The results of the vesselness operator are self normalised; whatever noise

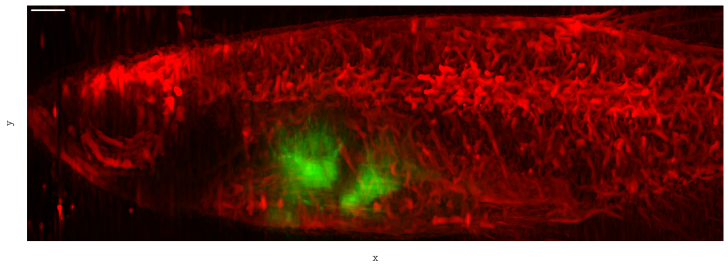

a 1 week post induction

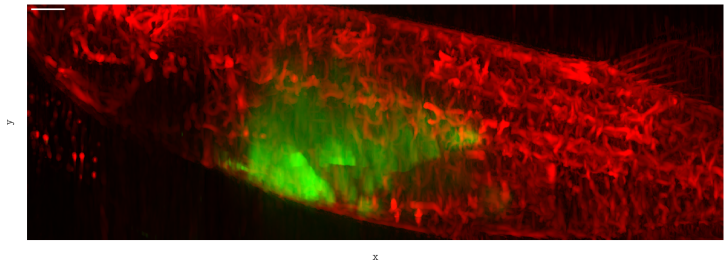

b 2 weeks post induction

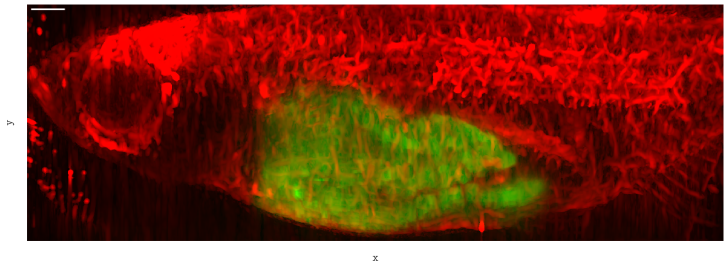

c 3 weeks post induction

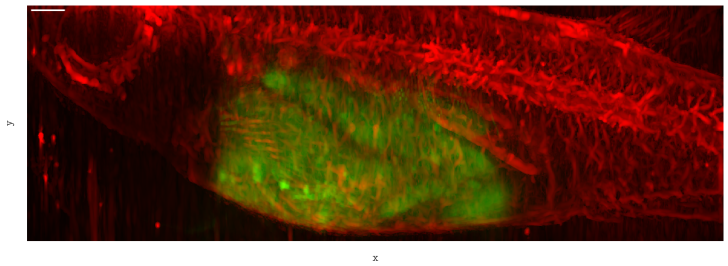

d 4 weeks post induction

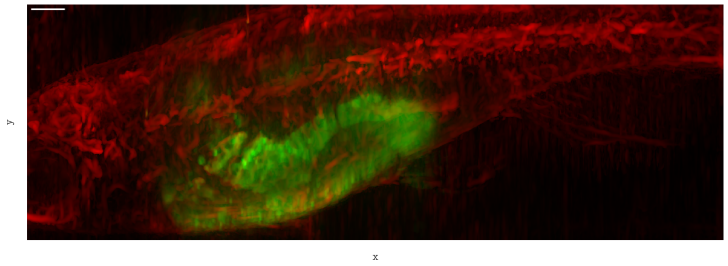

e 5 weeks post induction

Figure 4.10: MIPs of an adult zebrafish imaged with two channel angularly multiplexed OPT for 5 weeks after tumour liver induction showing eGFP (green) and vesselness of mCherryFP (red). Different gamma corrections and normalisations are used for each image to maximise contrast. Scalebar 1 mm.

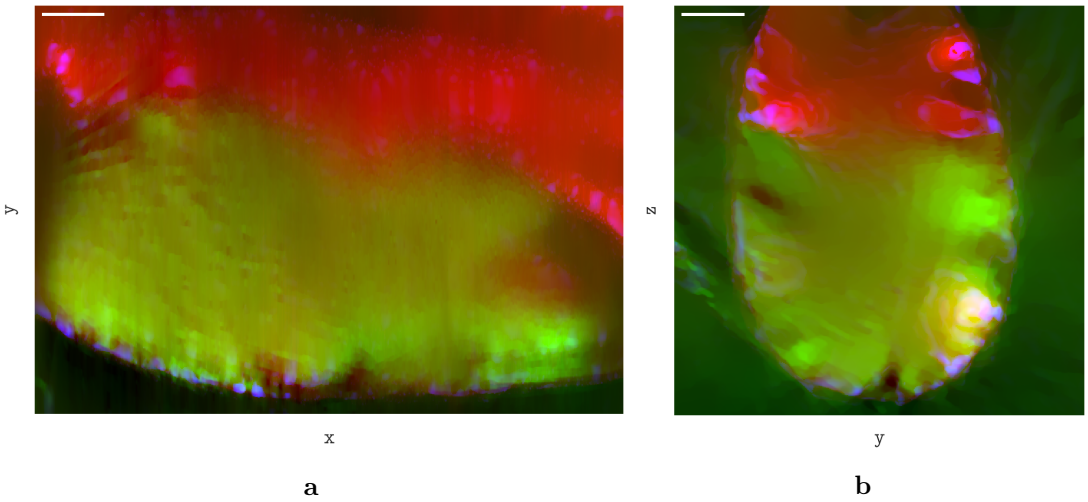

Figure 4.11: (**a**) x-y and (**b**) y-z slices through an adult zebrafish, 4 weeks post tumour induction, imaged with two channel angularly multiplexed OPT showing eGFP (green), mCherryFP (red), and mCherryFP vesselness (blue). Different gamma corrections and normalisations are used for each image to maximise contrast. Scalebar 1 mm.

or structure in the volume that looks most like a vasculature network will be amplified by the operator, and tautologically give a result that looks like a vasculature network. For example, figure 4.13 shows the result of applying the vesselness operator to a noisy Gaussian shell:

$$I(r) = \exp\left(\frac{-(r-r_0)^2}{\sigma^2}\right) + n, \tag{4.8}$$

where $I(r)$ is the intensity at radius r, $r_0 =$ 150 pixels is the radius of the shell, $\sigma =$ 40 pixels is the thickness of the shell, and n is Gaussian noise with a standard deviation of 0.03. Despite having no vessel like structure, the vesselness opertor amplifies the most vessel-like noise to give a result with the appearance of a tortuous vessel network. This network does not look exactly like those seen in figure 4.10 – which are less tortuous and may retain characteristics of the underlying vasculature. However, it does reduce confidence in results where the network is not visible in the raw reconstructions. Therefore, the operator should be limited to segmenting discernible networks, not for discovery.

To improve the utility of *in vivo* OPT of adult zebrafish, the impact of optical scattering must be reduced. If this is achieved, the imaging depth will be increased and the reconstructions improved.

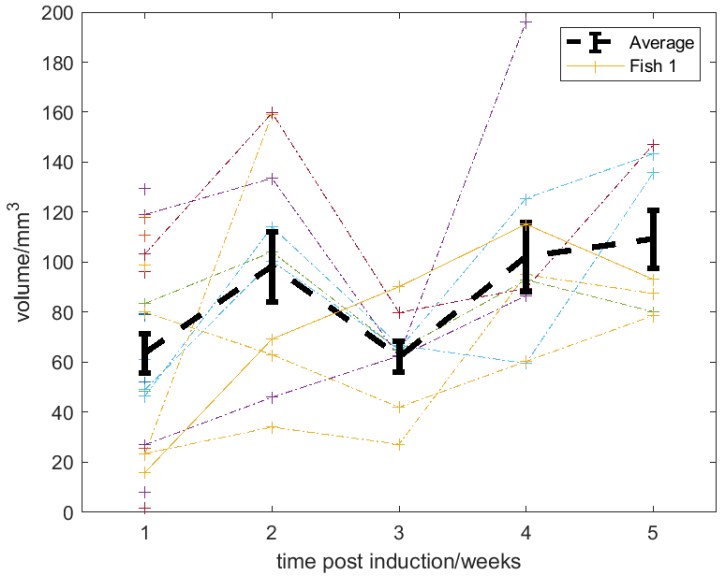

a

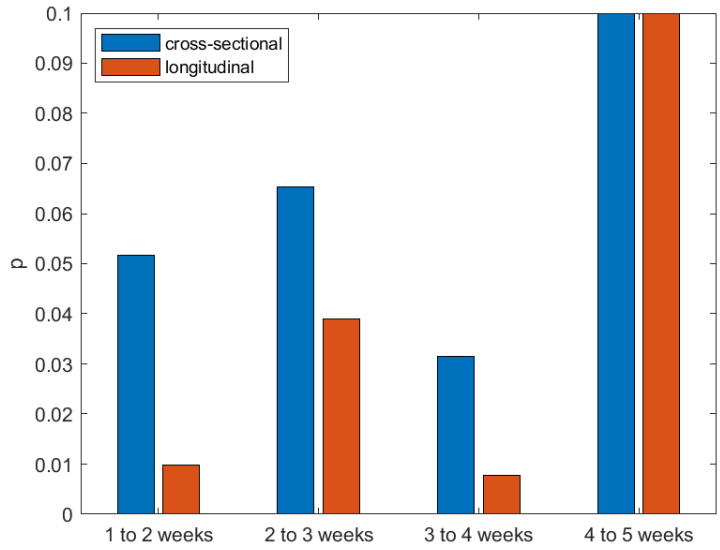

b

Figure 4.12: (**a**) Variation of tumour volumes over 5 weeks post induction. The black dashed line shows average volumes, and the coloured dash-dot lines show individual tumours. (**b**) Significance of tumour volume changes from week to week using an unpaired and paired test. The significance axis has been limited to 0.1 to make the first three results clearer.

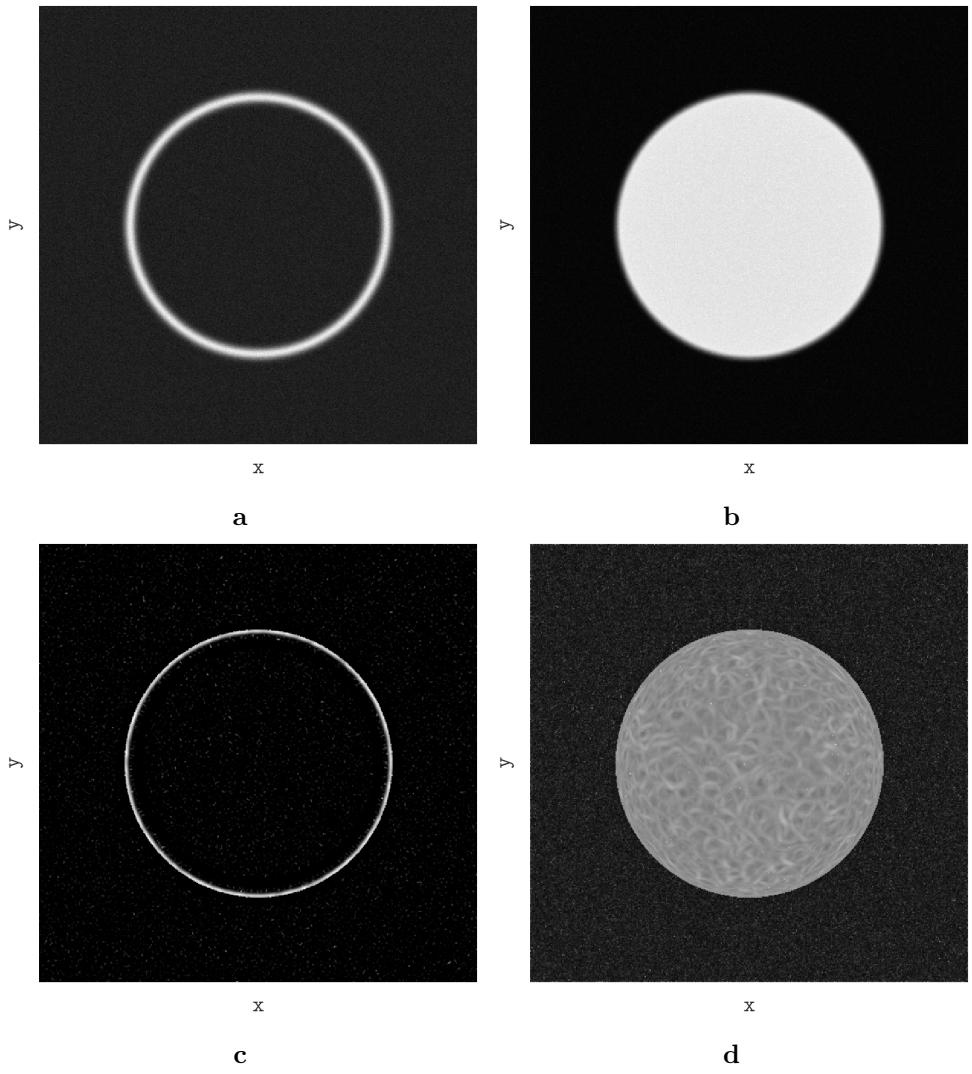

Figure 4.13: Amplification of noise by the vesselness operator. (**a**) Slice and (**b**) MIP of a spherical shell with Gaussian noise. (**c**) Slice and (**d**) MIP of the shell after application of the vesselness operator. Despite having no vessel like structure, the vesselness operator produced a result that looks like a tortuous vessel network.

Chapter 5

Convolutional neural networks for reconstruction of undersampled optical projection tomography data

In chapter 4, the drive to reduce acquisition times for *in vivo* OPT was discussed; it is highly desirable to reduce the length of time an animal is anaesthetized, thereby minimizing side-effects and possible confounding factors linked to anesthesia, and to reduce the likelihood of unwanted movement during the OPT data acquisition [136]. The angularly multiplexed OPT system reduced acquisition times with improvements to light collection efficiency, and by reducing the number of projection images acquired and reconstructing with the iterative CS algorithm TwIST [72, 108].

Unfortunately, due to the iterative nature of this and similar reconstruction algorithms, that require multiple rounds of regularization and both forward-projection and back-projection per reconstructed slice, CS introduces a significant computational cost. In our laboratory, for example, a typical OPT data set that would normally take a few minutes to reconstruct using FBP implemented on a graphical processing unit (GPU) accelerated desktop computer would require more than an hour to reconstruct using TwIST. This therefore introduces a data processing bottleneck for highly sampled longitudinal or high throughput studies.

Convolutional neural networks (CNN) provide an alternative computational approach for this and many other image data processing applications [140]. In X-ray CT, a U-net CNN has been used to remove the streak artifacts from FBP reconstructions calculated from 7 and 20 times undersampled data [141]. This chapter describes the application of CNNs to provide streak-artifact free reconstructions of undersampled OPT data that have been trained using high quality 3D images of chemically cleared tissue volumes reconstructed using FBP of densely sampled OPT data.

This CNN approach was found to enable undersampled OPT data to be reconstructed five times faster compared to the iterative CS-OPT approach, and could provide equivalent image quality to CS with 40% fewer projections, thereby further reducing the OPT data acquisition time. For *in vivo* applications, a CNN trained on *ex vivo* immunostained mouse tissue OPT

data could also be applied to reconstruct *in vivo* OPT data sets of zebrafish embryos expressing fluorescent proteins. This demonstrated the ability of the method to work across different types of biological sample and expands the scope of training data that can be used. The latter point is a particular advantage with live imaging, where the acquisition of sufficient high quality and fully sampled training data from live zebrafish would be technically challenging and undesirable in terms of the number of animals required.

The work in this chapter is adapted from [5]. Section 5.1 will explain the theory of convolutional neural network application and training, the specific architecture used, data preparation, network training, and sample acquisition. Section 5.2 shows the output of the network, for different degrees of undersampling, applied to *ex vivo* mouse tissue and *in vivo* zebrafish embryo data. Section 5.3 concludes with a discussion of the results and potential next steps.

5.1 Methods

5.1.1 Convolutional neural networks

5.1.1.1 Network

A neural network is a computing system that processes an input to an output by passing it through a network of layers of nodes. An example node is shown in figure 5.1a. It is connected by synapses to a selection of input nodes in the previous layer. The output, o_j, of the node, j, is computed by a non-linear activation function, ϕ, acting on the sum of its inputs, o_k of nodes k, weighted by the synapse strengths, w_{kj}:

$$o_j = \phi\left(\sum_{k\in K} w_{kj}x_k + b_j\right) = \phi\left(p_j\right), \tag{5.1}$$

where b_j is a bias for this node, and the sum is over the set of nodes K that feed into j. A neural network is made up of many such neurons placed in layers, which can have their synapse weights and biases optimised with training data to model, predict, and classify linear and non-linear effects. The layers of a neural network can contain multiple channels or feature maps – which can learn to identify different structures for further processing by deeper layers.

How the nodes of one layer are connected to the next depends on the type of layer. In a fully connected layer each node, j, takes every node from the previous layer as its input, i.e. the set K contains every node from the layer previous to the layer that contains j. An example neural network with two fully connected layers, each with a single channel, is shown in figure 5.1b. To connect the two channels requires OM synapses, where O is the number of neurons in the first layer, and M the number in the second. To connect a megapixel input image to a layer with a similar number of nodes would require 10^{12} synapses, which is nearly 4 GB per channel-to-channel map. This becomes unfeasible for even two or three feature maps. Instead, image processing tasks can be addressed with convolutional neural networks.

If the input and output of the neural network have strong local correlations, as is the case in image processing tasks, then layers that behave as convolutions – rather than matrix

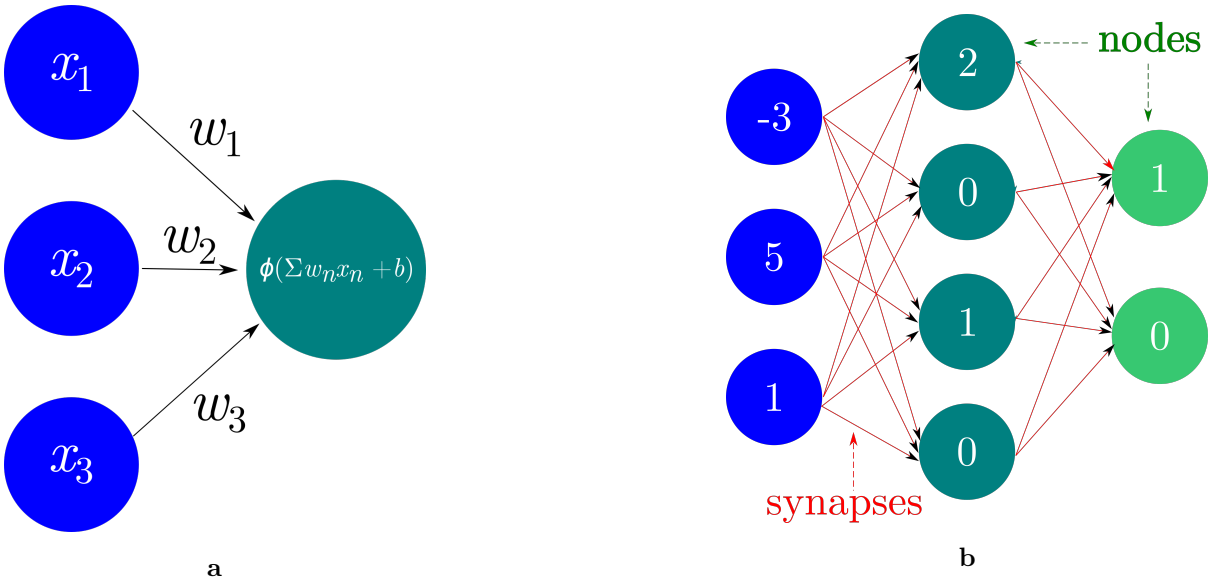

Figure 5.1: (**a**) A neural network node. The output of a node is a non-linear function applied to the weighted sum of its inputs. (**b**) A simple fully connected neural network. The value of each node is determined by its inputs, weighted by the trained strengths of the synapses that connect them – which then feed into the values of nodes in deeper layers.

multiplications – can be used [142]. Instead of defining synapses connecting every node, K contains the small number of nodes within the receptive field of a convolutional filter that uses the same synapse weights across the entire image. An example 2D convolutional layer is shown in figure 5.2a. These can be as small as 3x3 nodes, which only detect short range structure; longer range patterns are then recognised by subsequent convolutions that create larger and larger effective receptive fields (figure 5.2b).

After convolution, the value of each node is transformed by an activating function, which adds non-linearity into the computing system. In this work the rectified linear unit (ReLU) is used [143]:

$$\phi(x) = \begin{cases} 0 & x \leq 0, \\ x & x > 0. \end{cases} \tag{5.2}$$

Convolutional neural networks also include other layer types, that aid with minimising memory requirements and add more non-linearity. Figure 5.3a shows a max pooling layer, which is a maximum filter with a stride of two – i.e. the filter window slides by two nodes rather than one – so that the output size is halved in each dimension. In image denoising tasks, the desired output is typically the same size as the input. To return the image to its full size, transpose convolutional layers can be used, which can be viewed as convolutional layers acting in reverse (figure 5.3b).

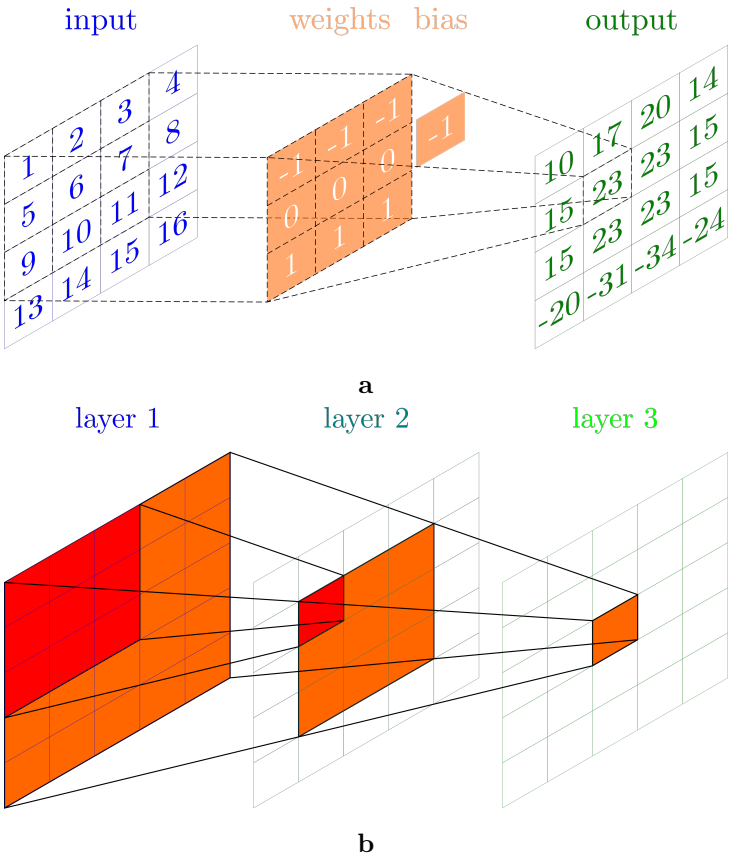

Figure 5.2: (**a**) An example of a 3x3 convolutional layer, which has a stride of one and zero padding. Instead of training synapses for the 256 node to node connections, a common set of 9 synapses is trained and applied as a convolution. (**b**) The small filter size means that nodes are only affected by those nodes in the local vicinity on the previous layer. However, longer range patterns will affect deeper layers after more convolutions.

5.1.1.2 Stochastic gradient descent and backpropagation

The neural network is trained by minimising the error, E, between the neural network output and the labelled ground truth for the entire training data set, with respect to each weight and bias. Consider the error after some small change, Δw_{ij}, in w_{ij}; if the change is small, a linear approximation to the Taylor expansion can be made:

$$E\left(w_{ij}+\Delta w_{ij}\right) \approx E\left(w_{ij}\right)+\frac{\partial E}{\partial w_{ij}}\Delta w_{ij} \tag{5.3}$$

$$\Delta E = E\left(w_{ij}+\Delta w_{ij}\right)-E\left(w_{ij}\right) \approx \frac{\partial E}{\partial w_{ij}}\Delta w_{ij}. \tag{5.4}$$

ΔE can be made negative by setting

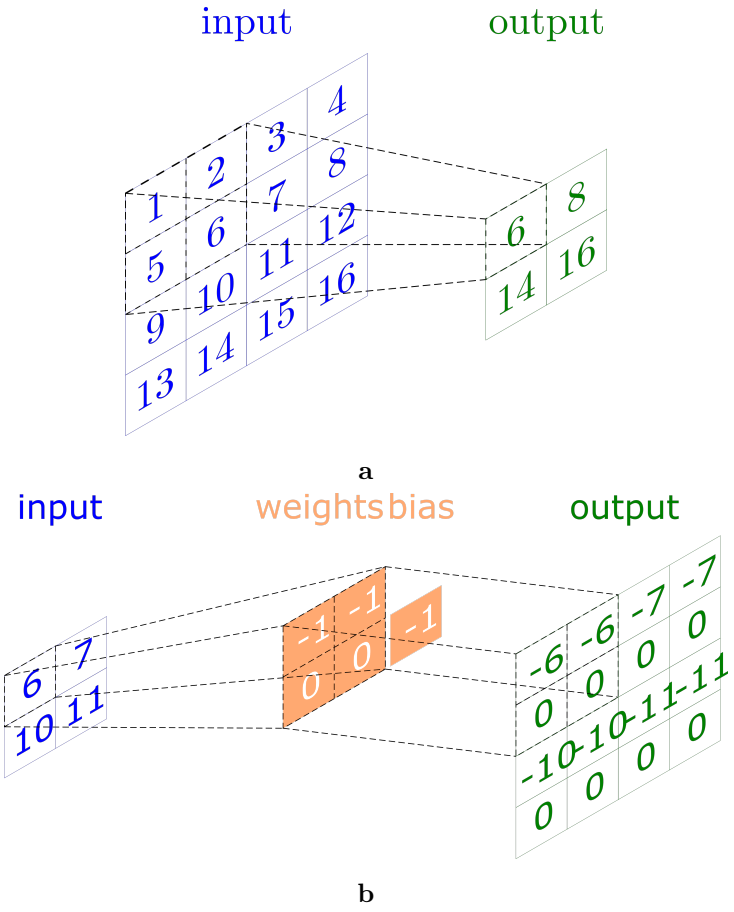

Figure 5.3: Other layer types used in convolutional neural networks. (**a**) A 2x2 max pool layer with a stride of two. (**b**) A 2x2 transpose convolutional layer with a stride of 2.

$$\Delta w_{ij} = -\eta \frac{\partial E}{\partial w_{ij}}, \tag{5.5}$$

$$\implies \Delta E \approx -\eta \left(\frac{\partial E}{\partial w_{ij}} \right)^2 < 0, \tag{5.6}$$

where η is the learning rate. By iteratively changing w_{ij} with this formula, the error will be minimised. This algorithm is called gradient descent.

Evaluating $\partial E / \partial w_{ij}$ over the entire data set would be impractical. In stochastic gradient descent (SGD), the data set is randomly divided into many mini-batches for practical gradient evaluation and updating:

$$\Delta w_{ij} = -\eta \frac{1}{N} \sum_{n=0}^{N} \frac{\partial E_n}{\partial w_{ij}}, \tag{5.7}$$

$$\Delta b_j = -\eta \frac{1}{N} \sum_{n=0}^{N} \frac{\partial E_n}{\partial b_j}, \tag{5.8}$$

where E_n is the error or loss function between the neural network output, $\hat{y}$, and the label, y, for the n_{th} of N paired sets from a mini-batch of the training data set, and η is the learning

rate. When every mini-batch has been processed, an epoch has passed. The data set is then randomly divided into a new set of mini-batches, and the process is repeated.

The learning rate, η, must be small enough that the linear appoximation to the error is valid. However, if it is too small, convergence will be slow and may potentially get stuck in local minima. Adaptive moment estimation (Adam) [144] is a development of SGD where the learning weight is adjusted based on a running average of the magnitude of recent gradients, and the update is given momentum by adding a running average of previous updates:

$$\Delta w_{ij}^t = -\eta \frac{1}{N} \sum_{n=0}^{N} \frac{1}{\sqrt{v^t} + \epsilon} \overline{\frac{\partial E_n}{\partial w_{ij}}}^t \tag{5.9}$$

where t refers to the iteration number, ϵ is a small number to stop divergence, and

$$v^t = \frac{1}{1-\beta_1} \left(\beta_1 v^{t-1} + (1-\beta_1) \left(\frac{\partial E_n^{t-1}}{\partial w_{ij}^{t-1}} \right)^2 \right), \tag{5.10}$$

$$\overline{\frac{\partial E_n}{\partial w_{ij}}}^t = \frac{1}{1-\beta_2} \left(\beta_2 \overline{\frac{\partial E_n}{\partial w_{ij}}}^{t-1} + (1-\beta_2) \frac{\partial E_n^{t-1}}{\partial w_{ij}^{t-1}} \right), \tag{5.11}$$

where β_1 and β_2 are forgetting rates. This algorithm is robust to the choice of η.

To follow this algorithm, the gradients of the error with respect to each weight and bias must be calculated. The partial derivative of E (where the subscript n has been made implicit) with respect to w_{ij} is:

$$\frac{\partial E}{\partial w_{ij}} = \frac{\partial E}{\partial o_j} \frac{\partial o_j}{\partial p_j} \frac{\partial p_j}{\partial w_{ij}}. \tag{5.12}$$

From equation 5.1, $\partial p_j / \partial w_{ij} = o_j$, and from equation 5.2,

$$\frac{\partial o_j}{\partial p_j} = \begin{cases} 0 & x < 0, \\ 1 & x > 0. \end{cases} \tag{5.13}$$

For the output layer, $o_j = \hat{y}$, so:

$$\frac{\partial E}{\partial o_j} = \frac{\partial E}{\partial y}, \tag{5.14}$$

which can be derived for the particular error function. For other layers, the gradients can be defined recursively:

$$\frac{\partial E}{\partial o_j} = \sum_{l \in L} \frac{\partial E}{\partial o_l} \frac{\partial o_l}{\partial o_j} = \sum_{l \in L} \frac{\partial E}{\partial o_l} \frac{\partial o_l}{\partial p_j} \frac{\partial p_j}{\partial o_j} = \sum_{l \in L} \frac{\partial E}{\partial o_l} \frac{\partial o_l}{\partial p_l} w_{jl}, \tag{5.15}$$

where L is the set of nodes that take o_j as an input. All the weights can then be updated working backwards from the output layer. Expressions for the biases can be similarly derived.

5.1.1.3 Batch normalisation

The activation functions applied to each node introduce non-linearities into the computation of the network. This means that $f(ax) \neq af(x)$, where $f(x)$ is the output of the network on some input x, and a is a constant. It is therefore necessary to normalise the inputs to the network to get consistent behaviour for FOVs that contain the same structure, but different brightness.

The same requirement is true of inner layers of the network. During training, each inner layer is adjusting its parameters to convert its input to the desired output distribution. However, as the parameters of shallower layers are trained, the distribution of inputs to the inner layers is also shifting, so that the inner layer is training towards a target that is constantly moving. This problem is called internal covariate shift, and causes a significant slow down to network training – particularly for deeper networks.

Batch normalisation is a method to address internal covariate shift that fixes the variance, $Var[o_j]$, and mean, $E[o_j]$, of a node's output to learned values, γ_j and β_j respectively [145]:

$$\hat{o_j} = \frac{o_j - E[o_j]}{Var[o_j] + \epsilon}\gamma_j + \beta_j, \tag{5.16}$$

where $Var[o_j]$ and $E[o_j]$ are measured over the current mini-batch. During training, running estimates of $Var[o_j]$ and $E[o_j]$ over the entire data set are calculated for use during evaluation.

5.1.2 Network architecture

To reconstruct undersampled OPT data (figure 5.4d), CNNs with a modified U-net architecture [146] – implemented using the Python package PyTorch (https://pytorch.org/) – were trained to output an estimate for the well-sampled reconstructed slice (figure 5.4c) from the streak-corrupted FBP reconstruction of under-sampled OPT data (figure 5.4e). This particular neural network was chosen because of the similarities between the requirements of streak removal, and the original design application of image segmentation. The U-net architecture (figure 5.5) combines a contracting and expanding network with skip paths at each length scale. The skip layers connect local information from the contracting path with global context from the expanding path. For this application, the true fluorescent signal must be locally preserved, while the streak artifacts must be recognised by their long range extent across the field of view. Therefore an architecture that combines multiple scales of information was chosen to address this problem.

The implemented U-net consisted of a contracting path of four blocks, each composed of two 3x3 convolutional layers followed by 2x2 max pooling layers. After each max pooling step, the number of features was doubled, starting from 64. The expanding path was also composed of four blocks, each up-scaling the features by a factor of two. Due to GPU memory limits, this up-scaling was performed using bilinear interpolation rather than with transpose convolutional layers. The expanded features were concatenated with those from the equivalent scale on the contracting path. The concatenated features were passed through two 3x3 convolutional layers and have their number quartered. Because transposed convolutional layers were not used, the

layer	channels		kernel	parameters			
	in	out		weights	bias	batch norm	total
1	1	64	3	576	64	128	768
2	64	64	3	36864	64	128	37056
3	64	128	3	73728	128	256	74112
4	128	128	3	147456	128	256	147840
5	128	256	3	294912	256	512	295680
6	256	256	3	589824	256	512	590592
7	256	512	3	1179648	512	1024	1181184
8	512	512	3	2359296	512	1024	2360832
9	512	512	3	2359296	512	1024	2360832
10	512	512	3	2359296	512	1024	2360832
11	1024	256	3	2359296	256	512	2360064
12	256	256	3	589824	256	512	590592
13	512	128	3	589824	128	256	590208
14	256	64	3	147456	64	128	147648
15	64	64	3	36864	64	128	37056
16	128	64	3	73728	64	128	73920
17	64	64	3	36864	64	128	37056
18	64	1	1	64	1	2	67

Table 5.1: Learnable parameters for the convolutional layers in the U-net architecture shown in figure 5.5

number of features on the expanding path were half what they would be in a conventional U-net. Zero padding was used in the convolutional layers to keep image sizes consistent between contracting and expanding paths. For the same reason the input slices were padded to a multiple of 16 pixels.

Each convolutional layer was followed by batch normalization and ReLU layers. The number of learnable parameters is shown in table 5.1 – corresponding to 50 MB of memory.

5.1.3 Data and training

For the CNN to learn how to remove streak artifacts from different sample intensity distributions, a large set of diverse training data is required. For *ex vivo* samples, such data can be readily obtained by acquiring the necessary large number of angular projections needed for a well-sampled reconstruction, as there is no upper limit on acquisition time beyond potential photobleaching of the fluorescent labels. Such well sampled data sets are already available from many previous *ex vivo* OPT studies.

The CNNs were trained on 400 projection OPT data sets from previous studies of *ex vivo* cleared mouse pancreas for which OPT was used to assay beta cell mass [147] and unpublished

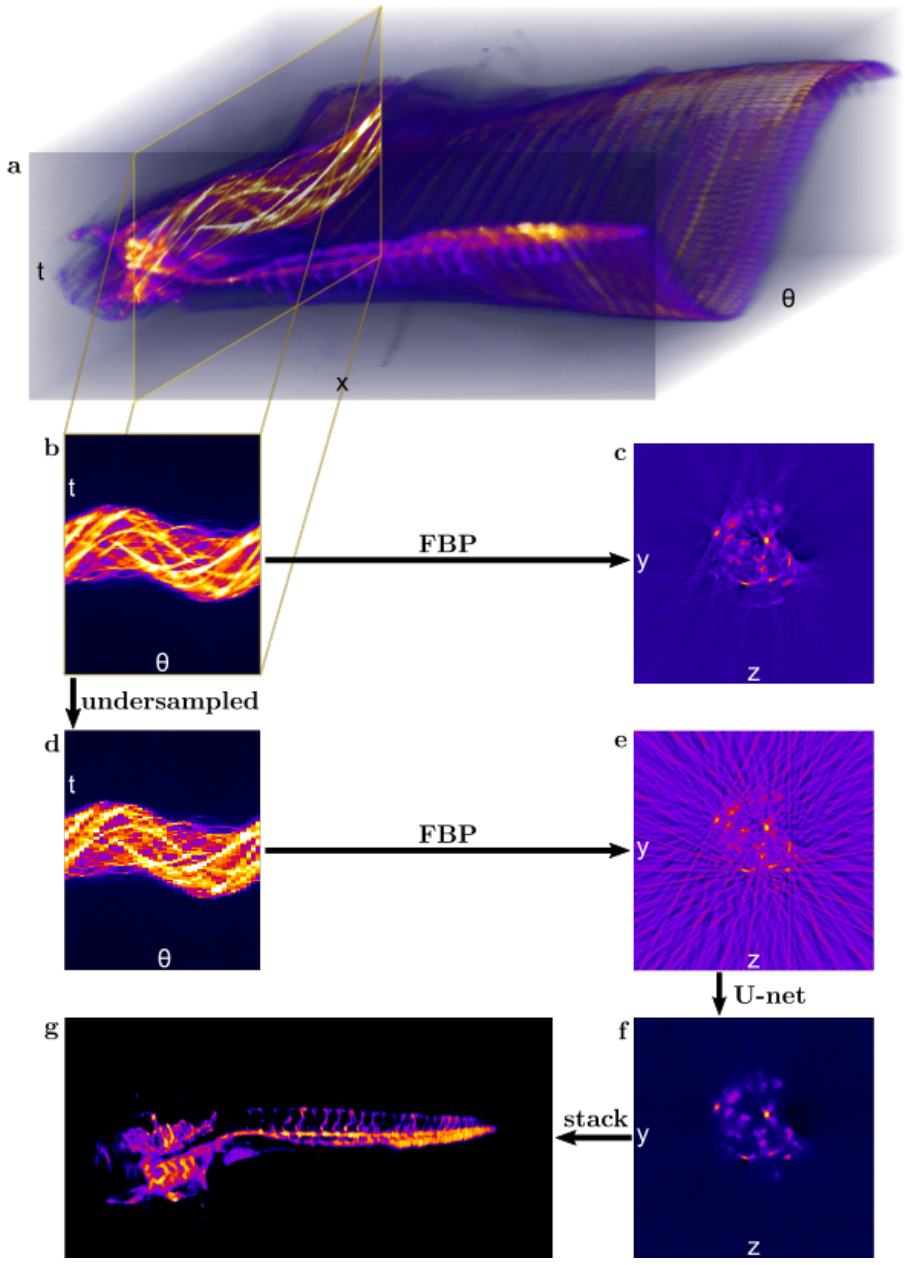

Figure 5.4: Convolutional neural networks for reconstructing undersampled OPT data sets: (**a**) represents an OPT data set of a 4 days post fertilization zebrafish larva, consisting of a series of 2D (x-t) projections acquired as the sample is rotated to a series of angles θ; Each (t-θ) cross section through the data set forms a sinogram, (**b**),(**d**), which can be processed with FBP to give a (y-z) reconstructed slice, (**c**),(**e**), of the sample volume. (**b**),(**c**) show the reconstruction of a highly sampled, 800 projection sinogram and (**d**),(**e**) show the result of reconstructing from an undersampled, 40 projection sinogram – resulting in a streak-corrupted slice. (**f**) shows the reconstruction obtained using a U-net deep learning architecture – consisting of convolutional layers, max-pooling, bilinear interpolation upscaling, and concatenated skip paths – to estimate the well-sampled reconstruction from the undersampled FBP reconstruction (**e**). (**g**) The 2D reconstructed slices are stacked together to give the 3D fluorescence distribution of the sample. Adapted from [5].

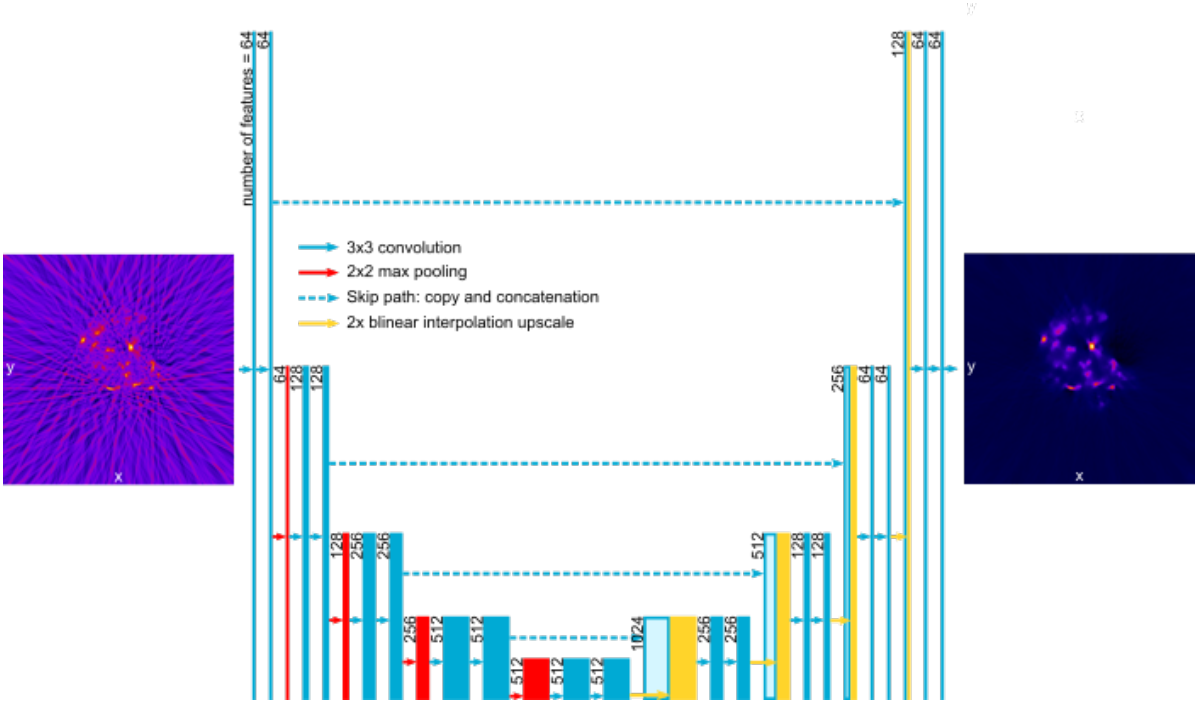

Figure 5.5: U-net architecture CNN which takes streak corrupted slices reconstructed from angularly undersampled OPT data sets as inputs, and outputs estimates of streak-free slices reconstructed from well sampled data sets. Adapted from [5].

OPT studies of mouse lung. 80% of the sinograms (14,416) were randomly assigned to training with the remaining 20% (3,342) reserved for testing. These were assigned in batches of ten neighboring slices to reduce correlations between testing and training data from adjacent sinograms.

Several CNNs were trained to remove streaks from slices reconstructed for a range of degrees of undersampling: 12, 16, 20, 24, 28, 32, 40, 48, 64, and 80 projections were used. Ground truth data (figure 5.4c), I, were calculated using FBP of the complete 400-projection sinogram data set (fig 5.4b), with an additional Hanning window applied to the ramp filter, scaled to 0.4. The input data, I_0, consisted of FBP reconstructions from a reduced number of projections spaced as equally as the subsampling allowed (for example, a 64 projection sinogram used the 1st, 7th, 14th, 20th, 26th, etc. within the 400 projections). To augment the training data, a random angle in each sinogram was selected as the starting point (i.e. labelled 0°) and random vertical and/or horizontal flips were applied. Both ground truth and input FBP reconstructed slice pairs were normalized such that the input had a mean of zero and unit variance, and during training were randomly cropped to 128x128 pixels to enable a batch-size of 32 to be processed by the GPU.

The CNN (fig 5.5) takes the streak-corrupted undersampled FBP reconstruction (fig 5.4e) as its input and outputs an estimate for the streak-free slice, $\hat{I}$ (fig 5.4f). The network was trained using the error between $\hat{I}$ and I using the $l1$-norm:

$$l1 = \frac{1}{n}\sum_{i=1}^{n}\left|\hat{I}_i - I_i\right| \tag{5.17}$$

where i is the pixel index. Training was performed using Adam – using the default parameters in PyTorch.

Early stopping was used during training; after each pass of the training data, the average error on the test data was calculated and the training terminated when the error did not improve for three epochs. The previous best network was kept. Training typically took 3 to 6 hours on a desktop computer equipped with a Nvidia Tesla K40c, with 12 GB of memory. The training and testing scripts can be found online [148].

The testing data was also reconstructed for the various degrees of undersampling with FBP and using TwIST (CS). To keep the CS results consistent with previously published results [72], τ was kept at the previously empirically selected value of 0.004.

5.1.4 Samples and optical projection tomography data acquisition

Cleared mouse tissue samples were imaged using a 0.5x telecentric lens (63-074, Edmund Optics Ltd) with a depth of field of 5 mm, imaging onto a CCD camera (QImaging, Retiga R1) for the pancreas samples and a 1x telecentric lens (58 430, Edmund Optics Ltd) with a 5 mm depth of field, imaging onto a sCMOS camera (Zyla 5.5, Andor Instruments) for the lung samples. Samples were suspended from a stepper motor (NM08AS-T4-MC04-HSM8 and X-MCB1-KX11BG, Laser 2000 (UK) Ltd) in a cuvette filled with index matching fluid, a 1:2 mixture of benzyl alcohol: benzyl benzoate, and imaged at 400 equally spaced angular positions over a full rotation.

Nine pancreas samples were prepared following the protocol as described in [130]; the beta-cell mass of whole fixed mouse pancreata were labelled with Alexa647-conjugated antibodies. They were mounted in 2% agarose, dehydrated in increasing concentrations of methanol up to 100% and subsequently chemically cleared in a 1:2 mixture of benzyl alcohol: benzyl benzoate. Fluorescence excitation was provided by a 660 nm LED (Cairn Research Ltd) in combination with a 705 ± 15 nm emission filter. Four lung samples were prepared as follows; $KRAS^{G12D}$ $TP53^{frt/frt}$ murine lung adenocarcinoma cells bearing yPET fluorescent protein were injected into the tail vein of ROSA26 dTomato C57BL/6 mice (under authority of PPL70/8380). After 21-28 days, or at the clinically applicable humane endpoint, mice were sacrificed, and trachea were perfused with 2% low melting point agarose. Following this, lungs were placed in 4% paraformaldehyde then 30% sucrose to allow lung specimen to retain fluorescence. Lastly, 30% sucrose was exchanged with clearing solution (Rapiclear RD: 1.52, SUNJin lab).

The fluorescence OPT data set of live zebrafish embryo was taken from Correia *et al.* [72]. The data acquisition was undertaken using a home-built x4 microscope (N4X PF objective lens and ITL200 tube lens, Thorlabs Inc.) with an aperture positioned directly behind the microscope objective lens to set the depth of field to 0.6 mm. The zebrafish embryo was suspended in a water filled cuvette from a stepper motor (T-NM17A200, Zaber Technologies Inc.) and images were recorded on an sCMOS camera (Zyla 5.5, Andor Instruments).

The zebrafish embryos (detailed description in [72]) were derived from a mutant TraNac background to suppress melanin production (a gift from Julian Lewis, Cancer Research UK, London Research Institute) and were subsequently genetically modified to express mCherry fluorescence protein (mCherryFP) in the vasculature. mCherryFP fluorescence was excited using a 561 nm laser (Jive, Cobolt AB) and imaged through a 641 ± 37 nm emission filter. The zebrafish embryos were imaged 4 days post fertilization, being anaesthetized and mounted in fluorinated ethylene tubing with a refractive index that matched that of water.

5.2 Results

5.2.1 Application to *ex vivo* data from test data set

Figure 5.6 shows a representative mouse pancreas slice reconstructed with a decreasing fraction of 400 acquired projections and processed using FBP, CS and CNN. As shown in chapter 3, the quality of the reconstructions produced with FBP degrades significantly as the number of projections is decreased. The images appear noisy from the streak aliasing artifacts.

The iterative CS approach produces a visually improved reconstruction with significantly reduced streak artifacts and improved contrast. For the 64 projection reconstruction streak rejection has been successful. The TV regularisation results in piecewise-constant flatter contrast compared to the well sampled reconstruction. For greater degrees of undersampling, the streaks are only partially suppressed in the background.

The CNN approach is better able to reject the background streaks, even for greater degrees of undersampling. The performance over the sample is comparable to CS – with no piecewise-constant contrast but with an increase in medium spatial frequency noise.

The performance of the three methods was quantified by calculating the peak signal to noise ratio (PSNR) between the fully sampled FBP reconstruction, and the reconstructions produced by FBP, CS, and CNN from the undersampled OPT data sets. This measurement was averaged over the $3,342$ pancreas and lung slices designated for testing.

The PSNR, in dB, is:

$$PSNR = 10\log_{10}\frac{I_{MAX}}{\frac{1}{N}\sum_{i}\left|\left|\hat{I}_i - I_i\right|\right|^2} \tag{5.18}$$

where I_{MAX} is the peak intensity in I, and the denominator term is the mean of the squared error between the i_{th} of n pixels of I and $\hat{I}$. Figure 5.7 shows the variation of PSNR with number of projection angles, N_θ, for the three reconstruction methods. Both the CS and CNN reconstructions have superior PSNR compared to the streak corrupted FBP reconstructions. The quality of the reconstructions decreases when fewer angular projections are used. However, CNN consistently outperforms the CS method. Therefore, employing CNN for the reconstruction should enable the OPT data acquisition times to be reduced compared to CS for equivalent PSNR in the reconstructed images.

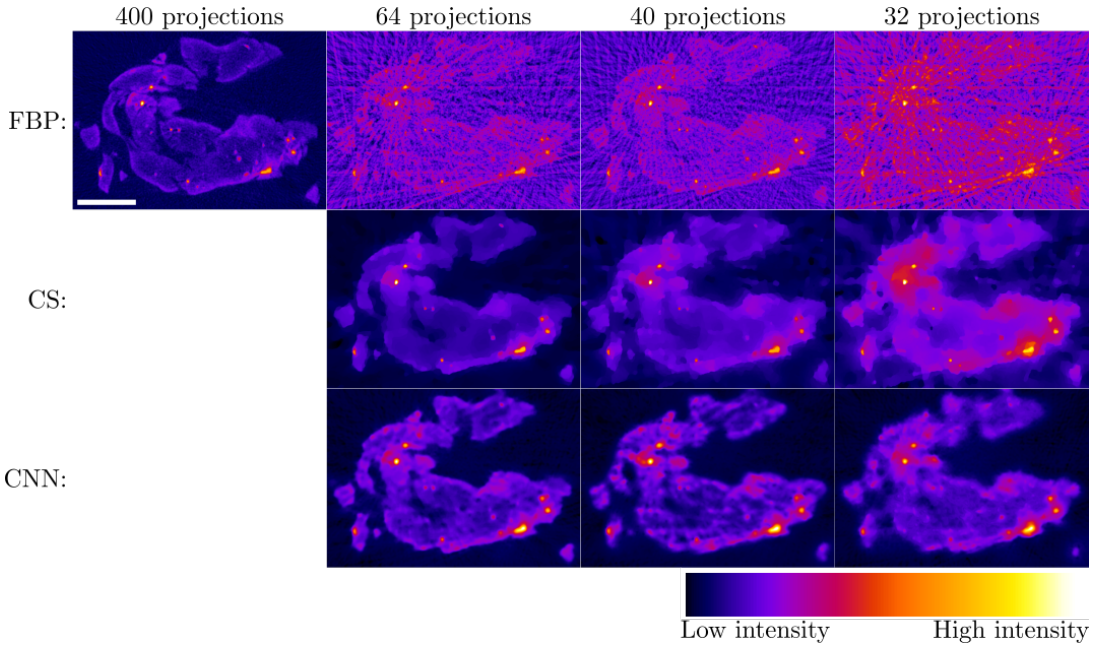

Figure 5.6: Comparison of a representative pancreas slice reconstructed using FBP, CS, and CNN, with decreasing numbers of projections, shown on a false colour intensity scale. Compared to FBP, the CS and CNN methods are both able to provide significantly improved reconstructions with fewer projections. For 40 and 32 projections, the CNN reconstructions have better rejection of background streaks compared to those produced with CS. Scalebar 2 mm. Adapted from [5].

5.2.2 Application to *in vivo* data from zebrafish embryo data set

Acquiring well-sampled *in vivo* training data is challenging, since the total acquisition time may be practically limited. As described in chapter 4, the total acquisition time was limited to 15 minutes by the need to recover the fish after the anaesthetic procedure. Furthermore, photobleaching of fluorescent proteins is significantly higher than for dyes [149]. This time was sufficient to acquire a 64 projection data set of the vasculature and tumour channels. This data was reconstructable with the CS approach, but for CNN training there is no *in vivo* labelled ground truth available in sufficient quanitities.

Fortunately, it is not necessary to acquire *in vivo* training data. One possible approach would be to acquire well-samped OPT data sets of a large number of terminally anaesthetised zebrafish – making the necessary corrections for photobleaching that may occur [95]. However, this would require sacrificing a significant number of zebrafish specifically to gather sufficient training data for this investigation. Instead, it can be reasoned that, despite being different in appearence to cleared mouse tissue, the fluorescent intensity of the reconstructed zebrafish slices are comparably sparse and structurally similar; the fluorescence signal is localised to multiple small regions, for example the islets in the mouse pancreas and vasculature in the zebrafish. In this case, the streak artifacts produced by FBP should also be structurally similar. Therefore, the CNNs trained to remove streaks from the undersampled *ex vivo* mouse sample data could

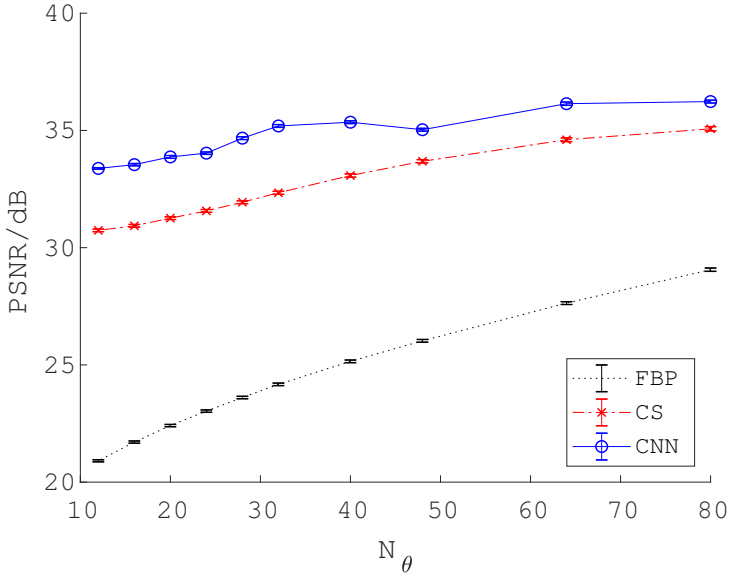

Figure 5.7: Variation of PSNR between reconstructions of well-sampled *ex vivo* data, and those produced using FBP, CS, and CNN methods from different numbers of projections. The graph plots mean and standard error of measurements across the test data set of 3,342 slices. Adapted from [5].

be directly applied to *in vivo* OPT data of a zebrafish embryo expressing mCherryFP in the vasculature. This well-sampled *in vivo* zebrafish data set was available from the previous CS-OPT study [72].

Figure 5.8 shows a representative *in vivo* zebrafish embryo slice reconstructed with a decreasing fraction of the 800 acquired projections and processed using FBP, CS and CNN. As previously observed, the FBP reconstructions rapidly decrease in quality as the number of angular projections is reduced. The CS method produced a good reconstruction with 64 projections, but streak artifacts are observed in the background of the 40 projection reconstruction. The CNN approach was able to produce a good estimate of the well-sampled slice with only 40 projections, with fewer apparent streaks and better preservation of the localised vasculature. With 32 projections the streak rejection is good but some of the vasculature has also been rejected; the specificity is good, but the accuracy has suffered. It is worth noting that the ground truth fully sampled reconstruction shown in figure 5.8 is itself partially corrupted by streak artifacts. These were caused by small sample movements during the *in vivo* acquisition. The presence of these artifacts raises the issue of whether this is a valid ground truth to compare the undersampled reconstructions to; the artifacts will introduce systematic errors to the PSNR measurement. However, all reconstructions are imperfect representations of the real object. In this instance, the degree of imperfection is greater than what might be desired, but there is no obvious alternative, so it will continue to be used.

Figure 5.9a plots the variation with number of projection images of PSNR between the well-sampled FBP reconstruction and those produced from undersampled OPT data with FBP, CS, and CNN, averaged over the 2,218 slices of the zebrafish embryo. The results follow a similar

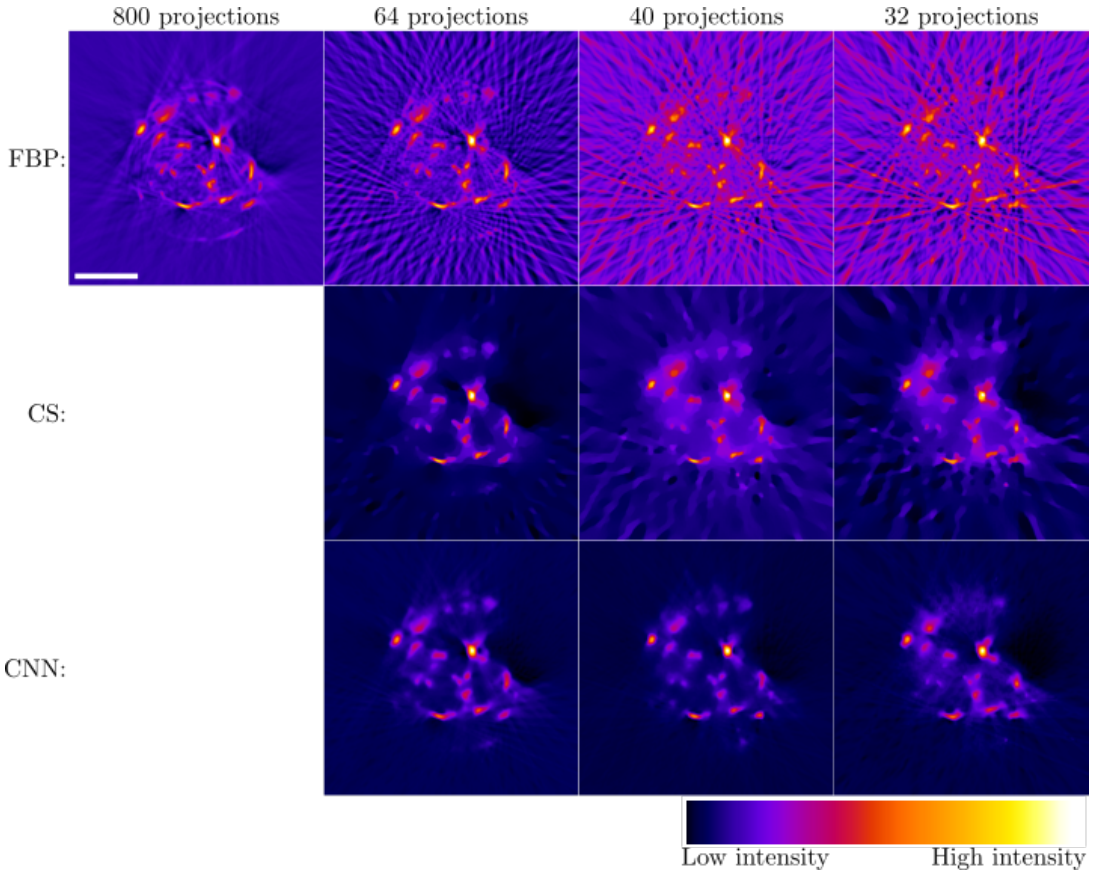

Figure 5.8: Comparison of a representative zebrafish slice reconstructed using FBP, CS, and CNN, with decreasing numbers of projections, shown on a false colour intensity scale. Compared to FBP, the CS and CNN methods are both able to provide significantly improved reconstructions with fewer projections. The slice produced by CNN from 40 projections is of acceptable quality. Scalebar 200 μm. Adapted from [5].

pattern to what was seen with the *ex vivo* mouse samples; the CS and CNN reconstructions are of higher quality than the FBP reconstruction, and the CNN method outperforms CS for all degrees of undersampling. The CNN reconstructions have an equivalent PSNR when using 40 projections, to the previously established limit of 64 projections when reconstructing with CS – enabling a acquisition time reduction of 40%.

Reconstructing undersampled OPT data with the CNN method rather than CS removes the use of iterative algorithms, which reduces the reconstruction time. Figure 5.9b, shows the average reconstruction time per slice for the FBP, CS, and CNN methods implemented on the same desktop computer with an Nvidia Tesla K40c GPU. FBP is orders of magnitude faster than the CS and CNN methods, with an average slice reconstruction time of $(8.75 \pm 0.01) * 10^{-3}$ s for the 64 projection case, but does not produce satisfactory reconstruction quality. The CS method, as described in chapter 4, involves repeated calls of forward and back projection, and the iterative denoising algorithm – which increases the reconstruction time by a factor of 250 to 2.18 ± 0.01 s. The CS reconstruction time increases with number of projections, as the computational cost of performing the FBP component increases. The CNN approach takes FBP

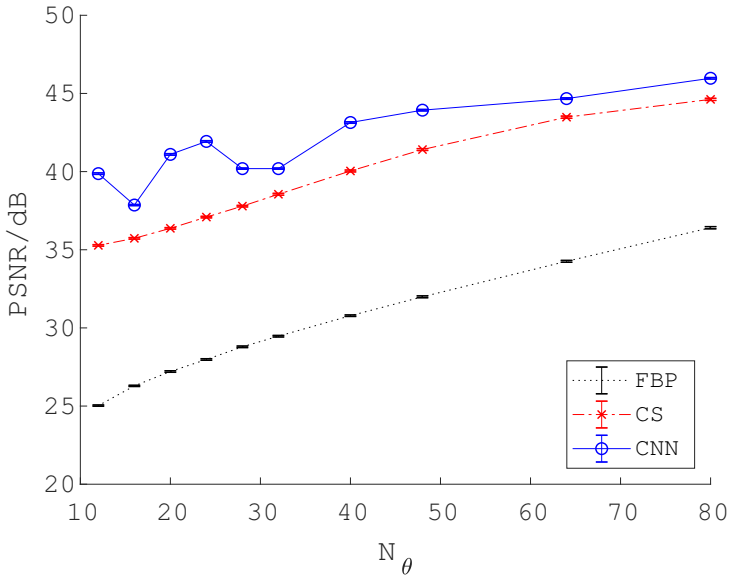

a

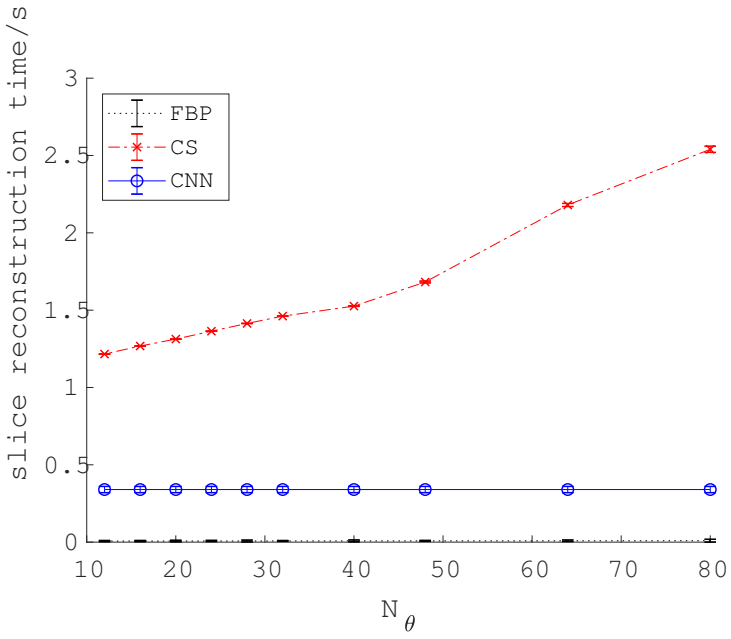

b

Figure 5.9: (**a**) Variation of PSNR between reconstructions of well-sampled *in vivo* data, and those produced using FBP, CS, and CNN methods from different numbers of projections. (**b**) Variation of slice recontruction time, using FBP, CS, and CNN. Both plots show mean and standard error of measurements across the zebrafish embryo data set of 2,218 slices. Adapted from [5].

reconstructions as input and performs one feedforward pass through the network, the speed of which is independent of number of projections. For 64 projections, the CNN reconstruction time is $(3.40 \pm 0.02) * 10^{-1}$ s – 6x faster compared to CS.

The total time taken to reconstruct the 2,218 slice zebrafish embryo follows a similar trend; The CS and CNN methods took 77 and 15 minutes respectively to reconstruct the 64 projection data set. This time includes overheads such as time to load and save the data.

5.2.2.1 Sensitivity of iterative CS and CNN methods

In chapter 4, the importance of the regularisation parameter τ was discussed. When selecting its value, a compromise is made between being specific, by rejecting streaks with a high value for τ, and accurate, preserving genuine signal with a low value. By enforcing greater sparsity, more streaks are removed, but at the cost of the less prominent features in the FOV being removed as well. A similar effect occurs in the training of the neural network; less prominent features will produce smaller errors, and therefore have a smaller affect on the adjustments of the weights than getting the bright features correct or removing streak artifacts. The end result of this is that the performance of both CS and CNN will be worse for dim features. These features will also not make a strong contribution to the quantification of reconstruction quality using the PSNR, shown in figure 5.9a.

Figure 5.10 shows regions of interest around features of differing intensity in a reconstructed slice of a zebrafish embryo. In the well-sampled FBP reconstruction, the peak intensities of the first, second, and third features are 53%, 25%, and 17% of the peak intensity of the brightest feature in the FOV, respectively. The regions of interest are shown from slices reconstructed with different numbers of projections with FBP, CS, and CNN.

All the features are visible in all the FBP reconstructions – which are accurate but not specific. The first feature is clearly visible in the CS and CNN reconstructions for all the degrees of undersampling shown. The second feature is resolvable in the CS reconstructions down to 48 projections, and in the CNN reconstructions down to 40, while the third is only resolved in the 80 projection CNN reconstruction. This illustrates a limitation of reconstructing from undersampled OPT data; that dimmer objects will be lost. However, in both instances the object is visible at greater degrees of compression in the CNN reconstructions than in those produced with CS.

5.3 Conclusion

Chapter 4 showed that OPT data acquisitions can be accelerated by imaging at fewer angular projections and reconstructing the sample volume with CS techniques. This is a necessary requirement for *in vivo* imaging to minimise the risks associated with extended anaesthesia. The work presented in this chapter builds on the previous iterative CS implementation to demonstrate the use of CNNs for significantly faster reconstruction with improved image quality.

The neural networks were trained to remove the streak artifacts from *ex vivo* fixed and cleared mouse tissue. Despite this limit in classes of sample type, the structural similarities of

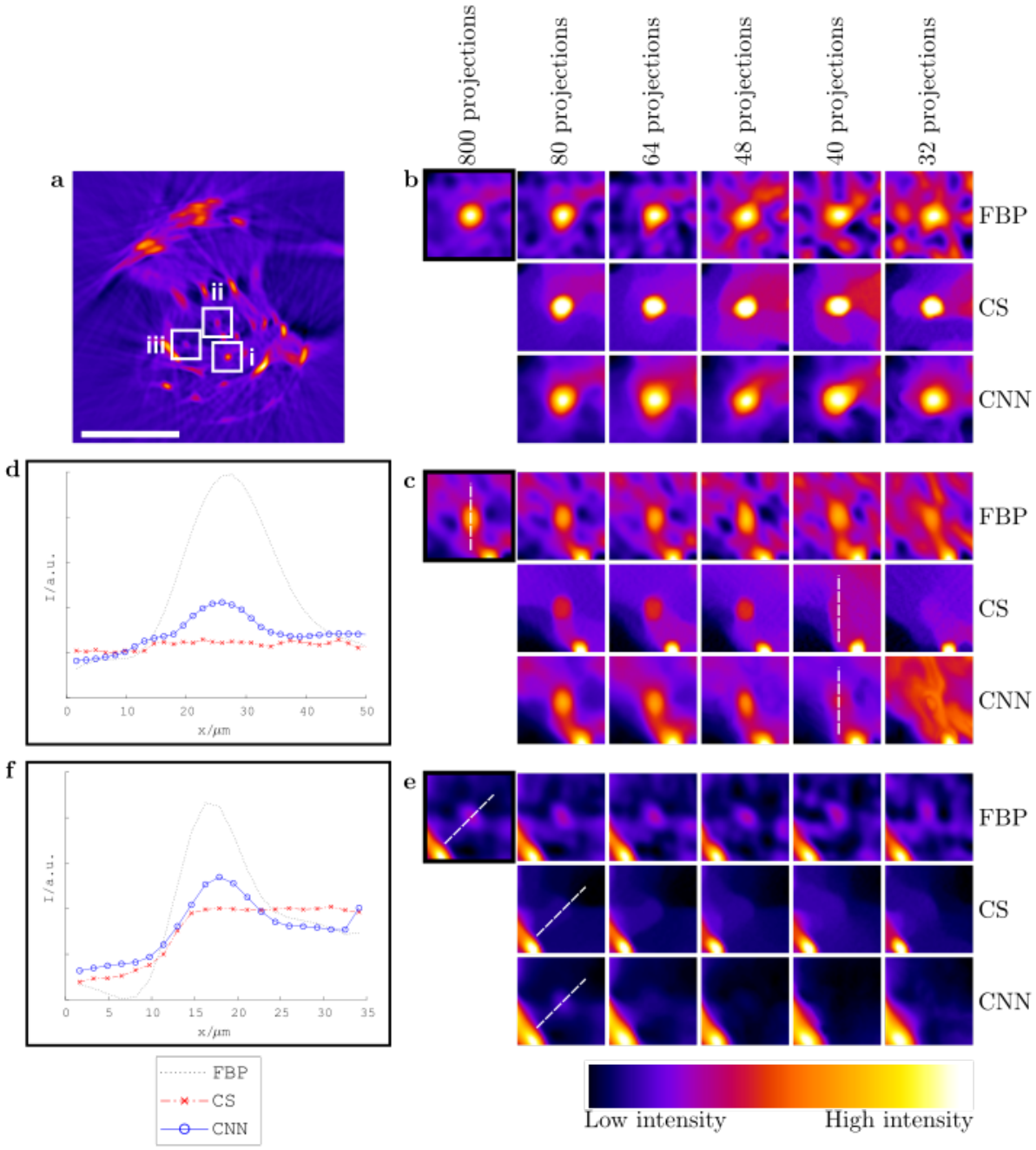

Figure 5.10: Sensitivity of iterative CS and CNN methods to dim features. (**a**) Slice of zebrafish embryo reconstructed with FBP from a well-sampled data set. Three regions of interest are highlighted. Scalebar 250 μm. (**b**) (**c**) (**e**) The indicated regions of interest (i, ii, iii) respectively, from the FBP, CS and CNN reconstructions for different numbers of angular projections. The feature in (i) is resolved in all cases shown. The feature in (ii) is resolved down to 48 and 40 projections for CS and CNN reconstructions respectively. (**d**) Line profiles through (ii) as indicated in (**c**). The feature (iii) is not resolved in the CS reconstructions but can be seen in the 80 projection CNN reconstruction. (**f**) Line profiles through feature (iii) as indicated in (**e**). Adapted from [5].

the streak artifacts created by sparse signals meant that the trained CNNs could be successfully applied to *in vivo* zebrafish data. This means no additional animals were necessary to build an appropriate training data set.

The reduction in processing time will improve the practicality of future high-throughput longitudinal studies. Extrapolating the total reconstruction time improvement, the OPT reconstruction time for the 24 zebrafish imaged in the baseline study would be improved from 62 to 12 hours – making the difference between the data being available the next morning and having to wait half the working week.

The approach taken in this chapter was to treat each individual slice as a 2D denoising problem. However, the samples, and their reconstructed volumes, are three dimensional. The sample volume presents equally high spatial correlations and equally great sparsity in all directions. Creating a full 3D convolutional network would require impractical GPU memory requirements to implement for the entire volume. However, it would be trival to take some of the neighbouring slices as additional input channels. This would have a negative impact on speed, but could provide an improvement in quality.

The denoising of FBP-reconstructed images may be less effective than working directly with the raw projections. Instead of acting to remove noise from the reconstructions, a network could be designed to guess at the missing projections, before any transformation has occured. This requires a different approach to how the data is treated – the projections are locally correlated in t and x, but not in θ. Working in 2D, one approach would be to use 1D convolutional filters in t and to treat each projection θ as a seperate input channel. This could then be extended into 3D by using 2D convolutional filters in t and x.

Chapter 6

Conformal high dynamic range optical projection tomography

One of benefits of imaging with OPT is the ability to image the 3D distribution of a variety of contrast mechanisms, including absorption [11], which can provide complementary contrast to fluorescence measurements [59, 118]. Depending on what is labelled, fluorescent structures can appear out of context of the sample's anatomy, and be challenging to interpret. While anatomy can be visualised using autofluorescence, this signal is comparitively weak – leading to long acquisition times, photobleaching and phototoxicity in live samples. In contrast, brightfield images with absorption contrast can be acquired rapidly with low illumination power.

Due to their size and optical density, acquiring brightfield images of adult zebfrafish is challenging. The extinction coefficient in soft tissue in the diagnostic window is $O\left(10\ cm^{-1}\right)$ (section 2.1). Assuming perfect coupling of light into the fish, the intensity of the light that goes through the sample will be 50 dB lower than the light that goes around the fish to reach the camera. This uses up most, if not all, of the dynamic range of a typical camera, so that the structure within the fish will be hidden by noise and only its silhouette will be seen. Therefore, a high dynamic range (HDR) imaging system is required to acquire useful projection image data through such optically opaque samples.

Time sequential multi-exposure acquisition is an HDR method that can be implemented without any additional hardware. The technique involves acquiring a number of images of the sample with different exposure lengths. Any given pixel may be saturated or below the noise floor in some of the images, but will be well exposed in others. Afterwards, an HDR image is produced by combining the differently exposed images, using knowledge of the camera's response [150]. This technique has been applied to increasing the dynamic range of OPT for imaging zebrafish embryos [122]. Theoretically, it allows for arbitrarily large dynamic range scenes to be recorded. In reality, however, the technique is limited by the effects of saturation on existing pixelated detector architectures. Excess carriers created in saturated pixels can diffuse away into neighbouring areas, increasing the measured intensity above its true value [151]. This effect is called blooming, and is particularly pronounced in CCD cameras, where it causes vertical streaks of saturation. Blooming limits how greatly a bright region can be over-exposed before

it affects the pixel values in the dim regions, and therefore the dynamic range of conventional HDR imaging.

The dynamic range can also be increased with alternative sensors or additional hardware. Sensors with alternative architectures have been designed to have a logarithmic intensity response [152]. Alternatively, a conventional camera can be combined with a spatial light modulator (SLM) to act as a mask, adapting its optical density for each pixel based on its intensity [153]. Here, this system is adapted for HDR OPT imaging. Instead of using a liquid crystal on silicon SLM, a lower cost DMD is used; an array of microscopic mirrors that can be individually rotated into "off" or "on" states to reflect light in one of two directions. Such a system was described in [154], where the sample was imaged onto a DMD, which was imaged onto a camera. In this configuration the NA of the imaging optics is constrained such that the DMD lies within the DOF, which causes a loss of collection efficiency and resolution. In contrast, for this work the DMD is used before the sample to provide spatially resolved control over how the sample is illuminated – which is here described as conformal-HDR (C-HDR), because of its similarities to conformal radiotherapy [155]. In C-HDR, as the exposure is increased, the previous recorded image is used to display a mask on the DMD that will illuminate only the parts of the sample that will not transmit sufficient light to saturate the camera.

This chapter is organised as follows: section 6.1 describes the optical set-up, its operation, and HDR fusion; section 6.2 describes the application of the C-HDR-OPT system to a bead phantom; and section 6.3 describes the application of the system to brightfield OPT imaging of an adult zebrafish.

6.1 Hardware and operation

6.1.1 Hardware

A schematic of the C-HDR-OPT set-up is shown in Figure 6.1. LED radiation at 740 nm (OptoLED, Cairn) was collimated by L_1 (FRP232, Thorlabs, $f = 32\ mm$) and directed to uniformly illuminate a DMD with 1920×1080 7.56 μm pixels (DLP Lightcrafter 6500, TI). The full field of the DMD was imaged onto the sample using a telecentric imaging relay comprising achromatic lenses, L_2 and L_3 (AC508-200-A-ML, $f = 200\ mm$ and AC508-400-A-ML, $f = 400\ mm$, Thorlabs) with an adjustable aperture stop AP (SM2D25D, Thorlabs) in the Fourier plane. The transmitted light was imaged using a commercial 0.5x magnification telecentric lens (TL) with an adjustable aperture (TECHSPEC SilverTL, Edmund Optics), onto a sCMOS camera (Iris 9, Photometrics). The illumination and imaging systems were configured with optical axes parallel at the sample and perpendicular to the axis of rotation. Their focal planes were coincident and the excitation and emission DOFs set to 4 mm to cover at least the front half of the sample – giving a diffraction-limited resolution of 26.3 μm. The samples were mounted in FEP tubing (06406-72, Cole-Parmer) and suspended in a water-filled cuvette (704-003-50-10, Hellma Analytics) from a stepper motor (NM11AS-T4, Laser 2000 UK) with tip-tilt adjustment (M-TTN80, Newport Corp) and 3-axis linear translation (M-423 and M-UMR12.63).

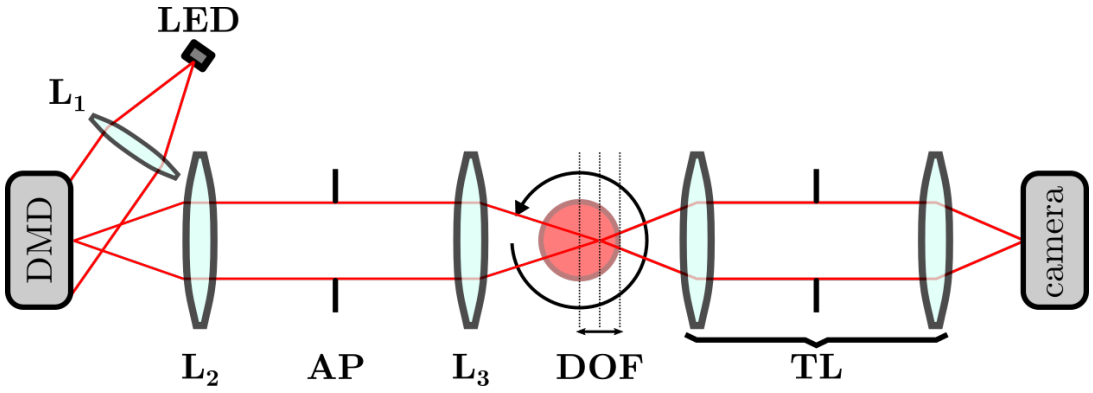

Figure 6.1: C-HDR-OPT setup. The addition of a DMD in the illumination path enables control over which parts of the FOV are illuminated.

6.1.2 Data acquisition

The system was controlled using scripts written in MATLAB. The sample was rotated to a number of equally spaced angles around 360°. At each of these a C-HDR projetion data set was acquired. Images were recorded on the camera with 2x2 binning using different exposure levels: 100 μs, 1 ms, 10 ms, and 200 ms. At each exposure level, a mask was displayed on the DMD to only illuminate that part of the FOV that was not expected to saturate the detector. These masks were calculated using (figure 6.2):

$$M_n^c(x,y) = \begin{cases} 1, & for\ n = 0 \\ M_{n-1}^c(x,y)\left(I_{n-1}(x,y) < (I_{sat} - I_{offset})\frac{t_{n-1}}{t_n}a + I_{offset}\right), & for\ n > 0, \end{cases} \tag{6.1}$$

where $I_n(x,y)$ is the recorded pixel value at coordinates (x,y) for the n_{th} of N exposures, with integration time t_n, and $M_n^c(x,y)$ is the conformal mask used for the n_{th} image. I_{sat} and I_{offset} are respectively the saturation point and offset of the camera, and a is an additional factor set to 1.2, to include some pixels over the predicted saturation boundary. The masks were further processed with a 7 pixel morphological opening to remove small regions, and a 3 pixel morphological erosion to create a margin for diffraction, scattering, and mis-calibration of the DMD orientation.

To correctly display the masks, the position of the image of the DMD on the camera was calibrated. A series of images were recorded of 5 pixel squares displayed at different positions on the DMD, and the M-estimator sample consensus algorithm was used to estimate the affine transormation between the set of input coordinates and output maxima of the images (*estimateGeometricTransform*, MATLAB, [156]). The masks were transformed from camera to DMD space and displayed using the Psychtoolbox package.

The DMD can be used as a monitor to adapt what is displayed upon it. When used in this way, the DMD mirrors are momentarily switched off by pixel reset pulses, and for 370 μs after each frame due to hardware timing requirements when using the DMD as a display. Combined with the rolling shutter of camera, this effect produces striping artifacts for exposures shorter

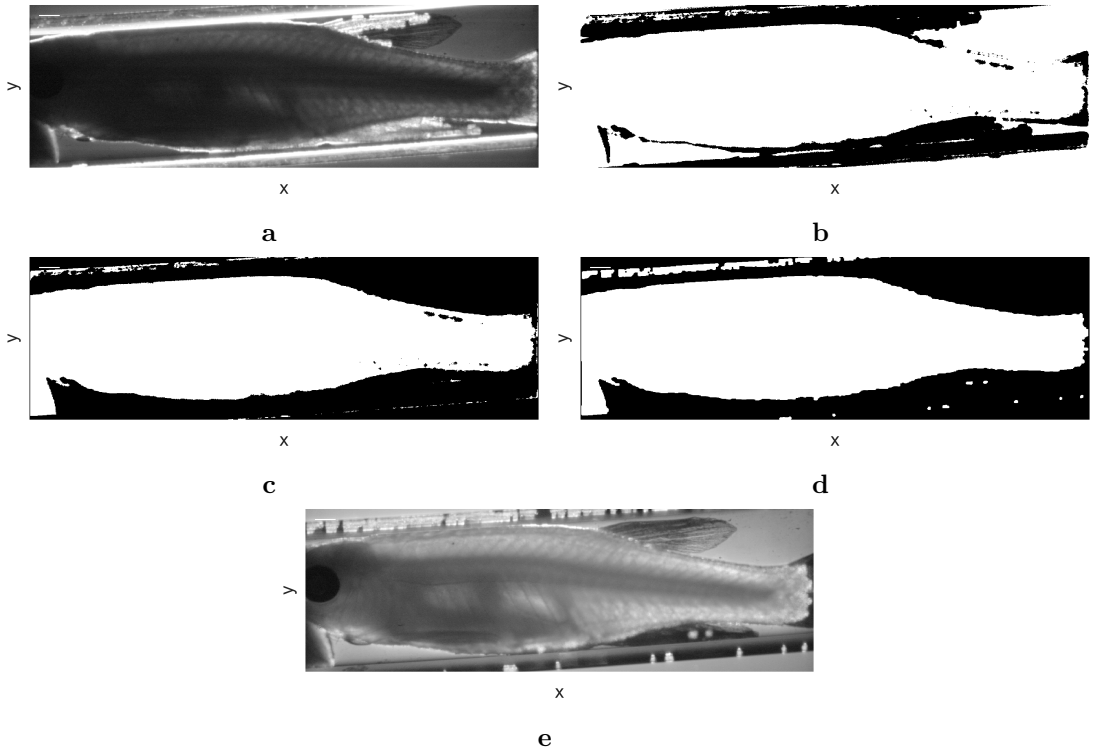

Figure 6.2: C-HDR-OPT mask calculation. (**a**) A 1 ms exposure image of a fish in transmission. The illumination has been masked so that only the sample body and fins, and the tubing are illuminated. (**b**) Based on the image in (**a**) a mask is made of all pixels that are not expected to be saturated at the next exposure. (**c**) This mask is multiplied by the previous mask, so that previously masked regions do not turn back on and over-saturate the detector. (**d**) The mask is cleaned with morphological processes. (**e**) A 10 ms image acquired with the mask in (**d**). (**a**) and (**e**) Displayed with logarithmic scale.

than the frame rate of the camera (figure 6.3). To address this artifact, short exposure images were acquired in bursts of 5, and the pixelwise maximum taken of the set of images. This caused an overestimation of pixel values because of noise. A better choice would be to take the pixelwise median.

To acquire more information about pixels near the mask boundaries (see section 6.1.3), additional images were acquired after each n with a longer exposure $2t_n$, but with the same M_n.

Conventional multiple exposure HDR-OPT data sets of the samples were also acquired. The sample was rotated to a number of equally spaced angles around 360°. Images were recorded on the camera with 2x2 binning using different exposure levels: 100 μs, 1 ms, 10 ms, and 200 ms. At every exposure level, the entire DMD was set to "on".

6.1.3 Projection fusion

In conventional multiple exposure HDR imaging, the masks for selecting which pixels come from which exposures are calculated *a posteriori*. Each pixel is taken from the longest exposure

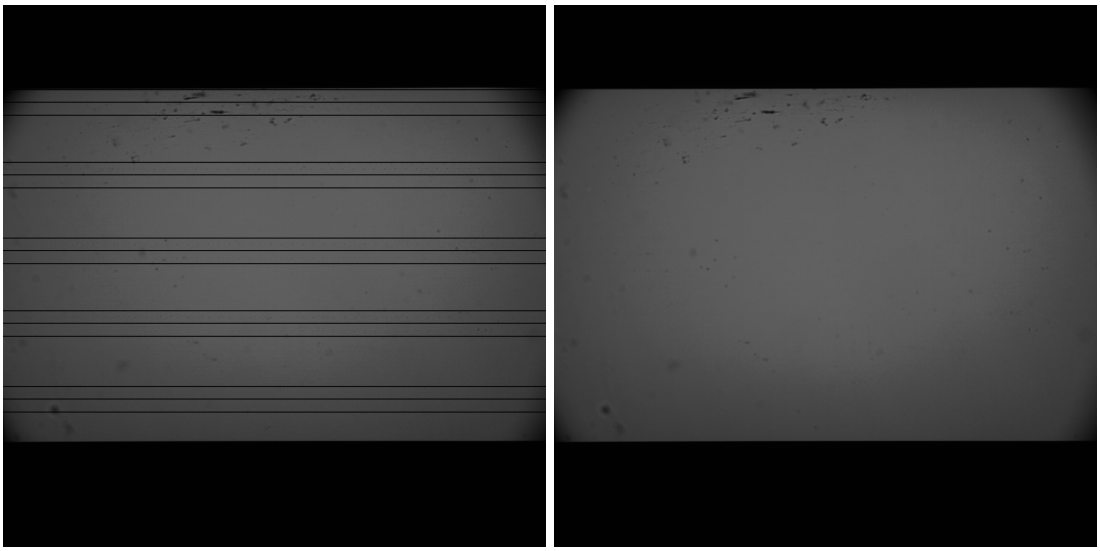

a **b**

Figure 6.3: Removal of striping artifact. (**a**) Striping artifact caused from DMD pixel resetting and rolling camera shutter. (**a**) 100 μs exposure image of DMD with all pixels "on", at maximum pixel value in video mode. (**b**) Pixelwise maximum of 5 100 μs exposure images.

image in which it is not saturated, and subsequently transformed to a uniform intensity scale. The pixel values for the n_{th} exposure are:

$$I_n(x,y) = t_n b I(x,y) + I_{offset} + noise, \tag{6.2}$$

where $I(x,y)$ is the intensity at the detector at pixel coordinate (x,y), and b is a constant. The pixel masks are calculated as

$$M_n(x,y) = \begin{cases} I_n(x,y) < I_{sat}, & for\ n = N \\ \left(1 - M_{n+1}(x,y)\right)\left(I_n(x,y) < I_{sat}\right), & for\ n < N, \end{cases} \tag{6.3}$$

and a HDR image recovered using

$$I_{out}(x,y) = \sum_n M_n(x,y)\left(I_n(x,y) - I_{offset}\right)/t_n. \tag{6.4}$$

If this is trivially extended to the conformal illumination approach with

$$I^c_{out}(x,y) = \sum_n M^c_n(x,y)\left(1 - M^c_{n+1}(x,y)\right)\left(I^c_n(x,y) - I_{offset}\right), \tag{6.5}$$

where I^c_n are the intermediate HDR images calculated from each pair of t_n and $2t_n$ using equation 6.4, sharp gradients are seen at the edges of the masks, and pixels taken from the longer exposures are underestimated (figure 6.4a). The fusion has sharp boundaries because it assumes that the mask is perfectly propogated through the system – as if it were applied on the image itself, as in [153, 154] rather than being diffracted and scattered through the system and sample. Figure 6.5 shows an adult zebrafish illuminated by a particular mask with a 200 ms

exposure. The illumination has been scattered out of the indicated mask shape. The scattering of light away from the illuminating mask has not been balanced by scattering into the mask from the portions of sample outside the mask – compared to what would be seen in an idealised high dynamic range widefield image. Therefore it is not a simple binary relation between the image recorded with and without the mask. Also of note is the background intensity across the FOV – caused by light scattering in the beam delivery optics and cuvette. This sets the current limit to the dynamic range that can be achieved with conformal HDR.

To remove the discontinuities at the mask boundaries, the dimmer regions must be amplified to account for their reduced illumination. To achieve this, an approximately uniform gain map was applied to the portions of I^c_{out} from the masked regions. The validity of this approach is explored as follows. $(I_3 - I_{offset})/(I_4 - I_{offset})$ over M^c_4 is shown in figure 6.6a. In an ideal case – i.e. no diffraction and no scattering – this ratio would be expected to be a noisy version of the mask M^c_4, with a value of t_3/t_4. Instead, the ratio is smoothly varying across the centre of the mask, and rises sharply at the boundaries of the illumination mask, making a smoothly varying correction invalid in these areas. Therefore, the boundary regions were re-assigned into the masks of the shorter exposures – where those pixels were less well exposed, but more predictably illuminated. This was achieved using a six-pixel erosion applied to each of the illumination masks; $M^{c\prime}_n = M^c_n \ominus B$, where B is a six-pixel radius circle structural element. The ratio map over $M^{c\prime}_4$ is shown in figure 6.6b; although it is spatially varying, that variation is smooth.

The gain map was created by interpolating the gain required for no discontinuities at the eroded mask boundary:

$$g_n(x,y) = \begin{cases} \dfrac{\sum_i u_i / \left(r_i(x,y)^2 + 1\right)}{\sum_i 1 / \left(r_i(x,y)^2 + 1\right)}, & for\ n = 2 \\ \dfrac{\sum_i u_i \left(\prod_{m=1}^{n} g_m(x_i, y_i)\right) / \left(r_i(x,y)^2 + 1\right)}{\sum_i 1 / \left(r_i(x,y)^2 + 1\right)}, & for\ n > 2, \end{cases} \tag{6.6}$$

where the sum is over all pixels on the edge of mask M_n, and u^n_i is the ratio at position (x_i, y_i), and $r_i(x,y)^2 = (x - x_i)^2 + (y - y_i)^2$:

$$u^n_i = \left(I_n(x_i, y_i) - I_{offset}\right) / \left(I_{n-1}(x_i, y_i) - I_{offset}\right).$$

The quadratic term was chosen empirically as it produced qualititatively acceptable results, and the additional one stops the gain becoming undefined at the edge of the mask.

The discontinuity corrected C-HDR projection was then calculated using

$$I^c_{out}(x,y) = \sum_n M^c_n(x,y)\left(1 - M^c_{n+1}(x,y)\right) g_n(x,y)\left(I_n(x,y) - I_{offset}\right), \tag{6.7}$$

which is shown in figure 6.4b. The logarithm of projections was taken, and the volume reconstructed as described in section 3.2.

Equation 6.7 appears to produce results that overestimate the signal in the centre of the sample. A more rigorous approach might recover the image using a minimisation approach,

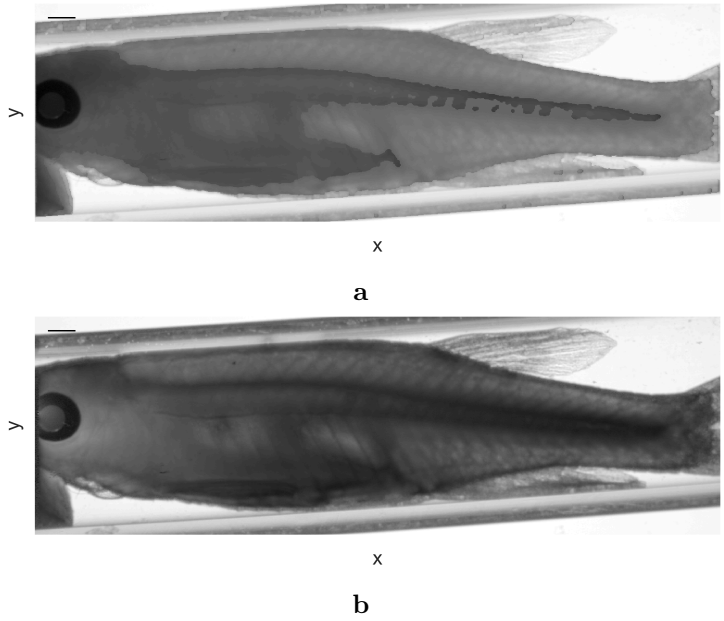

Figure 6.4: (**a**) Fusion of conformal HDR projection data using equation 6.4. (**b**) Fusion of conformal HDR projection data using equation 6.7. Scalebar 1 mm.

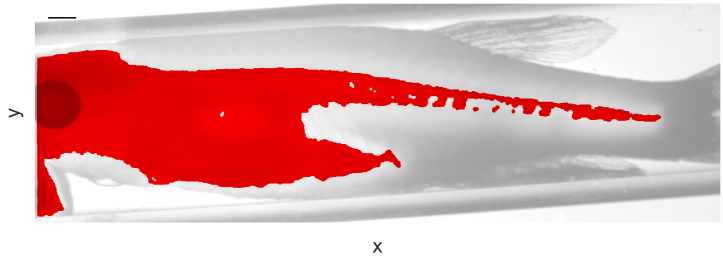

Figure 6.5: Adult zebrafish illuminated in transmission by the mask indicated in red. Background light can be seen across the FOV, and the illumination has been scattered beyond its boundaries.

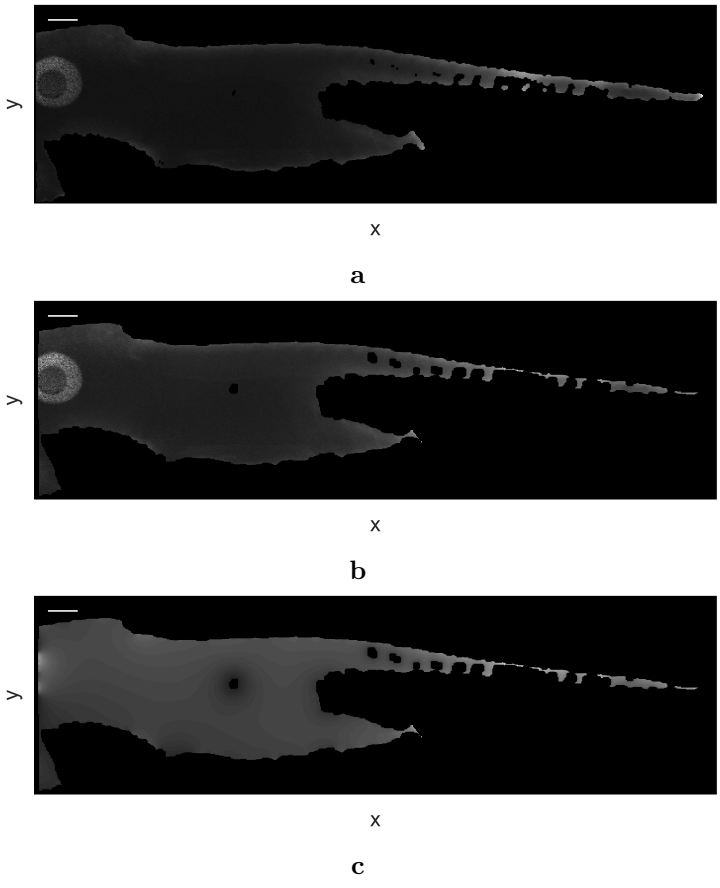

Figure 6.6: Calculation of correction gain map. (**a**) Ratio of intensity between I_3 and I_4 over M_4. The ratio is highest at the edges and quickly falls off. (**b**) The same ratio over the mask created with a 6-pixel erosion. The ratio is much more slowly varying over this mask. (**c**) Gain map calculated using equation 6.6.

which seeks to find a discontinuity-free full dynamic range image X. The forward model for the n_{th} exposure can be described as:

$$Y_n = A_n G_n X + noise, \tag{6.8}$$

where Y_n is the recorded image, G_n is the unknown modulation caused by the illumination pattern, and A_n is the camera response function:

$$A_n X = min\left(t_n X + I_{offset}, I_{sat}\right). \tag{6.9}$$

X and G_n can then be recovered by solving the minimisation problem:

$$minimise_{X,G_n} \sum_n \left(\|Y_n - A_n G_n X\|_2^2 + a \|M_n - G_n\|_2^2 + \tau_G \Phi(G) \right) + \tau_x \Phi(X), \tag{6.10}$$

where a, τ_x, and τ_G are regularisation parameters, and Φ is the total variation functional. The relationship between M_n and G_n could also be explored to measure scattering properties of the sample.

6.2 Characterisation on bead phantom

The C-HDR-OPT system was tested on a phantom of beads ($0.02\mu m$, Crimson $625/645nm$, Invitrogen) suspended in a 3D scattering medium of 2% agarose, with scattering provided by a 0.4% by volume suspension of microspheres (Plain $1990nm$, PL-Microspheres). The phantoms were made in a 1.5 ml tube (11926955, Fisher Scientific), giving it an approximately conical shape, 8 mm diameter and 2 cm in length.

The phantom was imaged with 400 projection HDR-OPT and C-HDR-OPT as described in section 6.1.2. The acquisition times were 20 and 44 minutes for HDR-OPT and C-HDR-OPT respectively. Transmission projections acquired conventionally, with HDR and C-HDR are shown in figure 6.7. The conventional transmission image only shows a silhouette of the phantom. The HDR image shows a less noisy silhouette, which has recorded some low spatial frequency signal through the sample, but no small features are visible. However, the superior signal to noise ratio enables several beads and imperfections in the agarose surface to be seen in the image acquired using C-HDR, as shown in the line profile in figure 6.7d. Also visible in the C-HDR line profile is the overestimate of signal in the centre, created by the fusion proposed in equation 6.7.

The dynamic range of a camera is defined as:

$$DR = 10\log_{10}\frac{I_{max}}{I_{min}}, \tag{6.11}$$

where I_{max} and I_{min} are the maximum and minimum detectable signal. The noise was measured in the 100 pixel dark region of interest indicated by the blue square in figure 6.7c. From this a dynamic range of 98 ± 1 dB was measured, which is likely an underestimate due to the over-correction of the centre. The datasheet dynamic range of the Iris 9 camera is 39 dB.

A slice of the phantom volume reconstructed from HDR and C-HDR projections is shown in figure 6.8. The indicated feature is reconstructed from the C-HDR data, but is not visible in the HDR reconstruction.

6.3 Application to *in vivo* imaging

To demonstrate C-HDR-OPT *in vivo*, the system was applied to imaging a terminally anaesthetised adult (fli:GFP) Casper zebrafish (6 months post fertilisation). The imaging parameters used were the same as described in section 6.2. Transmission projection images that were acquired conventionally, and with HDR and C-HDR imaging are shown in figure 6.9. Some features are visible in the tail of the conventional transmission projection, but little otherwise can be seen and the image is noisy. The HDR projection is less noisy, and more structure can be seen along the tail and dorsal side. Superior contrast across the whole fish is apparent in the C-HDR projection.

Figure 6.10 shows orthogonal slices through the adult zebrafish volumes reconstructed from the HDR and C-HDR projections. The C-HDR reconstructions have signficantly more contrast – of particular note is the visibility of the swim bladder (indicated by arrow).

6.4 Conclusion

C-HDR-OPT enables 3D brightfield contrast reconstructions of optically thick samples by adapting the illumination to the sample. This method increased the projection dynamic range from 39 dB to 98 ± 1 dB, and revealed features that are masked by blooming when imaged with conventional HDR. This will enable dual fluorescence and brightfield OPT imaging of adult zebrafish, to provide specific contrast and anatomical context.

The technique is not yet fully quantitative, due to the over-correction of longer exposures to try and account for scattering of the illuminating mask in the sample. This problem could be avoided by applying the mask after the sample. This would require using a non blazed SLM, for example a LCOS SLM. Alteratively, an optimisation approach (suggested in section 6.1.3), could be used to fuse the data with greater verisimilitude.

The contrast is still limited by optical scattering within the sample. Many bones and the swim bladder can be seen in figure 6.10, but other organs in the abdomen are not visible. However, this technique is applicable to imaging with short-wave infrared (SWIR) illumination (chapter 8), which should improve the imaging depth.

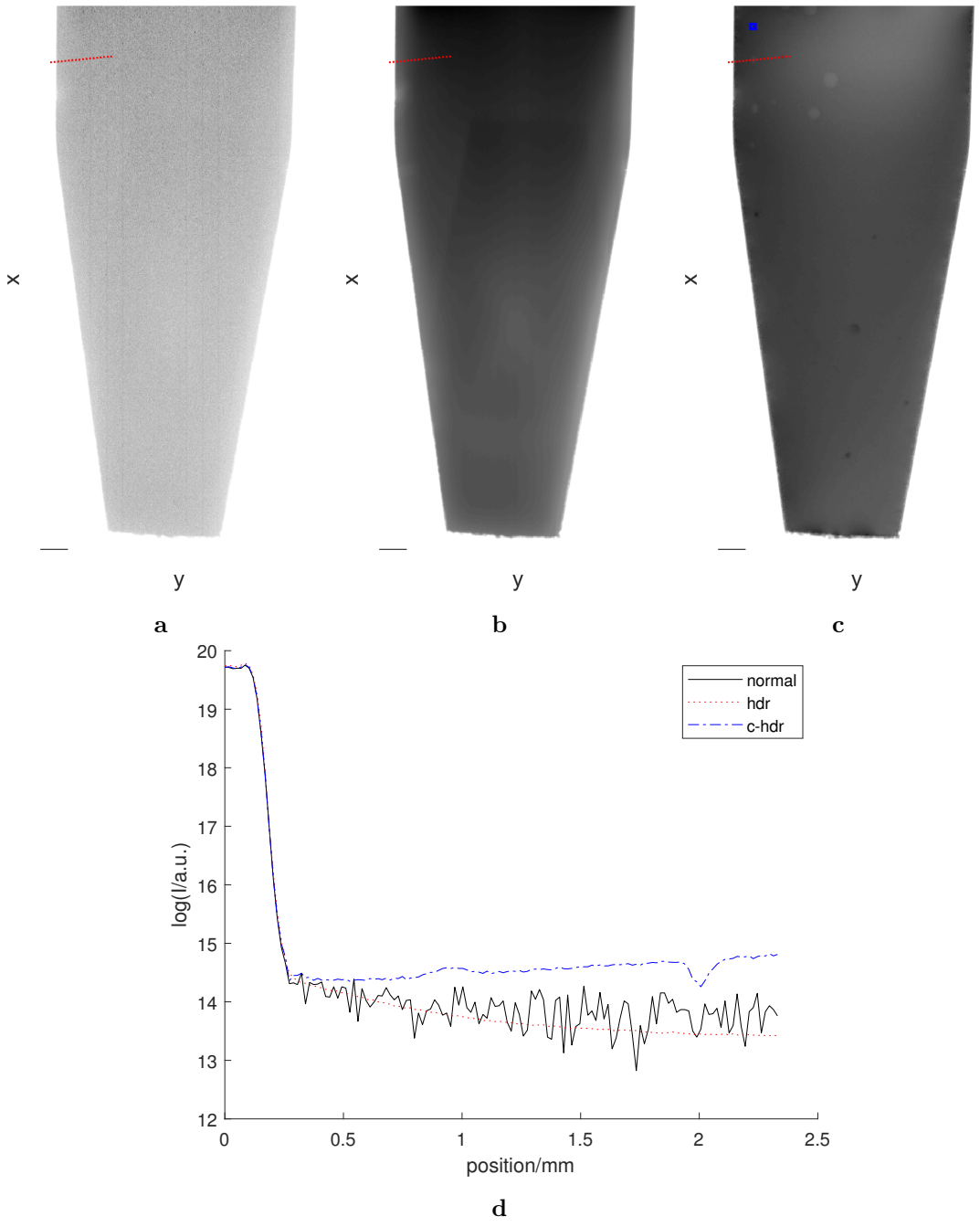

Figure 6.7: Transmission projections of a scattering bead phantom. (**a**) Conventional image. The phantom appears as a noisy silhouette (**b**) HDR image. The phantom appears as a silhouette without internal structure. (**c**) C-HDR image. Beads and surface features are visible. The blue box shows the 100 pixels over which the noise was measured. (**d**) Line profiles as indicated by red dashed line on (**a**)-(**c**). Scalebar 1 *mm*

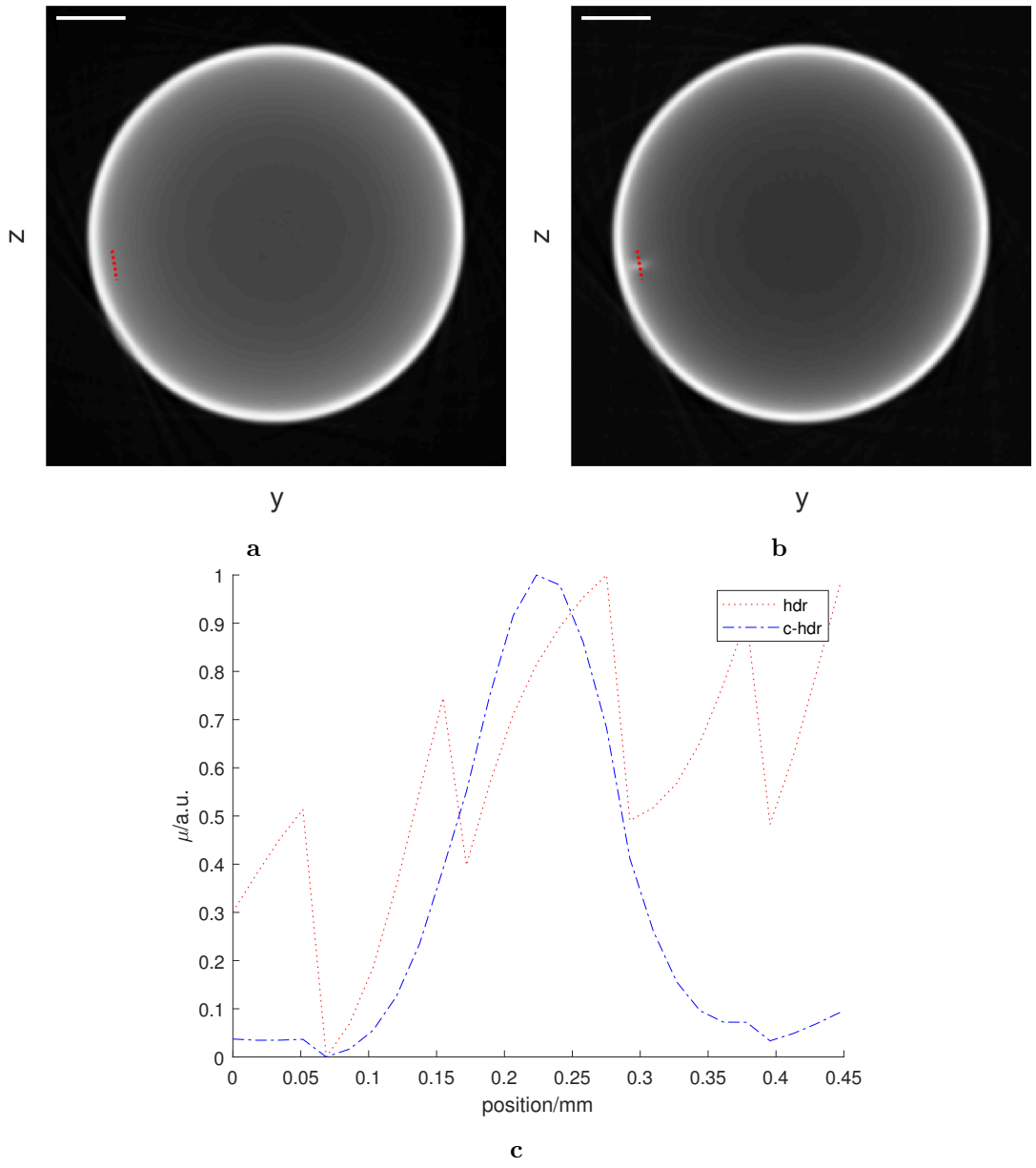

Figure 6.8: Slice from reconstruction of scattering agarose phantom. (**a**) Reconstruction produced with HDR-OPT data. (**b**) Reconstruction produced with C-HDR-OPT. (**d**) Line profiles as indicated in (**a**) and (**b**) Scalebar 1 *mm*

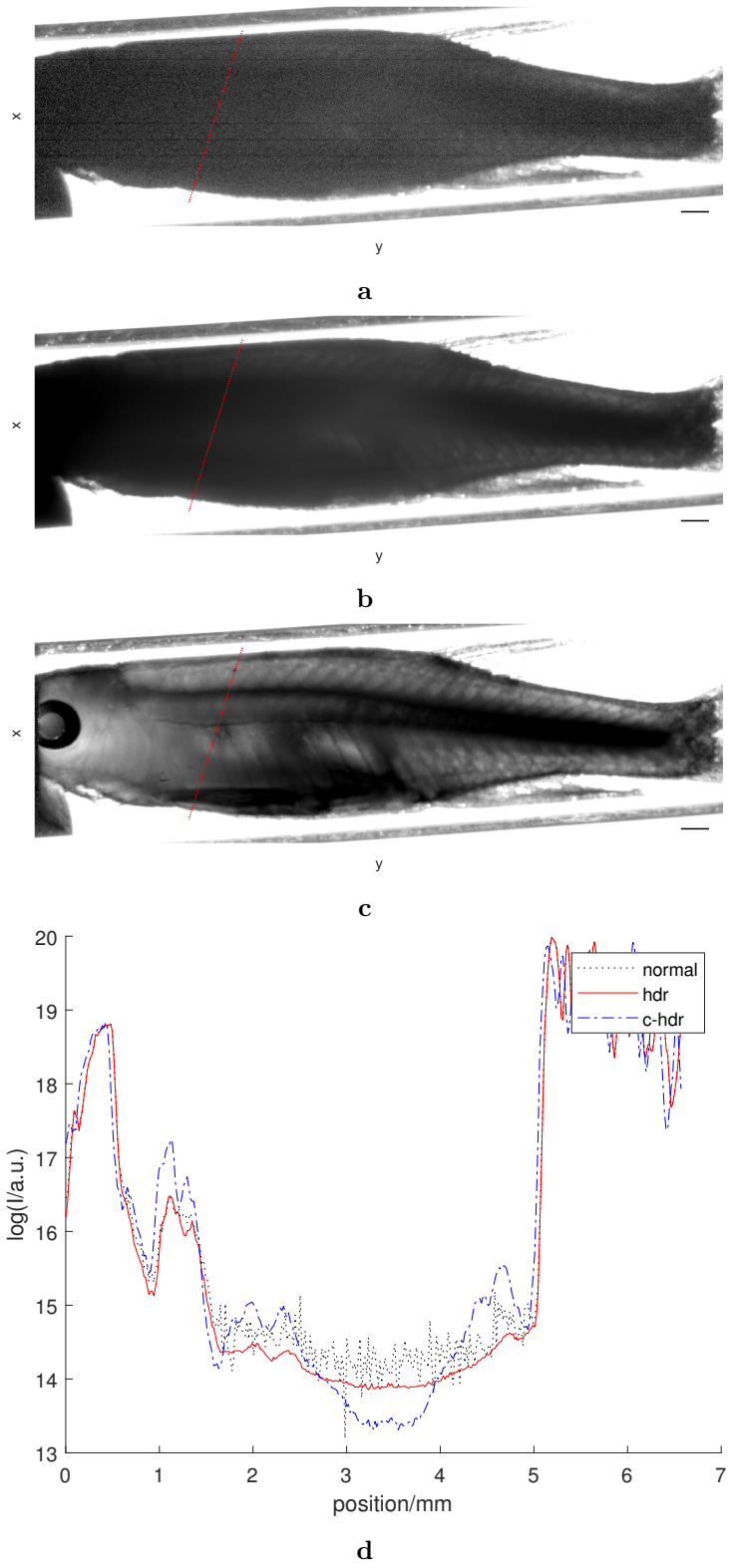

Figure 6.9: Transmission projections of an adult zebrafish. (**a**) Conventional image. (**b**) HDR image. (**c**) C-HDR image. (**d**) Line profiles as indicated on (**a**)-(**c**). Scalebar 1 mm

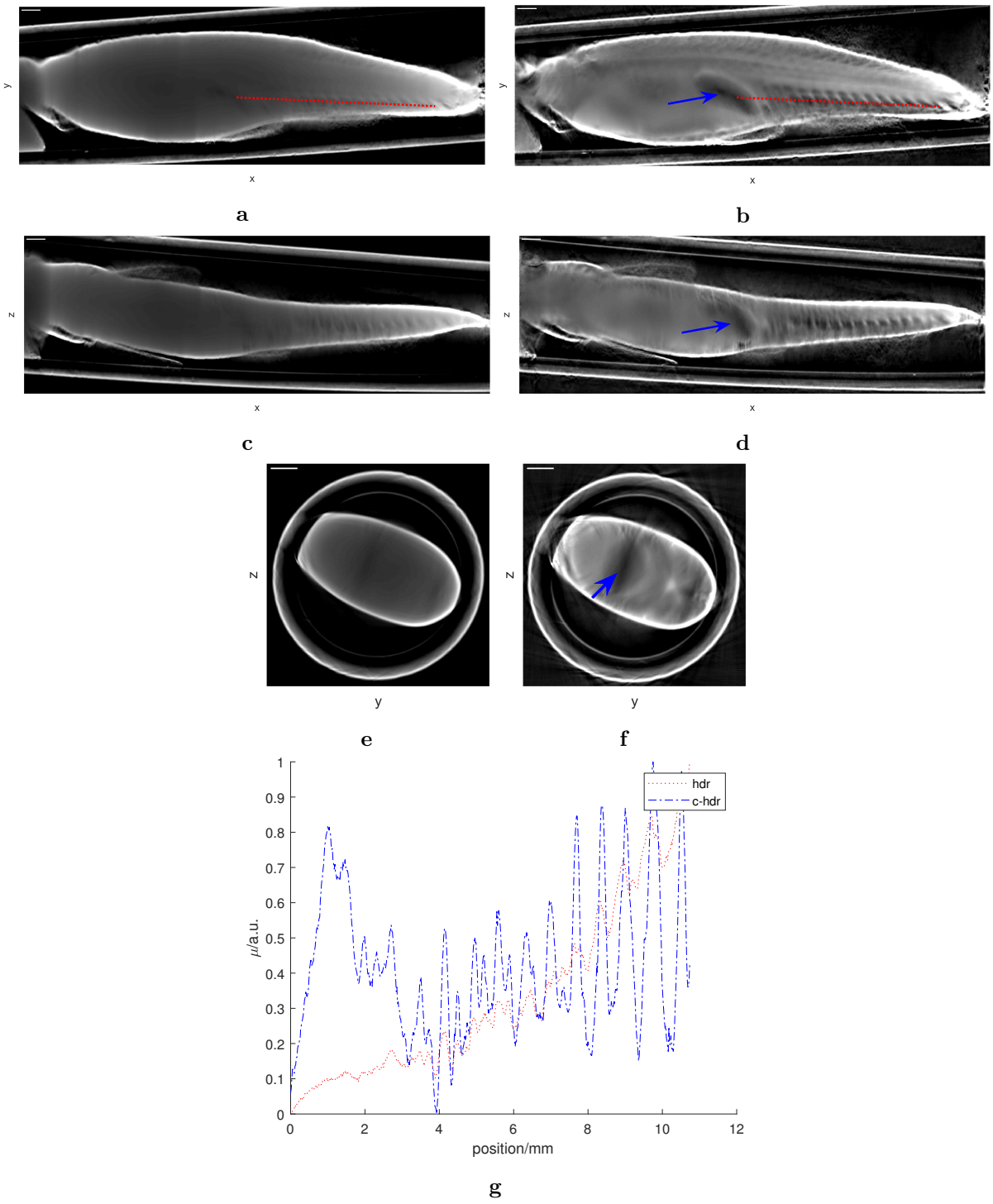

Figure 6.10: Orthogonal slices through *in vivo* adult zebrafish volumes reconstructed from (**a**), (**c**), (**e**) HDR and (**b**), (**d**), (**f**) C-HDR projections. (**a**), (**b**) *xy* plane, (**c**), (**d**) *xz* plane, and (**e**), (**f**) *yz* plane. The arrows indicate the swim bladder, which is visible in the C-HDR-OPT reconstruction. (**g**) Line profiles as indicated in (**a**), (**b**). Scalebar 1 *mm*

Chapter 7

Slice illuminated optical projection tomography

Chapter 4 described the application of angularly-multiplexed compressed-sensing OPT to longitudinal imaging of adult zebrafish. This combination of techniques enabled quantification of tumor development with repeated imaging under anesthesia and subsequent recovery [72,108,136]. However, although these non-pigmented fish are significantly more transparent than wild-type fish, they do present discernible optical scattering. This chapter describes the development of a system to improve the image quality by rejecting scattered light with semi-confocal illumination and detection [157], described as slice illuminated OPT (slice-OPT) [6].

In OPT the recorded projection images are formed of ballistic photons, which report the structure of the sample, and scattered photons, which degrade resolution and contrast. The impact of scattering has been reduced for absorption OPT by discriminating in favour of ballistic photons with an ultrafast optical Kerr gate [112], and structured illumination to discriminate against scattered light [113]. However, ballistic fluorescence photons cannot be time-gated – the lifetime of the fluorescent excited state is orders of magnitude longer than increases to photon arrival time caused by optical scattering – and the arithmetic operations involved in structured illumination reduce the available dynamic range [158].

Slice-OPT is intended to reduce the impact of optical scattering on fluorescence OPT projections, without reducing dynamic range. In slice-OPT the sample is illuminated with a series of parallel lines, to excite fluorescence from individual slices through the sample, as illustrated in figure 7.1. Detected fluorescence photons will originate from the excited slice, but also from neighbouring slices due to scattering. These scattered photons are rejected with a digital mask applied to the camera. A full slice-OPT projection is produced by scanning the illumination and mask.

Section 7.1.1 expands on 3.2 to describe the effects of Gaussian blurring on transfer function support in widefield and slice-OPT reconstructions. Section 7.2 describes the optical set-up, calibration, and operation of the slice-OPT system. Sections 7.3 and 7.4 describe the application of slice-OPT to a scattering bead phantom and to juvenile zebrafish. Finally, section 7.5 discusses the results and future outlook.

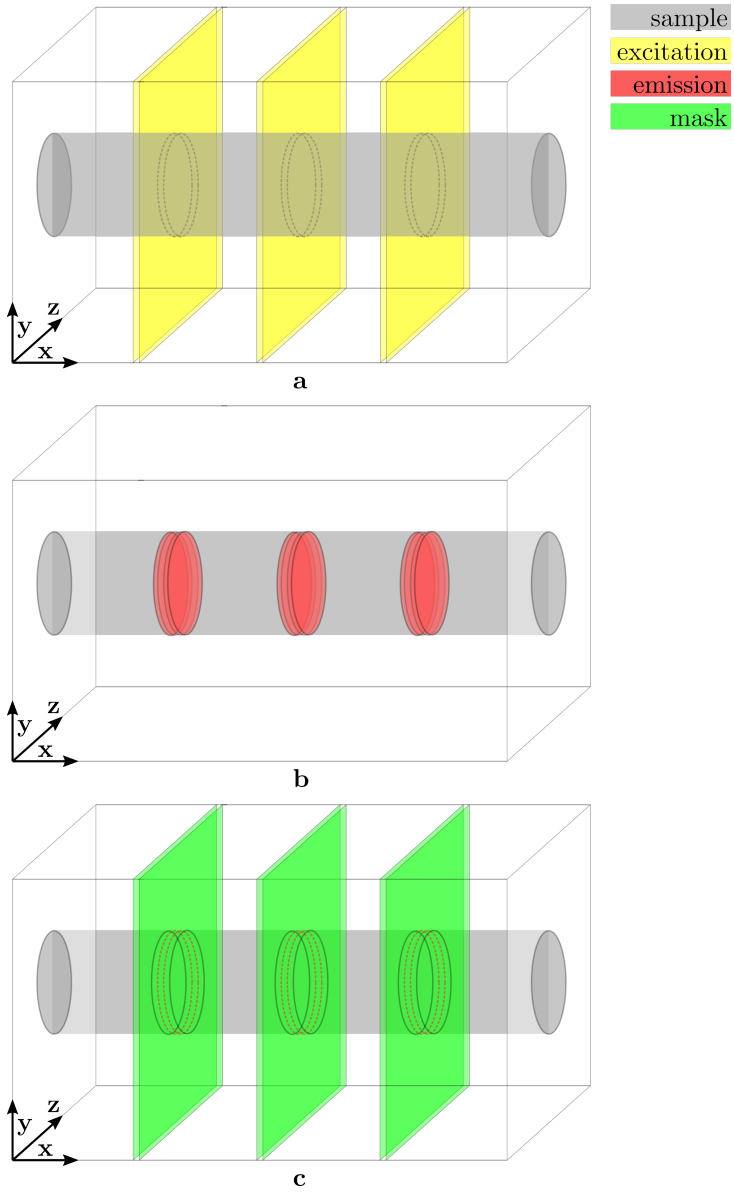

Figure 7.1: Diagram showing principle of Slice-OPT, the imaging and illumination systems are coaligned with the z axis (figure 7.3): (**a**) Separated slices of the sample are individually illuminated. (**b**) Fluorescence is detected from the illuminated slices, but also from neighbouring ones. (**c**) The spurious signal can be removed using a digital mask. A complete projection is built up by scanning the illumination and digital mask and repeating the process.

7.1 Theory

7.1.1 Optical projection tomography transfer function

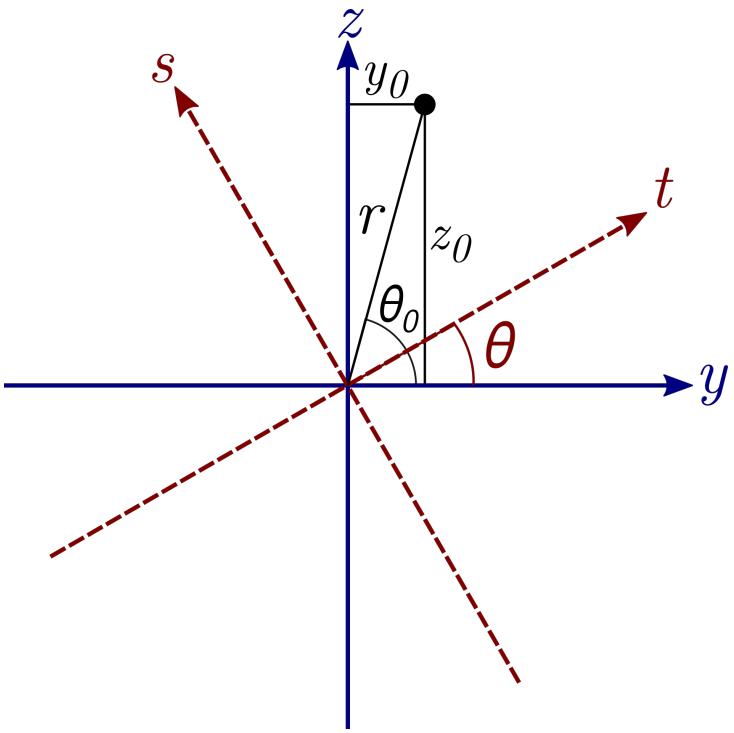

Figure 7.2: The transformation between object space (x, y, z) and camera space (x, t, s) is a rotation θ around the x axis, which goes into the page. A point object is placed at $(0, y_0, z_0)$ in object space.

In chapter 3.2 the process of projection and reconstruction was described for a perfect parallel projection system. However, the projections produced in OPT are only approximations to parallel projection, and are affected by diffraction and scattering. To describe the effect of slice-illumination, it is informative to explore the effect of a depth dependent point spread function on sampling.

Equation 3.1 can be extended to include a depth dependent intensity point spread function, $|h(x, t, s)|^2$:

$$p(x,t,\theta) = \int_{-\infty}^{\infty} f\left(t\cos\left(\theta\right) - s\sin\left(\theta\right), t\sin\left(\theta\right) + s\cos\left(\theta\right)\right) * |h(x,t,s)|^2 \mathrm{d}s \tag{7.1}$$

$$= \int_{-\infty}^{\infty}\int_{-\infty}^{\infty}\int_{-\infty}^{\infty} f\left(t\cos\left(\theta\right) - s\sin\left(\theta\right), t\sin\left(\theta\right) + s\cos\left(\theta\right)\right) |h(x-x', t-t', s)|^2 \mathrm{d}x'\mathrm{d}t'\mathrm{d}s. \tag{7.2}$$

Following the work of van der Horst et al. [99], a point object placed at $(0, y_0, z_0)$ is considered (figure 7.2),

$$\begin{aligned} f\left(x,t,s\right) &= \delta\left(x, t - r\cos\left(\theta_0 - \theta\right), s - r\sin\left(\theta_0 - \theta\right)\right) \\ r &= \sqrt{y_0^2 + z_0^2}, \theta_0 = \operatorname{atan}\left(z_0/y_0\right), \end{aligned} \tag{7.3}$$

A Gaussian approximation to the point spread function is used, which has been previously shown to match experimental data – and produces tractable expressions [99].

$$\left|h\left(x,t,s\right)\right|^2 = \frac{2}{\pi w^2\left(s\right)}\exp\left(-\frac{2\left(x^2+t^2\right)}{w^2(s)}\right), \tag{7.4}$$

where w(s) is the depth dependent beam waist,

$$w(s) = \sqrt{w_0^2 + \frac{\lambda^2\left(s - s_f\right)^2}{\pi^2 w_0^2} + w_{scatter}^2(s)}, \tag{7.5}$$

λ is the imaged wavelength, and w_0 the beam waist at the focal plane, s_f is the distance between the focal plane and rotation axis, and $w_{scatter}(s)$ an additional depth dependent Gaussian blur due to optical scattering. This expression assumes negligible absorption. For the point object this becomes

$$w(\theta) = \sqrt{w_0^2 + \frac{\lambda^2\left(r\sin\left(\theta_0 - \theta\right) - s_f\right)^2}{\pi^2 w_0^2} + w_{scatter}^2(r\sin\left(\theta_0 - \theta\right))}. \tag{7.6}$$

Substituting into equations 7.2, taking the Fourier transform, and transforming to (x, k_y, k_z) gives

$$\begin{aligned} p(x,t,\theta) &= \frac{2}{\pi w^2\left(\theta\right)}\exp\left(-\frac{2\left(x^2 + \left(t - t\left(\theta\right)\right)^2\right)}{w^2(\theta)}\right), \\ \mathcal{P}\left(x,k_t,\theta\right) &= \sqrt{\frac{2}{\pi w^2\left(\theta\right)}}\exp\left(-\frac{2x^2}{w^2(\theta)}\right)\exp\left(-\frac{\pi^2 k_t^2 w^2(\theta)}{2}\right)\exp\left(-2\pi i t(\theta) k_t\right), \\ \mathcal{P}\left(x,k_y,k_z\right) &= \sqrt{\frac{2}{\pi w^2\left(\theta\right)}}\exp\left(-\frac{2x^2}{w^2(\theta)}\right)\exp\left(-\frac{\pi^2\left(k_y^2 + k_z^2\right) w^2(\theta)}{2}\right)\exp\left(-2\pi i\left(y_0 k_y + z_0 k_z\right)\right). \end{aligned} \tag{7.7}$$

This expression can be reduced by transforming to a shifted and rotated coordinate system,

$$\begin{bmatrix} x \\ u \\ v \end{bmatrix} = \begin{bmatrix} 1 & 0 & 0 \\ 0 & \cos\left(-\theta_0\right) & -\sin\left(-\theta_0\right) \\ 0 & \sin\left(-\theta_0\right) & \cos\left(-\theta_0\right) \end{bmatrix} \begin{bmatrix} x \\ y - y_0 \\ z - z_0 \end{bmatrix},$$

centering the emitter at the origin, with the point spread function aligned with (u, v) axes:

$$\mathcal{P}\left(x,k_u,k_v\right) = \sqrt{\frac{2}{\pi w^2\left(\theta + \theta_0\right)}}\exp\left(-\frac{2x^2}{w^2(\theta + \theta_0)}\right)\exp\left(-\frac{\pi^2\left(k_u^2 + k_v^2\right) w^2(\theta + \theta_0)}{2}\right). \tag{7.8}$$

The last term in 7.8 shows how the support of the transfer function is limited and angularly varying - due to the Gaussian point spread function changing width as the point object is rotated.

7.1.2 Slice-illuminated optical projection tomography transfer function

7.1.2.1 Slice Illumination

In slice-OPT, parallel lines are imaged onto the sample, forming sheets of illumination. Consider a single line of illumination, normal to the rotation axis. If, for simplicity, the illumination and detection point spread functions are assumed to be equivalent (this assumption is invalid due to the Stokes shift), the illumination at the sample is

$$\begin{aligned} I\left(x, x_l, t, s\right) &= \delta\left(x - x_l\right) * \left|h\left(x, t, s\right)\right|^2 \\ &= \int_{-\infty}^{\infty}\int_{-\infty}^{\infty} \delta\left(x - x' - x_l\right)\left|h\left(x', t', s\right)\right|^2 \mathrm{d}x'\mathrm{d}t' \\ &= \int_{-\infty}^{\infty} \left|h\left(x - x_l, t', s\right)\right|^2 \mathrm{d}t' \\ &= \sqrt{\frac{2}{\pi w^2\left(s\right)}}\exp\left(-\frac{2\left(\left(x - x_l\right)^2\right)}{w^2(s)}\right), \end{aligned} \tag{7.9}$$

where x_l is the distance of the sheet from the origin. The striped projection formed is

$$\begin{aligned} p_s(x, x_l, t, \theta) &= \int_{-\infty}^{\infty}\int_{-\infty}^{\infty}\int_{-\infty}^{\infty} \delta\left(x - x', t - t' - t\left(\theta\right), s' - s\left(\theta\right)\right) \\ &\quad \sqrt{\frac{2}{\pi w^2\left(s'\right)}}\exp\left(-\frac{2\left(\left(x - x' - x_l\right)^2\right)}{w^2(s')}\right)\left|h\left(x', t', s'\right)\right|^2 \mathrm{d}x'\mathrm{d}t'\mathrm{d}s' \\ &= \sqrt{\frac{2}{\pi w^2\left(\theta\right)}}\exp\left(-\frac{2x_l^2}{w^2(\theta)}\right)\left|h\left(x, t - t\left(\theta\right), s\left(\theta\right)\right)\right|^2 \\ &= \sqrt{\frac{2}{\pi w^2\left(\theta\right)}}\exp\left(-\frac{2x_l^2}{w^2(\theta)}\right) p\left(x, t, \theta\right). \end{aligned} \tag{7.10}$$

An x-normal slice-illuminated projection, p_x, is then recovered by scanning the illumination and using a synthetic aperture to select the illuminated plane

$$\begin{aligned} p_x(x, t, \theta) &= \int_{-\infty}^{\infty} \mathrm{d}x_l p_s\left(x, x_l, t, \theta\right)\delta\left(x - x_l\right) \\ &= \sqrt{\frac{2}{\pi w^2\left(\theta\right)}}\exp\left(-\frac{2x^2}{w^2(\theta)}\right) p\left(x, t, \theta\right) \\ &= \left(\frac{2}{\pi w^2\left(\theta\right)}\right)^{3/2}\exp\left(-\frac{2\left(2x^2 + \left(t - t\left(\theta\right)\right)^2\right)}{w^2(\theta)}\right). \end{aligned} \tag{7.11}$$

Comparing equation 7.11 to equation 7.7 it can be seen that the synthetic projection is changed in two ways. Firstly, the intensity has been reduced by a factor $w(\theta)$, due to rejection of light. Secondly, the resolution is improved by $\sqrt{2}$ in the direction normal to the illumination line. A similar expression can be found for lines normal to the transverse axis:

$$p_t(x, t, \theta) = \left(\frac{2}{\pi w^2\left(\theta\right)}\right)^{3/2}\exp\left(-\frac{2\left(x^2 + 2\left(t - t\left(\theta\right)\right)^2\right)}{w^2(\theta)}\right). \tag{7.12}$$

These projections lead to reconstruction modulation transfer functions, P_x and P_t;

$$\begin{aligned} P_x\left(x,k_u,k_v\right) &= \frac{2}{\pi w^2\left(\theta+\theta_0\right)}\exp\left(-\frac{4x^2}{w^2(\theta+\theta_0)}\right)\exp\left(-\frac{\pi^2\left(k_u^2+k_v^2\right)w^2(\theta+\theta_0)}{2}\right), \\ P_t\left(x,k_u,k_v\right) &= \frac{2}{\pi w^2\left(\theta+\theta_0\right)}\exp\left(-\frac{2x^2}{w^2(\theta+\theta_0)}\right)\exp\left(-\frac{\pi^2\left(k_u^2+k_v^2\right)w^2(\theta+\theta_0)}{4}\right). \end{aligned} \tag{7.13}$$

This derivation is identical to that used for confocal illumination and detection, and therefore makes the same unreasonable assumption of infinitely narrow slits. The digital mask used in slice-OPT has a finite size, and discrete scan step. The benefits observed cannot be as strong as suggested here without pixel reassignment [159], but these derivations indicate the principle of operation of slice illumination and detection.

7.1.3 Structured illumination and confocal line detection

Conventional OPT is successful with larger samples because it can optically section with widefield illumination; optical scattering only degrades the imaging, not the illumination. Using structured illumination patterns can remove this advantage, and care must be taken in choosing what method to recover an improved projection.

At a certain depth, the structure applied to the illumination will be fully demodulated over the illumination's path into and the emission's path out of the sample. If structured illumination detection is used, all signal from this depth will be discarded. However, with confocal detection, this signal is retained – reduced in intensity by a factor equal to the number of scan positions, compared to widefield imaging. Therefore, confocal detection allows a compromise between improved reconstruction quality where the illumination is still modulated, and widefield signal from regions where the illumination is no longer modulated.

7.2 Hardware and operation

7.2.1 Hardware

A schematic of the slice-OPT set-up is shown in Figure 7.3. Laser radiation at 561 nm (Jive, Cobolt) was coupled into a multimode optical fiber (MMF) by lens L1 (M43L02, Thorlabs, $f = 30\ mm$), collimated using lens L2 (AC f 100, Linos, $f = 100\ mm$) and directed to uniformly illuminate a digital micromirror device (DMD) with $1920 * 1080$ 7.56 μm pixels (DLP Lightcrafter 6500, TI) with laser speckle being averaged out by vibrating the MMF. The full field of the DMD was imaged onto the sample, via a dichroic filter D (Di03-R488/561, Semrock), using a telecentric imaging relay comprising achromatic lenses, L3 and L4 (AC508-300-A-ML, $f = 300\ mm$ and AC508-500-A-ML, $f = 500\ mm$, Thorlabs) with an adjustable aperture stop AP (SM2D25D, Thorlabs) in the Fourier plane. The excited fluorescence was imaged using a commercial 0.5x magnification telecentric lens (TL) with an adjustable aperture (TECHSPEC SilverTL, Edmund Optics), onto a CCD camera (Clara, Andor) via an emission filter to block

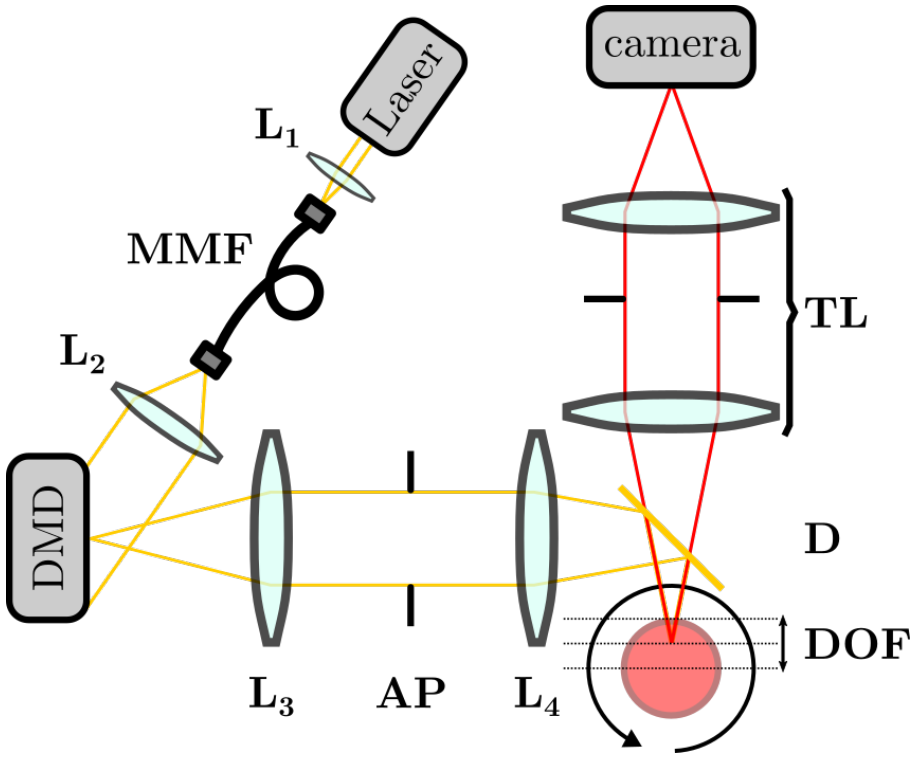

Figure 7.3: Slice-OPT set-up. Gratings were displayed on the DMD, which is imaged onto the sample to illuminate multiple individual slices.

reflected excitation light (BA610IF, Olympus). The excitation and imaging systems were configured with optical axes parallel at the sample and perpendicular to the axis of rotation. Their focal planes were coincident and the excitation and emission DOFs set to 5 mm to cover at least the front half of the sample – giving a diffraction-limited resolution of 25.8 μm. The samples were mounted in FEP tubing (06406-72, Cole-Parmer) and suspended in a water-filled cuvette (704-003-50-10, Hellma Analytics) from a stepper motor (NM11AS-T4, Laser 2000 UK) with tip-tilt adjustment (M-TTN80, Newport Corp) and 3-axis linear translation (M-423 and M-UMR12.63).

7.2.2 Alignment and calibration

The optical axis of the illumination and imaging optics had to be aligned, so that for any given sheet, emission from different depths in the sample was imaged onto the same line on the image plane. To ensure this was the case, a $2 * 2$ mirror spot was displayed on the DMD, which was imaged to form a 25.3 μm spot on a red fluorescent slide (92001, Chroma) – chosen to be approximately equal to the diffraction limit of the imaging optics. As the slide was scanned through the DOF of the imaging optics, any discrepancy between optic axes was seen as movement of the spot on the camera image. The alignment of the illumination optical axis was adjusted using the mounting of the dichroic beamsplitter.

For convenience of data fusion, though not strictly required, the x and y axes of the DMD and CCD were aligned at the sample. The alignment was assessed by displaying a grating on

the DMD, which was again imaged onto the red fluorescent slide. The emitted fluorescence was imaged onto the CCD. Taking the Fourier transform of this image, the angle of the DMD relative to the CCD was determined from the positions of the Fourier peaks. The angle of these was minimised by adjusting the DMD mount with pieces of shim.

7.2.3 Acquisition and reconstruction software

To illuminate individual slices, binary gratings were displayed on the DMD. These were formed of columns of "on" DMD pixels that were two micromirrors wide – 25.3 μm at the sample – separated by a number of pixels depending on the scattering properties of the sample; the slices must be separated enough such that there is no cross-talk between them, but larger separation increases the acquisition time unnecessarily. Figure 7.1 (**a**) shows a schematic of a sample with a few slices simultaneously illuminated. The fluorescence imaged onto the camera carried signal from the illuminated slices, but unwanted cross-talk from neighbouring slices was also present (figure 7.1 (**b**)). This spurious signal was rejected with a digital mask on the CCD (figure 7.1 (**b**)), which only accepted fluorescence emanating from the expected slices. A complete slice illuminated projection was built up by repeating the process with a set of L grating patterns that scan the illumination across the sample – each translated by one DMD pixel (12.65μm at the sample) for Nyquist sampling.

The system was controlled using scripts written for MicroManager. The sample was rotated to a number of equally spaced angles around 360°. At each of these, a slice-illuminated projection image data set was acquired by displaying each of the set of grating patterns on the DMD and recording an image on the camera. By discretising equation 7.10, the set of striped projections is expressed as $p_s(l, n_\theta)$ – where l is the pattern index in L total patterns, s is the slice separation, and n_θ is the angle index in N_θ angles.

To convert the raw slice-illuminated images into projections for reconstruction, the locations of the slices in the CCD recordings needed to be determined. This required a mapping between the DMD axes $\{x_{DMD}, y_{DMD}\}$ and CCD axes $\{x_{DMD}, y_{DMD}\}$, which could be determined *a priori* using a calibration measurement on a test object, or by using the raw data to calibrate itself. For the pre-acquisition calibration, a fluorescent dye filled FEP tube was used as a phantom. Individual 2 micromirror wide slices were displayed on the DMD and the resulting fluorescence recorded on the camera (figure 7.4a). The range of slices displayed on the DMD started at the 100th pixel and extended to the 1000th in 20 pixel increments – this covered the range that was within the FOV of the CCD. The calibration images were processed in MATLAB. After loading, each column of the images was summed to give a 1D intensity measurement for each slice position (figure 7.4b). To remove background, the median of the 1D measurements was subtracted (figure 7.4c). Then the location of the maximum of those 1D measurements was found. Finally, a linear fit was applied between the known DMD slice positions and measured CCD positions (figure 7.4d).

Self-calibration of a data set was suitable if the fluorescence extends through the sample – for example the vasculature in an adult zebrafish. For each l, the MIP of $p_s(l, n_\theta)$ was taken over n_{theta} (figure 7.5a). Then this signal was averaged along y_{CCD}, which gave an intensity

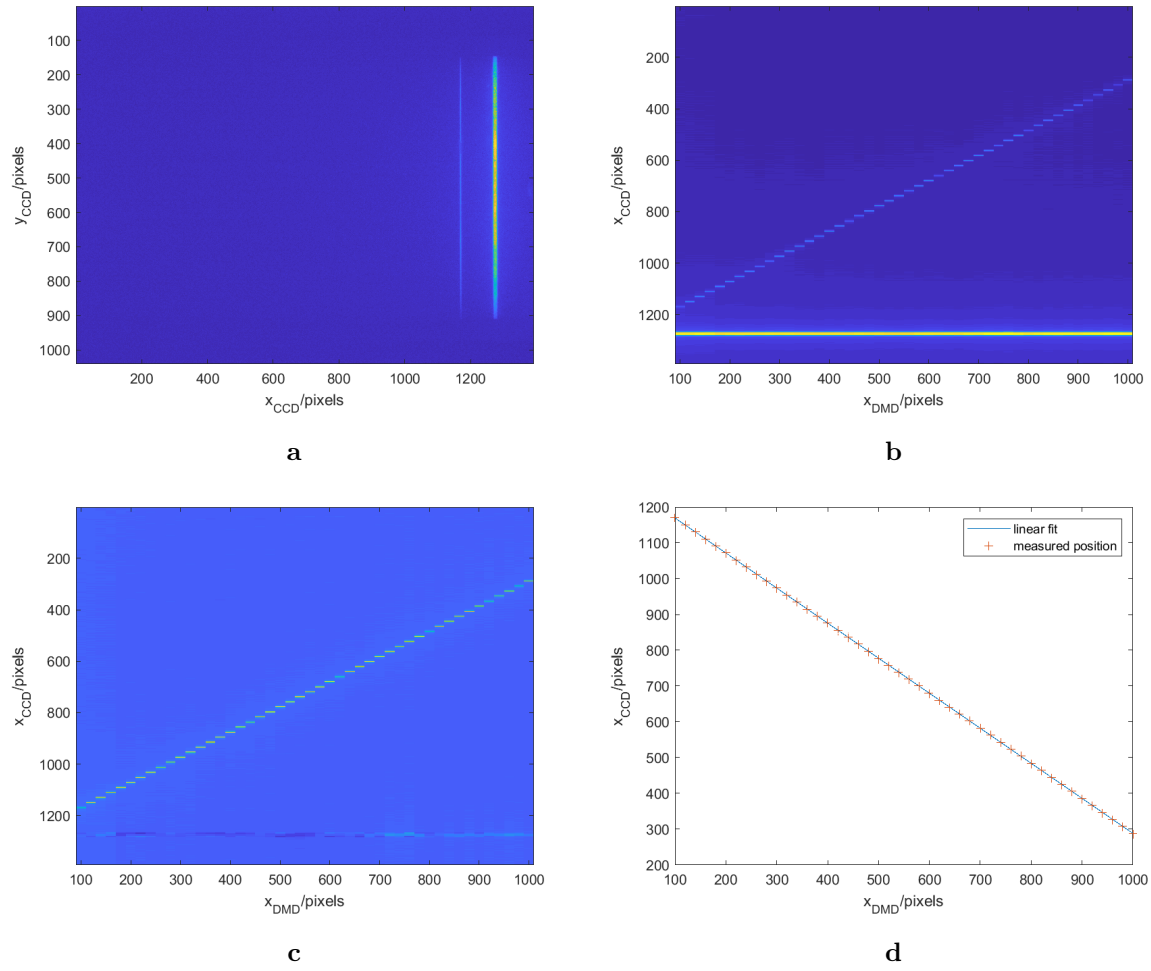

Figure 7.4: Calibration of mapping between DMD and CCD pixel positions using a test object calibration data set. (**a**) Raw camera image of fluorescent target illuminated with a two pixel wide slice. The fluorescence from the slice was imaged onto approximately the 1170th pixel column of the camera, the bright feature further along x_{CCD} was caused by reflection off the housing of the DMD. (**b**) The raw images for each slice position are averaged along y_{CCD}. (**c**) The median of the intensity map in the x_{DMD} direction was subtracted from each column to remove constant background features. (**d**) The location of the maximum of each column was used to fit the mapping between DMD and CCD pixel positions.

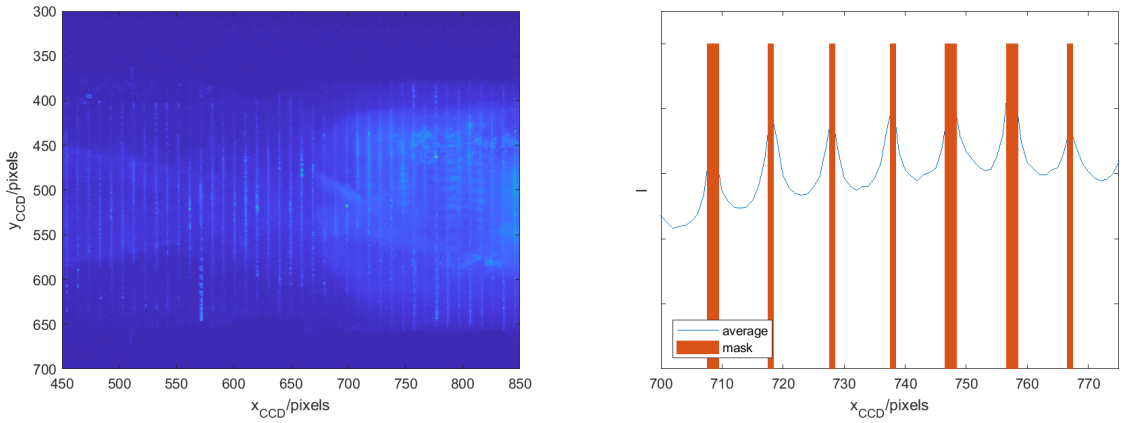

a **b**

Figure 7.5: Self calibration of mapping between DMD and CCD pixel positions. (**a**) MIP of images of a zebrafish OPT taken with a particular illumination pattern. (**b**) The MIP is averaged along y_{CCD}, the fundamental of the grating is subsequently identified using the Fourier transform, and used to create the transmission mask. To avoid stripe artifacts, some lines of the mask are two pixels wide

profile in x_{CCD} (figure 7.5b). To recover the illuminating grating, the Fourier transform of the intensity profile was taken, and the fundamental of the grating identified.

For both methods, masks $M(l)$ were created by including columns that were within 0.75 pixels of the predicted slice locations – which were either from the direct mapping of the *a priori* calibration or the peaks of the fundamental for self calibration. This synthetic slit width was the smallest that did not produce aliasing artifacts.

For each angle, slice-illuminated projections were calculated by averaging over the masks:

$$p(n_\theta) = \frac{\sum_{l=1}^{L} p_s(l, n_\theta) M(l)}{\sum_{l=1}^{L} M(l)}. \tag{7.14}$$

Pseudo-widefield projections were calculated by summing the raw projections together without masking:

$$p_w(n_\theta) = \sum_{l=1}^{L} p_s(l, n_\theta). \tag{7.15}$$

Volumes were reconstructed from well-sampled projection data sets using FBP, as described in chapter 3.4.3, and from undersampled data sets using TwIST, as described in chapter 4.2.3.3.

7.3 Characterisation on fluorescent beads in a scattering agarose phantom

The slice-OPT system was tested on a phantom of fluorescent beads (0.02 μm, Crimson 625/645 nm, Invitrogen) suspended in a 3D scattering medium of 2% agarose, with scattering provided by a 0.15% by volume suspension of microspheres (Plain 1990nm, PL-Microspheres). The

phantoms were made in a 1.5 *ml* tube (11926955, Fisher Scientific), giving it an approximately cylindrical shape, 8 *mm* diameter and 2 *cm* in length.

The phantom was imaged with 64 projection OPT, acquired with widefield and slice-illumination with slice separations of 50 μm, 75 μm, 100 μm, 125 μm, and 150 μm – corresponding to 4, 6, 8, 10, and 12 pixels on the DMD, which is also equal to the number of scan positions necessary to achieve Nyquist sampling. The integration time for each image was 500 *ms*, resulting in slice-OPT imaging times of 128 *s*, 192 *s*, 256 *s*, 320 *s*, and 384 *s*. It is important to keep in mind that the improvement to reconstruction quality comes at the cost of imaging speed; the need to scan the illumination pattern to acquire the full projection image increases the acquisition time with slice separation. The slice-illuminated projections were demodulated using the *a priori* method described in section 7.2.3.

Figure 7.6 shows MIPs through a three-pixel, 40 μm thick section of scattering bead phantom volume, reconstructed from widefield and 150 μm slice-separation slice-OPT. The contrast of the widefield reconstruction is reduced by spurious low spatial frequency intensity caused by optical scattering. The slice-OPT reconstruction does not have this additional background, the only signal visable is from the beads. The MIP through multiple slices is to ensure the same beads are visible in both images. The axial extent of objects is reduced by the slice illumination and detection, as shown in figure 7.7.

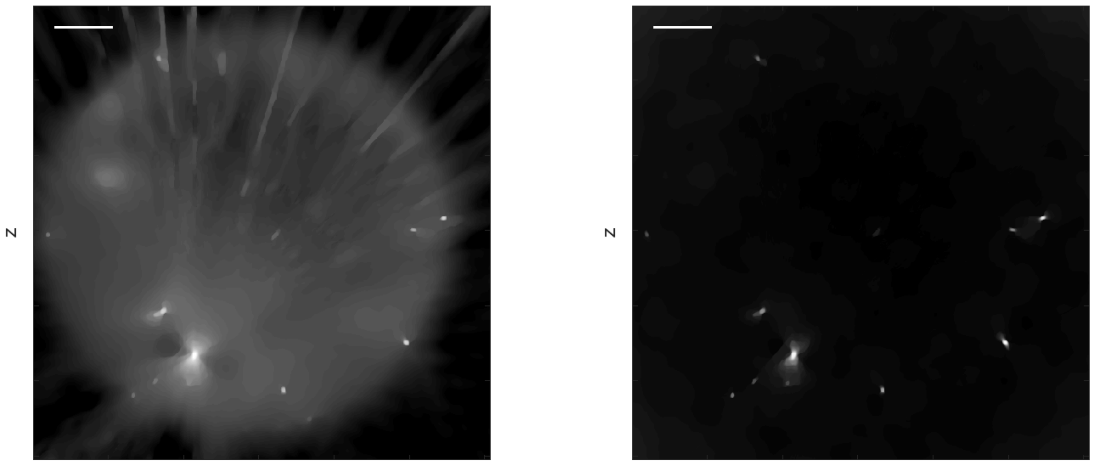

a **b**

Figure 7.6: 40 μm thick zy slice of scattering bead phantom reconstructed from (**a**) widefield OPT and (**b**) 150 μm slice-separation slice-OPT projections. A logarithmic intensity scale has been used to highlight background features. Scalebar 1 *mm*

Figures 7.6 and 7.7 show how slice-OPT improves reconstructions in a scattering sample. The diffuse background of low spatial frequency signal is reduced, providing better contrast, and the local blurring from weakly scattered photons is reduced in the axial direction. To quantify this improvement across the volume, the average radial spatial frequency power spectra were calculated:

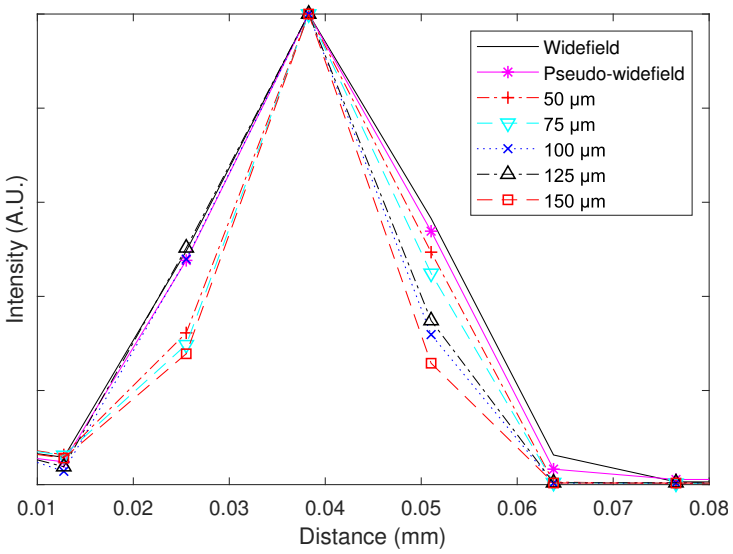

Figure 7.7: Line profile through the MIP of a single bead within the volume of a scattering bead phanton, along the x axis, reconstructed with widefield OPT and slice-OPT with different slice separations. The confocal line illumination and detection reduces the degradation to the PSF caused by optical scattering. Adapted from [6].

$$\rho(k_r) = \frac{1}{4\pi}\int_0^{2\pi}\int_0^{\pi}(1-\exp(-(\sigma k_r)^2))^2 FT[I]\sin k_\theta \mathrm{d}k_\theta \mathrm{d}k_\phi, \tag{7.16}$$

where I is the 3D intensity distribution of the sample, FT is the 3D Fourier transform, and k_r, k_θ, and k_ϕ are the 3D spatial frequencies in spherical coordinates. The first term is a high pass filter ($\sigma = 0.54\ mm^{-1}$) to remove any DC offset in the reconstruction. Figure 7.8 shows $\rho(k_r)$ for the different slice separations investigated. The reduction in degradation caused by scattering can be seen by the increased power at higher spatial frequencies with increasing slice separation up to 125 μm. Included in figures 7.7 and 7.8 is the volume reconstructed from pseudo-widefield projections, using equation 7.15. The results for widefield and pseudo-widefield OPT reconstructions are similar. Therefore, during *in vivo* experiments, widefield data was not acquired so that acquisition time and photobleaching was minimised.

To choose the optimal slice separation, a metric is derived based on $\rho(k_r)$, which measures the enhancement of the spatial frequencies in the top half of the support of the NA:

$$\text{enhancement} = \frac{\int_{k_{nyquist}/4}^{k_{nyquist}/2}\rho(k_r)\mathrm{d}k_r}{\int_{k_{nyquist}/4}^{k_{nyquist}/2}\rho_0(k_r)\mathrm{d}k_r}, \tag{7.17}$$

where $k_{nyquist}$ is the Nyquist sampling frequency, and ρ_0 is the radial spatial frequency power spectrum of the widefield reconstructed volume. Figure 7.9 shows how the enhancement of the contribution of high spatial frequencies increases with slice separation, up to 125 μm.

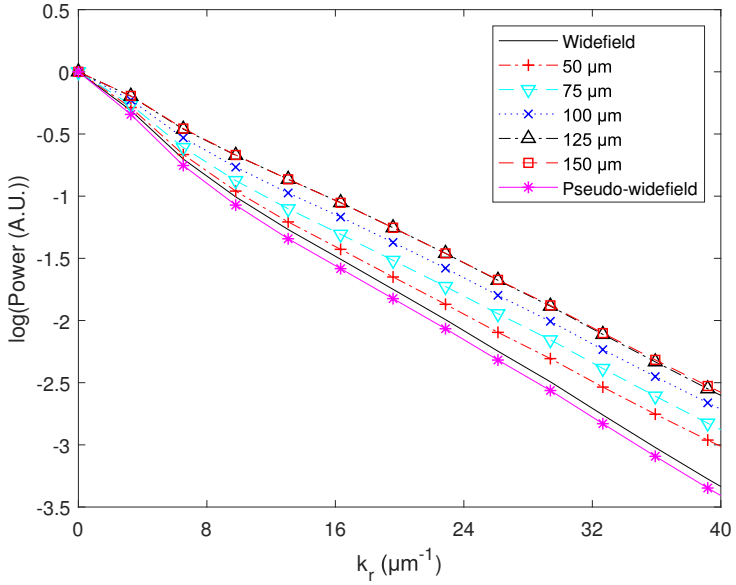

Figure 7.8: Radial spatial frequency power spectrum of scattering bead phantom volumes reconstructed with widefield OPT and slice-OPT with different slice separations. As the slice separation is increased spurious low spatial frequency information, caused by inter-pixel cross-talk, will be rejected – increasing the proportion of high spatial frequency information in the reconstruction. Adapted from [6].

7.4 Application to *in vivo* imaging

To demonstrate the reduction in image degradation due to scattering, a slice-OPT accquisition was performed on a terminally anaesthetised juvenile zebrafish (line described in chapter 4.2.2), 56 days post fertilisation. This model expresses mCherryFP in its vasculature, which was imaged in this study.

Acquisitions were performed with slice separations of 75 μm, 100 μm, and 125 μm, corresponding to 6, 8, and 10 pixels on the DMD. To minimise imaging time, pseudo-widefield projections – described in section 7.2.3 – were calculated using equation 7.15 on the 75 μm data. Also, 32 μm, and 50 μm acquisitions were calculated from 75 μm and 100 μm separated slice-OPT projections using

$$\text{for } l \in [L/2],\ p_{s/2}(l, n_\theta) = p_s(l, n_\theta) + p_s(l + L/2, n_\theta). \tag{7.18}$$

Figure 7.10 shows a comparison between pseudo-widefield and 100μm-separated slice illuminated projections. Details are clearer in the slice illuminated projection – for example in the brain – due to the rejection of some lower spatial frequency scattered light. These more detailed projections produce better reconstructions, as can be seen in the MIPs shown in figure 7.11 and orthogonal slices in figure 7.12.

To quantify this performance, we again make use of equations 7.16 and 7.17 – the results of which are plotted in figure 7.13. Compared to the scattering phantom results shown in figure 7.9, the maximum enhancement is similar within errors but occurs for a smaller slice separation

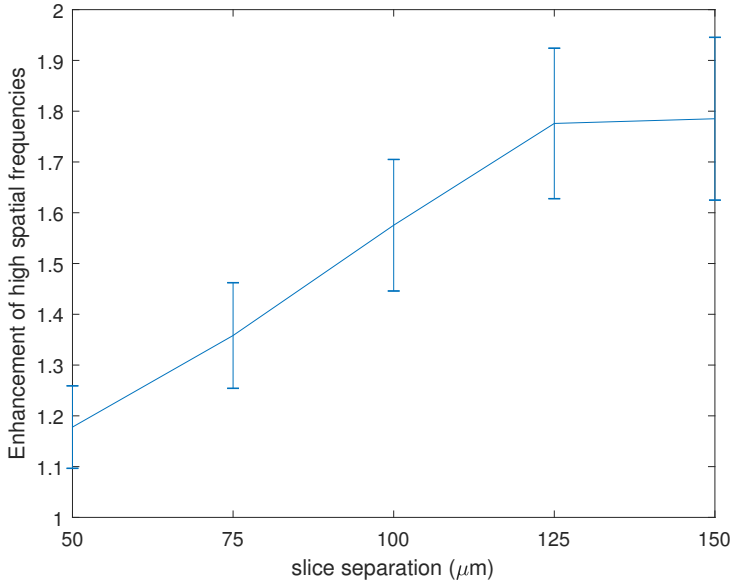

Figure 7.9: Enhancement of high spatial frequencies (equation 7.17) with increasing slice separation and acquisition time for slice-illuminated OPT applied to a scattering phantom. The rejection of spurious low spatial frequency signal increases with slice separation at the cost of imaging speed. Above ten times slower there is no additional benefit. Adapted from [6].

of 100 μm.

7.5 Conclusion

The reconstruction quality of *in vivo* OPT is limited by the blurring effects of optical scattering. Slice-OPT was developed to address this degradation in resolution. In the 2D projections (figure 7.10) and reconstructed volume MIPs (figure 7.11), the improvement to contrast is apparent, which has been quantified using equations 7.16 and 7.17 (figure 7.13b).

However, the cross-sectional images through the reconstructed volumes, e.g. figures 7.12e and 7.12f, show that this enhancement is occuring near the surface of the scattering sample. The camera used in the slice-OPT system inevitably has a finite dynamic range, a proportion of which is used up by scattered photons. As the imaging depth increases, the proportion of ballistic photons will fall beneath the noise floor. At that point, digital rejection of scattered photons cannot produce an improved image.

The slice-OPT and pseudo-widefield reconstructions, shown in figures 7.11 and 7.12, present complimentary contrast. In this chapter the spurious signal was rejected. However, this structure might be used to model the scattering properties of the sample.

As with C-HDR-OPT, Slice-OPT is equally applicable to imaging with longer wavelengths, where the improvements to image quality and imaging depth could be combined. The technique could also be applied to *ex vivo* cleared tissue; chemical clearing removes a large portion of refractive index inhomogeneities, but some remain. Slice-OPT could be applied to larger cleared samples, where the residual optical scattering impacts the reconstruction quality. Slice-OPT is

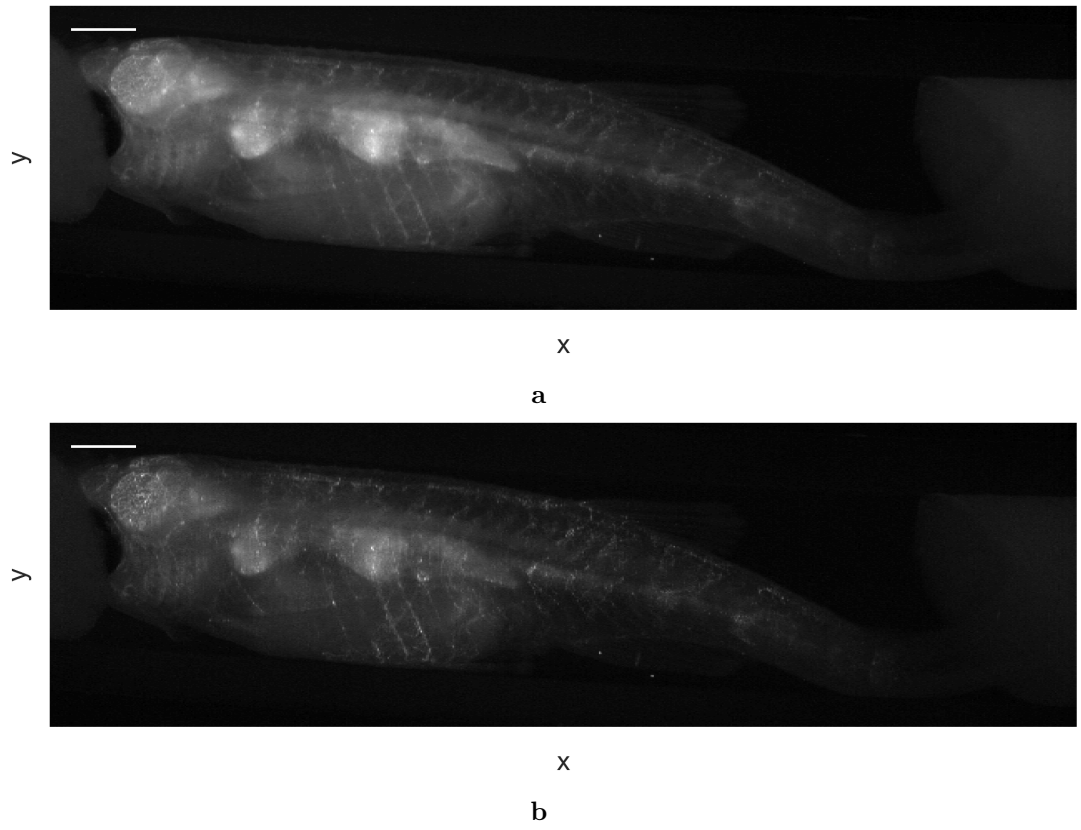

Figure 7.10: Projections used for OPT reconstructions: (**a**) pseudo-widefield projection (**b**) slice-illuminated projection. Scalebar 1 mm

unlikely to be compatible with C-HDR-OPT in adult zebrafish; some modulation is maintained in a back-scattering geometry, but in transmission it will be completely lost – adding a time cost without any benefit to contrast.

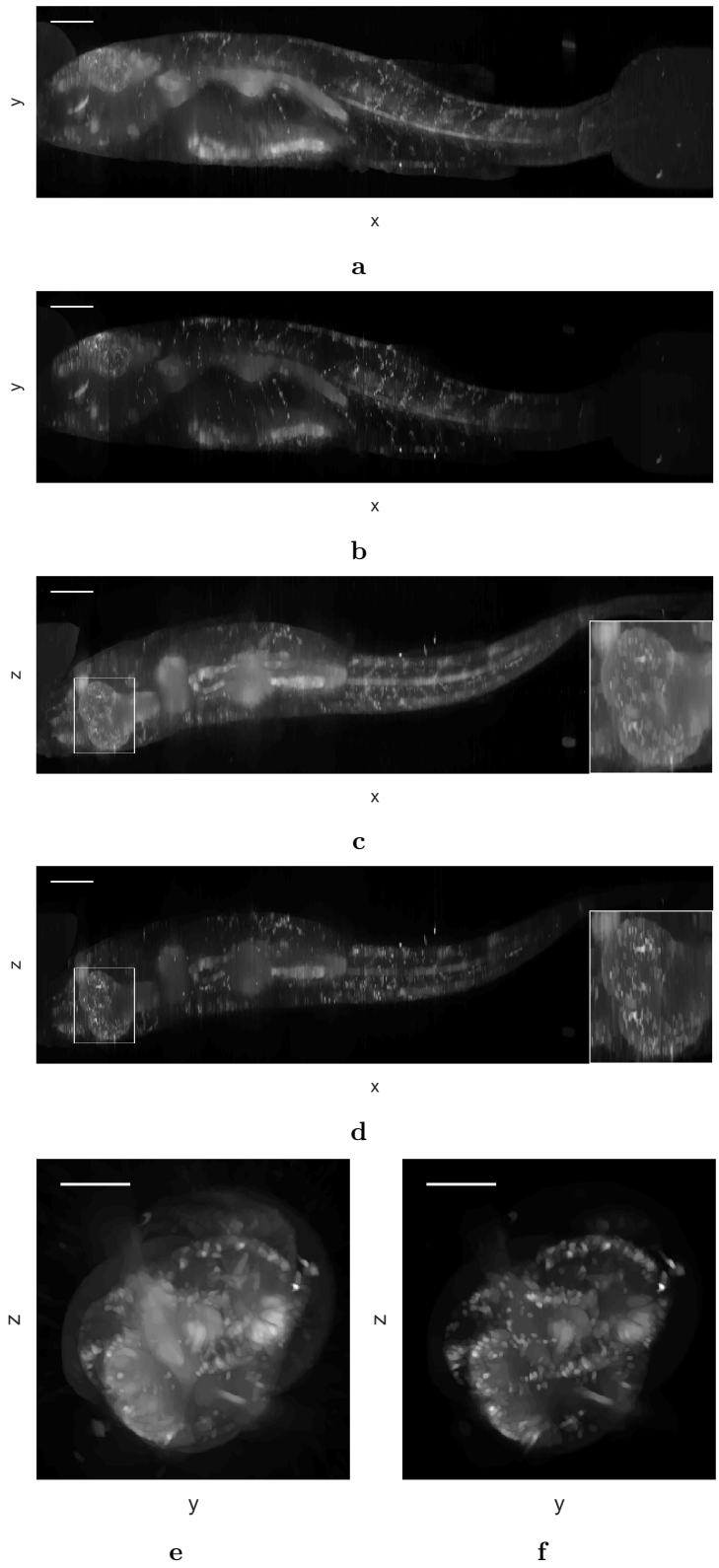

Figure 7.11: MIPs of *in vivo* juvenile zebrafish volumes reconstructed from (**a**), (**c**), (**e**) pseudo-widefield and (**b**), (**d**), (**f**) slice-illuminated projections, along the (**a**), (**b**) z axis, (**c**), (**d**) y axis, and (**e**), (**f**) x axis. Inset on (**c**) and (**d**) shows a region of interest around the brain. A logarithmic intensity scale is used. Scalebar 1 mm

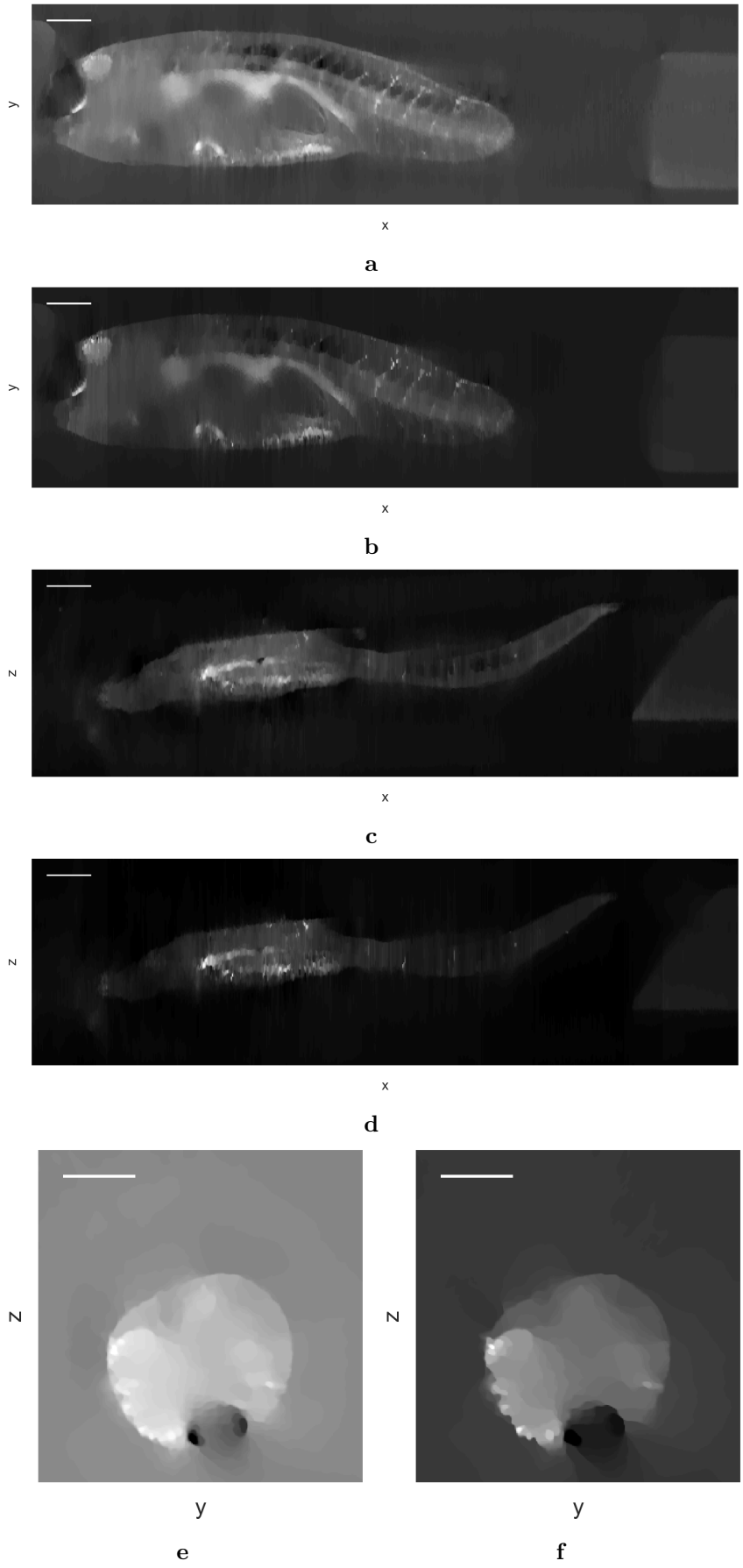

Figure 7.12: Orthogonal slices through *in vivo* juvenile zebrafish volumes reconstructed from (**a**), (**c**), (**e**) pseudo-widefield and (**b**), (**d**), (**f**) slice-illuminated projections. (**a**), (**b**) *xy* plane, (**c**), (**d**) *xz* plane, and (**e**), (**f**) *yz* plane. A logarithmic intensity scale is used. Scalebar 1 *mm*

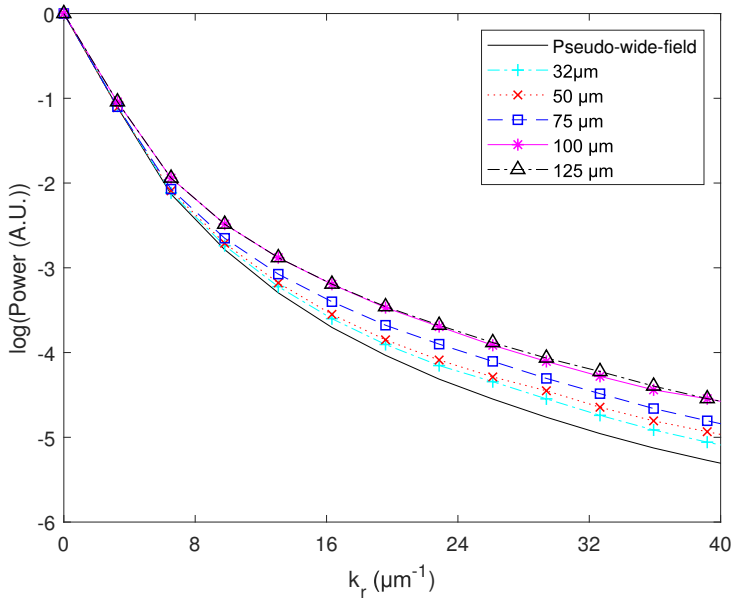

a

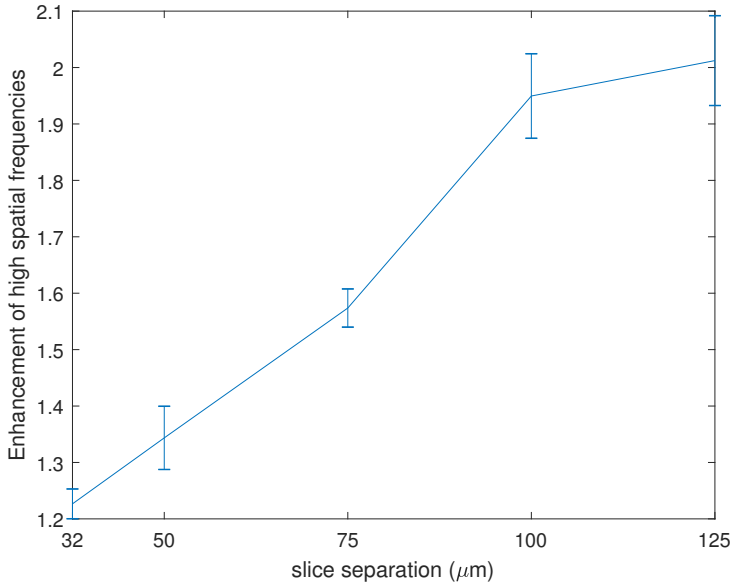

b

Figure 7.13: (**a**) Radial spatial frequency power spectrum of juvenile zebrafish volumes reconstructed with widefield OPT and slice-OPT with different slice separations. (**b**) Enhancement of high spatial frequencies (equation 7.17) with increasing slice separation and acquisition time. The rejection of spurious low spatial frequency signal increases with slice separation at the cost of imaging speed. Above 8 times slower there is no additional benefit. Adapted from [6].

Chapter 8

Single pixel optical projection tomography

This chapter describes work in progress developing single pixel camera based OPT, with the motivation to develop OPT systems that can work with radiation at wavelengths beyond the spectral response of silicon-based detectors.

Slice-OPT (chapter 7) was able to reject scattered light and gave improved contrast in regions near the surface of the sample. However, it did not significantly improve the imaging depth over conventional OPT. Measurement systems have finite dynamic range, an increasing proportion of which is used up by scattered photons when imaging thicker samples. Even if all scattered photons are successfully rejected, no ballistic signal will be seen if it has been reduced below the noise floor by optical scattering.

As discussed in chapter 2, the scattering coefficient of tissue decreases monotonically with wavelength from ultraviolet, through the visible, and into the infrared. As longer wavelengths are used, the proportion of ballistic signal at the detector will increase. Above 1350 nm the absorption coefficient of water sharply increases, which defines the edge of the exploitable low-scattering NIR window – where the scattering will be lowest, and absorption isn't impractically high. The region between 1000 nm and 1350 nm, referred to as near infrared II or short-wave infrared (SWIR) light, has been used for multiphoton excitation [160, 161], and imaging with epifluorescence [162–164] and light sheet [165] to achieve greater imaging depths.

Unfortunately, the responsivity of conventional silicon based cameras falls away rapidly above 1000 nm. Pixelated detectors based on SWIR responsive InGaAs and Ge are rapidly falling in price, but remain prohibitively expensive for widespread adoption. Single pixel cameras offer a lower cost alternative [166–168]. The object is imaged onto a spatial light modulator such as a digital micromirror device (DMD), which reflects light from its "on" pixels onto a photodetector. As the test function (a random binary image) displayed on the DMD is changed, the variation of the intensity on the photodetector forms a set of linear equations that can be solved to recover the image.

Single pixel cameras can be equivalently implemented by projecting the test functions onto the object; the DMD is placed in the illumination optics and a "bucket" detector collects

light from the sample [169]. With an illumination single pixel camera, the measurement is only affected by optical scattering on the illumination path. With an imaging single pixel camera, the measurement is only affected by optical scattering on the imaging path. The choice of implementation depends on where the greater degree of optical scattering is expected to occur. Examples of systems that can exploit lower scattering on the illumination path are temporally focused multi-photon microscopes [170] and opthalmascopes [171]. Illumination single pixel cameras also benefit from rejection of scattered light on the illumination path – in a similar manner to structured illumination [172]; the demodulated component of the image is rejected [173].

This chapter describes progress in the development of a single-pixel OPT (SP-OPT) system for low cost 3D SWIR imaging. Section 8.1 describes the function of a single pixel camera. Section 8.2 explains the theory of SP-OPT. Section 8.3 desribes the experimental set-up, acquisition, and reconstruction. Section 8.4 describes the imaging of a bead phantom. Potential methods to reduce acquisition time and increase dynamic range are discussed in section 8.5 Finally, section 8.6 discusses the system, and the necessary changes for *in vivo* application.

8.1 Single Pixel Camera

Instead of directly recording the spatial distribution of intensity at the image plane, a single pixel camera measures M inner products, $z_m = \phi_{mn} y_n$, between an N pixel image, y_n, and a set of test functions, ϕ_{mn} – where m and n are the test function and pixel indices respectively. These test functions are implemented with a DMD, the mirrors of which are mapped to the pixels, n, of y_n and ϕ_{mn}. All pixels that are on – corresponding to $\phi_{mn} = 1$ – reflect light from the object to be collected onto a photodetector. As the patterns displayed on the DMD are changed, the intensity measured on the photodetector will vary – providing information about the spatial distribution of the intensity at the DMD.

Test functions often require values of ± 1, which are implemented by first displaying a binary pattern for positive pixels, ϕ_{mn+}, then switching to a binary pattern for the negative values, ϕ_{mn-}:

$$\phi_{mn+} = \begin{cases} 1, & \text{if } \phi_{mn} = 1 \\ 0, & \text{if } \phi_{mn} = -1 \end{cases}, \phi_{m,n,-} = \begin{cases} 0, & \text{if } \phi_{mn} = 1 \\ 1, & \text{if } \phi_{mn} = -1 \end{cases}. \tag{8.1}$$

This produces an unsigned measurement, $z_{unsigned}(s, m)$, of size $2M$ (M positive test functions and M negative), with sign subscript s. Then,

$$z(m, \theta) = z_{unsigned}(+, m) - z_{unsigned}(-, m). \tag{8.2}$$

Combining the image pixels into a $N \times 1$ vector Y, the measurements into a $M \times 1$ vector Z, and the test functions into a $M \times N$ matrix Φ, Z can be recovered by solving

$$Z = \Phi Y. \tag{8.3}$$

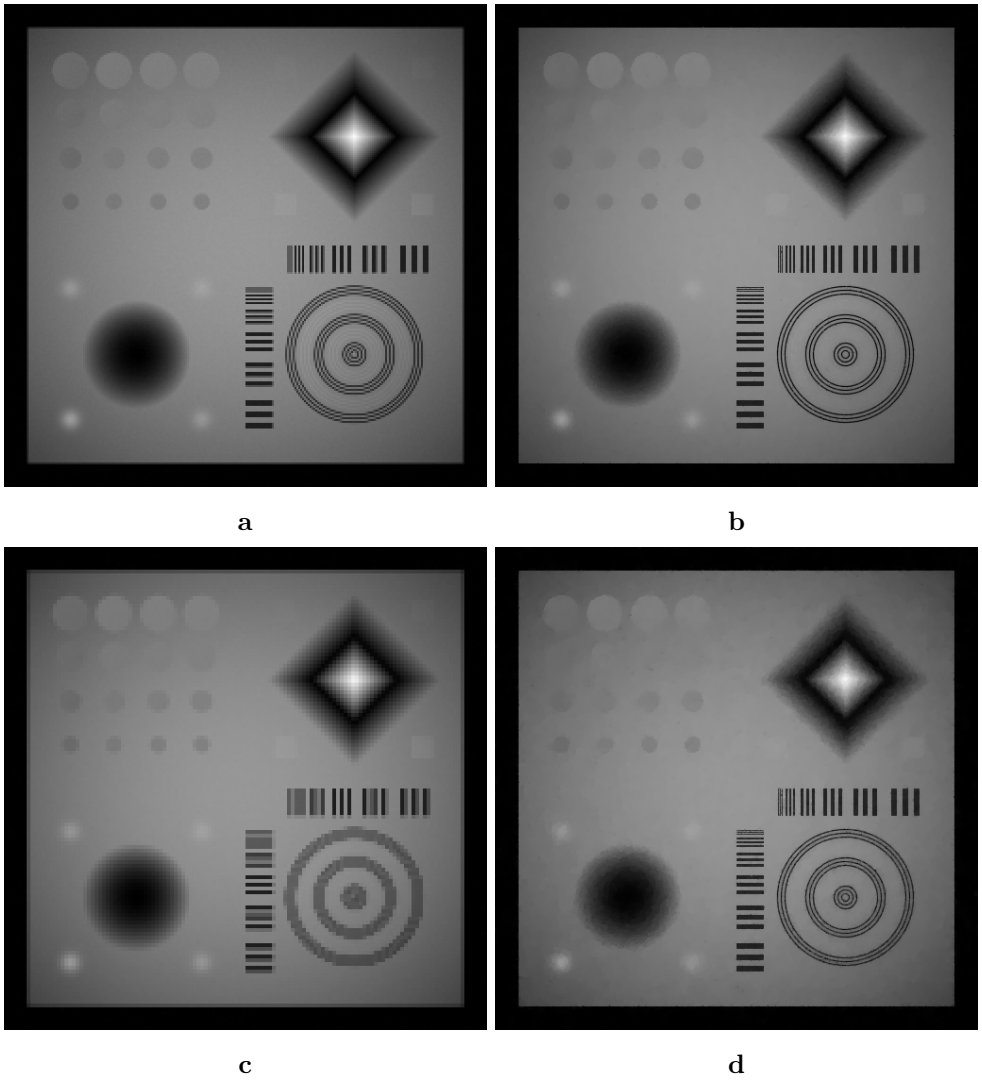

Figure 8.1: Demonstration of compressed sensing single pixel reconstruction on a (**a**),(**b**) 4x undersampled and (**c**),(**d**) 16x undersampled simulated measurement of a test chart: (**a**),(**c**) Low resolution images of the object can be acquired analytically with a complete set of low resolution Hadamard test functions, (**b**),(**d**) or the object can be reconstructed using an incomplete set of higher resolution test functions.

If $M < N$ the system of linear equations are underdetermined, and there are infinite solutions for Y. However, a close approximation can be found using compressive sensing (chapter 3.5). Figure 8.1 shows a simulated $N = 512 \times 512$ pixel object measured with $M = 256 \times 256$ and 128×128, reconstructed analytically at the lower resolution set by M, and at full resolution with IST (chapter 3.5) by solving

$$minimise_Y \frac{1}{2} \|Z - \Phi Y\|_2^2 + \tau\Phi(Y), \tag{8.4}$$

using TV regularisation, with a regularisation parameter of $\tau = 0.005$. The simulated single pixel measurement was given a signal to noise ratio of $4 * 10^{-5}$ to match the specifications of the amplified photodiode used (section 8.3.1).

The choice of test function basis, Φ, has a significant effect on the reconstruction speed and quality [174]. Using a Gaussian or Bernoulli distributed random matrix for Φ can achieve good results. However, these quickly become impractical for higher resolution measurements – as the requirements on memory and computation scale as N^2. Deterministic bases, such as Fourier or Hadamard, are far more practical – as they do not have to be stored in memory, and their transforms can be performed with efficient Cooley-Tukey type algorithms, that scale as $N\log N$.

The Fourier basis performs well, and is convenient in magnetic resonance imaging, where it is the natural basis of the measurement [175]. However, implementing Fourier measurements with a DMD requires temporal or spatial dithering [176, 177]. The binary Hadamard basis is a more natural choice for a DMD based system. Some care has to be taken when mapping between pixel index n and the position in the image; if the mapping is direct, the coherence between the Hadamard basis and the sparse domain – either TV or wavelet – will be particularly strong, and lead to reconstruction artifacts (figure 8.2a). However the order of pixels can be randomly permuted before applying the Hadamard transform to reduce this effect (figure 8.2b).

In chapter 4.2.3.3, TV regularisation was used with compressed sensing OPT. But there are other choices to consider; the performance of using TV or wavelet regularisation with single pixel imaging is shown in figure 8.3. TV regularisation out-performs wavelet compression for all cases, so shall continue to be used.

8.2 Mathematical representation of single pixel optical projection tomography

Single pixel imaging can be extended to 3D with time of flight measurements [178]. However, depth resolution was limited to 3 mm by the speed of the detector in this work. Instead, a 3D single pixel system can be created by replacing the camera in an OPT system with a DMD and bucket detection – creating a SP-OPT system. The measurement model then combines projection of a 3D volume to a set of 2D angular projections, and sampling of those angular projections onto a set of single pixel measurements. This can be expressed as

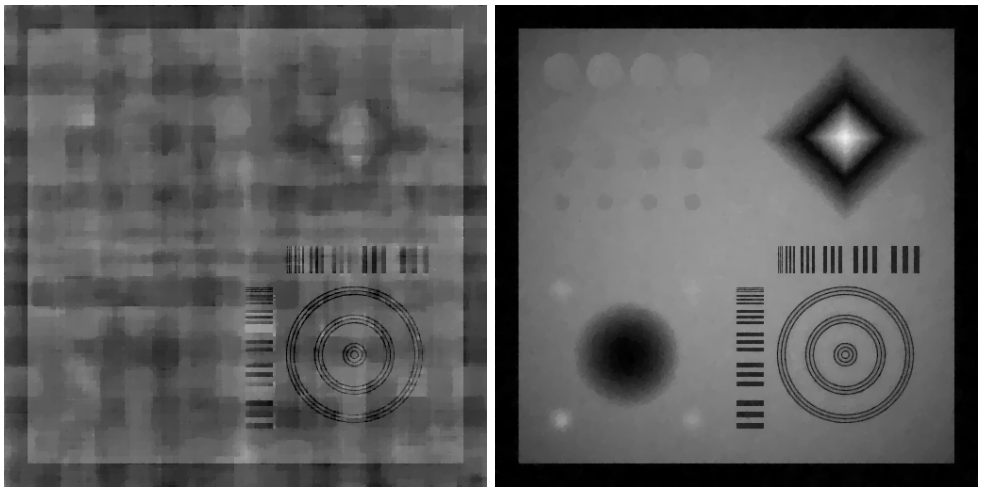

a **b**

Figure 8.2: Sampling considerations for single pixel reconstruction of a 4x undersampled acquisition: (**a**) If the positions of pixels are not randomly permuted before sampling with Hadamard test functions, the reconstruction is corrupted by artifacts. (**b**) Randomly permuting the positions of each pixel before Hadamard transforming, and re-ordering after inverse Hadamard transforming removes this artifact.

$$\begin{aligned} Z &= \Phi Y \\ &= \Phi R X \\ &= A X \end{aligned} \tag{8.5}$$

where: Z is the set of single pixel measurements, Y is the set of 2D angular projections, R is the Radon transform, A is the combined forward transform, and X is the set of voxel values.

For well sampled data, equation 8.5 can be solved by first solving equation 8.3 for each projection then using the inverse Radon transform, R^T, on each slice of the projection data set. For undersampled data, Z can be found by solving the optimisation problem

$$minimise_X \frac{1}{2} \|Z - AX\|_2^2 + \tau \Phi_{TV}(X), \tag{8.6}$$

where the first term is the l_2 norm of the residual, τ is the regularisation parameter, and Φ_{TV} is the total variation regularisation functional:

$$\Phi_{TV}(X) = \sum_i \sqrt{(D_i^0)^2 + (D_i^1)^2 + (D_i^2)^2} \tag{8.7}$$

where D_i^j is the gradient of X at i in the jth direction.

Equation 8.6 can be solved using the compressive sensing algorithm iterative shrinkage thresholding (IST):

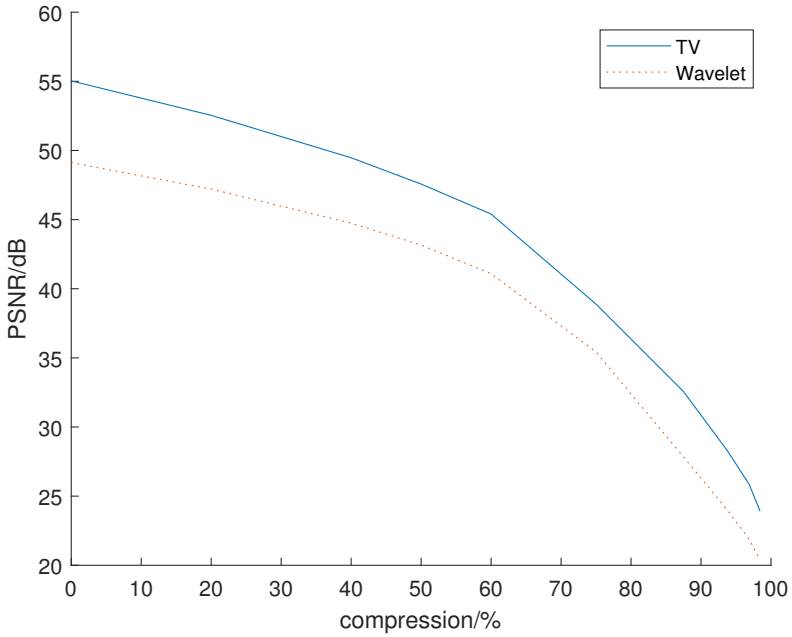

Figure 8.3: Single Pixel regularisation: Reconstruction quality, calculated using the PSNR metric introduced in chapter 5, produced using TV and wavelet regularisation with varying degrees of compression, $(1 - M/N)$.

$$\begin{aligned} X_0 &= \Psi_\tau(A^T Y), \\ X_{t+1} &= \Psi_\tau(X_t + A^T(Y - AX_t)), \end{aligned} \tag{8.8}$$

for $t > 0$, where A^T is the combined inverse operator and Ψ_τ is the total variation denoising operator. A^T is implemented by first calculating the least squares solution to equation 8.3 for each angle, and taking the inverse Radon transform of each sinogram of the resulting set of angular projections.

CS assumes that the measurement model is linear. This is not the case for brightfield OPT; the volume of absorption coefficients is linear with the logarithm of the intensity in the projections:

$$\ln(Y) = RX. \tag{8.9}$$

CS can still be applied to processing undersampled absorption SP-OPT data, but the problem must be broken into two seperate optimisation problems: first equation 8.4 is solved using IST, then the logarithms of the resulting projections are used to solve 3.12 using TwIST, as described in chapter 4.2.3.3.

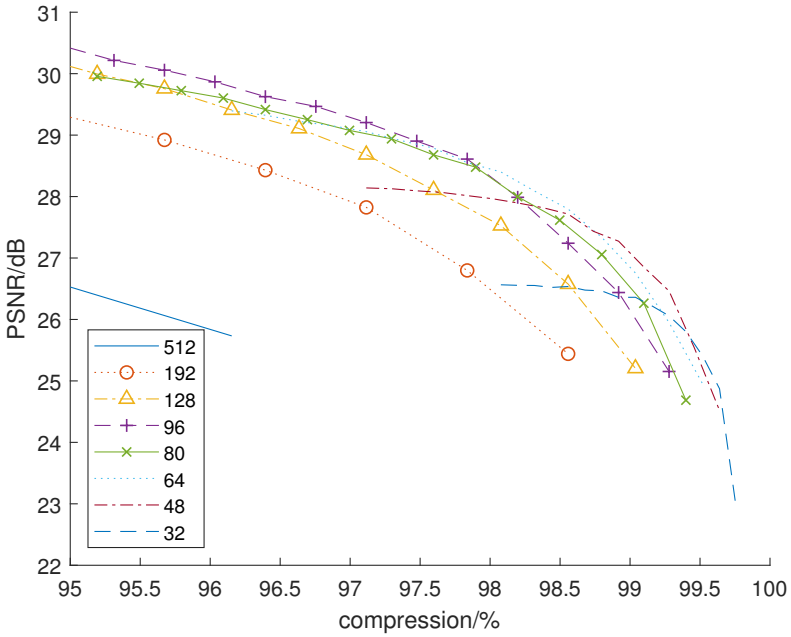

Figure 8.4: Variation of PSNR with degree of compression, $1-M/N*N_\theta/\pi$, between a simulated phantom and the IST reconstruction (equation 8.8) produced from SP-OPT measurements. Each line is of constant N_θ and varying M.

8.2.1 Undersampling in the 2D case

Before generalising to 3D samples it's worth exploring the compressibility of a SP-OPT acquisition of an $N \times N$ 2D slice. The PSNR for simulated single slice reconstructed using equation 8.8 with different numbers of projections and numbers of test functions is shown in figure 8.4.

For a given compression level, given by $1 - M/N * N_\theta/\pi$ where N_θ is the number of angular projections, the best choice of undersampling of angles and patterns is variable.

8.3 Hardware and operation

8.3.1 Single-pixel optical projection tomography experimental set up

The SP-OPT system consisted of illumination, sample mounting, imaging optics, and DMD and bucket detection – shown in figure 8.5. Excitation light was produced by a supercontinuum laser (WL-SC400-6, NKT Photonics) between 400 nm and 2500 nm. Light longer than 1400 nm was filtered out using longpass filters F_1 and F_2 (FELH1500 and FELH1400, Thorlabs) in reflection. SWIR light was then spectrally selected by a 1250 nm longpass filter F_3 (FELH1250, Thorlabs). The beam was directed to holographic diffuser, H (ED1-C50, Thorlabs), placed in the back focal plane of a fresnel lens, L_1 (FRP251, $f = 50\ mm$, Thorlabs). A further ground glass diffuser, G, was placed between the diffuser and the fresnel lens to control spatial coherence; the DMD is a blazed diffraction grating, so spatially coherent illumination would be diffracted in different directions for different test functions.

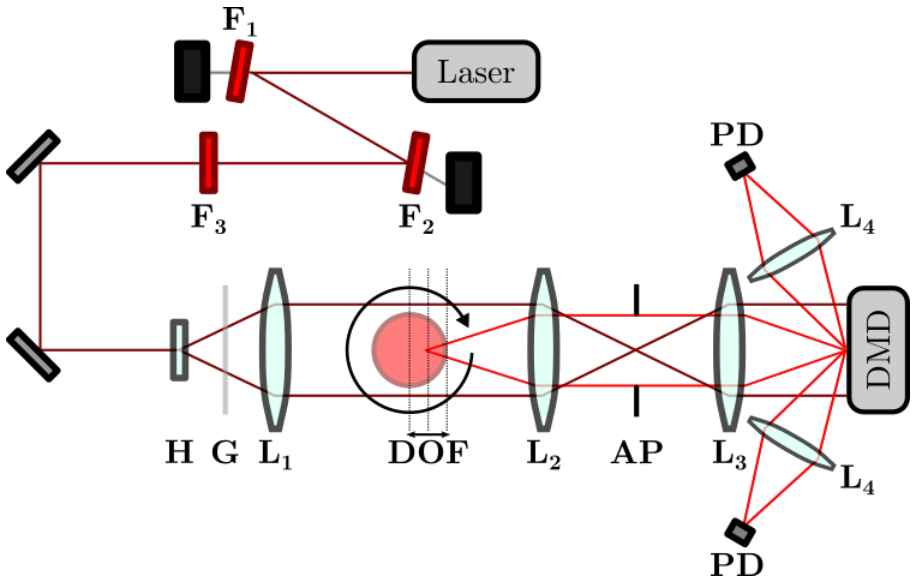

Figure 8.5: SP-OPT system set-up. Instead of a camera, the sample is imaged onto a DMD, the reflections from which are collected by two bucket detectors.

The samples were suspended in a water-filled cuvette (704-003-50-10, Hellma Analytics) from a stepper motor (NM11AS-T4, Laser 2000 UK) with tip-tilt adjustment (M-TTN80, Newport Corp) and three-axis linear translation (M-423 and M-UMR12.63).

The sample was imaged onto the DMD (DLP LightCrafter 6500, Texas Instruments), with 7.56 μm pixels, using a 0.5× telecentric imaging relay comprising achromatic lenses, L2 and L3 (AC508-400-C-ML, $f = 400\ mm$ and AC508-200-C-ML, $f = 200\ mm$, Thorlabs), with an adjustable aperture stop AP (SM2D25D, Thorlabs) in the Fourier plane. Light reflected off the "on" and "off" pixels of the DMD was collected by two condenser lenses, L_4 (ACL50832U, $f = 32mm$, Thorlabs) onto two photodiodes, PD (PDA50B2, Thorlabs). The triggering signals of the DMD and output voltage of the photodiode were recorded using an analogue to digital converter (NI USB 6363,Texas instruments).

The aperture stop diameter was set to an NA of 0.023, which at 1250 nm gives a DOF of $4mm$ and diffraction limited resolution of 33.1 μm – which is adequately sampled by the DMD when using full 1024×1024 resolution. If lower resolutions are used the resolution is pixel limited.

8.3.2 Single-pixel optical projection tomography data acquisition

8.3.2.1 Test function videos

The number of test functions, M, scales with the number of pixels in the image, N. For resolutions up to $64 \times 64 = 4096$ pixels – with sufficient undersampling – M can be as small as a few hundred. At this size the binary test functions can be directly loaded onto the memory on the DMD module and displayed at the maximum frame rate – 9,523 Hz. However, for desirable resolutions of $512 \times 512 = 262144$ pixels, this is not possible. Instead, the DMD must

be controlled with a video stream.

When the DMD is attached to a computer as a monitor it displays 24 bit colour images using temporal dithering; the image is composed of 24 binary images – one for each bit plane – displayed for different lengths of time. When displaying conventionally, the display time doubles for each bit plane within a colour; the second bit plane is displayed for twice as long as the first. In that way, integrated over the frame length, a frame appears like a 24 bit colour image. However, the DMD module can be programmed to display each bit plane for an equal length of time, giving a test function rate of 24×60 Hz $= 1440$ Hz, which corresponds to a fully sampled acquisition time of 6 minutes for a 512×512 image.

Test function videos were created in Matlab. In any give frame, the colour of each pixel encodes which of the 24 test functions it will be "off" or "on" for. For example, if a pixel is going to be on, off, on, off, off, on, on, off for the first 8 test functions of a frame, that pixel's red channel will be set to $1 * 2^0 + 0 * 2^1 + 1 * 2^2 + 0 * 2^3 + 0 * 2^3 + 1 * 2^5 + 1 * 2^6 + 0 * 2^7 = 101$. The effect for the first frame of a set of hadamard test functions is shown in figure 8.6.

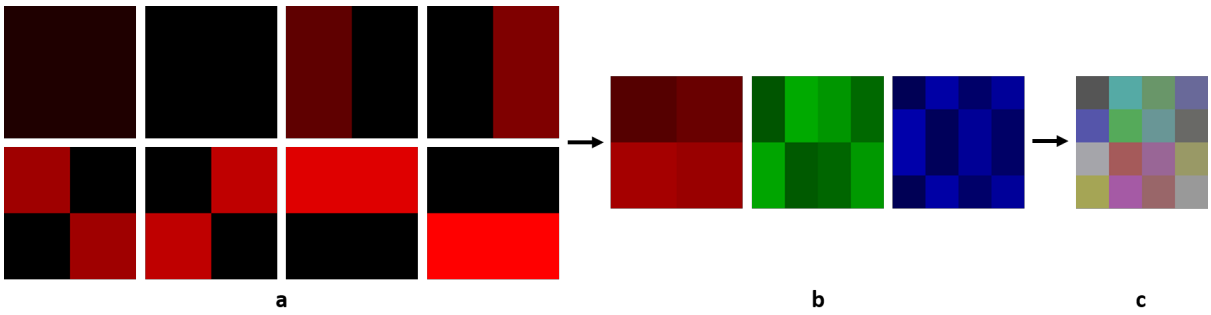

Figure 8.6: Frame encoding: Binary test functions are sent to the DMD, packaged in 24 bit color images. (**a**) The intensity of each set of eight test functions is set to occupy a bit plane of an 8 bit monochromatic image. (**b**) Three of these monochromatic images form the red, green, and blue channels of a (**c**) 24 bit RGB frame

8.3.2.2 Diagonal mounting

The axis of rotation of each micromirror is at 45° to the axes of the micromirror array. For laser safety and alignment considerations it is desirable to have this axis vertical in lab-space, so that reflections off "on" and "off" mirrors stay in the plane of the optical bench. This results in the axes of the DMD being aligned 45° to lab-space. To avoid spending time in the acquisition on pixels that will subsequently be cropped off to create lab-space projections for reconstruction, the pixels of the single pixel measurement are defined as rectangles arranged in such a way to make a square array at 45° to the DMD array (figure 8.7).

8.3.2.3 Frame synchronisation

Using the DMD as a monitor allows for arbitrarily long sets of test functions. Unfortunately, this not only comes at the cost of reduced display speed, but also display reliability. The

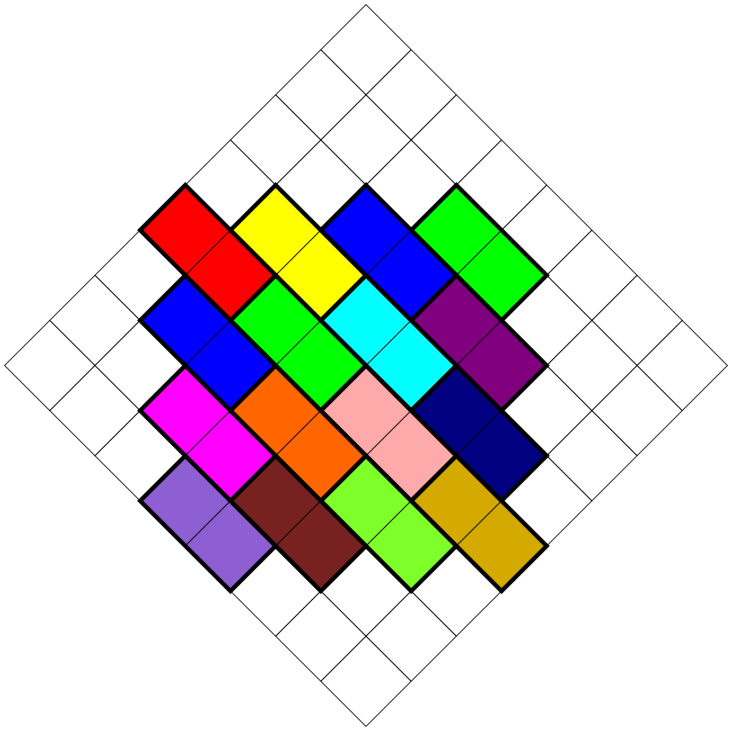

Figure 8.7: A 4x4 pixel arrangement, defined on an 8x8 mirror array, aligned at 45°, where colours indicate different pixels.

process of loading a video frame into memory, and sending for display by the GPU does not consistently occur within the 16 ms window given by the 60 Hz refresh rate. When this happens, the frame displayed on the DMD will not change – leading to a loss of synchronisation. This is, in principle, detectable by measuring the times between GPU buffer flips. However, how the system recovers from this loss of synchronisation is inconsistent. If the nth frame is not sent to be displayed, and the $(n-1)$th frame is displayed twice, two things may occur. In some instances the system will recover by entering a new, delayed synchronisation by displaying the nth frame and continuing, but in others the nth frame will be skipped entirely and the system will catch up to the old timing (figure 8.8).

To ensure that a frame's location in the sequence can be identified during processing, a bit plane per frame is dedicated to synchronisation, which has all the pixels "on". For any given test function, approximately half the pixels will be turned on. Signals measured will be very close to half the total intensity in the image, with a small change around this value depending on the precise structure of the image. If all 24 bit planes are dedicated to test functions, the signal for the frame will look like random noise around this average value. For synchronisation, one of the bit planes has all its pixels turned on – producing a significantly larger signal. This synchronisation bit plane's position within the 24 bit image is increased by one each frame, so that the location of the frame can be easily identified – modulo 24. This creates a 4% drop in imaging speed, as only 23 of the 24 bit planes are displaying new test functions.

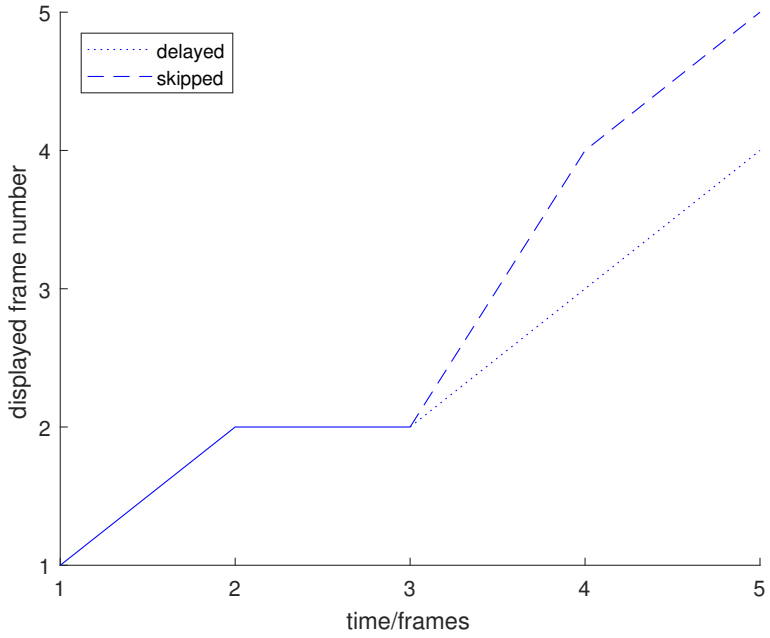

Figure 8.8: Frame desynchronisation: After displaying the first two frames correctly, the third is not sent in time and the second continues to display instead. After recovering, the system may catch up, by skipping the third frame, or it will display the third frame and enter a new delayed timeline. This creates an ambiguity about which frame is currently being displayed after these events.

8.3.2.4 Acquisition Software

The system was controlled using software written in Python. Single pixel acquisitions were taken at a number of equally spaced angles over a full rotation. The DMD was set to display each bit plane for 680 μs – the maximum length that enables a 60 Hz frame rate. At each angle the test function video is played and the voltages from the amplified photodiode and DMD triggers are recorded at 67500 samples per second – corresponding to 46 measurements per test function.

8.3.3 Reconstruction software

Volume reconstruction was performed using MATLAB. The voltages from the two photodiodes were differenced, and divided by the sum to account for power fluctuations. Using the DMD trigger pulses (figure 8.9), photodiode voltage data were grouped by frame, and binned by bit plane. At high enough detection bandwidths, the pixel reset pulse can be seen as a spike of high and low voltage – these values were removed before averaging over the bin. Padding frames, acquired before and after the video, were identified by the lack of signal, and removed. The synchronisation bit planes were identified as the maximum signal in the frame, and used to determine the correct frame number. Once the true position was identified for each frame, the data were assigned indices s and m. Repeat measurements, either from display problems

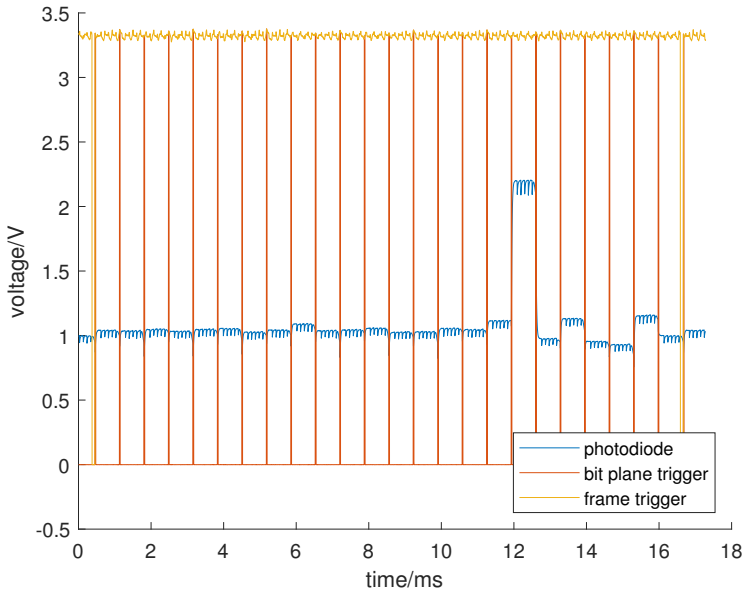

a

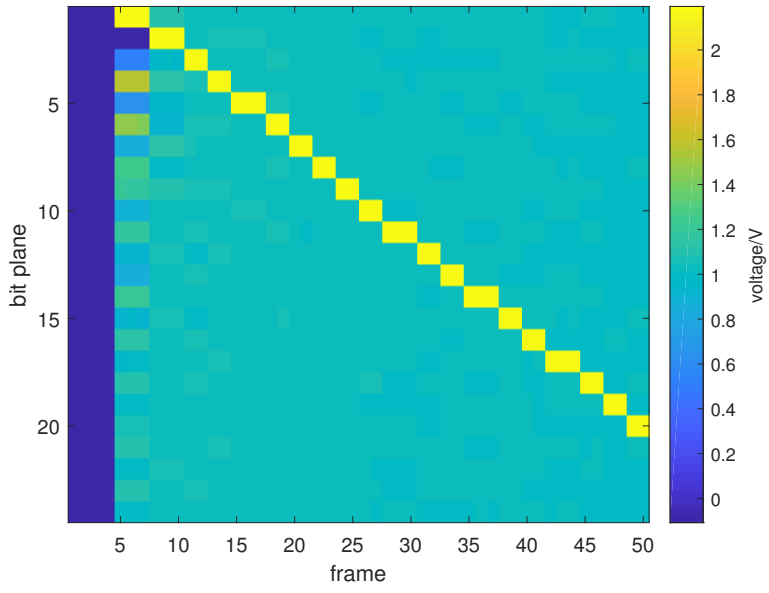

b

Figure 8.9: Extracting Y from raw data: (**a**) voltages recorded from the photodiode and DMD hardware transistor–transistor logic output triggers. The DMD bit change and frame change triggers are used to bin the data. (**b**) Data binned by frame and bit plane. The synchronisation bit can be seen as the brightest bin in each frame

or videos with repeating frames, were averaged over. If a missing frame caused a positive or negative measurement to lose its complement, it was set to zero. Z was then calculated using equation 8.2.

X was reconstructed using equation 8.8. The regularisation parameter τ was empirically selected for each data set.

8.4 System application to a bead phantom

The SP-OPT system was tested on a phantom of absorbing beads (0.02 μm, Crimson 625/645 nm, Invitrogen) suspended in a medium of 2% agarose. The phantoms were made in a 1.5 ml tube (11926955, Fisher Scientific), giving it an approximately cylindrical shape, 8 mm diameter and 2 cm in length.

The sample was imaged with fully sampled transmission single pixel data acquisitions at 50 evenly spaced angular positions around 360°. The test functions had a resolution of 256x256, the pixels of which were made up of 4x2 DMD mirrors, giving the system a pixel limited resolution of 86 μm. Each test function video was 189 s long, giving a total acquisition time of 2.65 hours. Each frame was displayed twice, to ensure all measurements would be available for analytic reconstruction.

Figure 8.10a shows a projection of the phantom reconstructed from a single pixel acquisition. The image quality is limited by laser speckle, which is challenging to remove using despeckling techniques, such as using a vibrating multimode fibre or a rotating diffusor, due to the short exposure time of each test function. Instead a single pixel image of the laser speckle in the absence of an object was acquired (figure 8.10b) for use in a flat-field correction: $y^f_{n\theta} = y_{n\theta}/f_n$, where f_n is the intensity of the n_{th} pixel of the speckle image, and $y^f_{n\theta}$ is the corrected pixel value. The flatfield corrected transmission projection of the phantom is shown in figure 8.10c. Figure 8.10d shows line profiles through the corrected and uncorrected projection images. The correction removes some of the noise in the background. However, the speckle pattern is affected by the refractive index distribution of the object, making the correction less effective.

The measurement model (equation 8.3) can be extended to $Z = \Phi Y \oslash F$, where $\oslash$ is Hadamard division, and equation 8.4 to:

$$minimise_Y \frac{1}{2} \|Z - \Phi Y \oslash F\|_2^2 + \tau\Phi(Y), \tag{8.10}$$

where F is the $N \times 1$ vector of f_n. Projection images of the phantom reconstructed using IST, with $\tau = 0.0125$, using a decreasing number of test functions are shown in figure 8.11. The tolerance of reconstruction quality to undersampling is significantly lower than what is seen for the simulated measurements shown in figure 8.2. The residual speckle over the phantom reduces the gradient sparsity, and therefore compressibility of Y.

Figures 8.12 and 8.13 show MIPs and slices of phantom volumes reconstructed from 50 projections, reconstructed from decreasing numbers of test functions. The reconstruction quality degrades quickly as the number of test functions decreases, with pronounced artifacts near the

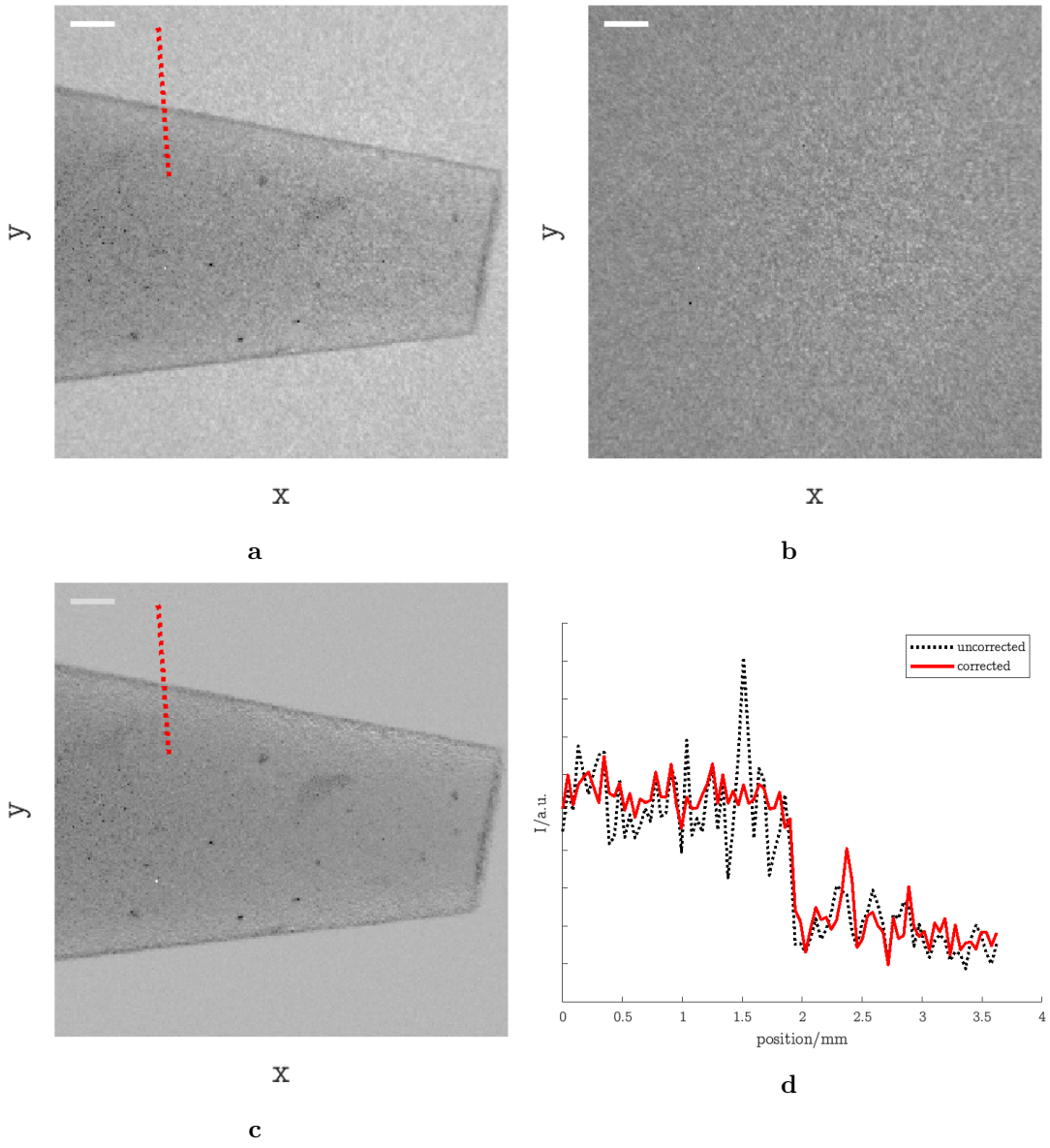

Figure 8.10: (**a**) Analytic reconstruction of a fully sampled bead phantom projection. (**b**) Analytic reconstruction of a fully sampled laser speckle background projection. (**c**) The analytic reconstruction shown in (**a**), after flatfield correction. (**d**) Line profiles, as indicated in (**a**) and (**c**). Scalebar 1 mm.

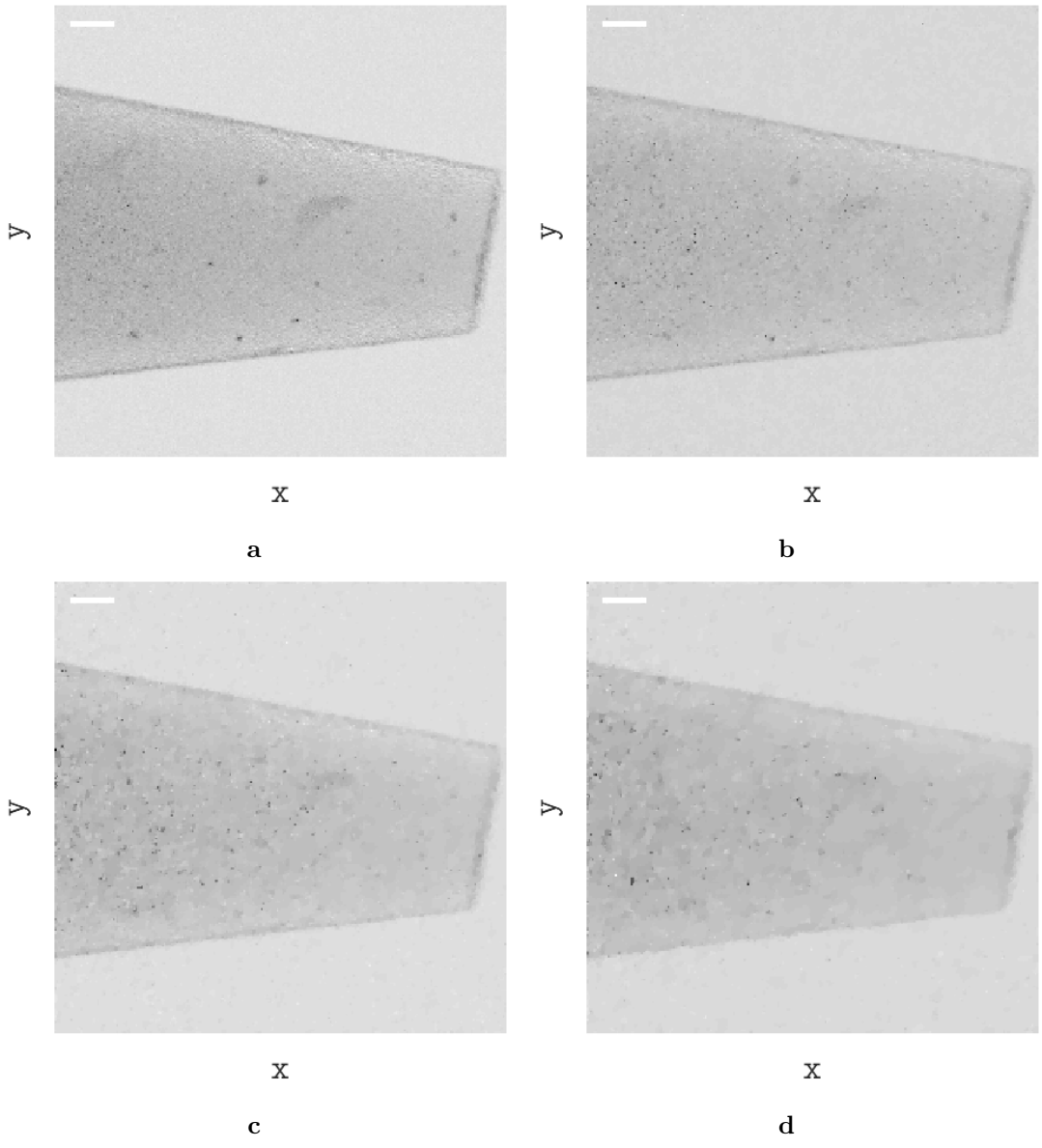

Figure 8.11: IST reconstructions of a bead phantom projection, with (**a**) no undersampling, (**b**) 2x undersampling, (**c**) 5x undersampling, and (**d**) 10x undersampling.

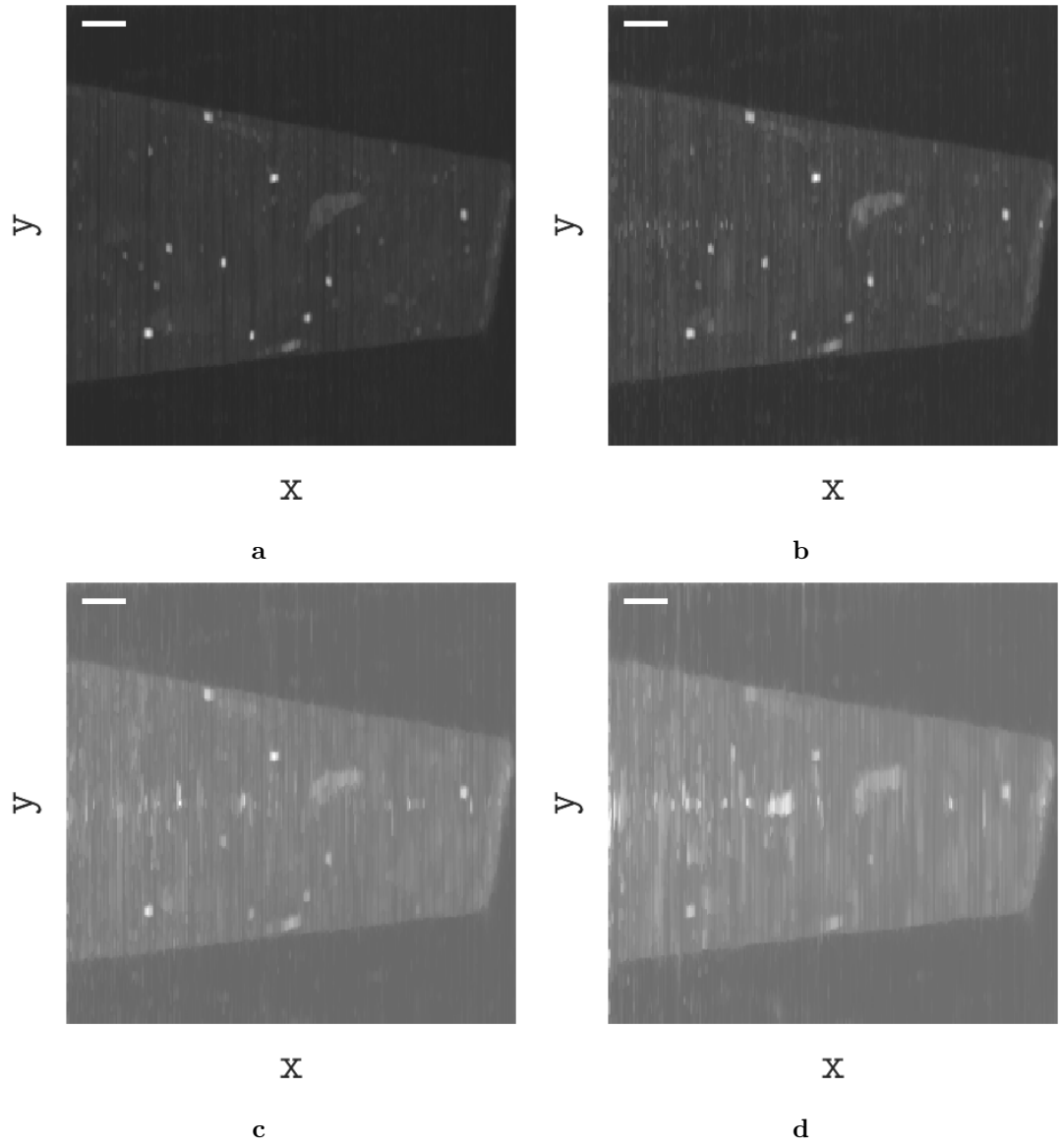

Figure 8.12: MIPs of bead phantom volumes reconstructed using TwIST from projections reconstructed using IST from single pixel data, with (**a**) no test function undersampling, (**b**) 2x test function undersampling, (**c**) 5x test function undersampling, and (**d**) 10x test function undersampling.

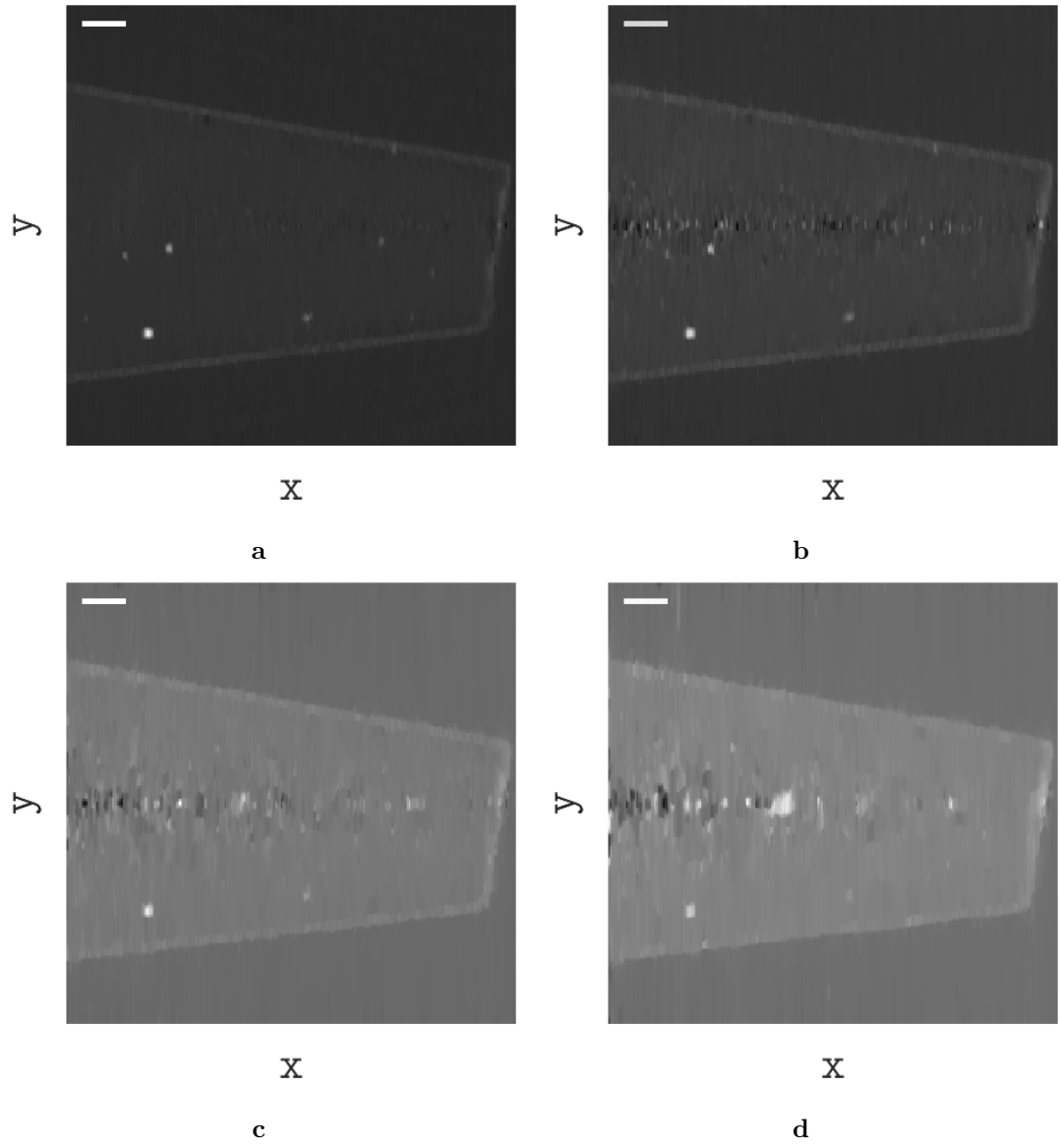

Figure 8.13: Slices of bead phantom volumes reconstructed using TwIST from projections reconstructed using IST from single pixel data, with (**a**) no test function undersampling, (**b**) 2x test function undersampling, (**c**) 5x test function undersampling, and (**d**) 10x test function undersampling.

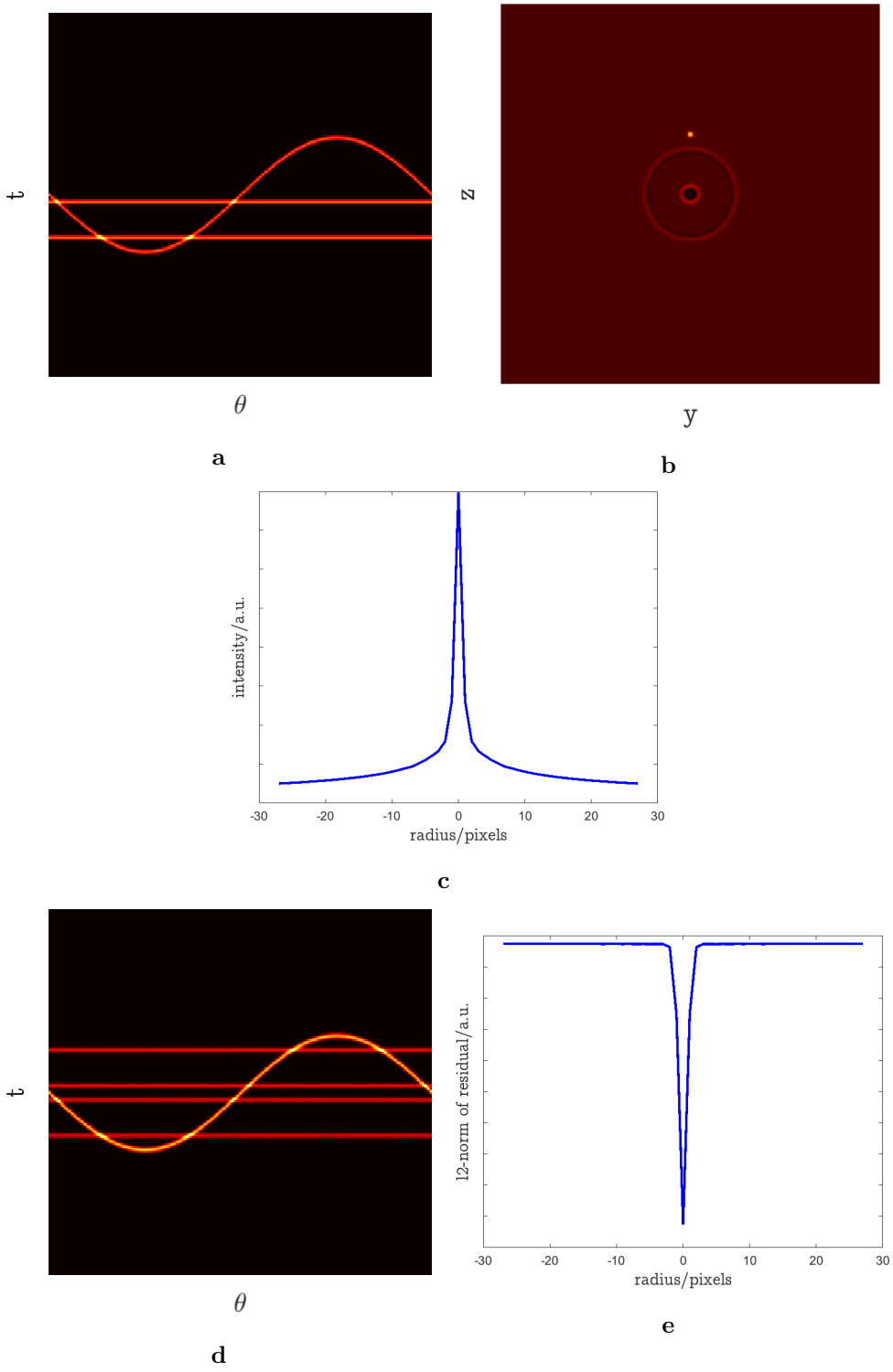

Figure 8.14: (**a**) Simulated sinogram of a point object with fixed pattern noise. (**b**) Reconstructed slice produced from (**a**). (**c**) Variation of ring artifact peak intensity with radius of a single point of fixed pattern noise. Fixed pattern noise near the rotation axis causes brighter artifacts. (**d**) Projection of slice shown in (**c**). The fixed pattern noise does not produce a self consistent result when back projected and projected. (**e**) Variation of $\frac{1}{2}\left\|Y - RR^TY\right\|_2^2$ with ring artifact radius. Fixed pattern noise near the axis of rotation is the most self consistent, so will produce stronger artifacts when iteratively reconstructed.

rotation axis. Beads visible in the figure 8.13b are obscured by artifacts even when using 50 % of test functions, shown in figure 8.13b.

In FBP fixed pattern noise leads to ring artifacts [95]. Figure 8.14b shows a slice, R^TY, reconstructed from a simulated sinogram of three point objects, Y (figure 8.14a), two of which are fixed while the other rotates correctly with angle of projection. The fixed objects lead to ring artifacts in the reconstructed slice, which have a radius equal to the distance of the fixed object from the rotation axis. They have lower peak intensities than the correctly reconstructed point, which reduce with greater radius (figure 8.14c).

Iterative reconstruction techniques are more robust to these artifacts than FBP; the ring artifacts produce inconsistent structures in RR^TY, shown in figure 8.14d, and are therefore suppressed by the $l2$-norm of the residual term in equation 3.12. However, near the rotation axis, a fixed object has greater verisimilitude and produces smaller errors (figure 8.14e) and strong reconstruction artifacts.

8.5 Future work: Region of interest and high dynamic range single pixel imaging

The SP-OPT system was able to produce a 3D reconstruction of a bead phantom, but it took 2.65 hours to acquire the required 50 fully sampled 256x256 angular projection images, which is too long for *in vivo* applications. If the speckle problem is addressed the acquisitions could be shortened by taking undersampled measurements. However, it is desirable to first minimise the fully sampled measurement time, so that compression requirements are reduced. In single pixel imaging, the acquisition time is directly proportional to the number of pixels, so using fewer would speed up the process.

In region of interest (ROI) single pixel imaging (ROI-SP), an initial low resolution image is used to segment the object, so that the high resolution acquisition can be adapted to only measure those pixels that make up the ROI. By doing this, minimal time is spent measuring background pixels, and the data acquisition time is reduced.

Restricting the measurement to pixels that make up the sample could also be used to implement C-HDR with a single pixel camera. As discussed in chapter 6, when acquiring a visible transmission image of an adult zebrafish, if the power or exposure is set such that the signal that does not pass through the sample does not saturate the detector, the signal through the sample will be below the noise floor. ROI single pixel imaging could be adapted for HDR imaging (ROI-HDR-SP) by acquiring the low resolution image at low power or low photodetector gain, and the high resolution image at high power or high photodetector gain. A similar approach has been described [179], but this acquires both the low power and high power image at full resolution, limiting speed.

The extinction coefficients of water and tissue are more similar for SWIR than for visible wavelengths (chapter 2.1), reducing the need for such large dynamic range in detection. However, even moderate oversaturation leads to reconstruction failure in single pixel imaging (section 8.5.2.1), so HDR-ROI single pixel imaging will likely be required for *in vivo* transmission

imaging of biological samples as large as adult zebrafish. ROI-SP and ROI-HDR-SP imaging are described here to combine with OPT, however they are general techniques, applicable to other SP implementations.

8.5.1 Region of interest single pixel camera

The acquistion speed of a single pixel camera scales with the number of pixels in the image, N. This creates a trade off between resolution and imaging speed; on the system described in chapter 8, acquiring a 8 mm FOV image at 242 μm resolution takes 1.5 s, and at 15 μm resolution it takes 380 s. These acquisition times assume that the resolution is constant across the FOV – as is the case for a pixelated detector. However, for a single pixel camera there is no requirement for the pixels in the single pixel camera to be of equal size – they can be defined as any arbitrary groupings of DMD mirrors – so the resolution can be varied to match the requirements for that region.

In Phillips *et al.* [180], a foveated pixel map was used, like that shown in figure 8.15c. This pixel map contains the same number of pixels – and therefore takes the same time to acquire – as the regular $64 * 64 = 4096$ pixel grid shown in figure 8.15a. Figures 8.15b and 8.15d show simulated reconstructions, produced from those pixel maps, of a $128 * 128 = 16384$ pixel phantom, which does not occupy the entire FOV. The foveated pixel map gives improved resolution in the fovea, and worse resolution outside.

The design goal of this map was to track a small object in a larger FOV in real time. Motion could be identified in the low resolution areas and the fovea moved to the required location to follow the object from frame to frame. This design is well suited to that task. However, when measuring an object that is larger than the fovea, artifacts caused by the irregular pixel sizes can be seen. For our application, there is no need to look for activity away from the object's position. Instead, it is desirable to have full resolution over the sample, and not look elsewhere. To this end, an adaptive region of interest approach could be implemented.

To minimise acquisition time, while maintaining homogeneous resolution over the sample, a two step acquisition could be used. In ROI single pixel imaging, a fully sampled low resolution $32 * 32 = 1024$ image of the FOV is first acquired. This image is thresholded to create a mask of the sample, and a second full resolution data set is acquired of the region of interest. An example mask pixel map is shown in figure 8.15e. The threshold here has been set to limit the number of pixels in the mask to be $4096 - 1024 = 3072$, so that the fully-sampled acquisition takes the same amount of time as the other two examples. However, the number of pixels included in the mask can be increased and decreased to fit the size of the object, as shown in figure 8.16a. Since there is no need for real time reconstruction, this application is also compatible with compressive sensing.

8.5.2 High dynamic range single-pixel camera

A single pixel camera has finite dynamic range. Figure 8.17a shows a simulated projection of a phantom, where the light through the sample is on average 5000 times dimmer than around

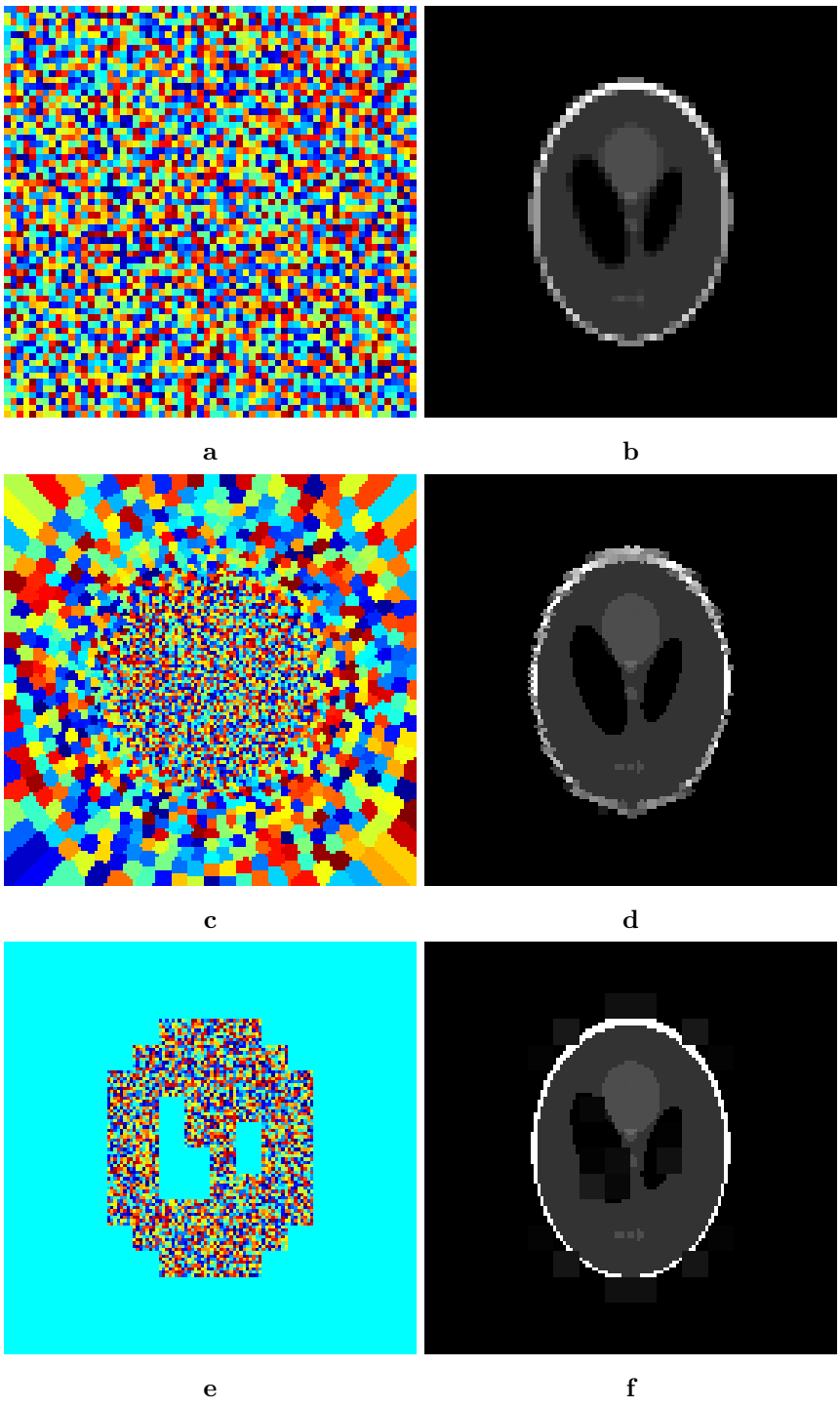

Figure 8.15: Simulated 4096 pixel maps **a,c,e** (different colours correspond to different super-pixels) and least squares reconstructions **b,d,f** of a 16384 pixel image: **a,b** Using 4096 test functions, a half resolution image can be acquired. **c,d** By using variable super-pixel sizes, 4096 test functions give full resolution in the fovea and worse resolution in the peripheries. **e,f** By using low resolution $(32 * 32)$ test functions to identify gross morphology, the brightest $4096 - 32 * 32 = 3072$ pixels can be segmented and high resolution acquired only over that region.

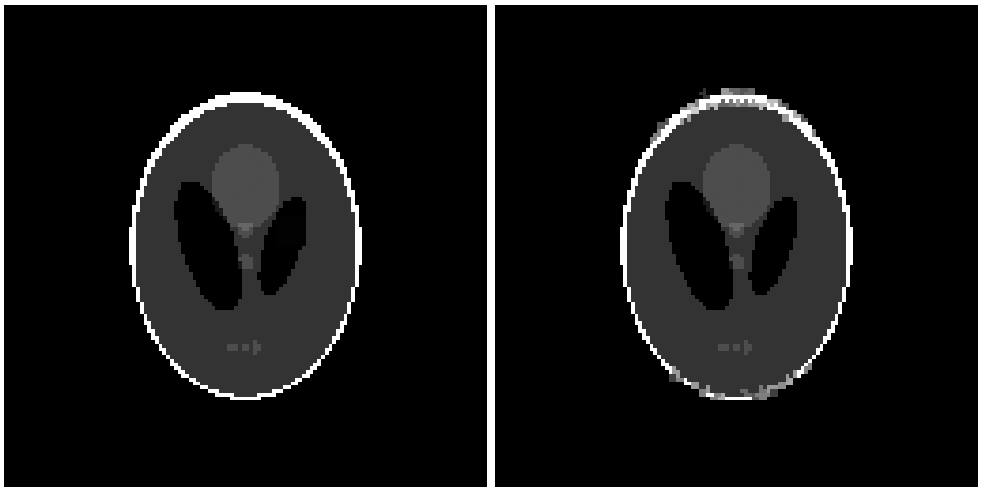

a **b**

Figure 8.16: Simulated least squares reconstructions using 5428 test functions. (**a**) ROI single pixel detection: the number of pixels included in the ROI can be adapted to suit the object. (**b**) Foveated single pixel detection: the size of the fovea can also be increased, but it is naturally circularly symmetric and includes pixels in the peripheries.

the outside. Using the noise characteristics of a commercial amplified photodiode (PDA50B2, thorlabs), a single pixel measurement of this projection was simulated that used all of the detector's dynamic range. The resulting reconstruction is shown in figure 8.17b.

8.5.2.1 Effects of saturation of single pixel detector

If the total light incident at the detector is too great, the output of the photodiode will saturate. In a conventional camera this would cause pixel values at the site of the saturation to be clipped and blooming into neighbouring pixels. With a single pixel camera, however, the saturated intensity affects the entire image – as equation 8.3 will no longer be correct.

The intensity at the photodiode is proportional to the correlation between the displayed test function and the image. For randomly ordered Hadamard patterns, half the pixels are on and half are off – with the appearence of random noise. Most images contain intensity in lower spatial frequencies, so the correlation between the image and any given test function is close to half the total intensity of the image.

The effect of the saturation on a simulated single pixel acquisition and reconstruction is shown in figure 8.18. Defining the degree of saturation as y_{max}/y_{sat}, where y_{max} is the maximum intensity incident on the photodiode during the measurement and y_{sat} is the intensity at which the detector saturates, it can be seen in figure 8.18b that degrees of saturation up to 200% are well tolerated. However, even slight increases in saturation (figures 8.18d and 8.18f) cause the image to be corrupted and lost.

The distributed nature of the single pixel measurement means that even moderate levels of saturation cause full loss of the image, even regions with low levels of light. Therefore, conventional HDR (described in chapter 6) is not possible.

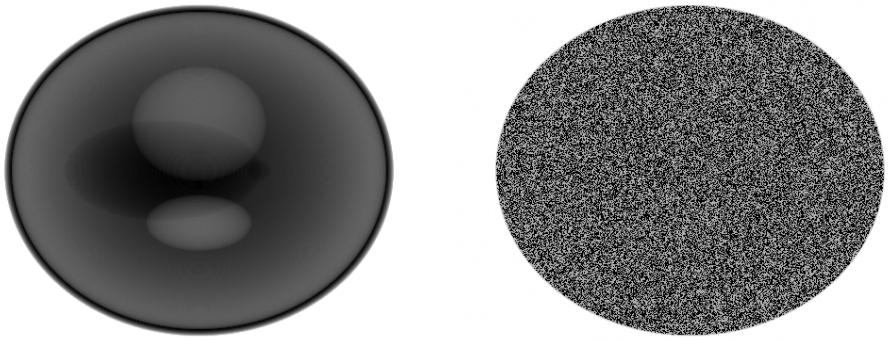

a **b**

Figure 8.17: Simulated transmission projection of a 3D phantom. Intensity is displayed on a logarithmic scale. (**a**) Ground truth: the signal through the centre is on average 5000 times less intense than outside the sample. (**b**) Reconstructed from single pixel measurement: the desired absorption structure has fallen beneath the noise floor.

8.5.2.2 Region-of-interest high-dynamic-range single pixel camera

To address the issues raised in section 8.5.2.1, Abolbashari *et al* [179] implemented an HDR single pixel camera using a variable gain photodiode. First a low gain acquisition was performed. Then additional single pixel acquisitions were performed at higher gain settings, with the pixels that would saturate the detector being attenuated by the DMD.

This method increases the acquisition time by a factor equal to the number of gain levels. This is undesirable for high resolution *in vivo* imaging; to stay within the anaesthetic window, the number of test functions will have to be lowered – reducing the reconstruction quality.

Instead ROI single pixel imaging could be used to acquire an HDR image without significantly increasing acquisition speed. First, a low power or low gain acquisition is performed at low resolution. Using this map, the image is masked into regions of different intensities. Then high resolution images are performed separately over the different masks, with the illumination power or detector gain adjusted so as to maximise the signal at the photodiode, without saturating it.

Figure 8.19 shows a simulated acquisition of the same absorbing phantom shown in figure 8.17. First a $64 * 64$ pixel was acquired at low power 8.19a. The pixels were then divided into bright background, those in the noise floor, and three intermediate masks (figure 8.19b). ROI single pixel acquisitions were then performed over each intensity mask – with the power varying so as to maximise the signal without saturation of the photodiode. The different measurements were then combined into a HDR composite (figure 8.19c). By acquiring different regions separately, the only additional time penalty is the time necessary to acquire the low resolution image.

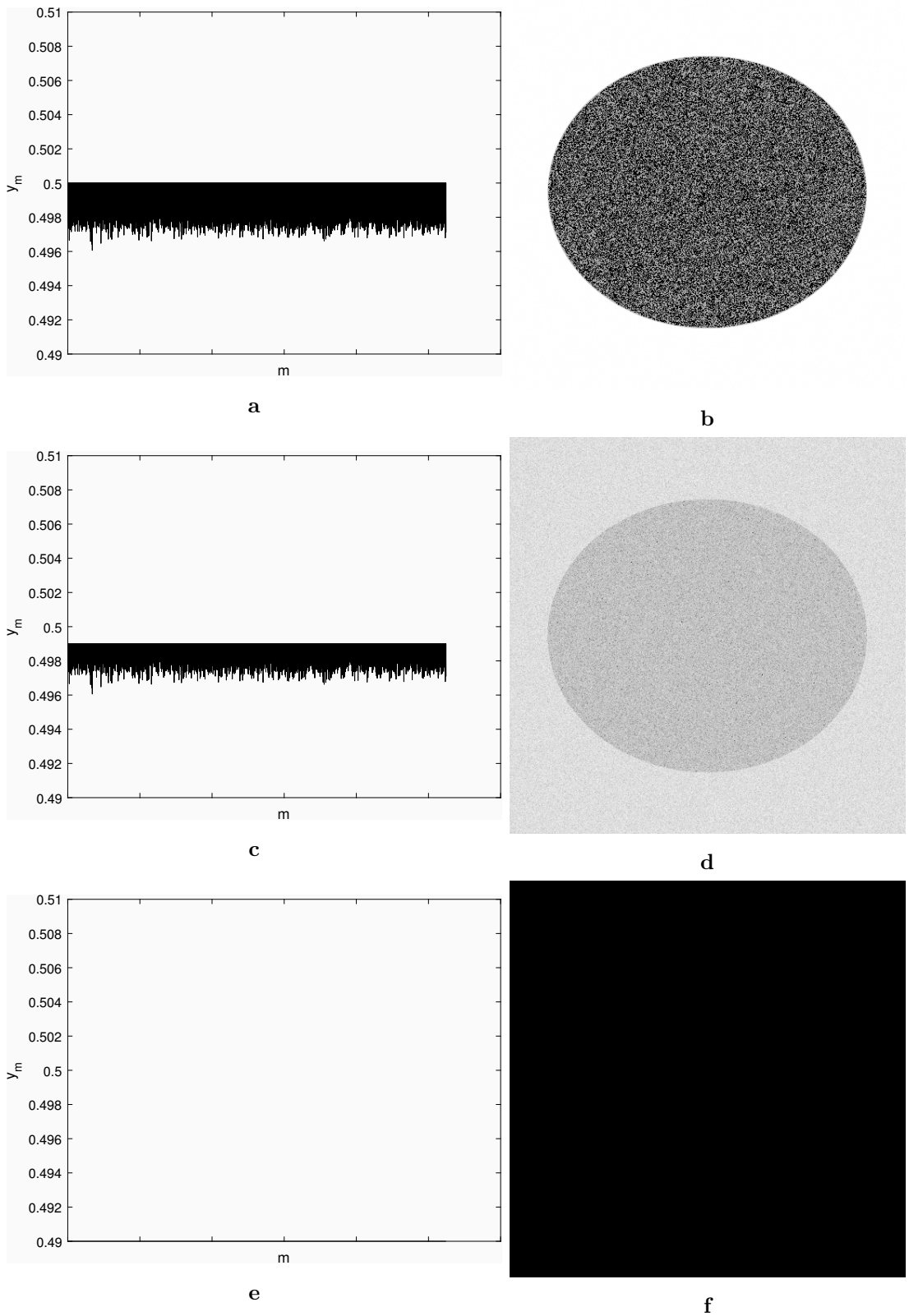

Figure 8.18: Simulated saturated single pixel signals **a,c,e** and reconstructions **b,d,f**: **a,b** With a degree of saturation of 200%, the image looks the same as in figure 8.17b. As the degree of saturation is increased, dim features do not become visible. In fact, even small further increases of saturation to 200.8% **c,d** and 208% **e,f** cause the image to be completely lost.

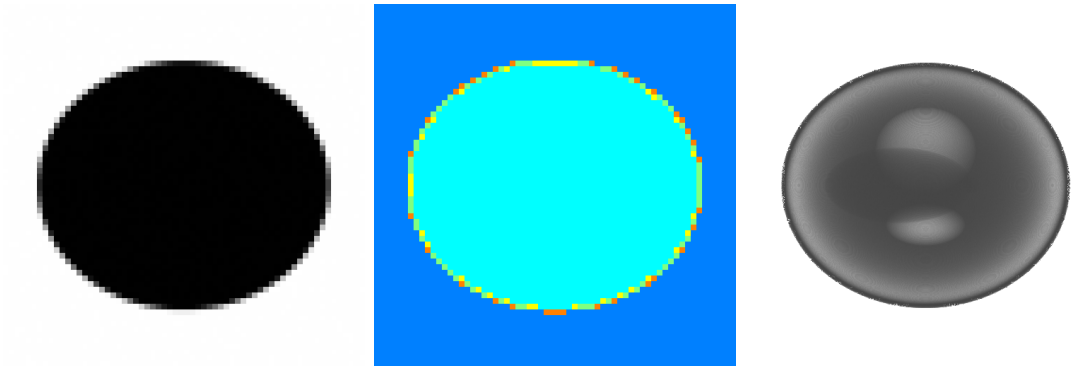

a **b** **c**

Figure 8.19: Simulation of an HDR single pixel acquisition. First a low resolution image was taken (**a**) (shown with linear intensity scale), which was used to mask out regions of different intensities (**b**), shown here with different colours. ROI single pixel acquisitions were performed over all or some of the masks to produce a HDR composite (**c**), here shown with a logarithmic intensity scale.

8.6 Conclusion

The reconstruction quality of *in vivo* OPT of adult zebrafish is limited by optical scattering. Chapter 7 described the development of slice-OPT to reduce the impact of scattering. However, the improvements were limited to regions within the transport mean free path of the surface (chapter 2.1.2). The transport mean free path increases with wavelength, so it is desirable to image at the long end of the biological optical window. However, cameras that are responsive at these wavelengths are currently prohibitively expensive for widespread adoption. To enable low-cost 3D imaging of SWIR wavelengths, a SP-OPT system has been developed and used to image a bead phantom in transmission.

A 3D SWIR absorption distribution was reconstructed from the SP-OPT bead phantom data acquisition. However, this acquisition took 2.65 hours to display all the test functions necessary for fully sampled 256x256 pixel images at 50 projection angles. This data acquisition should be highly compressible (figures 8.2 and 8.4), but laser speckle presented a sparsity challenge that produced strong reconstruction artifacts – particularly around the rotation axis of the system. The use of an incoherent SWIR illumination source could remove this problem, and enable the compression necessary for practical acquisition times for *in vivo* imaging at full resolution.

The acquisition time could be reduced without additional compression with the use of ROI-SP imaging, which could also be combined with HDR imaging for transmission imaging of adult zebrafish in the future.

The gain on the amplified photodetectors was too low for fluorescence emission to be detected. If the system were reconfigured as an illumination single pixel camera, the collection efficieny would be greatly improved – but there would no longer be the scattering benefit of SWIR imaging. Alternatively a higher gain detector may enable fluorescence SWIR SP-OPT.

Despite it's slow speed, the SP-OPT system enables 3D imaging of structures using SWIR

light, without requiring high cost Ge or InGaAs pixelated detectors.

Chapter 9

Conclusions and outlook

This chapter summarises the conclusions concerning the different developments and applications of OPT explored in this thesis and outlines proposed future development to extend the work reported here.

Optimisation of angularly multiplexed optical projection tomography

Acquiring undersampled angularly multiplexed OPT data and performing reconstructions with compressive sensing enables imaging of adult zebrafish with sample survival. In chapter 4, the capability of this system was demonstrated by applying it to a longitudinal study of tumour burdened adult zebrafish.

To better manage the amount of data generated in this study, several data processing tasks were automated, reducing the need for human intervention and improving consistency. This included automation of image registration between the two imaging arms, alignment of the rotation axis, and selection of the regularisation parameter for each sample.

The statistical power of longitudinal data, in comparison to cross-sectional data, was demonstrated. Statistical significance was observable in one out of four tests when the data was treated cross-sectionally. However, when the data was treated longitudinally, statistical significance was seen in three out of four of the tests.

Convolutional neural networks for reconstuction of undersampled optical projection tomography data

The CS reconstruction described in chapter 4 introduced a significant computational cost, requiring more than an hour per channel to reconstruct a typical data set using TwIST. This represented a data processing bottleneck for the longitudinal study. Chapter 5 described an alterative method of reconstructing undersampled OPT data sets, based on convolutional neural networks. The method reduced the reconstruction time by a factor of five, and achieved superior reconstruction quality for the same number of projections.

The neural network training was performed with *ex vivo* fixed and cleared mouse tissue data sets. Despite this limit in classes of sample type, the structural similarities of the streak artifacts created by sparse signals meant that the trained CNNs could be successfully applied to

in vivo zebrafish data. This means no additional animals were necessary to build an appropriate training data set.

The reduction in processing time will improve the practicality of future high-throughput longitudinal studies. Extrapolating the total reconstruction time improvement, the OPT reconstruction time for the 24 zebrafish imaged in the baseline study would be improved from 62 to 12 hours – making the difference between the data being available the next morning and having to wait half the working week.

Future development of this technique could improve the quality of reconstructions produced with fewer projections. The approach taken in this work was to treat each individual slice as a 2D denoising problem. However, the samples and their reconstructed volumes are three dimensional. The sample volume presents equally high spatial correlations and equally great sparsity in all directions. Therefore, improved reconstruction quality could be expected if the network took neighbouring slices as additional input channels.

The denoising of FBP-reconstructed images may be less effective than working directly with the raw projections. Instead of acting to remove noise from the reconstructions, a network could be designed to guess at the missing projections, before any transformation has occured. This requires a different approach to how the data is treated – the projections are locally correlated in t and x, but not in θ. Working in 2D, one approach would be to use 1D convolutional filters in t and to treat each projection θ as a seperate input channel. This could then be extended into 3D by using 2D convolutional filters in t and x.

Conformal high dynamic range optical projection tomography

Due to their size and optical density, the dynamic range required to capture brightfield images of adult zebfrafish is higher than what can be achieved with time sequential multi-exposure acquisition HDR. Chapter 6 demonstrated how control of the illumination onto the sample could improve the dynamic range further, with the development C-HDR-OPT.

C-HDR-OPT enables 3D brightfield contrast reconstructions of optically thick samples, including adult zebrafish. This method increased the projection dynamic range from 39 dB to 98 ± 1 dB, and revealed features that were masked by blooming when imaged with conventional HDR. This will enable dual fluorescence and brightfield OPT imaging of adult zebrafish, to provide specific contrast and anatomical context.

Future development could focus on improving the data fusion technique, using the optimisation approach suggested in section 6.1.3. Currently the centre of the sample appears bright, due to the over-correction of longer exposures when accounting for scattering. Alternatively, the technique could be reimplemented with a LCOS-SLM in the imaging path.

Although additional physiology was visbile in the C-HDR-OPT reconstructions, organs in the abdomen were not visible. The system could be adapted for NIR or SWIR illumination (chapter 8), which could improve the imaging depth.

Slice illuminated optical projection tomography

The reconstruction quality of OPT applied to cm sized samples, *in vivo*, is limited by optical scattering. Chapter 7 described the development of a system to improve the image quality by rejecting scattered light with semi-confocal illumination and detection. In slice-OPT the sample was illuminated with a series of parallel lines, to excite fluorescence from individual slices through the sample. Scattered fluorescence detected emitting from neighbouring slices were rejected with a digital mask applied to the camera, reducing the effects of inter-pixel cross-talk.

Slice-OPT projections and reconstructions had improved contrast over widefield OPT. This was measured by comparing their Fourier spectra. However, this enhancement was localised to near the surface of the scattering sample. As with C-HDR-OPT, Slice-OPT is equally applicable to longer wavelengths, where the improvements to image quality could be combined. The technique could also be applied to *ex vivo* cleared tissue; chemical clearing removes a large portion of refractive index inhomogeneities, but some remain. Slice-OPT could be applied to larger cleared samples, where the residual optical scattering impacts the reconstruction quality.

Single pixel optical projection tomography

The impact of optical scattering can be reduced by imaging SWIR light, which has the lowest scattering coefficient of wavelengths in the NIR biological optical window. Unfortunately, cameras that are sensitive to these wavelengths are currently prohibitively expensive for widespread adoption. Chapter 8 describes the ongoing development of a SP-OPT system, for lower-cost 3D SWIR imaging.

The SP-OPT system was designed and implemented, and applied to imaging of a bead phantom, demonstrating 3D SWIR absorption imaging. However, the compressibility of the acquisition was limited by laser speckle, which reduced the sparsity of the data. Therefore, the system was not applicable to *in vivo* imaging. Replacing the laser with an incoherent source would remove this problem, and could improve the compressibility to what was observed in simulated measurements.

The acquisition time could be further improved with ROI-SP imaging, which limits the measurement to the sample, and spends minimal time on measuring the background. If combined with a method to modulate illumination power or photodetector gain, ROI-SP imaging would also enable HDR imaging.

Bibliography

[1] S. L. Jacques and D. J. McAuliffe, "The melanosome: threshold temperature for explosive vaporization and internal absorption coefficient during pulsed laser irradiation," *Photochemistry and photobiology*, vol. 53, no. 6, pp. 769–775, 1991.

[2] R. L. van Veen, H. Sterenborg, A. Pifferi, A. Torricelli, and R. Cubeddu, "Determination of vis-nir absorption coefficients of mammalian fat, with time-and spatially resolved diffuse reflectance and transmission spectroscopy," in *Biomedical Topical Meeting*, p. SF4, Optical Society of America, 2004.

[3] G. M. Hale and M. R. Querry, "Optical constants of water in the 200-nm to 200wavelength region," *Applied optics*, vol. 12, no. 3, pp. 555–563, 1973.

[4] S. Jacques, "Generic tissue optical properties." `https://omlc.org/news/feb15/generic_optics/index.html`. Accessed: 2019-08-19.

[5] S. P. Davis, S. Kumar, Y. Alexandrov, A. Bhargava, G. da Silva Xavier, G. A. Rutter, P. Frankel, E. Sahai, S. Flaxman, P. M. French, *et al.*, "Convolutional neural networks for reconstruction of undersampled optical projection tomography data applied to in vivo imaging of zebrafish," *Journal of Biophotonics*, p. e201900128, 2019.

[6] S. P. Davis, L. Wisniewski, S. Kumar, T. Correia, S. R. Arridge, P. Frankel, J. McGinty, and P. M. French, "Slice-illuminated optical projection tomography," *Optics letters*, vol. 43, no. 22, pp. 5555–5558, 2018.

[7] J.-H. Lambert, *JH Lambert,... Photometria, sive de Mensura et gradibus luminis, colorum et umbrae*. sumptibus viduae E. Klett, 1760.

[8] V. Tuchin, "Tissue optics: light scattering methods and instruments for medical diagnosis," 2007.

[9] D. C. Harris and M. D. Bertolucci, *Symmetry and spectroscopy: an introduction to vibrational and electronic spectroscopy*. Courier Corporation, 1989.

[10] I. Georgakoudi, B. C. Jacobson, M. G. Müller, E. E. Sheets, K. Badizadegan, D. L. Carr-Locke, C. P. Crum, C. W. Boone, R. R. Dasari, J. Van Dam, *et al.*, "Nad (p) h and collagen as in vivo quantitative fluorescent biomarkers of epithelial precancerous changes," *Cancer research*, vol. 62, no. 3, pp. 682–687, 2002.

[11] J. Sharpe, U. Ahlgren, P. Perry, B. Hill, A. Ross, J. Hecksher-Sørensen, R. Baldock, and D. Davidson, "Optical projection tomography as a tool for 3d microscopy and gene expression studies," *Science*, vol. 296, no. 5567, pp. 541–545, 2002.

[12] D. C. Prasher, V. K. Eckenrode, W. W. Ward, F. G. Prendergast, and M. J. Cormier, "Primary structure of the aequorea victoria green-fluorescent protein," *Gene*, vol. 111, no. 2, pp. 229–233, 1992.

[13] A. Miyawaki, J. Llopis, R. Heim, J. M. McCaffery, J. A. Adams, M. Ikura, and R. Y. Tsien, "Fluorescent indicators for ca2+ based on green fluorescent proteins and calmodulin," *Nature*, vol. 388, no. 6645, pp. 882–887, 1997.

[14] S. L. Jacques, "Optical properties of biological tissues: a review," *Physics in Medicine & Biology*, vol. 58, no. 11, p. R37, 2013.

[15] T. Yu, Y. Qi, H. Gong, Q. Luo, and D. Zhu, "Optical clearing for multiscale biological tissues," *Journal of biophotonics*, vol. 11, no. 2, p. e201700187, 2018.

[16] X. Wen, Z. Mao, Z. Han, V. V. Tuchin, and D. Zhu*, "In vivo skin optical clearing by glycerol solutions: mechanism," *Journal of biophotonics*, vol. 3, no. 1-2, pp. 44–52, 2010.

[17] A. Ertürk, C. P. Mauch, F. Hellal, F. Förstner, T. Keck, K. Becker, N. Jährling, H. Steffens, M. Richter, M. Hübener, *et al.*, "Three-dimensional imaging of the unsectioned adult spinal cord to assess axon regeneration and glial responses after injury," *Nature medicine*, vol. 18, no. 1, p. 166, 2012.

[18] M. K. Schwarz, A. Scherbarth, R. Sprengel, J. Engelhardt, P. Theer, and G. Giese, "Fluorescent-protein stabilization and high-resolution imaging of cleared, intact mouse brains," *PloS one*, vol. 10, no. 5, p. e0124650, 2015.

[19] K. Becker, N. Jährling, S. Saghafi, R. Weiler, and H.-U. Dodt, "Chemical clearing and dehydration of gfp expressing mouse brains," *PloS one*, vol. 7, no. 3, p. e33916, 2012.

[20] N. Renier, Z. Wu, D. J. Simon, J. Yang, P. Ariel, and M. Tessier-Lavigne, "idisco: a simple, rapid method to immunolabel large tissue samples for volume imaging," *Cell*, vol. 159, no. 4, pp. 896–910, 2014.

[21] N. Renier, E. L. Adams, C. Kirst, Z. Wu, R. Azevedo, J. Kohl, A. E. Autry, L. Kadiri, K. U. Venkataraju, Y. Zhou, *et al.*, "Mapping of brain activity by automated volume analysis of immediate early genes," *Cell*, vol. 165, no. 7, pp. 1789–1802, 2016.

[22] C. Pan, R. Cai, F. P. Quacquarelli, A. Ghasemigharagoz, A. Lourbopoulos, P. Matryba, N. Plesnila, M. Dichgans, F. Hellal, and A. Ertürk, "Shrinkage-mediated imaging of entire organs and organisms using udisco," *Nature methods*, vol. 13, no. 10, p. 859, 2016.

[23] H. Hama, H. Kurokawa, H. Kawano, R. Ando, T. Shimogori, H. Noda, K. Fukami, A. Sakaue-Sawano, and A. Miyawaki, "Scale: a chemical approach for fluorescence imaging and reconstruction of transparent mouse brain," *Nature neuroscience*, vol. 14, no. 11, p. 1481, 2011.

[24] E. A. Susaki, K. Tainaka, D. Perrin, F. Kishino, T. Tawara, T. M. Watanabe, C. Yokoyama, H. Onoe, M. Eguchi, S. Yamaguchi, *et al.*, "Whole-brain imaging with single-cell resolution using chemical cocktails and computational analysis," *Cell*, vol. 157, no. 3, pp. 726–739, 2014.

[25] K. Chung, J. Wallace, S.-Y. Kim, S. Kalyanasundaram, A. S. Andalman, T. J. Davidson, J. J. Mirzabekov, K. A. Zalocusky, J. Mattis, A. K. Denisin, *et al.*, "Structural and molecular interrogation of intact biological systems," *Nature*, vol. 497, no. 7449, p. 332, 2013.

[26] V. Ntziachristos, "Going deeper than microscopy: the optical imaging frontier in biology," *Nature methods*, vol. 7, no. 8, pp. 603–614, 2010.

[27] R. H. Webb, "Theoretical basis of confocal microscopy," *Techniques in Confocal Microscopy*, p. 1, 2010.

[28] W. Denk, J. H. Strickler, W. W. Webb, *et al.*, "Two-photon laser scanning fluorescence microscopy," *Science*, vol. 248, no. 4951, pp. 73–76, 1990.

[29] J. Huisken, J. Swoger, F. Del Bene, J. Wittbrodt, and E. H. K. Stelzer, "Optical sectioning deep inside live embryos by selective plane illumination microscopy," *Science*, vol. 305, no. 5686, pp. 1007–1009, 2004.

[30] W. Supatto, A. McMahon, S. E. Fraser, and A. Stathopoulos, "Quantitative imaging of collective cell migration during drosophila gastrulation: multiphoton microscopy and computational analysis," *Nature protocols*, vol. 4, no. 10, pp. 1397–1412, 2009.

[31] T. Tanaami, S. Otsuki, N. Tomosada, Y. Kosugi, M. Shimizu, and H. Ishida, "High-speed 1-frame/ms scanning confocal microscope with a microlens and nipkow disks," *Applied Optics*, vol. 41, no. 22, pp. 4704–4708, 2002.

[32] J. Bewersdorf, R. Pick, and S. W. Hell, "Multifocal multiphoton microscopy," *Optics letters*, vol. 23, no. 9, pp. 655–657, 1998.

[33] J. Pawley and B. R. Masters, "Handbook of biological confocal microscopy," *Optical Engineering*, vol. 35, no. 9, pp. 2765–2766, 1996.

[34] P. J. Keller, A. D. Schmidt, J. Wittbrodt, and E. H. Stelzer, "Reconstruction of zebrafish early embryonic development by scanned light sheet microscopy," *science*, vol. 322, no. 5904, pp. 1065–1069, 2008.

[35] S. Kumar, N. Lockwood, M.-C. Ramel, T. Correia, M. Ellis, Y. Alexandrov, N. Andrews, R. Patel, L. Bugeon, M. Dallman, S. Brandner, S. Arridge, M. Katan, J. McGinty, P. Frankel, and P. French, "Quantitative in vivo optical tomography of cancer progression and vasculature development in adult zebrafish," *Oncotarget*, vol. 7, no. 28, 2016.

[36] P. P. V. Ramirez, J. Zammit, O. Vanderpoorten, F. Riche, F.-X. Blé, X.-H. Zhou, B. Spiridon, C. Valentine, S. P. Spasov, P. W. Oluwasanya, *et al.*, "Optij: Open-source optical projection tomography of large organ samples," *BioRxiv*, p. 656488, 2019.

[37] T. Watson, N. Andrews, S. Davis, L. Bugeon, M. D. Dallman, and J. McGinty, "Optim: Optical projection tomography integrated microscope using open-source hardware and software," *PloS one*, under review 2017.

[38] B. T. Moore, J. M. Jordan, and L. R. Baugh, "Wormsizer: high-throughput analysis of nematode size and shape," *PloS one*, vol. 8, no. 2, p. e57142, 2013.

[39] J. E. Sulston and H. R. Horvitz, "Post-embryonic cell lineages of the nematode, caenorhabditis elegans," *Developmental biology*, vol. 56, no. 1, pp. 110–156, 1977.

[40] J. E. Sulston, E. Schierenberg, J. G. White, and J. Thomson, "The embryonic cell lineage of the nematode caenorhabditis elegans," *Developmental biology*, vol. 100, no. 1, pp. 64–119, 1983.

[41] Z. Bao, J. I. Murray, T. Boyle, S. L. Ooi, M. J. Sandel, and R. H. Waterston, "Automated cell lineage tracing in caenorhabditis elegans," *Proceedings of the National Academy of Sciences*, vol. 103, no. 8, pp. 2707–2712, 2006.

[42] F. Long, H. Peng, X. Liu, S. K. Kim, and E. Myers, "A 3d digital atlas of c. elegans and its application to single-cell analyses," *Nature methods*, vol. 6, no. 9, p. 667, 2009.

[43] Y. Wu, A. Ghitani, R. Christensen, A. Santella, Z. Du, G. Rondeau, Z. Bao, D. Colón-Ramos, and H. Shroff, "Inverted selective plane illumination microscopy (ispim) enables coupled cell identity lineaging and neurodevelopmental imaging in caenorhabditis elegans," *Proceedings of the National Academy of Sciences*, vol. 108, no. 43, pp. 17708–17713, 2011.

[44] Y. Wu, P. Wawrzusin, J. Senseney, R. S. Fischer, R. Christensen, A. Santella, A. G. York, P. W. Winter, C. M. Waterman, Z. Bao, *et al.*, "Spatially isotropic four-dimensional imaging with dual-view plane illumination microscopy," *Nature biotechnology*, vol. 31, no. 11, p. 1032, 2013.

[45] N. Stroustrup, B. E. Ulmschneider, Z. M. Nash, I. F. López-Moyado, J. Apfeld, and W. Fontana, "The caenorhabditis elegans lifespan machine," *Nature methods*, vol. 10, no. 7, p. 665, 2013.

[46] J. G. White, E. Southgate, J. N. Thomson, and S. Brenner, "The structure of the nervous system of the nematode caenorhabditis elegans," *Philos Trans R Soc Lond B Biol Sci*, vol. 314, no. 1165, pp. 1–340, 1986.

[47] T. A. Jarrell, Y. Wang, A. E. Bloniarz, C. A. Brittin, M. Xu, J. N. Thomson, D. G. Albertson, D. H. Hall, and S. W. Emmons, "The connectome of a decision-making neural network," *Science*, vol. 337, no. 6093, pp. 437–444, 2012.

[48] J. P. Nguyen, F. B. Shipley, A. N. Linder, G. S. Plummer, M. Liu, S. U. Setru, J. W. Shaevitz, and A. M. Leifer, "Whole-brain calcium imaging with cellular resolution in freely behaving caenorhabditis elegans," *Proceedings of the National Academy of Sciences*, vol. 113, no. 8, pp. E1074–E1081, 2016.

[49] V. Venkatachalam, N. Ji, X. Wang, C. Clark, J. K. Mitchell, M. Klein, C. J. Tabone, J. Florman, H. Ji, J. Greenwood, *et al.*, "Pan-neuronal imaging in roaming caenorhabditis elegans," *Proceedings of the National Academy of Sciences*, vol. 113, no. 8, pp. E1082–E1088, 2016.

[50] R. B. Kopito and E. Levine, "Durable spatiotemporal surveillance of caenorhabditis elegans response to environmental cues," *Lab on a Chip*, vol. 14, no. 4, pp. 764–770, 2014.

[51] W. Keil, L. M. Kutscher, S. Shaham, and E. D. Siggia, "Long-term high-resolution imaging of developing c. elegans larvae with microfluidics," *Developmental cell*, vol. 40, no. 2, pp. 202–214, 2017.

[52] M. Westerfield, *The zebrafish book: a guide for the laboratory use of zebrafish (Brachydanio rerio)*. University of Oregon press, 1995.

[53] A. Kaufmann, M. Mickoleit, M. Weber, and J. Huisken, "Multilayer mounting enables long-term imaging of zebrafish development in a light sheet microscope," *Development*, vol. 139, no. 17, pp. 3242–3247, 2012.

[54] M. Mickoleit, B. Schmid, M. Weber, F. O. Fahrbach, S. Hombach, S. Reischauer, and J. Huisken, "High-resolution reconstruction of the beating zebrafish heart," *Nature methods*, vol. 11, no. 9, p. 919, 2014.

[55] Y. A. Pan, T. Freundlich, T. A. Weissman, D. Schoppik, X. C. Wang, S. Zimmerman, B. Ciruna, J. R. Sanes, J. W. Lichtman, and A. F. Schier, "Zebrabow: multispectral cell labeling for cell tracing and lineage analysis in zebrafish," *Development*, vol. 140, no. 13, pp. 2835–2846, 2013.

[56] D. H. Kim, J. Kim, J. C. Marques, A. Grama, D. G. Hildebrand, W. Gu, J. M. Li, and D. N. Robson, "Pan-neuronal calcium imaging with cellular resolution in freely swimming zebrafish," *Nature methods*, vol. 14, no. 11, p. 1107, 2017.

[57] J. McGinty, H. B. Taylor, L. Chen, L. Bugeon, J. R. Lamb, M. J. Dallman, and P. M. French, "In vivo fluorescence lifetime optical projection tomography," *Biomedical optics express*, vol. 2, no. 5, pp. 1340–1350, 2011.

[58] N. Andrews, M.-C. Ramel, S. Kumar, Y. Alexandrov, D. J. Kelly, S. C. Warren, L. Kerry, N. Lockwood, A. Frolov, P. Frankel, *et al.*, "Visualising apoptosis in live zebrafish using fluorescence lifetime imaging with optical projection tomography to map fret biosensor activity in space and time," *Journal of biophotonics*, 2016.

[59] A. Bassi, B. Schmid, and J. Huisken, "Optical tomography complements light sheet microscopy for in toto imaging of zebrafish development," *Development*, vol. 142, no. 5, pp. 1016–1020, 2015.

[60] C. Pardo-Martin, A. Allalou, J. Medina, P. M. Eimon, C. Wählby, and M. F. Yanik, "High-throughput hyperdimensional vertebrate phenotyping," *Nature communications*, vol. 4, p. 1467, 2013.

[61] E. J. Gualda, H. Pereira, T. Vale, M. F. Estrada, C. Brito, and N. Moreno, "Spim-fluid: open source light-sheet based platform for high-throughput imaging," *Biomedical optics express*, vol. 6, no. 11, pp. 4447–4456, 2015.

[62] N. Gengenbacher, M. Singhal, and H. G. Augustin, "Preclinical mouse solid tumour models: status quo, challenges and perspectives," *Nature Reviews Cancer*, vol. 17, no. 12, p. 751, 2017.

[63] M. J. Pittet and R. Weissleder, "Intravital imaging," *Cell*, vol. 147, no. 5, pp. 983–991, 2011.

[64] S. I. Ellenbroek and J. Van Rheenen, "Imaging hallmarks of cancer in living mice," *Nature Reviews Cancer*, vol. 14, no. 6, p. 406, 2014.

[65] V. Ntziachristos, C.-H. Tung, C. Bremer, and R. Weissleder, "Fluorescence molecular tomography resolves protease activity in vivo," *Nature medicine*, vol. 8, no. 7, p. 757, 2002.

[66] M. De Jong, J. Essers, and W. M. Van Weerden, "Imaging preclinical tumour models: improving translational power," *Nature Reviews Cancer*, vol. 14, no. 7, p. 481, 2014.

[67] C. Hoelen, F. De Mul, R. Pongers, and A. Dekker, "Three-dimensional photoacoustic imaging of blood vessels in tissue," *Optics letters*, vol. 23, no. 8, pp. 648–650, 1998.

[68] S. Kirchberger, C. Sturtzel, S. Pascoal, and M. Distel, "Quo natas, danio?—recent progress in modeling cancer in zebrafish," *Frontiers in oncology*, vol. 7, p. 186, 2017.

[69] K. Howe, M. D. Clark, C. F. Torroja, J. Torrance, C. Berthelot, M. Muffato, J. E. Collins, S. Humphray, K. McLaren, L. Matthews, *et al.*, "The zebrafish reference genome sequence and its relationship to the human genome," *Nature*, vol. 496, no. 7446, p. 498, 2013.

[70] J. F. Rawls, E. M. Mellgren, and S. L. Johnson, "How the zebrafish gets its stripes," *Developmental biology*, vol. 240, no. 2, pp. 301–314, 2001.

[71] R. M. White, A. Sessa, C. Burke, T. Bowman, J. LeBlanc, C. Ceol, C. Bourque, M. Dovey, W. Goessling, C. E. Burns, *et al.*, "Transparent adult zebrafish as a tool for in vivo transplantation analysis," *Cell stem cell*, vol. 2, no. 2, pp. 183–189, 2008.

[72] T. Correia, N. Lockwood, S. Kumar, J. Yin, M.-C. Ramel, N. Andrews, M. Katan, L. Bugeon, M. J. Dallman, J. McGinty, *et al.*, "Accelerated optical projection tomography applied to in vivo imaging of zebrafish," *PloS one*, vol. 10, no. 8, p. e0136213, 2015.

[73] P. Antinucci and R. Hindges, "A crystal-clear zebrafish for in vivo imaging," *Scientific reports*, vol. 6, p. 29490, 2016.

[74] B. Zhang, Y. Shimada, J. Kuroyanagi, Y. Nishimura, N. Umemoto, T. Nomoto, T. Shintou, T. Miyazaki, and T. Tanaka, "Zebrafish xenotransplantation model for cancer stem-like cell study and high-throughput screening of inhibitors," *Tumor Biology*, vol. 35, no. 12, pp. 11861–11869, 2014.

[75] S. Heilmann, K. Ratnakumar, E. M. Langdon, E. R. Kansler, I. S. Kim, N. R. Campbell, E. B. Perry, A. J. McMahon, C. K. Kaufman, E. Van Rooijen, *et al.*, "A quantitative system for studying metastasis using transparent zebrafish," *Cancer research*, vol. 75, no. 20, pp. 4272–4282, 2015.

[76] Q. Tang, J. C. Moore, M. S. Ignatius, I. M. Tenente, M. N. Hayes, E. G. Garcia, N. T. Yordán, C. Bourque, S. He, J. S. Blackburn, *et al.*, "Imaging tumour cell heterogeneity following cell transplantation into optically clear immune-deficient zebrafish," *Nature communications*, vol. 7, p. 10358, 2016.

[77] B. Zhang, Y. Shimada, T. Hirota, M. Ariyoshi, J. Kuroyanagi, Y. Nishimura, and T. Tanaka, "Novel immunologic tolerance of human cancer cell xenotransplants in zebrafish," *Translational Research*, vol. 170, pp. 89–98, 2016.

[78] N. Hinfray, F. Sohm, M. Caulier, E. Chadili, B. Piccini, C. Torchy, J.-M. Porcher, Y. Guiguen, and F. Brion, "Dynamic and differential expression of the gonadal aromatase during the process of sexual differentiation in a novel transgenic cyp19a1a-egfp zebrafish line," *General and comparative endocrinology*, vol. 261, pp. 179–189, 2018.

[79] K. Guesmi, L. Abdeladim, S. Tozer, P. Mahou, T. Kumamoto, K. Jurkus, P. Rigaud, K. Loulier, N. Dray, P. Georges, *et al.*, "Dual-color deep-tissue three-photon microscopy with a multiband infrared laser," *Light: Science & Applications*, vol. 7, no. 1, p. 12, 2018.

[80] J. Gore, M. Ranade, M. Maryanski, and R. Schulz, "Radiation dose distributions in three dimensions from tomographic optical density scanning of polymer gels: I. development of an optical scanner," *Physics in Medicine & Biology*, vol. 41, no. 12, p. 2695, 1996.

[81] R. Kelly, K. Jordan, and J. Battista, "Optical ct reconstruction of 3d dose distributions using the ferrous–benzoic–xylenol (fbx) gel dosimeter," *Medical physics*, vol. 25, no. 9, pp. 1741–1750, 1998.

[82] J. G. Wolodzko, C. Marsden, and A. Appleby, "Ccd imaging for optical tomography of gel radiation dosimeters," *Medical Physics*, vol. 26, no. 11, pp. 2508–2513, 1999.

[83] S. J. Doran, K. K. Koerkamp, M. A. Bero, P. Jenneson, E. J. Morton, and W. B. Gilboy, "A ccd-based optical ct scanner for high-resolution 3d imaging of radiation dose distributions: equipment specifications, optical simulations and preliminary results," *Physics in Medicine & Biology*, vol. 46, no. 12, p. 3191, 2001.

[84] N. Krstajić and S. J. Doran, "Focusing optics of a parallel beam ccd optical tomography apparatus for 3d radiation gel dosimetry," *Physics in Medicine & Biology*, vol. 51, no. 8, p. 2055, 2006.

[85] J. Kerwin, M. Scott, J. Sharpe, L. Puelles, S. C. Robson, M. Martínez-de-la Torre, J. L. Ferran, G. Feng, R. Baldock, T. Strachan, *et al.*, "3 dimensional modelling of early human brain development using optical projection tomography," *BMC neuroscience*, vol. 5, no. 1, p. 27, 2004.

[86] H. Sakhalkar, M. Dewhirst, T. Oliver, Y. Cao, and M. Oldham, "Functional imaging in bulk tissue specimens using optical emission tomography: fluorescence preservation during optical clearing," *Physics in Medicine & Biology*, vol. 52, no. 8, p. 2035, 2007.

[87] A. d'Esposito, P. W. Sweeney, M. Ali, M. Saleh, R. Ramasawmy, T. A. Roberts, G. Agliardi, A. Desjardins, M. F. Lythgoe, R. B. Pedley, *et al.*, "Computational fluid dynamics with imaging of cleared tissue and of in vivo perfusion predicts drug uptake and treatment responses in tumours," *Nature biomedical engineering*, vol. 2, no. 10, p. 773, 2018.

[88] L. McGurk, H. Morrison, L. P. Keegan, J. Sharpe, and M. A. O'Connell, "Three-dimensional imaging of drosophila melanogaster," *PLoS One*, vol. 2, no. 9, p. e834, 2007.

[89] M. E. Fisher, A. K. Clelland, A. Bain, R. A. Baldock, P. Murphy, H. Downie, C. Tickle, D. R. Davidson, and R. A. Buckland, "Integrating technologies for comparing 3d gene expression domains in the developing chick limb," *Developmental biology*, vol. 317, no. 1, pp. 13–23, 2008.

[90] R. J. Bryson-Richardson and P. D. Currie, "Optical projection tomography for spatio-temporal analysis in the zebrafish," in *Methods in cell biology*, vol. 76, pp. 37–50, Elsevier, 2004.

[91] T. Alanentalo, C. E. Loren, A. Larefalk, J. Sharpe, D. Holmberg, and U. Ahlgren, "High-resolution three-dimensional imaging of islet-infiltrate interactions based on optical projection tomography assessments of the intact adult mouse pancreas," *Journal of biomedical optics*, vol. 13, no. 5, p. 054070, 2008.

[92] D. Nguyen, V. Uhlmann, A. L. Planchette, P. J. Marchand, D. Van De Ville, T. Lasser, and A. Radenovic, "Supervised learning to quantify amyloidosis in whole brains of an alzheimer's disease mouse model acquired with optical projection tomography," *Biomedical Optics Express*, vol. 10, no. 6, pp. 3041–3060, 2019.

[93] M. Oldham, H. Sakhalkar, Y. M. Wang, P. Guo, T. F. Oliver, R. Bentley, Z. Vujaskovic, and M. W. Dewhirst, "Three-dimensional imaging of whole rodent organs using optical computed and emission tomography," *Journal of biomedical optics*, vol. 12, no. 1, p. 014009, 2007.

[94] K. Koshiba-Takeuchi, A. D. Mori, B. L. Kaynak, J. Cebra-Thomas, T. Sukonnik, R. O. Georges, S. Latham, L. Beck, R. M. Henkelman, B. L. Black, *et al.*, "Reptilian heart development and the molecular basis of cardiac chamber evolution," *Nature*, vol. 461, no. 7260, p. 95, 2009.

[95] J. R. Walls, J. G. Sled, J. Sharpe, and R. M. Henkelman, "Correction of artefacts in optical projection tomography," *Physics in Medicine & Biology*, vol. 50, no. 19, p. 4645, 2005.

[96] M. A. Haidekker, "Optical transillumination tomography with tolerance against refraction mismatch," *Computer methods and programs in biomedicine*, vol. 80, no. 3, pp. 225–235, 2005.

[97] U. J. Birk, A. Darrell, N. Konstantinides, A. Sarasa-Renedo, and J. Ripoll, "Improved reconstructions and generalized filtered back projection for optical projection tomography," *Applied optics*, vol. 50, no. 4, pp. 392–398, 2011.

[98] J. R. Walls, J. G. Sled, J. Sharpe, and R. M. Henkelman, "Resolution improvement in emission optical projection tomography," *Physics in medicine and biology*, vol. 52, no. 10, p. 2775, 2007.

[99] J. van der Horst and J. Kalkman, "Image resolution and deconvolution in optical tomography," *Optics Express*, vol. 24, no. 21, pp. 24460–24472, 2016.

[100] L. Chen, J. McGinty, H. B. Taylor, L. Bugeon, J. R. Lamb, M. J. Dallman, and P. M. French, "Incorporation of an experimentally determined mtf for spatial frequency filtering and deconvolution during optical projection tomography reconstruction," *Optics express*, vol. 20, no. 7, pp. 7323–7337, 2012.

[101] A. Darrell, H. Meyer, K. Marias, M. Brady, and J. Ripoll, "Weighted filtered backprojection for quantitative fluorescence optical projection tomography," *Physics in Medicine & Biology*, vol. 53, no. 14, p. 3863, 2008.

[102] C. Vinegoni, D. Razansky, J.-L. Figueiredo, M. Nahrendorf, V. Ntziachristos, and R. Weissleder, "Normalized born ratio for fluorescence optical projection tomography," *Optics letters*, vol. 34, no. 3, pp. 319–321, 2009.

[103] S. Dou, J. Liu, and L. Yang, "Dual-modality optical projection tomography reconstruction method from fewer views," *Journal of biophotonics*, vol. 12, no. 4, p. e201800407, 2019.

[104] Q. Miao, J. Hayenga, M. G. Meyer, T. Neumann, A. C. Nelson, and E. J. Seibel, "Resolution improvement in optical projection tomography by the focal scanning method," *Optics letters*, vol. 35, no. 20, pp. 3363–3365, 2010.

[105] L. Chen, S. Kumar, D. Kelly, N. Andrews, M. J. Dallman, P. M. French, and J. McGinty, "Remote focal scanning optical projection tomography with an electrically tunable lens," *Biomedical optics express*, vol. 5, no. 10, pp. 3367–3375, 2014.

[106] K. G. Chan and M. Liebling, "Direct inversion algorithm for focal plane scanning optical projection tomography," *Biomedical optics express*, vol. 8, no. 11, pp. 5349–5358, 2017.

[107] L. Chen, N. Andrews, S. Kumar, P. Frankel, J. McGinty, and P. M. French, "Simultaneous angular multiplexing optical projection tomography at shifted focal planes," *Optics letters*, vol. 38, no. 6, pp. 851–853, 2013.

[108] S. Kumar, N. Lockwood, M.-C. Ramel, T. Correia, M. Ellis, Y. Alexandrov, N. Andrews, R. Patel, L. Bugeon, M. J. Dallman, *et al.*, "Quantitative in vivo optical tomography of cancer progression & vasculature development in adult zebrafish," *Oncotarget*, vol. 7, no. 28, p. 43939, 2016.

[109] L. Chen, Y. Alexandrov, S. Kumar, N. Andrews, M. J. Dallman, P. M. French, and J. McGinty, "Mesoscopic in vivo 3-d tracking of sparse cell populations using angular multiplexed optical projection tomography," *Biomedical optics express*, vol. 6, no. 4, pp. 1253–1261, 2015.

[110] R.-A. Lorbeer, M. Heidrich, C. Lorbeer, D. F. R. Ojeda, G. Bicker, H. Meyer, and A. Heisterkamp, "Highly efficient 3d fluorescence microscopy with a scanning laser optical tomograph," *Optics express*, vol. 19, no. 6, pp. 5419–5430, 2011.

[111] L. Sinha, F. Massanes, V. Torres, C. Li, K. Tichauer, and J. Brankov, "Comparison of time-and angular-domain scatter rejection in mesoscopic optical projection tomography: a simulation study," *Biomedical optics express*, vol. 10, no. 2, pp. 747–760, 2019.

[112] A. Bassi, D. Brida, C. D'Andrea, G. Valentini, R. Cubeddu, S. De Silvestri, and G. Cerullo, "Time-gated optical projection tomography," *Optics letters*, vol. 35, no. 16, pp. 2732–2734, 2010.

[113] L. Fieramonti, A. Bassi, E. A. Foglia, A. Pistocchi, C. D'Andrea, G. Valentini, R. Cubeddu, S. De Silvestri, G. Cerullo, and F. Cotelli, "Time-gated optical projection tomography allows visualization of adult zebrafish internal structures," *PloS one*, vol. 7, no. 11, p. e50744, 2012.

[114] H. Meyer, A. Darrell, A. Metaxakis, C. Savakis, and J. Ripoll, "Optical projection tomography for in-vivo imaging of drosophila melanogaster," *Microscopy and Analysis-UK*, no. 127, p. 19, 2008.

[115] A. Arranz, D. Dong, S. Zhu, C. Savakis, J. Tian, and J. Ripoll, "In-vivo optical tomography of small scattering specimens: time-lapse 3d imaging of the head eversion process in drosophila melanogaster," *Scientific reports*, vol. 4, p. 7325, 2014.

[116] J.-F. Colas and J. Sharpe, "Live optical projection tomography," *Organogenesis*, vol. 5, no. 4, pp. 211–216, 2009.

[117] N. Andrews, M.-C. Ramel, S. Kumar, Y. Alexandrov, D. Kelly, S. Warren, L. Kerry, N. Lockwood, A. Frolov, P. Frankel, L. Bugeon, J. McGinty, M. Dallman, and P. French, "Visualising apoptosis in live zebrafish using fluorescence lifetime imaging with optical projection tomography to map fret biosensor activity in space and time," *JOURNAL OF BIOPHOTONICS*, vol. 9, pp. 414–424, 2016.

[118] T. Watson, N. Andrews, S. Davis, L. Bugeon, M. D. Dallman, and J. McGinty, "Optim: Optical projection tomography integrated microscope using open-source hardware and software," *PLOS ONE*, vol. 12, pp. 1–13, 07 2017.

[119] U. J. Birk, M. Rieckher, N. Konstantinides, A. Darrell, A. Sarasa-Renedo, H. Meyer, N. Tavernarakis, and J. Ripoll, "Correction for specimen movement and rotation errors for in-vivo optical projection tomography," *Biomedical optics express*, vol. 1, no. 1, pp. 87–96, 2010.

[120] S. Zhu, D. Dong, U. J. Birk, M. Rieckher, N. Tavernarakis, X. Qu, J. Liang, J. Tian, and J. Ripoll, "Automated motion correction for in vivo optical projection tomography," *IEEE transactions on medical imaging*, vol. 31, no. 7, pp. 1358–1371, 2012.

[121] A. Bassi, L. Fieramonti, C. D'Andrea, and G. V. andMarina Mione, "label-free three-dimensional imaging of zebrafish vasculature with optical projection tomography," *Journal of Biomedical Optics*, vol. 16, no. 10, pp. 1 – 4 – 4, 2011.

[122] P. Fei, Z. Yu, X. Wang, P. J. Lu, Y. Fu, Z. He, J. Xiong, and Y. Huang, "High dynamic range optical projection tomography (hdr-opt)," *Opt. Express*, vol. 20, pp. 8824–8836, Apr 2012.

[123] A. Cheddad, C. Nord, A. Hörnblad, R. Prunskaite-Hyyryläinen, M. Eriksson, F. Georgsson, S. J. Vainio, and U. Ahlgren, "Improving signal detection in emission optical projection tomography via single source multi-exposure image fusion," *Opt. Express*, vol. 21, pp. 16584–16604, Jul 2013.

[124] Y. A. Hideki Funamizu, "Three-dimensional quantitative phase imaging of blood coagulation structures by optical projection tomography in flow cytometry using digital holographic microscopy," *Journal of Biomedical Optics*, vol. 24, no. 3, pp. 1 – 6 – 6, 2018.

[125] J. Hsieh *et al.*, "Computed tomography: principles, design, artifacts, and recent advances," SPIE Bellingham, WA, 2009.

[126] R. N. Bracewell, "Strip integration in radio astronomy," *Australian Journal of Physics*, vol. 9, no. 2, pp. 198–217, 1956.

[127] T. Farquhar, A. Chatziioannou, G. Chinn, M. Dahlbom, and E. Hoffman, "An investigation of filter choice for filtered back-projection reconstruction in pet," *IEEE transactions on nuclear science*, vol. 45, no. 3, pp. 1133–1137, 1998.

[128] L. Rayleigh, "Xxxi. investigations in optics, with special reference to the spectroscope," *The London, Edinburgh, and Dublin Philosophical Magazine and Journal of Science*, vol. 8, no. 49, pp. 261–274, 1879.

[129] S. Inoué and K. Spring, "Video microscopy, 2nd edn., ch. 6–8," 1997.

[130] G. Sun, A. Tarasov, J. McGinty, A. McDonald, G. da Silva Xavier, T. Gorman, A. Marley, P. French, H. Parker, F. Gribble, *et al.*, "Ablation of amp-activated protein kinase $\alpha 1$ and $\alpha 2$ from mouse pancreatic beta cells and rip2. cre neurons suppresses insulin release in vivo," *Diabetologia*, vol. 53, no. 5, pp. 924–936, 2010.

[131] D. L. Donoho *et al.*, "Compressed sensing," *IEEE Transactions on information theory*, vol. 52, no. 4, pp. 1289–1306, 2006.

[132] E. J. Candès *et al.*, "Compressive sampling," in *Proceedings of the international congress of mathematicians*, vol. 3, pp. 1433–1452, Madrid, Spain, 2006.

[133] A. Chambolle, R. A. De Vore, N.-Y. Lee, and B. J. Lucier, "Nonlinear wavelet image processing: variational problems, compression, and noise removal through wavelet shrinkage," *IEEE Transactions on Image Processing*, vol. 7, no. 3, pp. 319–335, 1998.

[134] A. Chambolle, "An algorithm for total variation minimization and applications," *Journal of Mathematical imaging and vision*, vol. 20, no. 1-2, pp. 89–97, 2004.

[135] R. E. Carrillo, A. B. Ramirez, G. R. Arce, K. E. Barner, and B. M. Sadler, "Robust compressive sensing of sparse signals: a review," *EURASIP Journal on Advances in Signal Processing*, vol. 2016, no. 1, p. 108, 2016.

[136] N. Lockwood, J. Parker, C. Wilson, and P. Frankel, "Optimal anesthetic regime for motionless three-dimensional image acquisition during longitudinal studies of adult nonpigmented zebrafish," *Zebrafish*, vol. 14, no. 2, pp. 133–139, 2017.

[137] S. Raghunathan, D. Stredney, P. Schmalbrock, and B. D. Clymer, "Image registration using rigid registration and maximization of mutual information," in *Poster presented at: MMVR13. The 13th Annual Medicine Meets Virtual Reality Conference*, 2005.

[138] J. M. Bioucas-Dias and M. A. Figueiredo, "A new twist: two-step iterative shrinkage/thresholding algorithms for image restoration," *IEEE Transactions on Image processing*, vol. 16, no. 12, pp. 2992–3004, 2007.

[139] A. F. Frangi, W. J. Niessen, K. L. Vincken, and M. A. Viergever, "Multiscale vessel enhancement filtering," in *International conference on medical image computing and computer-assisted intervention*, pp. 130–137, Springer, 1998.

[140] A. Bhandare, M. Bhide, P. Gokhale, and R. Chandavarkar, "Applications of convolutional neural networks," *International Journal of Computer Science and Information Technologies*, vol. 7, no. 5, pp. 2206–2215, 2016.

[141] K. H. Jin, M. T. McCann, E. Froustey, and M. Unser, "Deep convolutional neural network for inverse problems in imaging," *IEEE Transactions on Image Processing*, vol. 26, no. 9, pp. 4509–4522, 2017.

[142] A. Waibel, T. Hanazawa, G. Hinton, K. Shikano, and K. J. Lang, "Phoneme recognition using time-delay neural networks," *IEEE transactions on acoustics, speech, and signal processing*, vol. 37, no. 3, pp. 328–339, 1989.

[143] R. H. Hahnloser, R. Sarpeshkar, M. A. Mahowald, R. J. Douglas, and H. S. Seung, "Digital selection and analogue amplification coexist in a cortex-inspired silicon circuit," *Nature*, vol. 405, no. 6789, p. 947, 2000.

[144] D. P. Kingma and J. Ba, "Adam: A method for stochastic optimization," *arXiv preprint arXiv:1412.6980*, 2014.

[145] S. Ioffe and C. Szegedy, "Batch normalization: Accelerating deep network training by reducing internal covariate shift," *arXiv preprint arXiv:1502.03167*, 2015.

[146] O. Ronneberger, P. Fischer, and T. Brox, "U-net: Convolutional networks for biomedical image segmentation," in *International Conference on Medical image computing and computer-assisted intervention*, pp. 234–241, Springer, 2015.

[147] G. da Silva Xavier, A. Mondragon, G. Sun, L. Chen, J. McGinty, P. French, and G. Rutter, "Abnormal glucose tolerance and insulin secretion in pancreas-specific tcf7l2-null mice," *Diabetologia*, vol. 55, no. 10, pp. 2667–2676, 2012.

[148] S. P. Davis, "Cnopt." `https://github.com/imperial-photonics/CNOPT/`. Accessed: 2019-08-29.

[149] N. Banaz, J. Mäkelä, and S. Uphoff, "Choosing the right label for single-molecule tracking in live bacteria: side-by-side comparison of photoactivatable fluorescent protein and halo tag dyes," *Journal of physics D: Applied physics*, vol. 52, no. 6, p. 064002, 2018.

[150] P. E. Debevec and J. Malik, "Recovering high dynamic range radiance maps from photographs," in *ACM SIGGRAPH 2008 classes*, p. 31, ACM, 2008.

[151] C. Sequin, "Blooming suppression in charge coupled area imaging devices," *The Bell System Technical Journal*, vol. 51, no. 8, pp. 1923–1926, 1972.

[152] Y. Ni and K. Matou, "A cmos log image sensor with on-chip fpn compensation," in *Proceedings of the 27th European Solid-State Circuits Conference*, pp. 101–104, IEEE, 2001.

[153] S. K. Nayar and V. Branzoi, "Adaptive dynamic range imaging: Optical control of pixel exposures over space and time," in *null*, p. 1168, IEEE, 2003.

[154] W. Feng, F. Zhang, W. Wang, W. Xing, and X. Qu, "Digital micromirror device camera with per-pixel coded exposure for high dynamic range imaging," *Applied optics*, vol. 56, no. 13, pp. 3831–3840, 2017.

[155] A. Eisbruch, J. A. Ship, M. K. Martel, R. H. Ten, L. H. Marsh, G. T. Wolf, R. M. Esclamado, C. R. Bradford, J. E. Terrell, S. S. Gebarski, *et al.*, "Parotid gland sparing in patients undergoing bilateral head and neck irradiation: techniques and early results.," *International journal of radiation oncology, biology, physics*, vol. 36, no. 2, pp. 469–480, 1996.

[156] P. H. Torr and A. Zisserman, "Mlesac: A new robust estimator with application to estimating image geometry," *Computer vision and image understanding*, vol. 78, no. 1, pp. 138–156, 2000.

[157] C. Sheppard and X. Mao, "Confocal microscopes with slit apertures," *Journal of Modern Optics*, vol. 35, no. 7, pp. 1169–1185, 1988.

[158] T. Breuninger, K. Greger, and E. H. Stelzer, "Lateral modulation boosts image quality in single plane illumination fluorescence microscopy," *Optics letters*, vol. 32, no. 13, pp. 1938–1940, 2007.

[159] V. Poher, G. T. Kennedy, H. B. Manning, D. M. Owen, H. X. Zhang, E. Gu, M. D. Dawson, P. M. French, and M. A. Neil, "Improved sectioning in a slit scanning confocal microscope," *Optics letters*, vol. 33, no. 16, pp. 1813–1815, 2008.

[160] N. G. Horton, K. Wang, D. Kobat, C. G. Clark, F. W. Wise, C. B. Schaffer, and C. Xu, "In vivo three-photon microscopy of subcortical structures within an intact mouse brain," *Nature photonics*, vol. 7, no. 3, p. 205, 2013.

[161] J. H. Yu, S.-H. Kwon, Z. Petrášek, O. K. Park, S. W. Jun, K. Shin, M. Choi, Y. I. Park, K. Park, H. B. Na, *et al.*, "High-resolution three-photon biomedical imaging using doped zns nanocrystals," *Nature materials*, vol. 12, no. 4, p. 359, 2013.

[162] G. Hong, J. C. Lee, J. T. Robinson, U. Raaz, L. Xie, N. F. Huang, J. P. Cooke, and H. Dai, "Multifunctional in vivo vascular imaging using near-infrared ii fluorescence," *Nature medicine*, vol. 18, no. 12, p. 1841, 2012.

[163] G. Hong, S. Diao, J. Chang, A. L. Antaris, C. Chen, B. Zhang, S. Zhao, D. N. Atochin, P. L. Huang, K. I. Andreasson, *et al.*, "Through-skull fluorescence imaging of the brain in a new near-infrared window," *Nature Photonics*, vol. 8, no. 9, p. 723, 2014.

[164] J. A. Carr, D. Franke, J. R. Caram, C. F. Perkinson, M. Saif, V. Askoxylakis, M. Datta, D. Fukumura, R. K. Jain, M. G. Bawendi, *et al.*, "Shortwave infrared fluorescence imaging with the clinically approved near-infrared dye indocyanine green," *Proceedings of the National Academy of Sciences*, vol. 115, no. 17, pp. 4465–4470, 2018.

[165] F. Wang, H. Wan, Z. Ma, Y. Zhong, Q. Sun, Y. Tian, L. Qu, H. Du, M. Zhang, L. Li, *et al.*, "Light-sheet microscopy in the near-infrared ii window," *Nature methods*, vol. 16, no. 6, p. 545, 2019.

[166] M. F. Duarte, M. A. Davenport, D. Takhar, J. N. Laska, T. Sun, K. F. Kelly, and R. G. Baraniuk, "Single-pixel imaging via compressive sampling," *IEEE signal processing magazine*, vol. 25, no. 2, pp. 83–91, 2008.

[167] N. Radwell, K. J. Mitchell, G. M. Gibson, M. P. Edgar, R. Bowman, and M. J. Padgett, "Single-pixel infrared and visible microscope," *Optica*, vol. 1, no. 5, pp. 285–289, 2014.

[168] M. P. Edgar, G. M. Gibson, R. W. Bowman, B. Sun, N. Radwell, K. J. Mitchell, S. S. Welsh, and M. J. Padgett, "Simultaneous real-time visible and infrared video with single-pixel detectors," *Scientific reports*, vol. 5, p. 10669, 2015.

[169] F. Magalhães, F. M. Araújo, M. V. Correia, M. Abolbashari, and F. Farahi, "Active illumination single-pixel camera based on compressive sensing," *Applied optics*, vol. 50, no. 4, pp. 405–414, 2011.

[170] A. Escobet-Montalbán, R. Spesyvtsev, M. Chen, W. A. Saber, M. Andrews, C. S. Herrington, M. Mazilu, and K. Dholakia, "Wide-field multiphoton imaging through scattering media without correction," *Science advances*, vol. 4, no. 10, p. eaau1338, 2018.

[171] B. Lochocki, A. Gambín, S. Manzanera, E. Irles, E. Tajahuerce, J. Lancis, and P. Artal, "Single pixel camera ophthalmoscope," *Optica*, vol. 3, no. 10, pp. 1056–1059, 2016.

[172] M. A. Neil, R. Juškaitis, and T. Wilson, "Method of obtaining optical sectioning by using structured light in a conventional microscope," *Optics letters*, vol. 22, no. 24, pp. 1905–1907, 1997.

[173] V. Durán, F. Soldevila, E. Irles, P. Clemente, E. Tajahuerce, P. Andrés, and J. Lancis, "Compressive imaging in scattering media," *Optics express*, vol. 23, no. 11, pp. 14424–14433, 2015.

[174] U. Dias and M. E. Rane, "Comparative analysis of sensing matrices for compressed sensed thermal images," in *2013 International Mutli-Conference on Automation, Computing, Communication, Control and Compressed Sensing (iMac4s)*, pp. 265–270, IEEE, 2013.

[175] M. Lustig, D. L. Donoho, J. M. Santos, and J. M. Pauly, "Compressed sensing mri," *IEEE Signal Processing Magazine*, vol. 25, no. 2, pp. 72–82, 2008.

[176] Z. Zhang, X. Ma, and J. Zhong, "Single-pixel imaging by means of fourier spectrum acquisition," *Nature communications*, vol. 6, p. 6225, 2015.

[177] Z. Zhang, X. Wang, G. Zheng, and J. Zhong, "Fast fourier single-pixel imaging via binary illumination," *Scientific reports*, vol. 7, no. 1, p. 12029, 2017.

[178] M.-J. Sun, M. P. Edgar, G. M. Gibson, B. Sun, N. Radwell, R. Lamb, and M. J. Padgett, "Single-pixel three-dimensional imaging with time-based depth resolution," *Nature communications*, vol. 7, p. 12010, 2016.

[179] M. Abolbashari, F. Farahi, F. Magalhaes, F. M. Araújo, and M. V. Correia, "High dynamic range compressive imaging: a programmable imaging system," *Optical Engineering*, vol. 51, no. 7, p. 071407, 2012.

[180] D. B. Phillips, M.-J. Sun, J. M. Taylor, M. P. Edgar, S. M. Barnett, G. M. Gibson, and M. J. Padgett, "Adaptive foveated single-pixel imaging with dynamic supersampling," *Science advances*, vol. 3, no. 4, p. e1601782, 2017.

Appendix A

Convolutional neural networks for undersampled optical projection tomography: source code

A.1 Neural network architecture

```
# U-Net model. Adapted from https://github.com/milesial/Pytorch-UNet

import torch
import torch.nn as nn
import torch.nn.functional as F


class double_conv(nn.Module):
    '''(conv => BN => ReLU) * 2'''
    def __init__(self, in_ch, out_ch):
        super(double_conv, self).__init__()
        self.conv = nn.Sequential(
            nn.Conv2d(in_ch, out_ch, 3, padding=1),
            nn.BatchNorm2d(out_ch),
            nn.ReLU(inplace=True),
            #nn.Dropout2d(),
            nn.Conv2d(out_ch, out_ch, 3, padding=1),
            nn.BatchNorm2d(out_ch),
            nn.ReLU(inplace=True),
            #nn.Dropout2d()
        )

    def forward(self, x):
        x = self.conv(x)
        return x


class inconv(nn.Module):
```

```
    def __init__(self, in_ch, out_ch):
        super(inconv, self).__init__()
        self.conv = double_conv(in_ch, out_ch)
        #self.conv = nn.Sequential(
        # nn.BatchNorm2d(in_ch),
        # double_conv(in_ch, out_ch)
        #)
    def forward(self, x):
        x = self.conv(x)
        return x


class down(nn.Module):
    def __init__(self, in_ch, out_ch):
        super(down, self).__init__()
        self.mpconv = nn.Sequential(
            nn.MaxPool2d(2),
            double_conv(in_ch, out_ch)
        )

    def forward(self, x):
        x = self.mpconv(x)
        return x


class up(nn.Module):
    def __init__(self, in_ch, out_ch, bilinear=True):
        super(up, self).__init__()

        # would be a nice idea if the upsampling could be learned too,
        # but my machine do not have enough memory to handle all those weights
        if bilinear:
            self.up = nn.Upsample(scale_factor=2, mode='bilinear', align_corners=True)
        else:
            self.up = nn.ConvTranspose2d(in_ch//2, in_ch//2, 2, stride=2)

        self.conv = double_conv(in_ch, out_ch)

    def forward(self, x1, x2):
        x1 = self.up(x1)
        diffX = x1.size()[2] - x2.size()[2]
        diffY = x1.size()[3] - x2.size()[3]
        x2 = F.pad(x2, (diffX // 2, int(diffX / 2),
                        diffY // 2, int(diffY / 2)))
        x = torch.cat([x2, x1], dim=1)
        x = self.conv(x)
        return x


class outconv(nn.Module):
    def __init__(self, in_ch, out_ch):
```

```
        super(outconv, self).__init__()
        self.conv = nn.Conv2d(in_ch, out_ch, 1)

    def forward(self, x):
        x = self.conv(x)
        return x



class UNet(nn.Module):
    def __init__(self, n_channels, n_classes):
        super(UNet, self).__init__()
        self.inc = inconv(n_channels, 64)
        self.down1 = down(64, 128)
        self.down2 = down(128, 256)
        self.down3 = down(256, 512)
        self.down4 = down(512, 512)
        self.up1 = up(1024, 256)
        self.up2 = up(512, 128)
        self.up3 = up(256, 64)
        self.up4 = up(128, 64)
        self.outc = outconv(64, n_classes)

    def forward(self, x0):
        x1 = self.inc(x0)
        x2 = self.down1(x1)
        x3 = self.down2(x2)
        x4 = self.down3(x3)
        x5 = self.down4(x4)
        x = self.up1(x5, x4)
        x = self.up2(x, x3)
        x = self.up3(x, x2)
        x = self.up4(x, x1)
        x = self.outc(x)
        return x#F.sigmoid(x)
```

A.2 Optical projection tomography data set

```
"""
Dataset class for loading sinograms and transforming them to well-sampled and
undersampled slices for neural network training.

input_folder: path to folder of sinogram tifs

crop_size: [Lx Ly] size of random crop to apply to slices - if you want the
whole slice, use a -ve value

augment: If True, sinograms will permuted to start at a different angle, and
randomly flipped

number_angles: How many angles you want to use in your sub-sampling
```

```
"""

import torch
from torch.utils.data.dataset import Dataset
from os import listdir
from skimage import io
import os
import numpy as np
import astra

class OPT_dataset(Dataset):
    def __init__(self, input_folder, crop_size, augment, number_angles):
        self.input_folder = input_folder
        self.input_files = [f for f in listdir(input_folder) if f.endswith(".tif")]
        self.crop_size = crop_size
        self.augment = augment

        # This assumes your fully sampled data—set has 400 equally spaced
        # projections
        N = 400

        # Create arrays of angles for well—sampled and under—sampled
        self.angles = np.linspace(0,2*np.pi,N,False)
        self.under_angle_indices = np.round(np.linspace(0,400,number_angles,False)).astype(int)
        self.under_angles = self.angles[self.under_angle_indices]

    def __len__(self):
        return len(self.input_files)

    def __getitem__(self, idx):

        # Get file path to tif and load sinogram
        input_name = os.path.join(self.input_folder,self.input_files[idx])
        sino = np.transpose(io.imread(input_name)).astype(np.float64)

        # make sure it has 400 projections
        if sino.shape[0] == 800:
            sino = sino[0:800:2,:]

        # apply random starting projection and random flips
        if self.augment:
            start_position = np.random.randint(sino.shape[0])
            sino = np.concatenate((sino[start_position:,:],sino[:start_position,:]))
            if np.random.randint(2):
                sino = np.flipud(sino)
            if np.random.randint(2):
                sino = np.fliplr(sino)


        # set up bits for ASTRA reconstruction
        vol_geom = astra.create_vol_geom(752, 752)
```

```
rec_id = astra.data2d.create('-vol', vol_geom)

proj_geom = astra.create_proj_geom('parallel', 1.0, sino.shape[1], self.angles)
sinogram_id = astra.data2d.create('-sino', proj_geom, sino)

under_geom = astra.create_proj_geom('parallel', 1.0, sino.shape[1], self.under_angles)
undersino_id = astra.data2d.create('-sino', under_geom, sino[self.under_angle_indices,:])

# configure reconstruction settings
cfg = astra.astra_dict('FBP_CUDA')
cfg['FilterType'] = 'Hann'
cfg['FilterD'] = 0.4
cfg['ReconstructionDataId'] = rec_id

# configure for full sinogram
cfg['ProjectionDataId'] = sinogram_id

# reconstruct full sinogram
alg_id = astra.algorithm.create(cfg)
astra.algorithm.run(alg_id)

# grab reconstruction
label_image = astra.data2d.get(rec_id)

# stop GPU memory leak
astra.algorithm.delete(alg_id)

# configure for undersampled sinogram and reconstruct
cfg['ProjectionDataId'] = undersino_id
alg_id = astra.algorithm.create(cfg)
astra.algorithm.run(alg_id)
input_image = astra.data2d.get(rec_id)

# stop GPU memory leak
astra.algorithm.delete(alg_id)
astra.data2d.delete(rec_id)
astra.data2d.delete(sinogram_id)
astra.data2d.delete(undersino_id)

# zero mean unit variance input
input_max = np.amax(input_image)
input_min = np.amin(input_image)
input_image = (input_image-input_min)/(input_max-input_min)
label_image = (label_image-input_min)/(input_max-input_min)

input_mean = np.mean(input_image)

input_image = input_image - input_mean
label_image = label_image - input_mean

# apply random crop to slice
```

```
        h, w = input_image.shape[:2]
        if self.crop_size[0] > 0:
            new_h,new_w = self.crop_size
            top = np.random.randint(0,h-new_h)
            left = np.random.randint(0,w-new_w)

            input_image = input_image[top:top+new_h, left: left+new_w]
            label_image = label_image[top:top+new_h, left: left+new_w]

        # reshape images to Pytorch style [C X Y]
        input_image = input_image.reshape((1,input_image.shape[0],input_image.shape[0]))
        label_image = label_image.reshape((1,label_image.shape[0],label_image.shape[0]))

        return(torch.from_numpy(input_image).float(), torch.from_numpy(label_image).float(), input_max,
            input_min, input_mean)
```

A.3 Optical projection tomography data set without labels

```
"""
Dataset class for loading sinograms and reconstructing
undersampled slices for neural network speed test.

input_folder: path to folder of sinogram tifs

number_angles: How many angles you want to use in your sub-sampling
"""

import torch
from torch.utils.data.dataset import Dataset
from os import listdir
from skimage import io
import os
import numpy as np
import astra

class OPT_dataset(Dataset):
    def __init__(self, input_folder, number_angles):
        self.input_folder = input_folder
        self.input_files = [f for f in listdir(input_folder) if f.endswith(".tif")]

        # This assumes your fully sampled data-set has 400 equally spaced
        # projections

        N = 400
        self.angles = np.linspace(0,2*np.pi,N,False)
        self.under_angle_indices = np.round(np.linspace(0,400,number_angles,False)).astype(int)
        self.under_angles = self.angles[self.under_angle_indices]


    def __len__(self):
        return len(self.input_files)
```

```
def __getitem__(self, idx):

    # Get file path to tif and load sinogram
    input_name = os.path.join(self.input_folder,self.input_files[idx])
    sino = np.transpose(io.imread(input_name)).astype(np.float64)

    # make sure it has 400 projections
    if sino.shape[0] == 800:
        sino = sino[0:800:2,:]

    # set up bits for ASTRA reconstruction
    vol_geom = astra.create_vol_geom(702, 702)
    under_geom = astra.create_proj_geom('parallel', 1.0, sino.shape[1], self.under_angles)
    rec_id = astra.data2d.create('-vol', vol_geom)

    # configure reconstruction settings
    cfg = astra.astra_dict('FBP_CUDA')
    cfg['FilterType'] = 'Hann'
    cfg['FilterD'] = 0.4
    cfg['ReconstructionDataId'] = rec_id

    undersino_id = astra.data2d.create('-sino', under_geom, sino[self.under_angle_indices,:])
    cfg['ProjectionDataId'] = undersino_id
    alg_id = astra.algorithm.create(cfg)

    # do filtered back projection
    astra.algorithm.run(alg_id)

    # grab reconstruction
    input_image = astra.data2d.get(rec_id)

    # stop memory leak
    astra.algorithm.delete(alg_id)
    astra.data2d.delete(rec_id)
    astra.data2d.delete(undersino_id)

    # normalise
    I_max = np.amax(input_image)
    I_min = np.amin(input_image)
    input_image = (input_image-I_min)/(I_max-I_min)

    I_mean = np.mean(input_image)

    input_image = input_image - I_mean

    # reshape for Pytorch
    input_image = input_image.reshape((1,input_image.shape[0],input_image.shape[0]))

    return(torch.from_numpy(input_image).float(), I_max, I_min, I_mean)
```

A.4 Training

```
"""
Function for training Unet to remove streaks from undersampled OPT reconstructions

train_input: path to folder with sinograms for training

test_input: path to folder with sinograms for testing

savename: file name for network to save to

number_angles: number of angles to be used for undersampled sinogram
"""
import torch
import torch.nn as nn
from OPT_dataset import OPT_dataset
import numpy as np
from unet_model_original import UNet
import copy
import matplotlib.pyplot as plt
import os

def train_unet_OPT(train_input,test_input,savename,number_angles):
    # Device configuration
    device = torch.device('cuda' if torch.cuda.is_available() else 'cpu')

    # OPT dataset
    train_dataset = OPT_dataset(input_folder = train_input, crop_size = [128,128], augment = True,
        number_angles = number_angles)
    test_dataset = OPT_dataset(input_folder = test_input, crop_size = [512,512], augment = True,
        number_angles = number_angles)

    # Data loader
    train_loader = torch.utils.data.DataLoader(dataset=train_dataset,
                                               batch_size=32,
                                               shuffle=True)
    test_loader = torch.utils.data.DataLoader(dataset=test_dataset,
                                              batch_size=8,
                                              shuffle=False)
    # create network
    model = UNet(1,1).to(device)

    # Hyper-parameters
    num_epochs = 60
    learning_rate = 0.001

    # Loss and optimizer
    criterion = nn.L1Loss()
    optimizer = torch.optim.Adam(model.parameters(), lr=learning_rate)

    # For updating learning rate
```

```
def update_lr(optimizer, lr):
    for param_group in optimizer.param_groups:
        param_group['lr'] = lr

# Train the model
total_step = len(train_loader)
curr_lr = learning_rate

# track train error
epoch_steps = total_step*num_epochs
train_error = np.zeros(epoch_steps)
ii = 0

# track validation error
validate_steps = len(test_loader)*num_epochs
validate_error = np.zeros(validate_steps)
iii = 0

# set starting point for early stopping
last_error = 0.5
fail_count = 0

# training loop
model.train()
for epoch in range(num_epochs):
    # loop over all sinograms
    for i, (images, labels, I_max, I_min, I_mean) in enumerate(train_loader):
        # Move images to GPU
        images = images.to(device)
        labels = labels.to(device)

        # Forward pass
        optimizer.zero_grad()
        outputs = model(images)
        loss = criterion(outputs, labels)

        # Backward and optimize
        loss.backward()
        optimizer.step()
        train_error[ii] = loss.item()
        ii = ii + 1


        if (i) % 10 == 0:
            print ("Epoch [{}/{}], Step [{}/{}] Loss: {:.4f}"
                   .format(epoch+1, num_epochs, i+1, total_step, loss.item()))

    # plot training error
    plt.plot(train_error[:ii])
    plt.xlabel('steps')
    plt.ylabel('training l1 error')
```

```
        plt.show()

        # evaluate current network on validation set for early stopping
        model.eval()
        with torch.no_grad():
            error = 0
            count = 0
            for images, labels, I_max, I_min, I_mean in test_loader:
                count = count + 1
                images = images.to(device)
                labels = labels.to(device)
                outputs = model(images)
                loss = criterion(outputs, labels)
                error = error + loss.item()
                validate_error[iii] = loss.item()
                iii = iii + 1

            error = error/count
            print('Current error: {}, Last error: {}'.format(error, last_error))

        # plot validation error
        plt.plot(validate_error[:iii])
        plt.xlabel('steps')
        plt.ylabel('validation l1 error')
        plt.show()

        # check if network hasn't been getting better
        if epoch > 0 and error > last_error:
            fail_count = fail_count + 1
            if fail_count == 3:
                break
        else:
            # reset early stopping clock and save current network
            fail_count = 0
            last_error = copy.copy(error)
            torch.save(model.state_dict(), savename)

        model.train()

        # Decay learning rate
        if (epoch+1) % 10 == 0:
            curr_lr /= 3
            update_lr(optimizer, curr_lr)

if __name__ == "__main__":

    dirname = os.path.dirname(__file__)
    train_input = os.path.join(dirname, 'trainingData/train')
    test_input = os.path.join(dirname, 'trainingData/validate')
    save_name = os.path.join(dirname, 'trainedNetworks/Unet_OPT_40_angles')
    number_angles = 40
```

```
    train_unet_OPT(train_input, test_input, save_name, number_angles)
```

A.5 Testing

```
"""
Function for testing Unet trained to remove streaks from undersampled OPT reconstructions

net: file name of trained network

test_input: path to folder with sinograms for testing

savename: folder path to save results to

number_angles: number of angles to be used for undersampled sinogram
"""


import torch
from skimage import io
from OPT_dataset import OPT_dataset
from unet_model_original import UNet
import os
import numpy as np

def test_network(net,test_input,savename,number_angles):
    # set up GPU
    device = torch.device('cuda' if torch.cuda.is_available() else 'cpu')

    # load network
    model = UNet(1,1).to(device)
    model.load_state_dict(torch.load(net))
    model.eval()

    # set up data set and data loader
    test_dataset = OPT_dataset(input_folder = test_input, crop_size = [-1,-1], augment = False,
          number_angles = number_angles)
    test_loader = torch.utils.data.DataLoader(dataset=test_dataset,
                                              batch_size=1,
                                              shuffle=False)
    # make save folders
    save_folder = savename
    save_folder1 = save_folder +'/output'
    save_folder2 = save_folder +'/label'
    save_folder3 = save_folder +'/input'

    if not os.path.isdir(save_folder):
        os.mkdir(save_folder)
    if not os.path.isdir(save_folder1):
        os.mkdir(save_folder1)
    if not os.path.isdir(save_folder2):
```

```
        os.mkdir(save_folder2)
    if not os.path.isdir(save_folder3):
        os.mkdir(save_folder3)

    count = 0
    with torch.no_grad():
        # loop over sinograms
        for images, labels, Imax, Imin, Imean in test_loader:
            images = images.to(device)
            labels = labels.to(device)
            outputs = model(images)

            out_image = outputs[0,0,:,:].cpu().numpy()
            label_image = labels[0,0,:,:].cpu().numpy()
            in_image = images[0,0,:,:].cpu().numpy()

            Imax = np.amax((np.amax(out_image), np.amax(label_image), np.amax(in_image)))
            Imin = np.amin((np.amin(out_image), np.amin(label_image), np.amin(in_image)))

            out_image = (65536*(out_image-Imin)/(Imax-Imin)).astype(np.uint16)
            label_image = (65536*(label_image-Imin)/(Imax-Imin)).astype(np.uint16)
            in_image = (65536*(in_image-Imin)/(Imax-Imin)).astype(np.uint16)

            io.imsave(os.path.join(save_folder1,str(count)+'.tif'), out_image)
            io.imsave(os.path.join(save_folder2,str(count)+'.tif'), label_image)
            io.imsave(os.path.join(save_folder3,str(count)+'.tif'), in_image)

            count = count + 1

if __name__ == "__main__":

    dirname = os.path.dirname(__file__)
    net = os.path.join(dirname, 'trainedNetworks/Unet_OPT_40_angles')
    test_input = os.path.join(dirname, 'fishData/sinograms')
    savename = os.path.join(dirname, 'fishData/40_projections')
    number_angles = 40

    test_network(net,test_input,savename,number_angles)
```

A.6 Speed test

```
"""
Function for testing speed of Unet trained to remove streaks from undersampled
OPT reconstructions

net: file name of trained network

test_input: path to folder with sinograms for testing

savename: folder path to save results to
```

```
number_angles: number of angles to be used for undersampled sinogram
"""

import torch
from OPT_dataset_no_labels import OPT_dataset
from unet_model_original import UNet
import os
import time
import numpy as np
from skimage import io
def speed_test(net,test_input,savename,number_angles):

    # start clock for total reconstruction time
    full_start = time.time()

    # check if GPU available
    device = torch.device('cuda' if torch.cuda.is_available() else 'cpu')

    # prepare network
    model = UNet(1,1).to(device)
    model.load_state_dict(torch.load(net))
    model.eval()

    # prepare data loading
    batch = 5
    test_dataset = OPT_dataset(input_folder = test_input, number_angles = number_angles)
    test_loader = torch.utils.data.DataLoader(dataset=test_dataset,
                                              batch_size=batch,
                                              shuffle=False)
    # prepare savefolder
    save_folder = savename
    if not os.path.isdir(save_folder):
        os.mkdir(save_folder)

    # prepare volume
    number_slices = 2118
    slice_size = 702
    volume = np.zeros((number_slices,1,slice_size,slice_size))

    chunks = np.arange(0,number_slices,batch)
    chunks = np.append(chunks,number_slices)

    # prepare speed measurement
    speed = np.zeros(chunks.size)

    count = 0
    with torch.no_grad():

        # make sure GPU is being honest about what it has done
        torch.cuda.synchronize()
```

```
        # time how long it takes to get streak corrupted slices
        load_data_time = time.time()
        for images, Imax, Imin, Imean in test_loader:

            torch.cuda.synchronize()
            print('loading_data_time')
            print(time.time()-load_data_time)

            # time how long it takes to put streak corrupted slices on GPU
            to_gpu_start = time.time()
            images = images.to(device)
            torch.cuda.synchronize()
            print('gpu_mount_time')
            print(time.time()-to_gpu_start)

            # time how long it takes to apply network to slices
            start = time.time()
            outputs = model(images)
            torch.cuda.synchronize()
            speed[count] = time.time()-start
            print('model_time')
            print(time.time()-start)

            # time how long it takes to prep re-normalisation
            prepare_normalisation_time = time.time()
            Imaxs, c, x, y = np.meshgrid(Imax,1,np.arange(slice_size),np.arange(slice_size))
            Imins, c, x, y = np.meshgrid(Imin,1,np.arange(slice_size),np.arange(slice_size))
            Imeans, c, x, y = np.meshgrid(Imean,1,np.arange(slice_size),np.arange(slice_size))
            print('NormPrep')
            print(time.time()-prepare_normalisation_time)

            # time how long it takes gather results from GPU
            move_data_time = time.time()
            numpy_outputs = np.multiply(outputs.cpu().numpy()+Imeans,Imaxs-Imins)+Imins
            #numpyOutputs = outputs.cpu().numpy()
            torch.cuda.synchronize()
            print('move_data_time')
            print(time.time()-move_data_time)

            put_in_volume = time.time()
            volume[chunks[count]:chunks[count+1],0,:,:] = numpy_outputs[0:(chunks[count+1]-chunks[count
                ]),0,:,:]
            print('intoVolumeTime')
            print(time.time()-put_in_volume)
            count = count + 1
            load_data_time = time.time()

    # save volume
    volume = (65536*(volume-np.amin(volume))/(np.amax(volume)-np.amin(volume))).astype(np.uint16)
    for count in range(number_slices):
        io.imsave(os.path.join(save_folder,str(count)+'.tif'), np.squeeze(volume[count,0,:,:]))
```

```
    print('reconstruction_time')
    print(np.mean(speed))
    print('standard_error')
    print(np.std(speed)/np.sqrt(speed.size))
    print('Total_time')
    print(time.time()-full_start)

    return (np.mean(speed), np.std(speed), time.time()-full_start)

if __name__ == "__main__":

    dirname = os.path.dirname(__file__)
    net = os.path.join(dirname, 'trainedNetworks/UnetSinoFinal64')
    test_input = os.path.join(dirname, 'fishData/sinograms')
    savename = os.path.join(dirname, 'fishData/speedtest')
    number_angles = 64

    speed_test(net,test_input,savename,number_angles)
```